



HAL
open science

The effect of morphology on the electrochemical properties of nanostructured metal oxide thin films: the studies based on multi-scale time-resolved fast electrogravimetric techniques

Fatemeh Razzaghi

► **To cite this version:**

Fatemeh Razzaghi. The effect of morphology on the electrochemical properties of nanostructured metal oxide thin films: the studies based on multi-scale time-resolved fast electrogravimetric techniques. Chemical Physics [physics.chem-ph]. Université Pierre et Marie Curie - Paris VI, 2016. English. NNT: 2016PA066346 . tel-01477408

HAL Id: tel-01477408

<https://theses.hal.science/tel-01477408>

Submitted on 27 Feb 2017

HAL is a multi-disciplinary open access archive for the deposit and dissemination of scientific research documents, whether they are published or not. The documents may come from teaching and research institutions in France or abroad, or from public or private research centers.

L'archive ouverte pluridisciplinaire **HAL**, est destinée au dépôt et à la diffusion de documents scientifiques de niveau recherche, publiés ou non, émanant des établissements d'enseignement et de recherche français ou étrangers, des laboratoires publics ou privés.

Thèse de doctorat

Pour l'obtention du grade de Docteur

De l'Université Pierre et Marie Curie

École doctorale 388 - Chimie Physique et Chimie Analytique de Paris Centre

**The Effect of Morphology on the Electrochemical
Properties of Nanostructured Metal Oxide Thin Films:
The Studies based on Multi-scale Time-resolved Fast
Electrogravimetric Techniques**

Par **Fatemeh Razzaghi**

Directeur de thèse : Dr Hubert Perrot

Présentée et soutenue publiquement le 29 septembre 2016,

Devant un jury composé de :

Nicole Jaffrezic	DR CNRS Émérite	Rapporteur
Francois Tran-Van	Prof. Univ. F. Rabelais	Rapporteur
Christine Mousty	DR CNRS	Examineur
Farzaneh Arefi-Khonsari	Prof. UPMC	Présidente de Jury
Hubert Perrot	DR CNRS	Directeur de thèse
Patricia Beaunier	IR UPMC	Invitée

Dedicated to my mother. . .

Acknowledgements:

First of all, I would like to express my love to my dearest mother for her always unconditional love and support, particularly during my education years in France, it is with no doubt because of her high standard expectations for me if today I stand at this glamorous point in my life. My deepest love and appreciation to my late father, thinking about him at this moment of my life refreshes all the sweet memories of a joyful childhood I spend around him, may his soul rest in peace.

I would like to express my highest regards to my thesis supervisor, Dr Hubert Perrot, for his seriousness, kindness and full support during all the steps of this project from beginning to the end. Today, he is one of the pioneers of EQCM and fast electrogravimetric studies in the country and it was indeed a great honor to have him as my mentor. I will be always grateful for all that I have learned from him.

I am thoroughly grateful for the prosperous collaboration we had with Prof Farzaneh Arefi and Dr Jerome Pulpytel, Plasma field specialists in LISE.

I am really thankful to Dr Christine Mousty (ICCF, Clermont University) for the fruitful collaboration we had regarding the studies on layered double hydroxide (LDHs) materials.

I am indeed grateful to Dr Patricia Beaunier for her high quality work and for all that I've learned from her in the field of surface classical characterization techniques (SAED, TEM, HR-TEM).

I am thankful to: Dr Francois Huet (LISE) director, Mrs Françoise Pillier (LISE) SEM-FEG Microscopy, Mr Cyril Bazin (LISE) and Mr Benoit Baptiste (IMPIC lab) X-ray Diffractometry analysis, Dr Houssam Fakhouri (LISE) RF reactive Sputtering, Dr Catherine Debiemme-Chouvy (LISE) XPS analysis, Mrs Sandra Casale (LRS) HR-TEM, Mr Axel Desnoyers de Marbaix (LISE) Mecanicien, Mr Daniel Rose (LISE) Electrician, Mrs Florence Billon (LISE) Engineer and Mrs Veronique Martin (LISE) documentalist.

During these three years of my PhD project I received the permanent kindness on the behalf of all my friends and colleagues, my kindest regards to Dr Mireille Turmine and Dr Vincent Vivier, my colleague Freddy Escobar, PhD Students: Pierre, Marie S, Thomas, Azadeh, Larbi.

I am also thankful to Miss Marie Brel, our previous M1 student, with whom I have initiated the work on composite materials.

Lastly, I would like to thank all my other friends for their support, special thanks to my lovely sister Maryam.

Table of Contents

General Introduction	1
Résumé du Chapitre I	3
Chapter I: Bibliography	6
I. Supercapacitors as Energy Storage Devices	6
I-1. Basic principle of Electrochemical Supercapacitors	8
Two types of Electrochemical Supercapacitors	9
I. 1.1. Electrostatic supercapacitors	9
I .1.2 Faradaic supercapacitors	9
II. State of the Art of Different Types of Electrochemical Capacitors (ECs):	10
II-1. EC based on Carbon materials	11
II-2. Pseudocapacitive oxide materials	14
II. 2. 1. WO ₃	14
II. 2. 2. TiO ₂	19
II. 2. 3. MnO ₂	20
II. 2. 4. RuO ₂	21
II-3. Conducting Polymers	23
II-4. Carbon-MO _x Composites	26
III. Strategies Toward New Ways of Materials Design for High Performance ECs	29
III. 1. Elaboration Methods and Process	29
III-2. Materials Nanostructuration for Development of Flexible Device Architectures	31
IV. Diagnostics Tools for MO_x based Electrodes for Energy Storage	34
IV-1. Surface and Structural Analysis: SEM, TEM, XRD, XPS, FT-IR.....	34
(i) SEM images	34
(ii) TEM images	36
(iii) XRD analysis	38
(iv) FTIR methods	38
IV-2. Electrochemical Tools	39
(i) Cyclic voltammetry	39
(ii) EIS technique	41
(iii) Quartz Crystal Microbalance	43
V. The Scope and Principle Objectives of Thesis Project	45
VI. References	47
Résumé du Chapitre II	56

Chapter II. Theoretical and Experimental Section	60
I. Introduction	60
II. Experimental	60
II-1. Electrochemical and (Electro)gravimetric Characterization Techniques	60
II-1.1. Quartz Crystal Microbalance (QCM)	60
II-1.1.1. Principle of QCM	61
II-1.1.2. Experimental Set-up	63
II-1.2. Cyclic Electrogravimetry (EQCM)	63
II-1.2.1. Principle	63
II-1.3. Electrochemical Impedance Spectroscopy (EIS)	65
II-1.3.1. Principle	65
II-1.3.2. Experimental Set-Up	67
II-1.4. <i>ac</i> -electrogravimetry; Fast Electrogravimetric Method	68
II-1.4.1. Principle	68
II-1.4.2. Experimental Method: $\Delta V_f/\Delta V$	69
II-1.4.3. Calibration and the System Corrections	71
II-1.4.4. Transfer Function of the Frequency/Voltage Converter: $\Delta V_f/\Delta e(\omega)$	72
II-1.4.5. Calibration of the Synthesizer: $\Delta f_s/\Delta e$	73
II-2. Preparation of MO _x based Thin Films Electrodes	74
II-2.1. Elaboration of Compact, Less Porous and Highly Porous TiO ₂ by RF Reactive Magnetron Sputtering	74
II-2.2. Electrochemical Elaboration of Amorphous Compact & Amorphous Mesoporous WO ₃	76
II-2.3. Electrochemical Elaboration of Compact and Mesoporous RuO _x .nH ₂ O	79
II-2.4. Elaboration of CNTs/RuO _x .nH ₂ O Films	81
II-3. Structural and Morphological Investigation Methods	81
II-3.1. Scanning Electron Microscopy (SEM) and Energy Dispersive X-rays (EDX)	81
II-3.2. Transmission Electron Microscopy (TEM).....	82
II-3.3. High-Resolution Transmission Electron Microscopy (HR-TEM)	83
II-3.4. Selected Area Electron Diffraction (SAED)	84
II-3.5. X-ray Diffraction (XRD)	86
II-3.6. X-ray Photoelectron Spectroscopy (XPS).....	87
III. Theory of <i>ac</i>-electrogravimetry	89
III-1. A Three Species Model with a Cation, Anion and Free Solvent Contribution	89
III-2. Electrochemical reactions and kinetics	90
III-3. Dynamic regime and flux of each species	91

III-4. Charge/ potential transfer function	92
III-5. Electrochemical impedance transfer function	93
III-6. Mass/potential transfer function	94
References	95
Résumé du Chapitre III	98
Chapter III: TiO₂.....	102
I. Introduction	102
II. Structure and Morphology Study of Dense, Less Porous and Highly porous Thin TiO₂ Films	104
III. Electrochemical Study of Dense, Less Porous and Highly Porous TiO₂ Thin Films	107
III-1. Cyclic voltammetry and EQCM study in LiClO ₄	107
III-2. Molecular Mass Estimation	108
IV. <i>ac</i>-electrogravimetry studies of TiO₂ Thin Films	109
IV-1. <i>ac</i> -electrogravimetric studies of Less Porous and Highly Porous TiO ₂ Thin Films in 0.5M aqueous solution of LiClO ₄	110
IV-2. <i>ac</i> -electrogravimetric studies of Less Porous and Highly Porous TiO ₂ Thin Films in 0.5M aqueous solution of NaClO ₄	118
IV-3. <i>ac</i> -electrogravimetric studies of Highly Porous TiO ₂ Thin Films in 0.5M LiClO ₄ , Comparison between Aqueous LiClO ₄ (aq) and Organic LiClO ₄ (PC) Solutions	125
V. Conclusion	133
VI. References	135
Résumé du Chapitre IV	137
Chapter IV: WO₃.....	141
I. Introduction	141
II. Structure and Morphology Study of Dense and Mesoporous Thin Films	143
III. Electrochemical studies Study of Dense and Mesoporous WO₃ Thin Films	146
III-1. The cyclic voltammetry and EQCM study	147
III-2. <i>ac</i> -electrogravimetric study of dense and mesoporous WO ₃ films	150
(i) <i>ac</i> -electrogravimetric exploration at -0.3V vs Ag/AgCl	150
(ii) <i>ac</i> -electrogravimetric measurements versus potential	157
IV. Conclusion	161
V. References	163
Résumé du Chapitre V	167

Chapter V: RuO_x.xH₂O	171
I. Introduction	171
II. Structural Characterizations	172
II-1. XRD Characterization of as-prepared RuO _x .xH ₂ O and RuO ₂ heated at 450 °C	172
II-2. SEM-FEG Characterization	173
(i) Compact and Mesoporous RuO _x .nH ₂ O	173
(ii) SWCNTs / RuO _x .nH ₂ O	175
II-3. Targeting Evolution of Morphology and Crystallography by SAED: The effect of calcination	176
(i) The Effect of Heat Treatment on Compact Ruthenium oxide	176
(ii) The Effect of Heat Treatment on Porous Ruthenium oxide	176
(iii) The Effect of Structuration on Hydrous Ruthenium Oxide Films	177
II-4. HR-TEM Results	178
(i) Mesoporous Ruthenium oxide	178
(ii) SWCNTs / RuO _x .nH ₂ O	179
II-5. XPS Characterization, The impact of Heat Treatment	179
(i) XPS results of RuCl ₃ .xH ₂ O Precursor	180
(ii) RuO _x .nH ₂ O and RuO ₂	182
III. Electrochemical Characterization: The Cyclic Voltammetry and Classical EQCM Study	184
III-1. Cyclic electrogravimetry	184
III-2. Specific Capacitance Calculation	186
III-3. Relative Molecular Mass Estimation	188
IV. <i>ac</i>-electrogravimetric results for compact and mesoporous RuO_x.nH₂O	189
IV-1. <i>ac</i> -electrogravimetric results for compact and mesoporous RuO _x .nH ₂ O in H ₂ SO ₄ 0.5 M aqueous solutions	189
IV-2. <i>ac</i> -electrogravimetric results for compact and mesoporous RuO _x .nH ₂ O in Na ₂ SO ₄ 0.5 M aqueous solution	198
V. Nanocomposite films of CNTs / RuO₂.xH₂O Investigated by <i>ac</i>-Electrogravimetric Methods	204
V-1. EQCM study of SWCNTs/RuO _x .nH ₂ O film in aqueous solution	204
V-2. <i>ac</i> -electrogravimetric study of SWCNTs/RuO _x .nH ₂ O film in H ₂ SO ₄ aqueous solution	205
VI. Conclusion	211
VII. References	213
General Conclusion & Perspectives	216

General Introduction

During this thesis project, it was attempted to underline the importance of investigating the ion's exchange phenomena at the metal oxides electrode/electrolyte interface in order to understand and to furtherly improve their promised energetic performances mostly as highly functional electrodes for supercapacitors. Indeed, the key phenomena for all these electrodes functionalities originates in the ion's exchange at the interface of electrode/electrolyte, it is crucial to investigate the role of electrolyte composition, to identify the status of transferred ions and the solvation effect also to investigate their dynamics of transfer at the interface. Consequently, we have decided to focus on the capabilities of a non-classical methodology so-called, *ac*-electrogravimetry.

Another subject of crucial matter for our attention was to illustrate the most fundamental reasons of the electrochemical improvements brought by nanostructuration. In fact, the materials structuration with favorable morphologies and unique properties would alter their functionalities and this can effectively be deeply characterized by *ac*-electrogravimetry. Different morphologies of TiO₂, WO₃ and RuO₂ metal oxides were prepared as furtherly detailed. As a consequent, during this thesis project, the investigations were performed to see what differences in behavior are brought by procuring porosity within these films. In other words, how mesoporous films with small pore sizes, and large surface area to volume ratios could facilitate the ion intercalation/electroadsorption process involved with our chosen synthesized MO_x electrodes. More importantly it was attempted to see how *ac*-electrogravimetry as a non-classical coupled methodology would be served for our study to extract fine dynamics details unreachable with classical tools. To pursue this major goal our results were systematically categorized as following:

- The first chapter provides a general look toward the highlighted aspects and applications of materials with potential usefulness in energy storage devices. Different examples of each category of materials with emphasizing on MO_x based devices are brought to attention. The recent utile elaboration methods for fabrication of MO_x based electrodes are mentioned. The new ways of materials design in order to upgrade high performance in the electrodes are discussed and finally, the various diagnostics tools for MO_x based electrodes including both structural and electrochemical techniques are introduced. Based on these methodologies the scope of this thesis project which underlines the importance of *ac*-electrogravimetry as our main chosen methodology is presented.

- The second chapter is dedicated to necessary theoretical and experimental basics commonly used during this thesis project. In the first part, the different components of the model used for *ac*-electrogravimetric fittings are introduced. It is shown how different *ac*-electrogravimetric transfer functions for an electroactive electrode system with responses to ions transfer are obtained. Another part is focused on the description of various structural and electrochemical characterization techniques applied as diagnostic tools to study the influence of the different electrochemical and physical preparation methods used for fabricating our MO_x electrodes with different morphologies.
- The third chapter underlines the results obtained for different morphologies of amorphous non-porous and amorphous porous TiO₂ deposited by reactive magnetron RF Sputtering. SEM-FEG accompanied with EDX analysis and HR-TEM were used for the structural studies. Both classical EQCM and then, *ac*-electrogravimetry were used in LiClO₄ and NaClO₄ aqueous medium to investigate the impact of a porous morphology and also identify and separate the contribution of the charged and/or uncharged species during the charge compensation process. A comparison is also made to understand the impact of accompanying solvent whether it is organic or aqueous.
- The fourth chapter includes the results obtained for electrochromic mesoporous WO₃ prepared by surfactant-assisted electrodeposition. A comparison in behavior is made between the mesoporous electrode with the compact tungsten trioxide electrode fabricated by electrodeposition but in the absent of surfactant molecules. XPS, SEM-FEG, EDX analysis and HR-TEM were used for the primary structural studies. Then, classical EQCM and *ac*-electrogravimetry were used in LiClO₄ aqueous medium to investigate the impact of the nanostructuration, and to identify/separate the contribution of the charged and/or uncharged species during the charge compensation process.
- The last chapter was dedicated to the results obtained for pseudocapacitive hydrous RuO_x.nH₂O films prepared in both compact and mesoporous morphologies via the same electrochemical route used for WO₃ electrode preparation. The structure, the morphology and the composition of these electrodes were analyzed by XRD, XPS, TEM, SAED, HR-TEM and SEM-FEG. Both classical EQCM and *ac*-electrogravimetric techniques were exploited to study the impact of structuration and the ions transfer behavior of the as-prepared compact and mesoporous hydrous RuO_x.nH₂O films in aqueous H₂SO₄ and Na₂SO₄. The second part of this chapter was attributed to the electrogravimetric investigations of CNTs/RuO_x.nH₂O in order to

pursue the ion's kinetics evolution involved with a new 3D composite structure in aqueous H_2SO_4 electrolyte.

Résumé du Chapitre I

Ce chapitre fournit un état de l'art rapide en ce qui concerne les matériaux potentiellement utiles dans les dispositifs de stockage d'énergie, notamment les supercondensateurs. Tout d'abord, le principe des supercondensateurs électrochimiques ainsi que les principales catégories de dispositifs sont brièvement présentées. Deuxièmement, les différentes catégories de matériaux qui présentent de grandes potentialités pour ces dispositifs **les oxydes de métaux, les polymères conducteurs, les films carbone / carbone et les composites MO_x -carbone**, seront détaillés avec différents exemples pour chacune des catégories. Le sujet de thèse met l'accent principalement sur les systèmes à base de MO_x où différents exemples d'oxydes métalliques sont discutés.

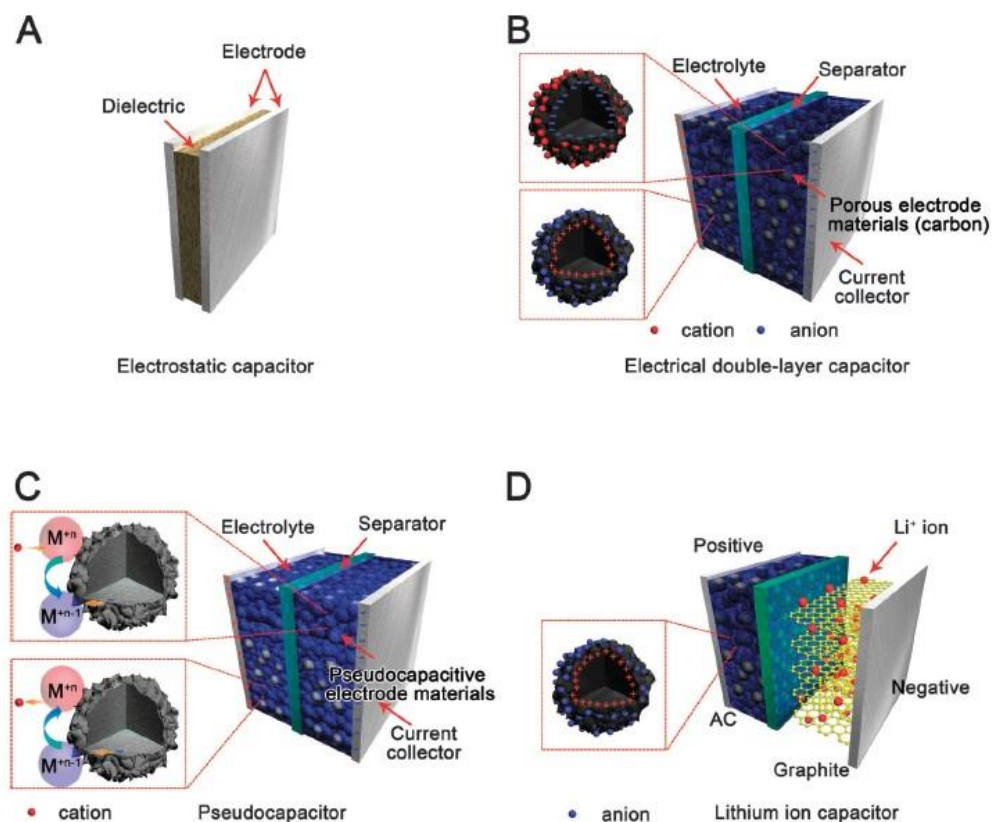
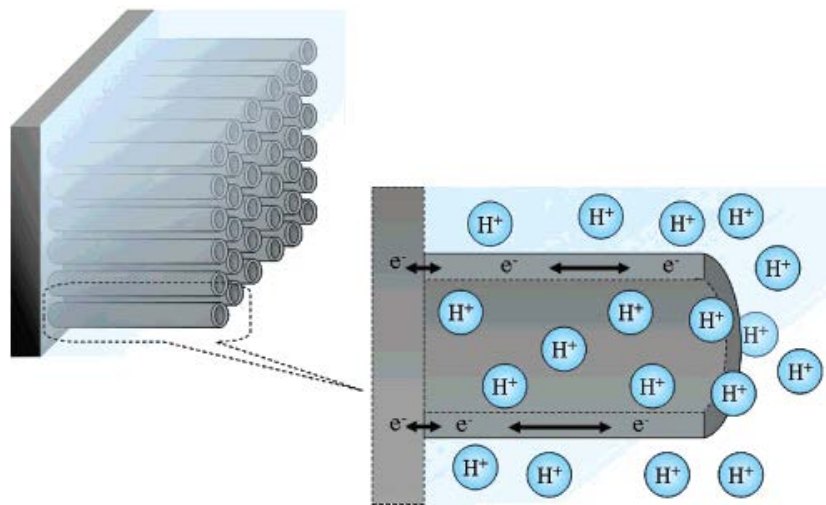


Schéma de principe d'un condensateur électrostatique (A), d'un condensateur à double couche électrique (B), d'un pseudocondensateur (C) et d'un condensateur hybride [9].

Pour améliorer les performances d'électrodes à base d'oxyde métallique, une attention a été portée sur l'effet de la nanostructuration de ces films, selon diverses morphologies et propriétés pour la mise au point de dispositifs de stockage d'énergie électrochimique. De nouvelles

nanostructures, avec des pores de petite taille et de grands rapports surface sur volume, sont censées faciliter les processus de transfert d'ions à l'interface film structuré/électrolyte. En effet, ce phénomène est essentiel car il intervient dans tous les dispositifs de stockage d'énergie y compris les supercondensateurs. Ces améliorations peuvent être attribuées à (i) un transport facilité avec une très faible longueur de diffusion, (ii) une zone de contact électrode/électrolyte élargie, et (iii) une meilleure gestion du stress mécanique/déformation du matériau lors de l'intercalation/l'électroadsorption d'ions. En conséquence, divers procédés de synthèse ont été développés et sont mentionnés dans une section appropriée.



Dessin idéal d'un matériau d'électrode pour des supercondensateurs de type $\text{RuO}_2 \cdot x\text{H}_2\text{O}$ nanotubulaires. L'architecture mésoporeuse, la nature hydratée des surfaces, et la conductivité métallique fournissent aux protons et aux électrons des "autoroutes" qui doivent favoriser les différents processus électrochimiques et ainsi permettre d'obtenir des condensateurs très efficaces [68].

Dans une seconde partie de ce chapitre I, les différentes techniques d'imagerie et les outils de diagnostic électrochimique pour des électrodes à base de MO_x sont présentés.

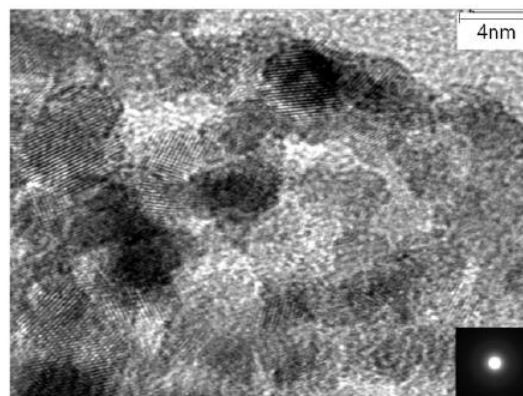
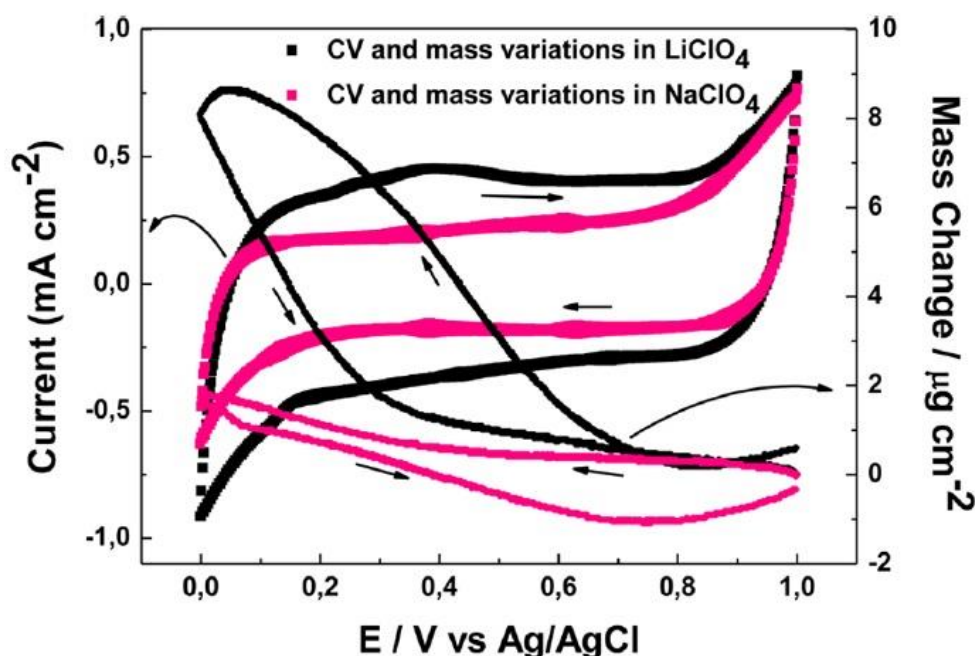


Image HR-TEM d'un échantillon $\text{RuO}_2 \cdot x\text{H}_2\text{O}$ synthétisé en utilisant un agent tensio-actif pour nanostructurer le film [74].

Une méthodologie attractive pour étudier l'intercalation / l'électroadsorption des ions au sein de ces matériaux est basée sur des dispositifs de type microbalance à quartz (QCM). Il y a eu diverses études utilisant une microbalance à quartz comme sonde gravimétrique in-situ afin d'étudier ces phénomènes au sein d'oxydes métalliques ou d'électrodes à base de carbone.



Caractérisation EQCM d'un film de Li-MnO_2 de type Birnessite dans des électrolytes aqueux de LiClO_4 et NaClO_4 [107].

Malgré les informations utiles données par EQCM lorsqu'il s'agit de décrire les mécanismes d'intercalation ou d'électroadsorption ioniques, impliqués lors du stockage de charges dans des matériaux capacitifs, quelques limitations apparaissent. Les microbalances à quartz classiques donnent une réponse globale correspondant en fait à plusieurs processus possibles et plus ou moins simultanés. Des ions nus, des ions avec des coquilles de solvation et des molécules de solvant libre peuvent ainsi être associés, directement ou indirectement, aux différents processus électrochimiques. En outre, les ions peuvent perdre une partie de leur solvation pour accéder aux sites situés dans les plus petits pores. Ces différentes voies possibles associées à des aspects cinétiques n'ont jamais été suivies à l'aide de dispositifs classiques d'EQCM.

L'objectif majeur de ce projet de thèse est de mettre en valeur un outil de caractérisation alternatif afin de surmonter les limitations des EQCM classiques pour étudier les mécanismes d'électroadsorption/d'intercalation dans les électrodes associées aux systèmes pseudo-capacitif. Cette méthode, dite d'électrogravimétrie à courant alternatif ou *ac*-électrogravimétrie est constituée d'un couplage entre la spectroscopie d'impédance électrochimique (EIS) et une

microbalance à quartz rapide (QCM). Cette approche a été développée dans un nombre limité de laboratoires dans le monde.

Chapter I: Bibliography

This Chapter provides an introduction to the highlighted aspects and applications of materials with potential usefulness in energy storage devices, more importantly supercapacitors and/or micro-capacitors. First, the functionality of electrochemical supercapacitors and their main categories are briefly introduced. Secondly, different categories of materials with great potentialities in these devices are mentioned including metal oxide, conducting polymers, carbon/carbon and MO_x-Carbon composites based supercapacitors. Different examples of each category are brought to attention. Since the thesis subject emphasizes mainly on MO_x based devices, a few examples of different metal oxides are also discussed. Then, the recent utile elaboration methods for fabrication of MO_x based electrodes are mentioned. Another alternatively interesting followed aspect is the new ways of materials design in order to upgrade high performance in the electrodes. Finally, the various diagnostics tools for MO_x based electrodes including both structural and electrochemical techniques are introduced and based on these methodologies the scope of this thesis project is presented.

I. Supercapacitors as Energy Storage Devices:

With the rapid development of the global economy, the depletion of fossil fuels, and increasing environmental pollution, there is an urgent need for efficient, clean, and sustainable sources of energy, as well as new technologies associated with energy conversion and storage. In many application areas, some of the most effective and practical technologies for energy conversion and storage are fuel cells and batteries/electrochemical supercapacitors. In recent years, electrochemical supercapacitors have attracted significant attention, mainly due to their high power density, long lifecycle, and bridging function for the power/energy gap between traditional dielectric capacitors (which have high power output) and batteries (which have high energy storage). The earliest electrochemical supercapacitors patent was filed in 1957. However, not until the 1990s did electrochemical supercapacitors technology begin to draw some attention, in the field of hybrid electric vehicles. It was found that the main function of electrochemical supercapacitors could be to boost batteries or fuel cells in a hybrid electric vehicle to provide the necessary power for acceleration, with an additional function being to recuperate brake energy [1–10]. Further developments have led to the recognition that

electrochemical supercapacitors can play an important role in complementing batteries or fuel cells in their energy functions by providing back-up power supplies to protect against power disruptions. As a result, the US Department of Energy has designated electrochemical supercapacitors to be as important as batteries for future energy storage systems. Many other governments and enterprises have also invested time and money into exploring, researching, and developing electrochemical supercapacitors technologies [1–10].

Recent years have yielded major progress in the theoretical and development of electrochemical supercapacitors, as evinced by a large number of research articles and technical reports [4–10]. At the same time, the disadvantages of electrochemical supercapacitors including low energy density and high production cost have been identified as major challenges for the furtherance of electrochemical supercapacitors technologies. To overcome the obstacle of low energy density, one of the most intensive approaches is the development of new materials for electrodes. Most popular today are carbon particle materials, which have high surface areas for charge storage. But in spite of these large specific surface areas, the charges physically stored on the carbon particles in porous electrode layers are unfortunately limited. Electrochemical Supercapacitors (ES) of this kind, called Electrical Double-Layer Supercapacitors (EDLS), have a limited specific capacitance (measured in Faraday per gram of the electrode material) and a low electrochemical supercapacitors energy density.

Advanced approaches to increase the ES energy density are to hybridize the electrode materials by adding electrochemically active materials to a carbon-particle-based ES electrode layer or to completely replace the carbon materials with another electrochemically active material. ES with electrochemically active materials as electrodes are called pseudo-supercapacitors [4]. It has been demonstrated that faradaic or hybrid double-layer supercapacitors can yield much higher specific capacitance and electrochemical supercapacitors energy density than EDLS. Regarding advanced electrochemical supercapacitors materials, metal oxides such as ruthenium oxides and manganese oxides are considered the most promising materials for the next generation of electrochemical supercapacitors. Therefore, in this project we pay particular attention to metal oxides and their applications in electrochemical supercapacitors electrodes. First, however, we provide some introductory background on electrochemical supercapacitors, which we hope will facilitate our review and analysis of the literature. Finally, we will discuss the direction that future research in electrochemical supercapacitors might be expected to take.

I-1. Basic principle of Electrochemical Supercapacitors

An electrochemical supercapacitor is a charge-storage device similar to batteries in design and manufacturing. As shown in Fig. I-1, an ES consists of two electrodes, an electrolyte, and a separator that electrically isolates the two electrodes. The most important component in an electrochemical supercapacitor is the electrode material. In general, the ES's electrodes are fabricated from nanoscale materials that have high surface area and high porosity. It can be seen from Fig. I-1 that charges can be stored and separated at the interface between the conductive solid particles (such as carbon particles or metal oxide particles) and the electrolyte. This interface can be treated as a capacitor with an electrical double-layer capacitance, which can be expressed as the following equation:

$$C = \frac{A\varepsilon}{d}$$

where A is the area of the electrode surface, which for a supercapacitor should be the active surface of the electrode porous layer; ε is the medium (electrolyte) dielectric constant, which will be equal to 1 for a vacuum and larger than 1 for all other materials, including gases; and d is the effective thickness of the electrical double layer.

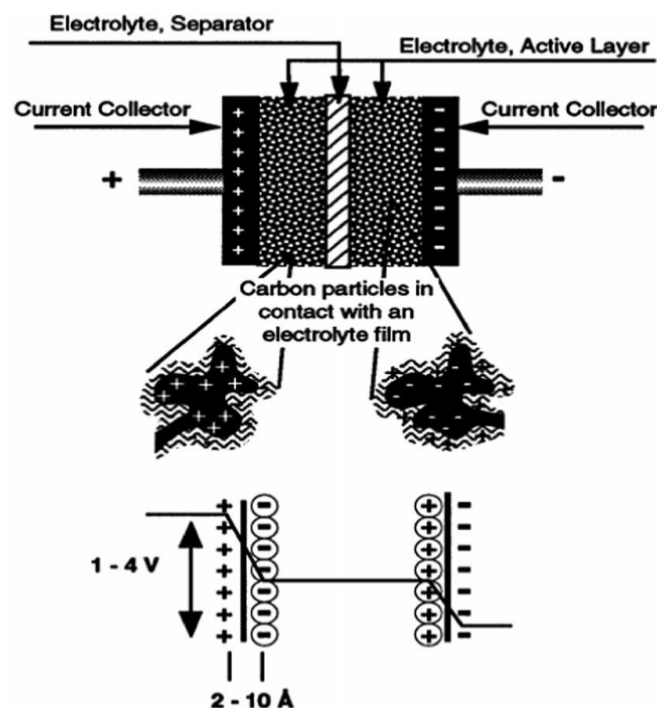


Fig. I-1. Principles of a single-cell double-layer capacitor and illustration of the potential drop at the electrode/electrolyte interface [11].

As described in the Introduction, two types of ES exist. One is the EDLS, in which the electrode material, such as carbon particles, is not electrochemically active. In other words, there is no electrochemical reaction on the electrode material during the ES charging and discharging

processes, and pure physical charge accumulation occurs at the electrode/electrolyte interface. The other type is the faradaic supercapacitors, in which the electrode material is electrochemically active, e.g. metal oxides, which can directly store charges during the charging and discharging processes.

Two types of Electrochemical Supercapacitors

1.1.1. Electrostatic supercapacitors

The capacitance of the electrode/interface in an electrostatic or EDLS is associated with an electrode-potential-dependent accumulation of electrostatic charge at the solid/electrolyte interface. As shown in Fig. I-1, this electrical double-layer capacitance comes from electrode material where an excess or a deficit of electric charges can be accumulated on the electrode side as electrolyte ions must counterbalance them on the electrolyte side in order to meet electroneutrality.

During the process of charge, the electrons travel from the negative electrode to the positive electrode through an external load. Within the electrolyte, cations move towards the negative electrode while anions move towards the positive electrode. During discharge, the reverse processes take place. In this type of supercapacitors, no charge transfer across the electrode/electrolyte interface is observed and no net ion exchanges occur between the electrode and the electrolyte.

1.1.2 Faradaic supercapacitors

Faradaic supercapacitors or pseudocapacitors are different from electrostatic or EDLS. When a potential is applied to a faradaic supercapacitor, fast and reversible faradaic reactions (redox reactions) take place on the electrode materials and involve the passage of charge across the interface, similar to the charging and discharging processes that occur in batteries, resulting in faradaic current passing through the supercapacitor cell. Materials undergoing such redox reactions include conducting polymers and several metal oxides, including RuO₂, MnO₂, or Co₃O₄. Three types of faradaic processes can occur at faradaic supercapacitors electrodes: direct electrochemical reactions it is a little bit confused as in EDLC it is electro adsorption (for example, adsorption of hydrogen on the surface of platinum or gold), redox reactions of transition metal oxides (e.g. RuO₂), and reversible electrochemical doping–dedoping in conducting polymer based electrodes. It has been demonstrated that these faradaic electrochemical processes not only extend the working voltage but also increase the specific

capacitance of the supercapacitors. Since the electrochemical processes occur both on the surface and in the bulk near the surface of the solid electrode, a faradaic supercapacitor exhibits far larger capacitance values and energy density than an EDLS. As reported by Conway et al. [11] the capacitance of a faradaic supercapacitors can be 10–100 times higher than the electrostatic capacitance of an EDLS. However, a faradaic supercapacitor usually suffers from relatively lower power density than an EDLS because faradaic processes are normally slower than nonfaradaic processes. Moreover, because redox reactions occur, faradaic supercapacitors often lack stability during cycling, similarly to batteries. It is worth mentioning that hybrid faradaic supercapacitors with an asymmetrical electrode configuration (e.g. one electrode consists of electrostatic carbon material while the other consists of faradaic capacitance material) have been extensively studied recently to capitalize on both electrode materials advantages in improving overall cell voltage, energy, and power densities. In this kind of hybrid supercapacitor, both electrical double-layer capacitance and faradaic capacitance mechanisms occur simultaneously, but one of them plays a greater role. The different configurations are presented in figure I-2.

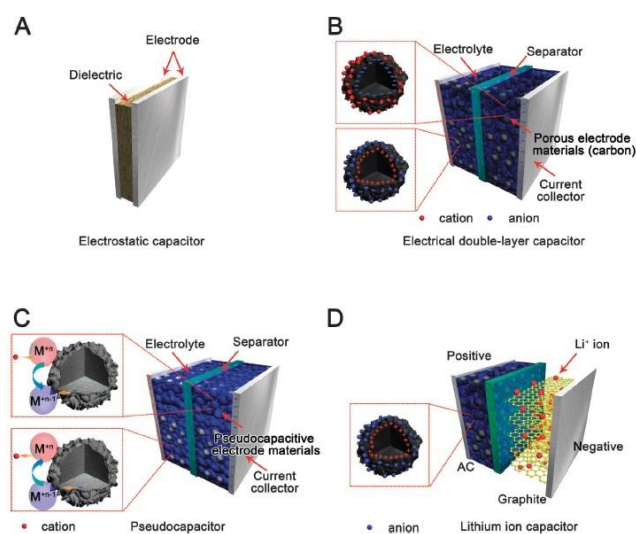


Fig. I-2. Schematic diagram of (A) an electrostatic capacitor, (B) an electric double-layer capacitor, (C) a pseudocapacitor, and (D) a hybrid-capacitor [9].

II. State of the Art of Different Types of Electrochemical Capacitors (ECs):

The most promising materials for electrochemical supercapacitors should utilize both the fast and reversible faradaic pseudocapacitance coming from the redox transitions of the interfacial electroactive species and the indefinitely reversible capacitance of electric double-layer formed at the electrolyte–electrode interface. Based on this point of view, the electrochemical

supercapacitors can be considered as a hybrid device exhibiting transitional behavior between batteries and capacitors. Potential candidates of electrodes should be consisted of electroactive materials with very high surface areas, which prosecute the fast reversible redox transitions in the potential window of charge and discharge.

ECs are intermediate systems between dielectric capacitors and batteries. While batteries able to store higher energy density than supercapacitors, they deliver less power; as compared to dielectric capacitors, supercapacitors can store higher energy density with less delivered power. These particular properties make them suitable for numerous applications such as power electronics, spatial or military field; they can also be used in hybrid electric vehicle in order to help the stop and go function, to provide peak power for improved acceleration, for energy recovery.

Three main classes of supercapacitors are described in the literature: **metal oxide** [12–22], **electronically conducting polymer** [23–30] and **Carbon/Carbon supercapacitors** [31,32–37]. Recently, hybrid supercapacitors have been developed where an activated carbon electrode is associated with a faradic electrode [38–53].

II-1. EC based on Carbon materials:

Carbon/Carbon supercapacitors have been largely investigated because of their low-cost, high cycling-life and high capacitance. Small (few farads) up to large-size (5000 F) devices are commercially available (Maxwell, Epcos, Panasonic, etc.). Highly-porous carbons are used as electrode material due to their high surface area, good electronic conductivity and high electrochemical stability; the most frequently used is activated carbon ($1500\text{--}2000\text{ m}^2\text{ g}^{-1}$). Charge storage is performed through the reversible electro adsorption of the ions at the active material/electrolyte interface; no faradaic reactions occur during the charge–discharge of the supercapacitor [54].

Carbon materials, such as activated carbons (ACs) and carbon nanotubes (CNTs) (Fig. I-3), usually exhibit good stability but limited capacitance values. It is clear that EDLCs processes are surface phenomena, and hence the performance greatly depends on the electrolyte-accessible surface area. The micropores in carbon materials are inaccessible by the electrolyte, resulting in the inability of the double layer to be formed inside the pores. This result leads to a decrease in the capacitance value (10–20% of the ‘theoretical’ capacitance) of ACs. Good electrical conductivity, high chemical and mechanical stability, and an optimized nanostructure are also other important factors that are responsible for achieving high capacitance values. The

potential windows in nonaqueous electrolytes are generally larger than those obtained in aqueous media, although the overpotential of hydrogen evolution on carbons is high, especially in neutral electrolytes.

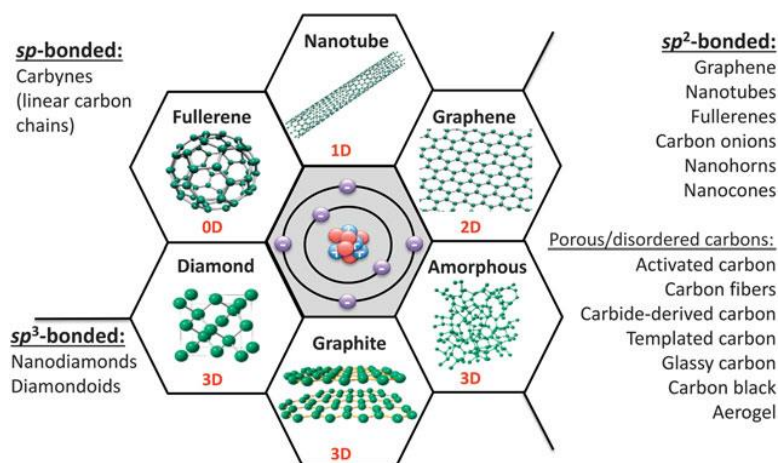


Fig. I-3. The most common carbon materials classified based on their bonding (hybridization of orbitals of carbon atoms) and dimensionality (i.e., the number of dimensions not confined to the nanoscale). Whereas graphite, carbon fibers, glassy carbon, activated carbons, carbon black, and diamond are already widely used in industry, fullerenes and fullerides, carbon onions (multishell fullerenes), nanotubes, whiskers, nanofibers, cones, nanohorns, nanorings, nanodiamonds, and other nanoscale carbons are being explored for future technologies. Note: 0D, zero-dimensional; 1D, one-dimensional; 2D, two-dimensional; 3D, three-dimensional [10].

The most recent advances in supercapacitor materials include the development of nanoporous carbons with the pore size tuned to fit the size of ions of the electrolyte with Ångström accuracy. In a recent review by P. Simon and co-workers [55] it was attempted to achieve an improved understanding of charge storage and ion desolvation in sub-nanometer pores. It has also stressed the requirement of matching the active materials with specific electrolytes and the need to use a cathode and anode with different pore sizes. The very large number of possible active materials and electrolytes requires better theoretical guidance for the design of more powerful and long-lasting EDLCs (Fig. I-4).

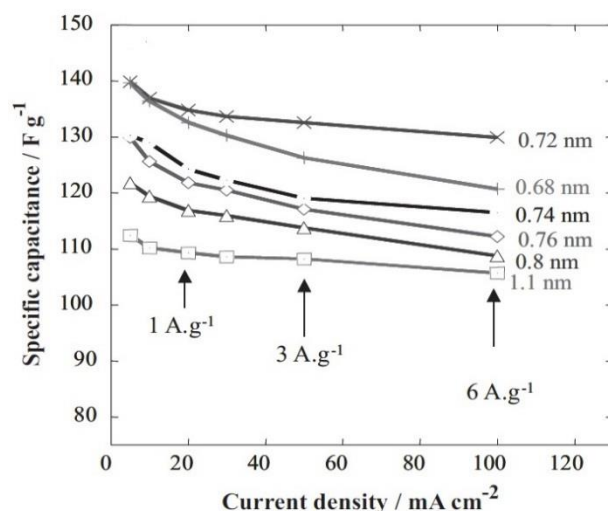


Fig. I-4. Capacitance change *versus* current density for laboratory cells assembled with CDCs with various pore sizes [55].

Many attempts have been made to increase the specific capacitance of carbon nanotubes (CNTs). Electrochemical enhancement by adding redox active functional groups on CNTs increases the specific capacitance, while excessive oxidation decreases conductivity and leads to poor cycle life. X. Xiao et al. [37] reported on the electrochemical enhancement methods followed by annealing at different temperatures in air to add and adjust the redox active functional groups. Functionalized freestanding CNT films were used as positive electrodes, assembled with freestanding CNT/MoO_{3-x} negative electrodes to fabricate carbon nanotube-based solid-state asymmetric supercapacitors (ASCs).

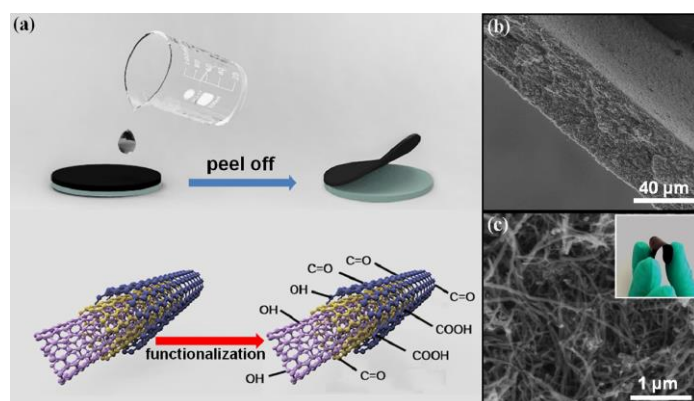


Fig. I-5. (a) Schematic of the fabrication procedure for functionalized free standing CNT films. (b) Cross section SEM image of the functionalized freestanding CNT film. (c) Enlarged cross-section SEM image of the functionalized free standing CNT films. The inset is a digital image of a functionalized freestanding CNT film [56].

J Tang et al. [56] synthesized of nitrogen-doped hierarchical porous carbons and by this way a three-dimensional interconnected framework (NHPC-3D) was developed (Fig. I-5). This device

showed a high capacitance retention of 75,7% at a higher current density of 20 Ag⁻¹ in aqueous electrolyte. This value is due to a sufficient surface area for charge accommodation, reversible pseudocapacitance, and a minimized ion-transport resistance, as a result of the advantageous interconnected hierarchical porous texture.

II-2. Pseudocapacitive oxide materials

In energy sources, there is a need, particularly with transportation and grid storage applications, of a large amounts of energy delivered quickly, within seconds or minutes. Although carbon based electrochemical capacitors possess the required power density, their relatively low energy density limits their usefulness for these applications. Instead, transition metal oxides that exhibit pseudocapacitance are very attractive. Pseudocapacitance occurs when reversible redox reactions occur at or near the surface of an electrode material and are fast enough so that the device's electrochemical features are those of a carbon-based capacitor, but with significantly higher capacitances. It is important to recognize that pseudocapacitance in materials is a relatively new property, with the first materials identified in the 1970's. To date, transition metal oxides exhibit the widest range of materials with pseudocapacitive behavior. By selecting the proper transition metal oxide, utilizing the most effective electrode architecture, and analyzing the electrochemical behavior for pseudocapacitive behavior, such materials are expected to become the basis for electrochemical energy storage devices which can offer high energy density. The following part involves several examples of various pseudocapacitive metal oxides as potential materials for energy storage.

II. 2. 1. WO₃

Tungsten oxides are great electrochemically active materials for energy storage. They have intriguingly fast and reversible surface redox reactions, which is associated with the similar W–O bond lengths in tungsten oxides with different oxidation states. Furthermore, the intrinsic high densities of tungsten oxides show potential applications in the fabrication of compact devices with excellent power performance. Theoretically, tungsten oxides are formed by corner and edge sharing of the WO₆ octahedra. By ordered stacking of WO₆ octahedra, a considerable number of interstitial sites can be formed. Such interstitial sites are effective accommodations for guest ions, rendering the absorption and desorption of ions at the surface, as well as insertion and deinsertion into the inner parts [57].

formula	specific capacitance	synthesis method	morphology	crystal structure
<i>h</i> -WO ₃	421 F g ⁻¹	hydrothermal synthesis	aligned nanopillar bundles	hexagonal
<i>m</i> -WO _{3-x} -C-s	103 F g ⁻¹	block-polymer-assisted synthesis	hexagonal porous	triclinic
tOMC-WO _{2.83}	175 F g ⁻¹	ordered mesoporous carbon-assisted synthesis	particles in mesoporous carbon	monoclinic
<i>m</i> -WO ₃	199 F g ⁻¹	template-assisted synthesis	mesoporous	cubic
WO ₃ -WO ₃ ·0.5H ₂ O	293 F g ⁻¹	microwave-assisted hydrothermal synthesis	disordered nanorods	hexagonal + cubic
a-WO ₃	231 F cm ⁻³	microwave irradiation	amorphous	amorphous
NiO	309 F g ⁻¹	chemical bath deposition	nanosheets	cubic
CuCo ₂ O ₄ @MnO ₂	296 F g ⁻¹	hydrothermal synthesis	core-shell	cubic
Co ₉ S ₈ /Co ₃ O ₄ @RuO ₂	4.28 F cm ⁻³	hydrothermal synthesis	nanorods@nanosheets	
RuO ₂ ·xH ₂ O	502 F g ⁻¹	hydrolysis	hollow fusiform	amorphous
In ₂ O ₃	64 F g ⁻¹	filtration	nanowires	
SnSe	1.8 mF cm ⁻²	sol-gel	nanowire	orthorhombic

Table I-1. Comparison of the Performances of Supercapacitors Based on Tungsten Oxides and Other Popular Active Materials [57].

In a recent paper by M. Zhu et al. [57], it is reported that proton insertion, a faradaic mechanism, may effectively enhance the global capacitance of metal oxides with low surface area but specific structures. According to this report performance could be improved when an assembly structure of hexagonal phase WO₃ (*h*-WO₃) nanopillars is synthesized which favors enhanced proton insertion mechanism. As it is demonstrated in Fig. I-6 d high capacitance of up to 422 F g⁻¹ under the current density of 0,5 A g⁻¹ could be achieved by this electrode (Table I-1).

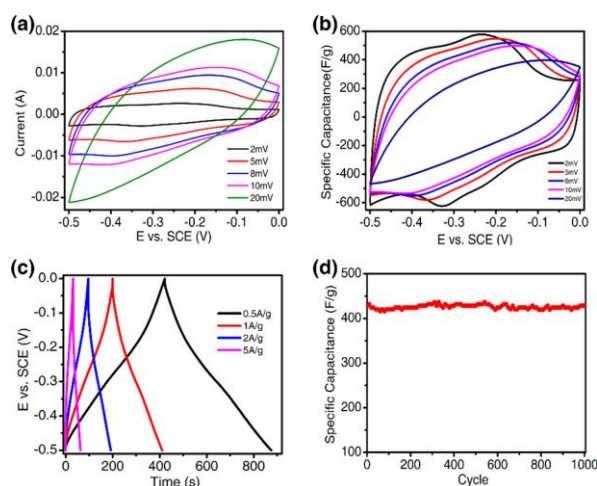


Fig. I-6. CV curves (a), profiles of capacitance versus potential (b), and charge–discharge profiles (c) measured at different rates and (d) cycling stability of the as-synthesized *h*-WO₃ nanopillars [57].

Recently, J. Xu et al. [58] reported on the fabrication of WO₃ mesoscopic microspheres composed of nanofibers and prepared via a hydrothermal process (Fig. I-7). Then, an asymmetric supercapacitor was constructed using these as-prepared WO₃ mesoscopic microspheres as positive electrode and an activated carbon as negative electrode. The favorable

electrochemical performances are attributed to the mesoscopic structure of the WO_3 which consist of a self-assembled interconnected WO_3 nanofibers framework. Thus, films have open porous characteristics and abundant active sites accessible to charge storage leading to high specific capacitance of 797 F g^{-1} at a current density of $0,5 \text{ A g}^{-1}$. The specific capacitance reported by author is much higher than that of tungsten oxide materials.

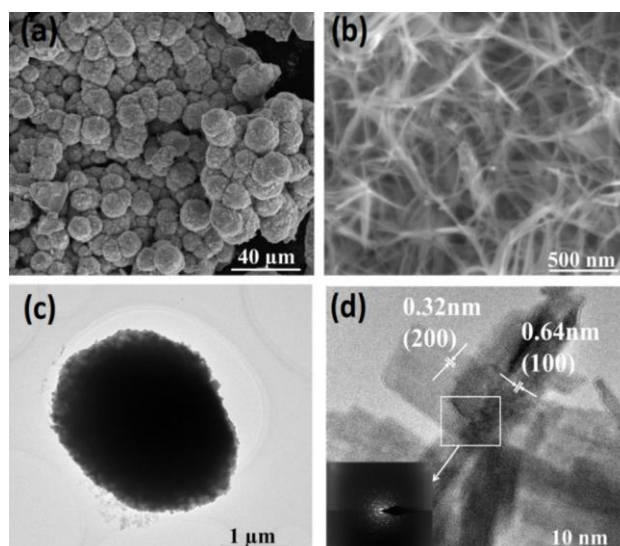


Fig. I-7. (a) Low and (b) High magnification SEM images; (c) TEM image of a single WO_3 microsphere; (d) HRTEM image of WO_3 nanofibers. The inset is selected area electron diffraction (SAED) of the selected area in (d) [58].

Nano- $\text{WO}_3 \cdot \text{H}_2\text{O}/\text{MnO}_2$ was synthesized on $\text{Ti}/\text{RuO}_2+\text{TiO}_2$ substrate via anodic electrodeposition by C. Yuan et al. [59]. The advantageous aspects of this new nanostructure is firstly related to good electron conduction of the nano- $\text{WO}_3 \cdot \text{H}_2\text{O}$ due to MnO_2 . In their study, tungsten oxide had a conductivity of $1,76 \text{ S cm}^{-1}$ which is several orders of magnitude higher than that of MnO_2 ($10^{-5} - 10^{-6} \text{ S cm}^{-1}$). Secondly, thin layer of MnO_2 on each nanosheet enables fast faradic reaction and provides a short ion diffusion path and therefore improved capacitive performance, finally, the porous structure can create channels for effective transport of electrolyte and consequently increase electrochemical active sites.

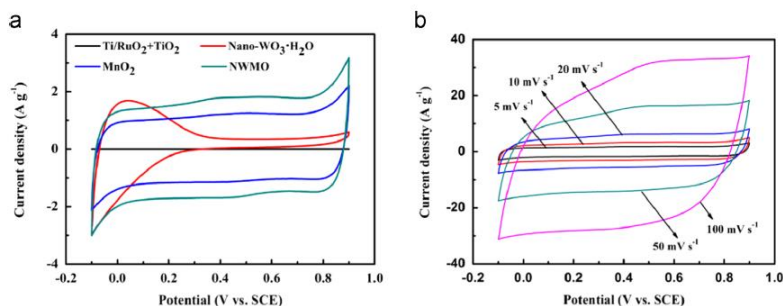


Fig. I-8. (a) Cyclic voltammograms of Ti/RuO₂+TiO₂ substrate, nano-WO₃·H₂O, MnO₂ and NWMO within a potential window of -0.1 – 0.9 V at 5mVs⁻¹ scan rate (b) cyclic voltammograms of NWMO at different scan rates [59].

Based on their electrochemical characterizations (Fig. I-8), this new electrode exhibits excellent capacitive performance including high specific capacitance of 363 F g⁻¹ and long-term stability, which is resulted from this special nanostructure [59].

In another work reported by Z Chen et al. [21] a mixed protonic-electronic conductor was synthesized by building the proton conducting water chains within a matrix of electron-conducting hydrous hexagonal tungsten oxide (h-WO₃) (Fig I-9).

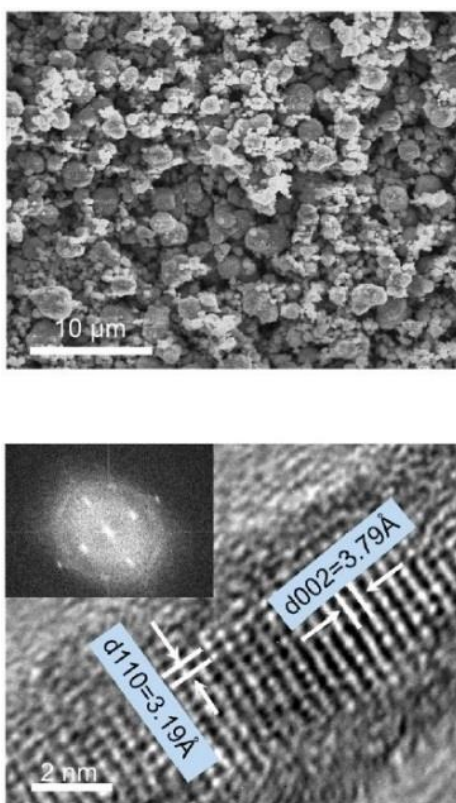


Fig. I-9. (a) SEM image of as-synthesized h-WO₃·nH₂O particles. (b) High-resolution TEM image and fast Fourier transform (FFT) images (inset) of a single h-WO₃·nH₂O nanorods [21].

The mixed conductivity affords the $\text{h-WO}_3 \cdot n\text{H}_2\text{O}$ with unprecedented energy storage performance. Cyclic voltammograms (CVs) in Figure I-10 show highly reversible peaks of reduction ($1/1'$) and oxidation ($2/2'$) reactions in acidic electrolyte. These reversible peaks are responsible for progression of reduction/oxidation of tungsten accompanied by proton insertion into the crystal structure from surface sites and through channels, respectively. The “mirror-like” CV curves reveal a capacitive behavior, which is commonly observed for hydrous RuO_2 the best-performing pseudocapacitive materials known so far. By comparison, in Li_2SO_4 and Na_2SO_4 electrolytes the voltametric current are smaller, and the electrodes displayed featureless CV response over the whole potential range, suggesting H^+ insertion/extraction is the most favorable process for $\text{h-WO}_3 \cdot n\text{H}_2\text{O}$.

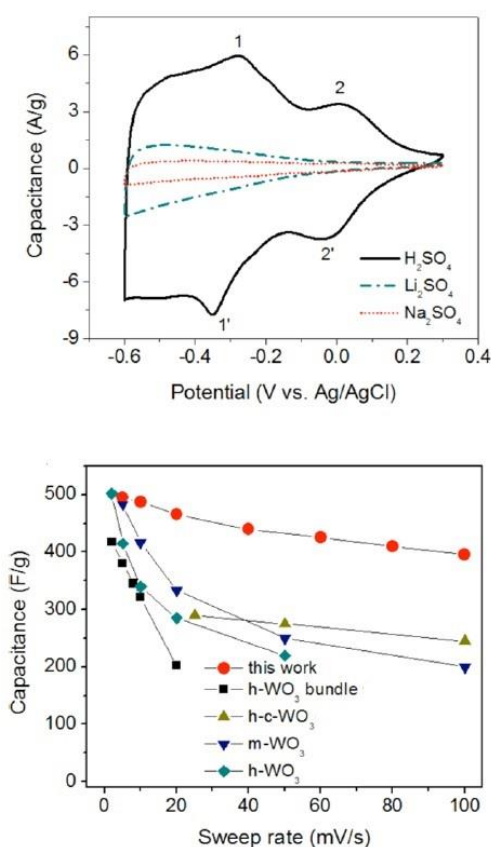


Fig. I-10. Electrochemical performance of $\text{h-WO}_3 \cdot n\text{H}_2\text{O}$ electrodes. (a) CV curves of $\text{h-WO}_3 \cdot n\text{H}_2\text{O}$ electrodes at voltage sweep rate of 10 mV s^{-1} in $0.2 \text{ M H}_2\text{SO}_4$, Li_2SO_4 and Na_2SO_4 electrolytes in three-electrode cells with Ag/AgCl and Pt foil as the reference and counter electrode, respectively. (b) Comparison of electrochemical capacitive performance of our $\text{h-WO}_3 \cdot n\text{H}_2\text{O}$ with other WO_3 structures (h-WO_3 with CNT, h-WO_3 bundle structure, hexagonal-cubic mixed phase WO_3 , monoclinic WO_3 thin film) [21].

The high rate performance is mainly due to the coexistence of high ionic and electronic conductivity in the hierarchical $\text{h-WO}_3 \cdot n\text{H}_2\text{O}$ crystal structure. Besides the high mass-, area-, and volumetric-specific capacitances and extraordinarily fast charge/discharge kinetics, the

unique hierarchical nanostructure with proton-conducting channels also endows the $\text{h-WO}_3 \cdot n\text{H}_2\text{O}$ with outstanding cycling stability.

II. 2. 2. TiO₂

Using TiO₂ anatase nanosheets interfaced with lithium ion-containing electrolytes as an example, J Kang et al. [60] revealed a microscopic mechanism for lithium intercalation in this system. They have demonstrated that a TiO₂ nanosheet is a hybrid between supercapacitor and battery, possessing characteristics of both depending on the electrode potential. At positive electrode potential above 2.2 V versus Li/Li⁺, the system behaves as a capacitor with the formation of electric double layers at the surface. As the electrode potential decreases below the threshold, lithium intercalation into the interior takes place. Their findings provide a coherent picture of how a transition from pure capacitors to batteries or pseudocapacitors occurs in these nanostructured materials.

In another work by T. Brezesinski et al. [61], the considerable enhancement of the electrochemical properties of self-organized TiO₂ results are shown when the films are both made from nanocrystals and mesoporous structures. Such materials show high levels of capacitive charge storage and high insertion capacities. When nanocrystal-based films are formed without mesoscale porosity, a high fraction of the total stored charge is again capacitive, but the total capacity is low, likely because most of the film is not accessible to the electrolyte/solvent. By contrast, when mesoscale porosity is created in a material with “dense” walls (rather than porous walls derived from the aggregation of nanocrystals), insertion capacities comparable to templated nanocrystal materials can be achieved, but the capacitance is much lower. These results underscore the importance of pseudocapacitive behavior which is developed in high surface area mesoporous oxide films. Moreover, the data suggest that both a mesoporous morphology and the use of nanocrystals as the basic building blocks are very promising for the rational development of metal oxide pseudo/supercapacitors. Through this combination, it may become possible to attain greater power densities while maintaining energy density in the next-generation of electrochemical capacitors that utilize this bimodal nanoporous architecture.

X. Sun et al. [62] fabricated pseudo supercapacitors by depositing amorphous TiO₂ thin films onto the surface of both graphene and CNT samples by atomic layer deposition (ALD). An ultrathin Al₂O₃ adhesion layer was employed to obtain conformal and amorphous TiO₂ films. The electrochemical characteristics of TiO₂ films in 1 M KOH electrolyte were then determined

using a variety of techniques including cyclic voltammetry, galvanostatic charge/discharge curves, and electrochemical impedance spectroscopy. The relatively low electrical conductivity and ionic diffusivity of TiO₂ did not limit these measurements because the TiO₂ films were ultrathin. The pseudocapacitance of the TiO₂ films greatly exceeded the electric double layer capacitance of the uncoated graphene and CNT samples. The measurements determined that the specific capacitances of the TiO₂-coated graphene and CNT samples were 97,5 and 135 F g⁻¹, respectively, after 50 TiO₂ cycles at 1 A g⁻¹. An asymmetric cell was also developed based on TiO₂ ALD coated CNT samples as the positive electrode and uncoated CNT samples as the negative electrode. This energy storage device could be reversibly operated over a wide voltage range of 0–1,5 V in aqueous electrolyte. A high energy density of 4,47 W·h kg⁻¹ was achieved on the basis of the total weight of both electrodes. This energy density was ~4 times higher than the symmetric CNT cell. The TiO₂ ALD-coated G and CNT electrodes and the asymmetric cell based on the TiO₂ ALD coated electrode also exhibited excellent stability over >1000 cycles. The results of this study demonstrate that metal oxide on high surface area conducting substrates can be used to fabricate high energy storage supercapacitors.

II. 2. 3. MnO₂

The pseudocapacitive behavior of MnO₂ was first investigated in 1999 by Lee and Goodenough [63–66] as they studied the properties of amorphous MnO₂.nH₂O in a KCl aqueous electrolyte. The presence of a rectangular voltammogram and the storage of approximately 200 F g⁻¹ (240 C g⁻¹, 4 min) indicated that rapid faradaic reactions were responsible for charge storage in this material.

Q Qu et al. [67] investigated the electrochemical behavior of MnO₂ nanorods prepared from a precipitation reaction in 0,5 mol L⁻¹ Li₂SO₄, Na₂SO₄, and K₂SO₄ aqueous electrolytes (Fig. I-11). The MnO₂ nanorods show the superior rate behavior in the K₂SO₄ electrolyte due to the smallest hydrated radius of K⁺, highest ionic conductivity, and smallest equivalent series resistance. Moreover, the initial cycles could be an effective way to activate the MnO₂ electrode and make the electrolyte solution soak into the material surface completely. The assembled asymmetric AC/K₂SO₄/MnO₂ nanorods supercapacitor shows an excellent cycling behavior between 0 and 1,8 V and also exhibits a large energy density of 17 Wh kg⁻¹ at a power density of 2 kW kg⁻¹.

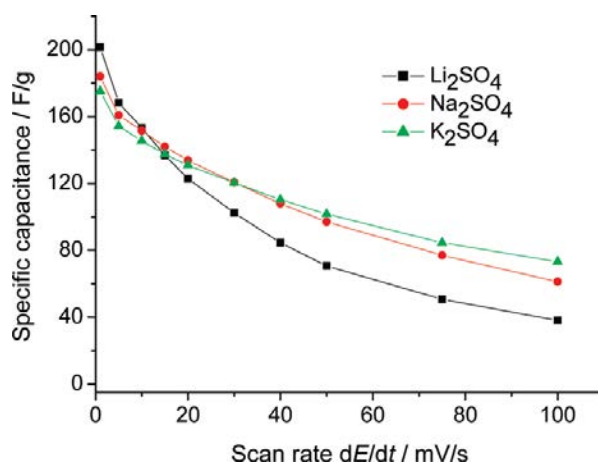


Fig. I-11. Capacitance variations of MnO₂ nanorods at different scan rates in 0,5 mole L⁻¹ aqueous Li₂SO₄, Na₂SO₄, and K₂SO₄ electrolytes [67].

Layered δ -MnO₂ thin films, featuring 3-D porous morphology and high hydrophilicity, were fabricated directly on inexpensive stainless steel (SS) foil substrates through a chemical bath deposition method (CBD) at low temperature by Y. Hu et al. [66]. The δ -MnO₂/SS electrode exhibits a high C_{sp} of 447 F g⁻¹ at 2 mV s⁻¹ and maintains 264,4 F g⁻¹ even at the high scan rate of 500 mV s⁻¹. A good capacitance retention ratio of 87% is obtained after 1000 CV cycles at 10 mV s⁻¹ in 0.5 M Na₂SO₄. The δ -MnO₂/SS electrodes also exhibit excellent mechanical flexibility and electrochemical stability after 200 bending cycles. The capacitance of the thin film electrodes becomes better with the operating temperature rising up from 10 to 45°C and the capacitance retention ratio can still remain up to 97,9% at 10°C. These results demonstrate that the δ -MnO₂ thin films have potential applications as electrode materials for flexible ECs.

II. 2. 4. RuO₂

In 1971, a new type of electrochemical capacitance was discovered using RuO₂, termed pseudocapacitance because it involved faradaic charge-transfer reactions. The storage of protons from the electrolyte resulted in a faradaic charge-transfer reaction on the RuO₂ thin film electrode. Despite the faradaic nature of the charge storage process, the cyclic voltammogram (CV) was that of capacitor i.e. rectangular in shape (Fig. I-12) as electroadsorption phenomena also remain. While this first report resulted in low gravimetric capacitance values (only 4–7% of the Ru⁴⁺ atoms participated in the redox reaction), it demonstrated the unique electrochemical features of pseudocapacitive processes. This study also demonstrated the need for a porous and hydrous oxide as the bulk, single-crystal material did not exhibit a rectangular CV. Subsequent studies improved the capacitance to over 700 F g⁻¹ by identifying the importance of structural water (specifically, RuO₂ nH₂O where x=0.5) and a porous, nanoscale architecture [27]. RuO₂

$0.5\text{H}_2\text{O}$ exhibits four unique features that enable rapid faradaic reactions with high capacitance: (1) the redox behavior of the Ru^{4+} cation that allows for faradaic energy storage; (2) the metallic conductivity of RuO_2 that allows for rapid electron transport; (3) the presence of structural water that enables rapid proton transport within the so-called “inner surface”; and (4) a large “outer” surface area that decreases diffusion distances. Unfortunately, the high cost of ruthenium (currently at ~ 2000 USD per kg) makes devices based on RuO_2 impractical for widespread application, except in small-size devices such as microsupercapacitors. Nevertheless, the behavior of hydrous RuO_2 first demonstrated that in certain systems, reversible faradaic reactions can result in similar electrochemical features as those of a capacitor. The study of RuO_2 also led to the understanding of what constitutes an ideal pseudocapacitive material in aqueous electrolytes.

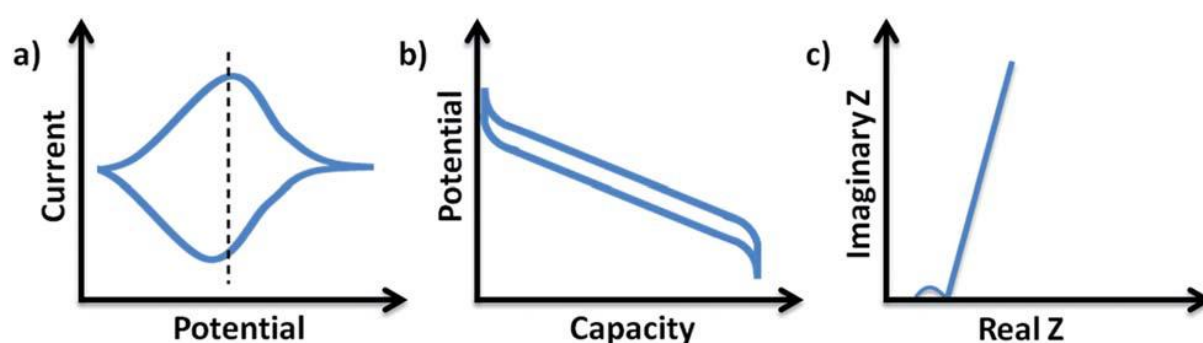


Fig. I-12. The general electrochemical features of pseudocapacitive materials. (a) In a cyclic voltammetry experiment, the shape is rectangular and if peaks are present, they are broad and exhibit a small peak-to-peak voltage separation. (b) In a galvanostatic experiment, the shape is sloping so that a capacitance value, dQ/dE , may be assigned at each point, and the voltage hysteresis is small. Here, Q is the capacity and E is the potential window. (c) In an AC impedance experiment, the Nyquist representation will contain a vertical line with a phase angle of 90° or less. A semi-circle at high frequencies, associated with charge-transfer resistance, may also be present [27].

Both amorphous and microcrystalline ruthenium oxides have been employed as electrode materials for the EC supercapacitors although ruthenium is a noble metal. The kinetics of electron transfer and/or the diffusion of protons within the electroactive materials determined the reversibility of redox transitions. An integration relating the electrochemical characteristics and textural properties to their preparation methods are very important in searching and optimizing the suitable materials for the application of EC supercapacitors [68–70]. Even though RuO_2 has a great advantage in terms of attractive high specific capacitance, it is somewhat expensive for commercial electrochemical capacitors. However, if one would be able to develop a thin film process for preparing RuO_2 electrode, this would reduce significantly the cost of these electrodes.

Hu et al. [70] produced nanotubular hydrous RuO₂ electrodes using the anodized aluminium oxide (AAO) membrane template and showed a specific capacitance of 1300 Fg⁻¹. Zheng et al. [71] synthesized hydrous RuO₂ films through a sol–gel process and showed specific capacitance depending on hydrate species contents and surface area. A maximum specific capacitance of 720 Fg⁻¹ was obtained for RuO₂·0,5H₂O with a surface area of 68,6 m² g⁻¹. Suh et al. [72] produced high surface area RuO₂ aerogels of 350 m² g⁻¹ with the high hydrate contents of RuO₂·0.5H₂O by carbon dioxide supercritical drying method and showed a specific capacitance of 595 Fg⁻¹. Subramanian et al. [73] prepared the mesoporous anhydrous crystalline RuO₂ by using nonionic surfactant template and achieved a specific capacitance of 58 Fg⁻¹. In RuO₂ as a pseudocapacitor, in which both electrons and cations have to be transported, facile transport paths for both types of carriers should exist. Anhydrous RuO₂ has the rutile structure and is composed of RuO₆ octahedra in the three-dimensional structure, the ordering of RuO₆ octahedra is able to promote electron transport, but not cation transport. However, hydrous RuO₂ may comprise the chains of disordered RuO₆ octahedra and exhibit the three-dimensional disorder, which is able to promote cation transport, but less electron transport. Therefore, pseudocapacitance should be optimized and increased when the hydrated contents and ordered RuO₆ octahedra in amorphous RuO₂ are balanced. The control of the hydrated contents of (RuO₂·xH₂O) in the porous nanoarchitectures of RuO₂ is an important parameter to obtain a high specific capacitance.

In a recent study in this regard, H-S Nam et al. [74] proposed a new process for preparing nanoporous and hydrous RuO₂ using sodium dodecyl sulfate (SDS) at a low temperature below 100° C. Their resulted nanoporous and hydrous RuO₂ displayed a good specific capacitance behavior. The proposed nanoporous RuO₂·3.38H₂O and RuO₂·2.56H₂O showed maximum specific capacitances, i.e., 870 Fg⁻¹ and 833 Fg⁻¹, respectively, at a scan rate of 10 mV s⁻¹, and exhibited pure electrochemical capacitive behavior. From their results it is suggested that the nanoporous ruthenium oxide with more hydrated is more suitable for high performance capacitors than other materials.

II-3. Conducting Polymers:

Generally, ECs performance is considered in specific capacitance which either can be estimated from the cyclic-voltammogram or from the discharge measurement. Each class of materials has its unique advantages and disadvantages. Some of the transition-metal oxides suffer from poor electrical conductivity and high cost. On the other hand, conducting polymers are highly

conducting, can follow easy synthesis process, are associated to fast rate of redox transfer and present low cost, etc. But their poor cycle life and low mechanical stability are major barriers for practical applications. Therefore, many studies have recently been addressed to increase their electrochemical performances [24–27, 31].

Various research groups are trying to investigate a hybrid nanostructure containing RuO₂ and conducting polymers such as polyaniline, polypyrrole etc., for ECs application. Employing template-free anodic deposition of cone-shaped nanostructure of polypyrrole with ultrathin layer of RuO₂, a specific capacitance of 302 Fg⁻¹ has been reported. Polyaniline/nafion/hydrous RuO₂ ternary composite electrode has demonstrated a 475 Fg⁻¹ specific capacitance at 100 mV s⁻¹ [24–27,31].

In recent years, polypyrrole (PPy), an important conducting polymer, has been successfully employed as redox electrode material. The specific capacitance of PPy has been measured to be 180–250 Fg⁻¹. In spite of its high charge storage capacitance, PPy and other conducting polymers lack in long-term stability [24–31].

In a report from F. Tran-Van's group, the capacity of chemically synthesized PPy, as well as its stability during cycling was optimized. In their work [28,29] polymerization of pyrrole is performed in a colloidal solution of Fe₂O₃ and in the presence of PTS anions. In this conditions, improvements are reached in terms of the charge storage capacity of the material. This is attributed to a morphological modification of the composite. Nanoparticles role as a support to the polymerization process of pyrrole and eventually this leads to a more porous structure with a higher specific surface area. By this way, it increases the accessibility of the conducting polymer sites during the electrochemical process. As a consequence, the kinetics of charge transfer is altered amplified in this nanocomposite structure. The insertion–extraction of anions during the charge–discharge process was reported to be easier and it may allow higher rates of charge–discharge and higher power density to be obtained.

S. F. Shaikh et al. [25] reported on the superior electrochemical supercapacitive performance of hybrid structure over organic and inorganic structures (Fig. I-13). According to their work electrodeposited H-RuO₂ (hybrid nanostructure electrode) plays an important role for transportation of ions through PANI films in acidic electrolyte. Presence of the H-RuO₂ electrode enhanced length of PANI nanowires. Hybrid structure is not only reducing diffusion resistance of electrolyte in the electrode material but also increasing specific capacitance. The formation of hybrid H-RuO₂ and PANI structure is confirmed from the Raman study. The

obtained specific capacitance of 322 F g^{-1} at 50 mV s^{-1} scan rate for this hybrid electrode is promising.

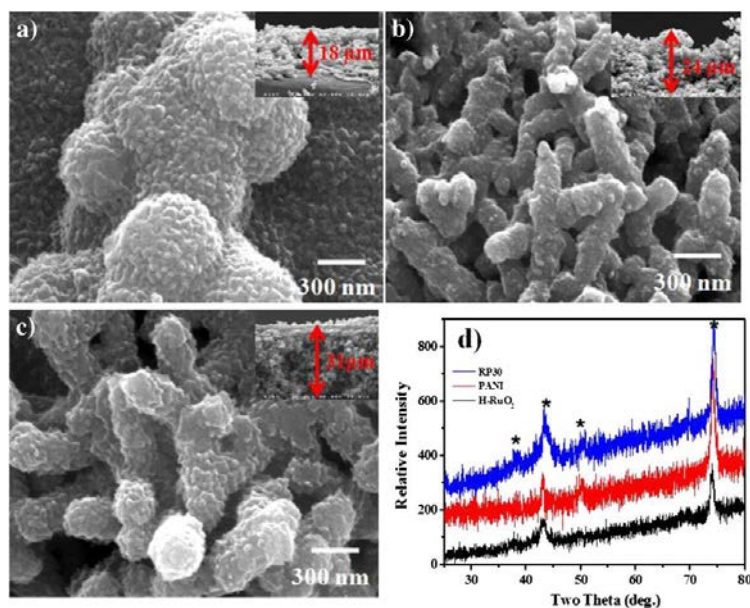


Fig. I-13. Scanning Electron Microscopy images of; a) H-RuO₂, b) PANI, c) RP30 (Electrodeposition of PANI was performed at a constant potential of 0.7 V for 30 min at room temperature) and d) X-ray diffraction patterns of electrodes [25].

B-X Zou et al. [75] have reported on the pseudocapacitive properties of WO₃/PANI composite films electrodeposited by cyclic voltammetry in solutions of aniline and precursor of the oxide prepared from tungstic acid and H₂O₂. These composite films exhibited good pseudocapacitive performance in a wide potential range of -0,5 to 0,7 V vs. SCE due to the electroactivities of WO₃ in negative potential range and its fine distribution in PANI matrix. Fig. I-14 presents the specific capacitance of WO₃, PANI and WO₃/PANI composite (WP) with different mass of films. It is assumed that with the mass of films increasing, the specific capacitance of WO₃ decreases. This is attributed to the diffusion limitation in the WO₃ dense film. Due to the distribution of WO₃ in the PANI network, WO₃/PANI composite displays only a minor decrease in the specific capacitance, with the mass of film increasing from 2,4 to 8,1 mg. This implies that the pseudocapacitive reaction takes place not only at the surface but also in the bulk of the film.

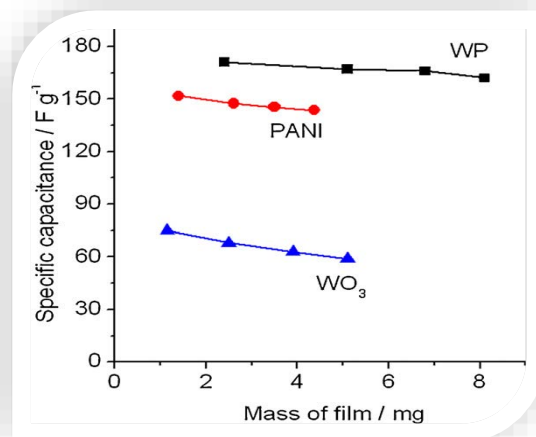


Fig. I-14. The specific capacitance of PANI, WO₃ and the composite WP as a function of the film mass measured through constant current charge–discharge at 1 Ag⁻¹ in 1M H₂SO₄ [63].

In a reported work by J. Zang et al. [24] a well-aligned cone-shaped nanostructure of PPy was successfully grown on Au substrate by using a simple, one-step, cost-effective, template-free, and anodic deposition method. Furthermore, the 3D, arrayed, nanotubular architecture coated with an ultrathin layer of RuO₂ was tailored to construct a supercapacitor. The unique structure and design not only reduces the diffusion resistance of electrolytes in the electrode material but also enhances its electrochemical activity. The specific capacitance and conductivity of RuO₂/PPy by the modification with an ultrathin layer of RuO₂ was significantly improved in comparison to that of the bare PPy, which was verified by CVs and EIS for the two electrodes. The good stability of the RuO₂/PPy electrode is very promising for applications in microsupercapacitor devices.

II-4. Carbon-MO_x Composites:

Owing to their high conductivity, permeability (resulting in high power density) and chemical inertness (long cycle lifetime), single wall carbon nanotube (SWCNT) thin films are promising candidates for active supercapacitor electrode materials [56,76]. In nanocomposite form, metal oxides and conducting polymers could improve electrochemical and mechanical properties of the supercapacitors. Therefore, recent researches have been focused on the exploration of potential pseudocapacitive metal oxides have been investigated [44–53,77–79].

R. Yuksel et al. [80] have recently reported on the fabrication of ternary nanocomposite SWCNT/WO₃/PANI thin films as supercapacitor electrodes. High electrical conductivity of SWCNT thin films allowed the possibility of the fabrication of supercapacitors without a separate charge collector and enhanced the properties solely arising by the WO₃ and PANI

components in a synergistic manner. These fabricated ternary nanocomposite supercapacitor electrodes were found to have a specific capacity of 28.5 mF/cm^2 at a current density of 0.13 mA/cm^2 therefore they could be promising electrode active materials for electrochemical energy storage systems if an air-stable conducting polymer can be integrated into the structure.

In a study by A Eftekhari et al. [38,39], manganese oxide films were galvanostatically deposited in the presence of a small amount of carbon nanotube (CNT). The resulting film cannot be considered as a CNT based nanocomposite, as no CNT is detected by electron microscopy. However, the manganese oxide electrodeposited delivers an excellent pseudo-capacitive behavior to be used as a superior supercapacitor. The samples showed a specific capacitance of 280 F g^{-1} . As it seems that the capacitance of this electrode is related to the chemisorption of the alkali cation, an extremely high specific capacitance of 434 F g^{-1} was achieved in a saturated medium of Li electrolyte. This high specific capacitance can be attributed to the presence of carbon nanotubes results in the formation of nanostructured films which provide a better ion accessibility. Although the exact mechanism for this phenomenon is still vague, the presence of carbon nanotubes (probably as a solid charge carrier) close to the electrode surface is apparently responsible for a different pathway for the electrodeposition process.

Graphene has also been considered as a promising candidate for a supercapacitor electrode material due to its attractive characteristics such as large surface area, good flexibility, excellent electrical conductivity and wide potential windows. The intrinsic capacitance of single-layer graphene reaches ca. 21 mF cm^{-2} when the entire surface area is used or accessible. It is also an excellent substrate to host active nanomaterials for charge storage due to its abundant surface functional groups. Recent advances on graphene/metal oxide composites for electrochemical applications inspired some groups to synthesize T-Nb₂O₅/graphene nanocomposites. They may greatly improve the behavior of active T-Nb₂O₅ nanocrystals and consequently achieve excellent performance [14].

L Kong et al. [14] presented a simple and one-pot hydrothermal method to decorate Nb₂O₅ nanoparticles onto the surface of reduced graphene oxide (rGO) sheets. After post-treatment at $700 \text{ }^\circ\text{C}$, rGO converted into graphene with improved electric conductivity while the amorphous Nb₂O₅ nanoparticles recrystallized into T-Nb₂O₅ nanocrystals. The synergistic effects between graphene and T-Nb₂O₅ nanocrystals results in excellent electrochemical capacitive properties including high capacitance/rate capability and excellent cyclic stability.

Among the metal oxides investigated, NiO with a high theoretical capacitance value of 2573 F g^{-1} , a low cost, a distinct redox reaction, and a controllable morphology have become a popular

pseudocapacitive material for supercapacitors. However, both NiO and Ni(OH)₂ have poor electrical conductivity, resulting in reduced capacitive performance and slow electron transport at high electrical rates, limiting its practical application. To resolve the issue, researchers commonly incorporate carbon black into the nickel compounds to maximize the capacitance. Although, investigations to find more suitable carbon support other than carbon black for NiO/Ni(OH)₂ were followed by B. K. Kim group [15]. They have synthesized a flower structured NiO/Ni(OH)₂ hybrid composite by tailoring the calcination period, and in the process discovered that the hybrid composite outperforms pure NiO and Ni(OH)₂ individually. The hybrid composite without any carbon supports demonstrated a capacitance of 474 F g⁻¹ even at a very high current density of 10 A g⁻¹. To further improve the performance and capacitance value at high current density, they have studied the impact of different carbon supports, including carbon black, carbon nanotubes, and reduced graphene oxide (rGO), on the hybrid composite. The study revealed that the nickel hybrid composite supported with single-walled carbon nanotubes (SWCNTs) outperformed rGO and exhibited the best performance. The composite with 20 wt% addition of SWCNTs demonstrated a capacitance of 828 F g⁻¹ at current discharge of 2 A g⁻¹ and 810 F g⁻¹ at a high current discharge of 10 A g⁻¹. These results clearly showed that the addition of the carbon supports dramatically enhances the capacitive performance of the nickel hybrid composite. The hybrid nickel oxide/hydroxide with the support of different carbon supports, especially SWCNTs, due to its lowest ionic resistance, is a good candidate for development of electrodes for high performance supercapacitors

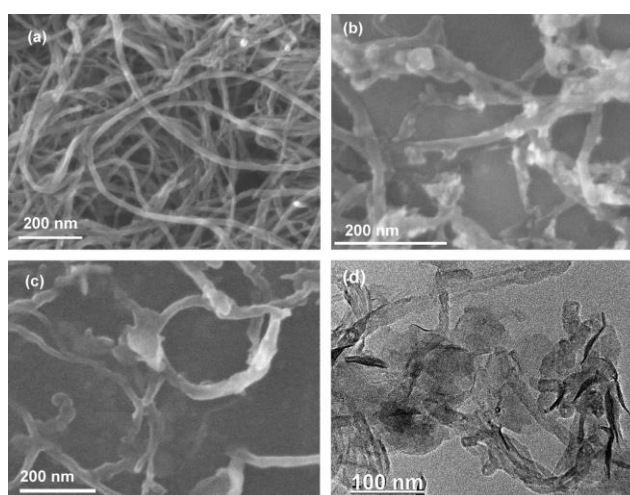


Fig. I-15. SEM images of (a) acid-treated CNTs, (b) Al₂O₃/CNTs, (c) Ni-Al LDHs/CNTs and (d) TEM image of Ni-Al LDHs/CNTs [81].

Recently, Ni-Al layered double hydroxides (LDHs) with hydrotalcite-like structure have shown outstanding performances in electrochemical field with their high specific capacitance, low cost

and environmental benignity (Fig. I-15). A lot of efforts have been devoted to improve their lifecycle and rate capability. Some work declared that incorporating Ni–Al LDHs with highly conductive carbon materials could greatly improve the rate stability and cycle life. For example, Liu et al. [82] grew in situ Ni–Al LDHs on carbon nanoparticles, which displayed excellent pseudo-capacitive behavior and cycling stability in an asymmetric supercapacitor. F. He et al. [83] used an in situ method to fabricate Ni–Al LDHs nanosheets on hollow carbon nanofibers and the composite had a specific capacitance of 1613 F g^{-1} and a capacitance retention of 83.4% after 1000 cycles. Yang et al. [84] synthesized NiCoAl LDHs/CNTs composites with a specific capacitance of 1035 F g^{-1} and good cycling stability. Ni–Al LDHs/rGO composites synthesized by M. Li et al. [85] gained a specific capacitance of 1630 F g^{-1} and good cycling performance.

III. Strategies Toward New Ways of Materials Design for High Performance ECs

III. 1. Elaboration Methods and Process

S. Music et al. [86,87] presented a new route in the synthesis of RuO_2 powder. This synthesis is based on the addition of strong organic alkali, tetramethylammonium hydroxide, into an alcoholic solution of $\text{RuNO}(\text{NO}_3)_3$ and thermal treatment of amorphous ruthenium hydrous oxide, previously precipitated at 90°C . They have also investigated conditions for the precipitation of amorphous ruthenium hydrous oxide in water medium at high pH. Similarly reported by U. M. Patil et al. [88], the amorphous hydrous RuO_2 thin films have been successfully synthesized at low temperature on glass and stainless steel substrates using chemical bath deposition (CBD) method which is single step, simple, easy, and efficient. SEM images reveal that porous and spherical grained morphology of their synthesized films. The equivalent series resistance, ESR, power corresponding to heat production due to internal resistance and higher loss factor of hydrous RuO_2 thin film, restricts maximum specific capacitance up to the 73 F g^{-1} . The specific power, specific energy and coulombic efficiency (%) of the prepared electrode is found to be $0,151 \text{ kW kg}^{-1}$, $3,57 \text{ Wh kg}^{-1}$ and 94%, respectively.

G-H Jeong et al. [19] reported on the synthesis of porous $\text{ZrO}_2\text{--SiO}_2$ sheets with well-defined ultrasmall WO_3 nanoparticles for energy storage performance. To overcome relatively low surface areas in binary composites, they have synthesized a new ternary oxide system of porous $\text{ZrO}_2\text{--SiO}_2$ sheets with ultrasmall WO_3 NPs as shown in figure I-16. Therefore, in their system, ultrasmall WO_3 NPs are synthesized on porous $\text{ZrO}_2\text{--SiO}_2$ sheets by an impregnation process.

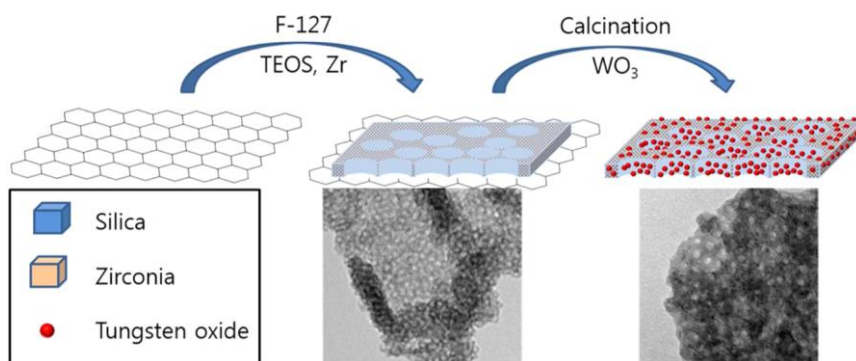


Fig. I-16. ZrO₂-SiO₂ sheets impregnated with WO₃ nanoparticle electrode [19].

The advantageous aspect of their work is the utilization of WO₃ NPs as a real active material for capacitance generation which was greatly enhanced by distributing WO₃ NPs on the framework wall. The synthesized electrode with about 13 nm thickness and about 10 nm pores, has a maximum capacitance value of 313 F g⁻¹ at a current density of 1 A g⁻¹ and a minimum value of 160 F g⁻¹ at a current density of 30 A g⁻¹.

In a report from T.P. Gujar et al. [89] network like amorphous RuO₂ electrodes were synthesized successfully by spray pyrolysis method. The specific capacitance of RuO₂ electrode decreased with an increase of scan rate and a maximum capacitance 551 F g⁻¹ was observed at 5 mV s⁻¹. According to their work the spray pyrolysis method is useful for preparation of large area RuO₂ electrodes with amorphous structure for supercapacitive applications at the expense of small amount of initial ingredients.

Y-Y Liang et al. [90] have successfully developed a novel solid state synthetic route for the preparation of mesoporous hydrous ruthenium oxide. The efforts in this work have been focused on exploring the relationships among the annealing conditions, structural changes and the electrochemical performances. Combined with the existing results, it was found that the specific capacitance of RuO₂·xH₂O is strongly dependent on the corresponding crystalline structure. Based on their results the high value of specific capacitance can be obtained only from the amorphous phase, once the crystalline phase was formed, the specific capacitance dropped rapidly. For example, a maximum capacitance of 655 F g⁻¹ was obtained by annealing at 150°C, higher temperatures (exceeding 175°C) presumably contributed amorphous phase of RuO₂·xH₂O into crystalline one and the corresponding specific capacitance dropped rapidly from 547 F g⁻¹ at 175 °C to 87 F g⁻¹ at 400 °C.

There are also many examples of MO_x preparation in the literature based on sol-gel route [91–93]. In a work by J.P. Zheng et al. [94] a specific capacitance of 768 F g⁻¹ has been obtained from an amorphous hydrous ruthenium oxide prepared by sol-gel method. MWCNTs coated

with RuO₂ have been fabricated on a noble stainless steel substrate by M. Kahram et al. [95]. Structure and composition analyses by their group was based on the effects of film preparation parameters such as pH, the concentration of the sol and the heat treatment temperature.

The electrodeposition of various metal oxides is also a strategy of growing interest [68–70]. It offers control of the film thickness, good uniformity, and modifiable deposition rates. It is especially attractive owing to its low equipment cost and materials. Due to the use of an electric field, electrodeposition is particularly suited for the formation of uniform films on substrates of complicated shapes, impregnation of porous substrates and deposition on selected areas of the substrates [96–100].

I. Zhitomirsky et al. synthesised RuO₂ by cathodic electrodeposition on Ni, Ti, Pt foils and Si wafers [98]. Following the same concept B-O Park et al. [96,97] reported on the synthesis of Ruthenium oxide (RuO₂) films of different thicknesses by cathodic electrodeposition on titanium substrates from aqueous acidic Ru(III)Cl₃ solution. The effects of various deposition parameters such as pH of the solution, storage time, temperature were studied in their work.

III-2. Materials Nanostructuration for Development of Flexible Device Architectures:

For the improvement of the performance of metal oxide based electrodes, main attention has been attributed to their nanostructuration with various morphologies due to the unique properties and functionalities that can be effectively exploited in electrochemical energy storage devices [100]. The new nanostructures, with small sizes, and large surface area to volume ratios, are expected to facilitate the ion transfer process which is the key phenomena in all energy storage devices including electrodes for supercapacitors. These improvements are attributed to (i) a facilitated transfer and short diffusion length for ions transport, (ii) a high electrode/electrolyte contact area, and (iii) a better stress/strain management of the material during ion intercalation/extraction. As a consequent of these advantages various synthesis methods some of them mentioned in the previous section could provide tremendous possibilities in order to have favorable new nanoarchitectures for ideal electrode materials. The following part brings few examples of these efforts in order to procure materials with large surface areas.

C-C Hu et al. [68] successfully designed and tailored advanced RuO₂.xH₂O NTs as electrode material with a 3D, arrayed, nanotubular architecture by membrane templated route; these RuO₂.xH₂O NTs achieve the high standard performances (ultrahigh-power characteristics and high capacity) required for next generation supercapacitors by using a very simple, one-step,

cost-effective, anodic deposition technique. This unique structure not only reduces the diffusion resistance of electrolytes but also enhances the facility of ion transportation and maintains the very smooth electron pathways for the extremely rapid charge/discharge reactions as shown in figure I-17.

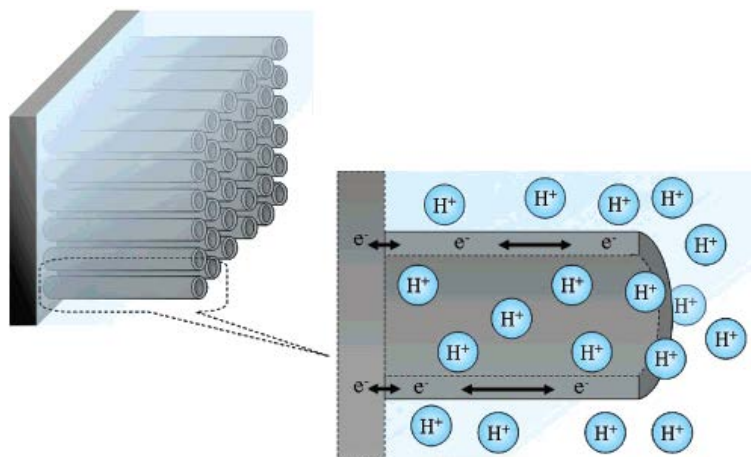


Fig. I-17. An ideal design of the electrode material for next generation of supercapacitors, $\text{RuO}_2 \cdot x\text{H}_2\text{O}$ nanotubular arrayed electrode. The mesoporous architecture, hydrous nature, and metallic conductivity provide the proton and electron “superhighways” for the extremely rapid charge/discharge processes [68].

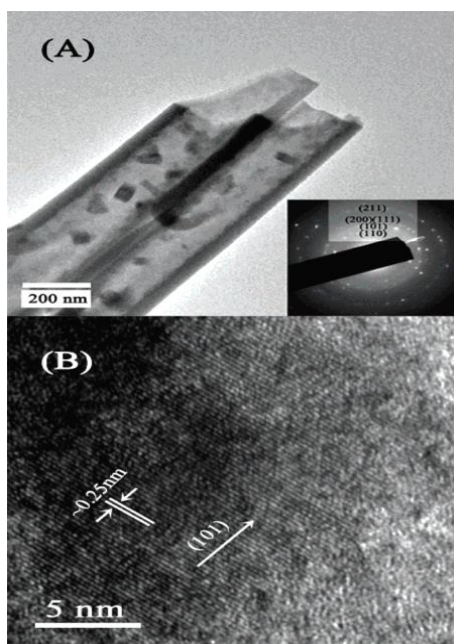


Fig. I-18. (A) The bright-field and (B) high-resolution TEM images of $\text{RuO}_2 \cdot x\text{H}_2\text{O}$ NTs annealed in air at 200 °C for 2 h. The inset of electron diffraction pattern shows typical diffraction rings of RuO_2 polycrystals in the rutile form [68].

This ordered, 3D, porous architecture is favorable for the penetration of electrolytes into the whole oxide matrix, and the hydrous structure shortens the proton diffusion distance (Fig. I-18). Therefore, high specific capacitance of 740 F g^{-1} for the as-deposited $\text{RuO}_2 \cdot x\text{H}_2\text{O}$ NTs is obtained. The great performance is reasonably attributed to the novel nanotubular arrayed

structure of $\text{RuO}_2 \cdot x\text{H}_2\text{O}$, which not only reduces the diffusion distance of protons but also increases the facility of ion transportation during the rapid charge/discharge reactions. In addition, the metallic conductivity of annealed, crystalline $\text{RuO}_2 \cdot x\text{H}_2\text{O}$ NTs provides the “superhighways” for electron motion.

Brzezinski et al. [61] showed that considerable enhancement of the electrochemical properties of self-organized TiO_2 results when the films are both made from nanocrystals and mesoporous. Such materials show high levels of capacitive charge storage and high insertion capacities. When nanocrystal-based films are formed without mesoscale porosity, a high fraction of the total stored charge is again capacitive, but the total capacity is low, likely because most of the film is not accessible to the electrolyte/solvent. By contrast, when mesoscale porosity is created in a material with “dense” walls (rather than porous walls derived from the aggregation of nanocrystals), insertion capacities comparable to templated nanocrystal materials can be achieved. These results underscore the importance of pseudocapacitive behavior developed with high surface area of mesoporous oxide films. Moreover, the data suggest that both a mesoporous morphology and the use of nanocrystals as the basic building blocks are very promising for the development of metal oxide pseudo/supercapacitors. Through this combination, it may become possible to attain greater power densities while maintaining energy density in next-generation electrochemical capacitors that use this bimodal nanoporous architecture [62].

In another work by R B Rakhi et al. [17], they have demonstrated that the rate performance of mesoporous Co_3O_4 nanosheet arrays grown directly over carbon cloth collectors can be improved by the uniform dispersion of hydrous RuO_2 nanoparticles. The $\text{Co}_3\text{O}_4/\text{RuO}_2$ nanostructured electrode morphology was tuned by controlling the electrodeposition time to achieve a balance between good electrode conductivity and efficient electrolyte access to the RuO_2 nanoparticles, hence optimizing performance. A high specific capacitance value (905 F g^{-1} at 1 A g^{-1}), high rate performance of 78% at the current density ranging from 1 to 40 A g^{-1} , and excellent cycling stability (96% after 5000 charge discharge cycles) were achieved using symmetric two-electrode configuration. Mesoporous cobalt oxide (Co_3O_4) nanosheet electrode arrays are directly grown over flexible carbon paper substrates using an economical and scalable two-step process for supercapacitor applications. The interconnected nanosheet arrays form a three-dimensional network with great supercapacitor performance in standard two electrode configuration. Dramatic improvement in the rate capacity of the Co_3O_4 nanosheets is achieved by electrodeposition of nanocrystalline, hydrous RuO_2 nanoparticles dispersed on the

Co₃O₄ nanosheets. As a result, an excellent specific capacitance of 905 F g⁻¹ at 1 A g⁻¹ is obtained, and a nearly constant rate performance of 78% is achieved at current density ranging from 1 to 40 A g⁻¹.

K-H Kim et al. [101] have performed an electrodeposition method for the synthesis of mesoporous RuO₂ electrodes with very uniform pore sizes. They synthesized successfully these films using a mixture of SDS (sodium dodecyl sulfate) and CTAB (cetyl trimethyl ammonium bromide) as a templating agent. When SDS was used as a templating agent, collapse of porous structure, resulting in the formation of disordered porous structure, was observed after removal of this surfactant. The addition of small amount of CTAB significantly improved the stability of the porous structure. Electrochemical behaviors of synthesized RuO₂ electrodes were investigated. Compared with non-porous RuO₂ electrodes, mesoporous RuO₂ electrode showed much higher specific capacitance and current density during charge-discharge processes. Furthermore, mesoporous RuO₂ showed higher supercapacitor performance which is attributed to the high surface area and facilitated charge transport of mesoporous structure.

IV. Diagnostics Tools for MO_x based Electrodes for Energy Storage

IV-1. Surface and Structural Analysis: SEM, TEM, XRD, XPS, FT-IR:

(i) SEM images:

Scanning Electron Microscope (SEM) has widely used for morphological analysis of various MO_x materials. This diagnostic tool was employed by L Li et al. [42] in order to show their synthesized pristine CNTs and MnO₂/CNTs composite. From this image it can be seen that the pristine CNTs exhibit regular morphology with a measurable diameter of about 90–120 nm and the wall is smooth (fig. I-19). The cross-linked MnO₂ flakes on the carbon nanotubes to form an open porous nanostructure, which is favorable for the transfer of electrolyte cations into the electrochemically active film. In a way, the present work shows and interprets that the microstructure of the resultant MnO₂/CNTs composite plays an important role in enhancing its capacitive performances.

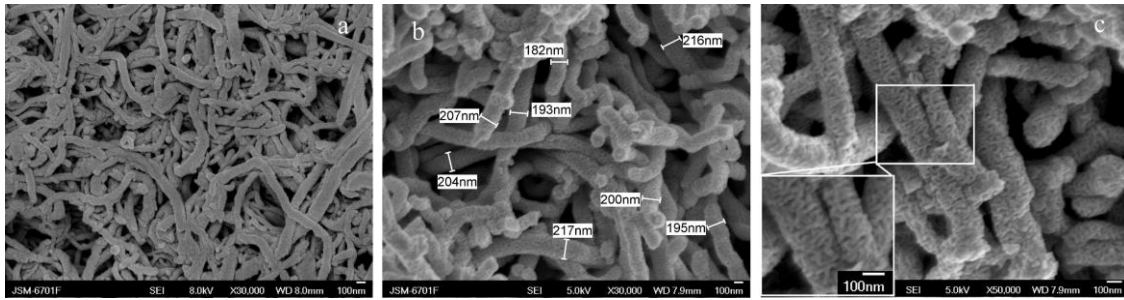


Fig. I-19. SEM images of (a) the pristine CNTs, (b) low-magnification, and (c) high-magnification view of MnO₂/CNTs composite [42].

Flower-like WO₃·H₂O/reduced graphene oxide composites have been synthesized through a mild hydrothermal approach by L. Ma et al. [78]. In this work SEM results manifest that the WO₃·H₂O in the composites displays a 3D hierarchical flower-like morphology with uniform sizes and are well dispersed and closely anchored on the flexible reduced graphene oxide as given in figure I-20.

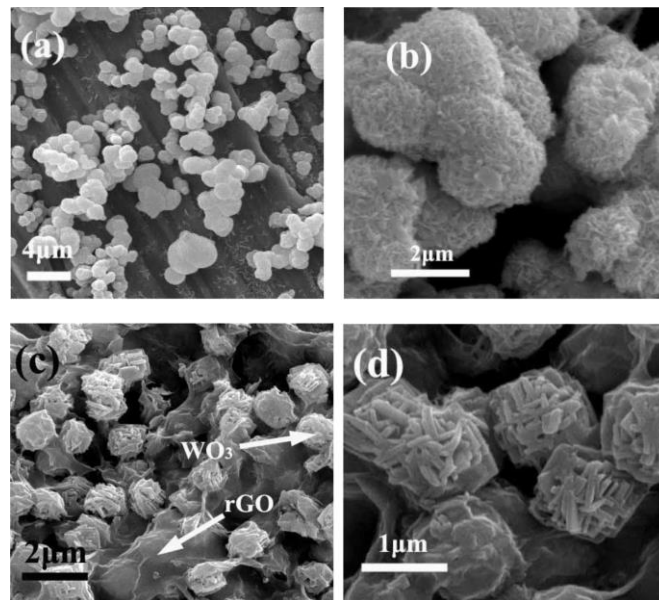


Fig. I-20. SEM images of the as-prepared (a, b) bare WO₃·H₂O and (c, d) WO₃·H₂O/rGO [78].

As a result of this observation, the composite exhibit superior electrochemical performance with high specific capacitance, good cycling stability and rate capability. It is believed that the unique hierarchical WO₃·H₂O microstructures and the synergistic effect originated from the intimate combination of WO₃·H₂O with reduced graphene oxide are responsible for the enhanced electrochemical properties including large surface area for the electrolyte access and therefore promoting ions or electrons rapid transport [78].

(ii) TEM images

M. Sasidharan et al. [20] have demonstrated a simple method for fabrication of WO_3 hollow nanospheres of size ~ 42 nm using polymeric micelles with core-shell-corona architecture as a soft template under mild conditions. From Transmission Electron Microscopy (TEM) observation of hollow nanospheres with a void space diameter of 2 nm with thin shell domain of size 10 nm is evident (see figure I-21). As a result, the retention capacity of this nanostructured material when used as anode was very high compared to dense tungsten trioxide. The author has observed that improved electrochemical behavior is attributed to nanosize effect coupled with hollow void space of WO_3 hollow particles that facilitates fast lithium transfer kinetics.

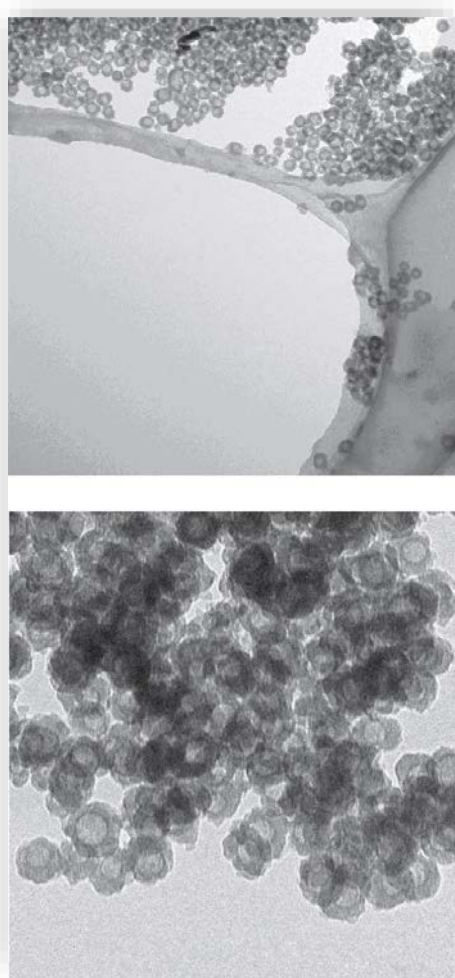


Fig. I-21. TEM images of WO_3 hollow nanospheres/ (A) low-magnification and (B) high-magnification [20].

D Muñoz-Rojas reported on the effect of crystallite/particle size on the electrochemical lithiation of RuO_2 films prepared by a hydrothermal route. A panel of samples with different

particle/crystallite sizes was obtained by annealing the $\text{RuO}_2 \cdot x\text{H}_2\text{O}$ precipitate at 200, 300, 400, 500 and 800 °C for 1 h in air. High Resolution Transmission Electron Microscopy (HR-TEM) is employed in order to follow up the effect of annealing temperature on the structuration and in order to target the crystallographic evolution of the film as given in figure I-22 [102].

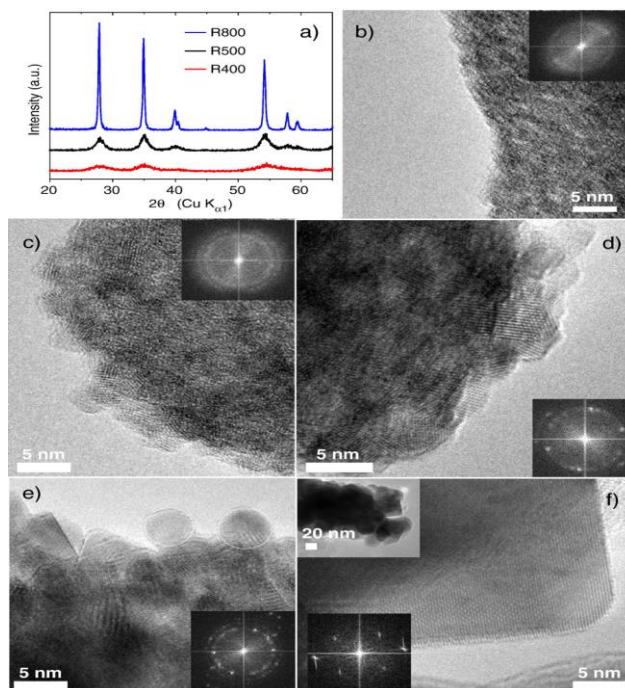


Fig. I-22. Characterization of the panel of materials prepared through a ‘chimie douce’ process (a) Evolution of the XRD patterns as a function of annealing temperature ($\text{Cu K}\alpha$) (b)–(f) TEM pictures and Fourier transforms for (b) R200 (c) R300, (d) R400, (e) R500 and (f) R800 [102].

Nanoporous $\text{RuO}_2 \cdot 3.38\text{H}_2\text{O}$ films were synthesized using a surfactant template (SDS) by H-S Nam et al. [74]. High-resolution transmission electron microscopy (HR-TEM) revealed spherical shapes with nanoporous structure composed of the nanoparticles about 4 nm (figure I-23). The corresponding selected area electron diffraction (SAED) pattern of samples annealed at low temperatures showed the faint ring image and displays the amorphous structure of RuO_2 .

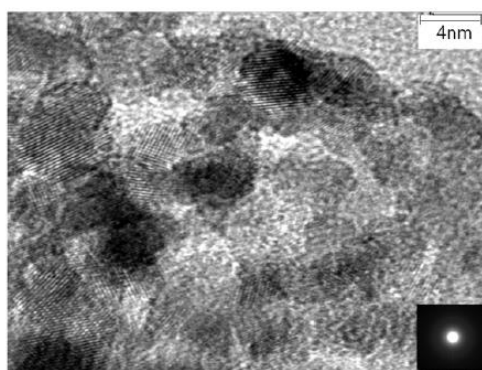


Fig. I-23. HR-TEM image of the as-prepared $\text{RuO}_2 \cdot x\text{H}_2\text{O}$ sample. The inset shows the SEAD Pattern [74].

(iii) XRD analysis

B-O Park et al. [96,97] have used X-ray Diffraction (XRD) to characterize ruthenium oxide (RuO_2) films of different thicknesses synthesized by cathodic electrodeposition on titanium substrates and prepared in aqueous acidic Ru(III)Cl_3 solution.

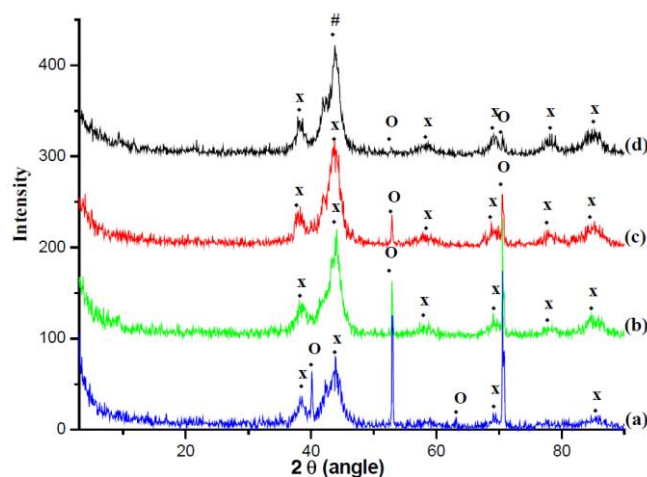


Fig. I-24. X-ray diffraction patterns of RuO_2 films deposited on titanium substrate for different time at a current density of 5.0 mAcm^{-2} : (a) 30 min, 0.0014 g cm^{-2} ; (b) 60 min, 0.0023 g cm^{-2} ; (c) 120 min, 0.0040 g cm^{-2} and (d) 180 min, 0.0059 g cm^{-2} . The marks (#), (x) and (O) correspond to Ru, RuO_2 and Ti materials, respectively [96,97].

The RuO_2 film crystallinity was then analyzed using X-ray diffraction for films with different deposited weights (Fig. I-24). The peak intensities of titanium substrate were reduced with increasing thickness (weight cm^{-2}) of RuO_2 film. However, the peaks corresponding to RuO_2 were observed for all film thickness, indicating that the as-deposited film is not the amorphous form of RuO_2 , contradicting to the observations made by Zhitomirsky et al. [98], and Hu et al. [69,70]. According to the illustrated results the broadening of RuO_2 peaks suggests that the deposited RuO_2 consists of grains of nanometer size. The intensities of RuO_2 peaks were increased with increasing film thickness (g cm^{-2}). The peak at 40.1° (d -value = 2.05 \AA) could not be well resolved, as it can be attributed to the both, deposition of metallic ruthenium or ruthenium oxide. Therefore, it is concluded that in their study, RuO_2 and Ru have been co-deposited [96,97].

(iv) FTIR methods

The Fourier Transform Infra-Red spectroscopy (FT-IR) was used by UM Patil et al. [88] in order to verify the formation of chemically prepared RuO_2 powders.

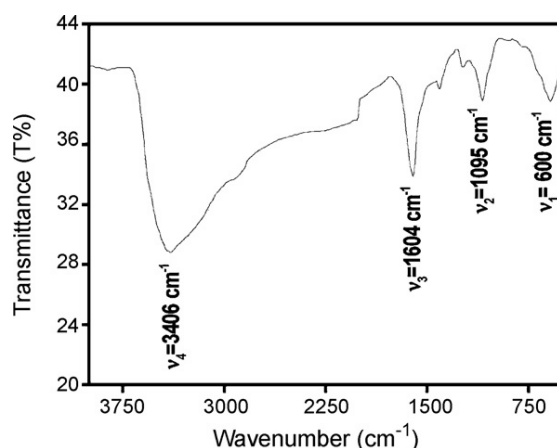


Fig. I-25. FT-IR spectra of RuO₂ deposited by CBD method [88].

The FT-IR absorption spectrum of RuO₂ in the range 4000–400 cm⁻¹ is shown in Fig. I-25. The strong band (ν_1) around at 600 cm⁻¹ is associated with the characteristic vibrational mode of rutile RuO₂. The absorption peak (ν_2) at around 1095 cm⁻¹ is assigned to characteristic stretching vibration of peroxy groups. The absorption peak around 1604 cm⁻¹ is due to the bending vibration of hydroxyl groups of molecular water (ν_3). The sharp absorption band (ν_4) at 3406 cm⁻¹ is attributed to the stretching vibrations of OH⁻. Shoulder of the ν_4 bond attributed to the hydrous nature of the RuO₂ material. These results revealed that, deposited film contained hydroxide bonds indicates the formation of hydrous RuO₂.

IV-2. Electrochemical Tools:

(i) Cyclic voltammetry

The examples of using cyclic voltammetry in order to study the electrochemical behavior of pseudocapacitive materials are numerous. In order to improve the capacitive performance of WO₃, in a recent paper by Y-H Wang et al. [79] this metal oxide was introduced to carbon aerogels, in a form of well-dispersed single crystalline nanoparticles with a simple immersion–calcination process. The carbon aerogels serve as the conducting, mesoporous template to host the dispersion of WO₃. Therefore, the capacitive performance of WO₃ was greatly improved over that of the plain WO₃ electrode through the dispersion design achieved with the carbon aerogels template. As chosen in figure I-26 specific capacitance as high as 700 F g⁻¹ were obtained at the scan rate of 25 mV s⁻¹ in 0.5 M H₂SO₄ over a potential window of -0.3 to 0.5 V (vs. Ag/AgCl).

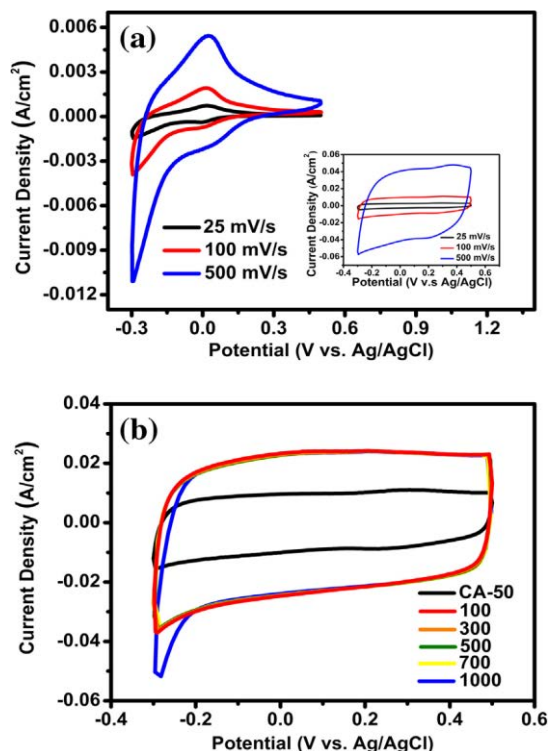


Fig I-26. (a) CVs of WO_3 nanoparticles at three scan rates, 25, 100, and 500 mV/s. Inset shows corresponding CVs of carbon aerogels calcined at 400 °C were also included for comparison. (b) CVs of WO_3 /Carbon aerogels composites at 100 mV/s recorded at cycle numbers of 100, 300, 500, 700, and 1000. Also included was CV for plain CA recorded at the 50th cycle [79].

On a similar attempt to promote MO_x performances for electrochemical capacitors, K. H. Chang et al. [103] have synthesized crystalline tungsten oxide mixtures, $\text{WO}_3\text{--}\text{WO}_3\cdot 0.5\text{H}_2\text{O}$, by microwave-assisted hydrothermal, CV was used in order to determine the specific capacitance, a capacitive-like behavior was observed at 200 mVs^{-1} and $C_s \approx 290\text{ Fg}^{-1}$ at 25 mVs^{-1} in $0.5\text{M H}_2\text{SO}_4$ between -0.6 and 0.2 V . The oxide mixtures prepared by this method, with annealing in air at temperatures $\leq 400\text{ }^\circ\text{C}$, show promising performances. Furtherly, an aqueous EC of the asymmetric type, consisting of a $\text{WO}_3\text{--}\text{WO}_3\cdot 0.5\text{H}_2\text{O}$ anode and a $\text{RuO}_2\cdot x\text{H}_2\text{O}$ cathode, with a potential window of 1.6V was demonstrated, which showed the device energy and power densities of 23.4 W kg^{-1} and 5.2 kW kg^{-1} , respectively (Fig. I-27).

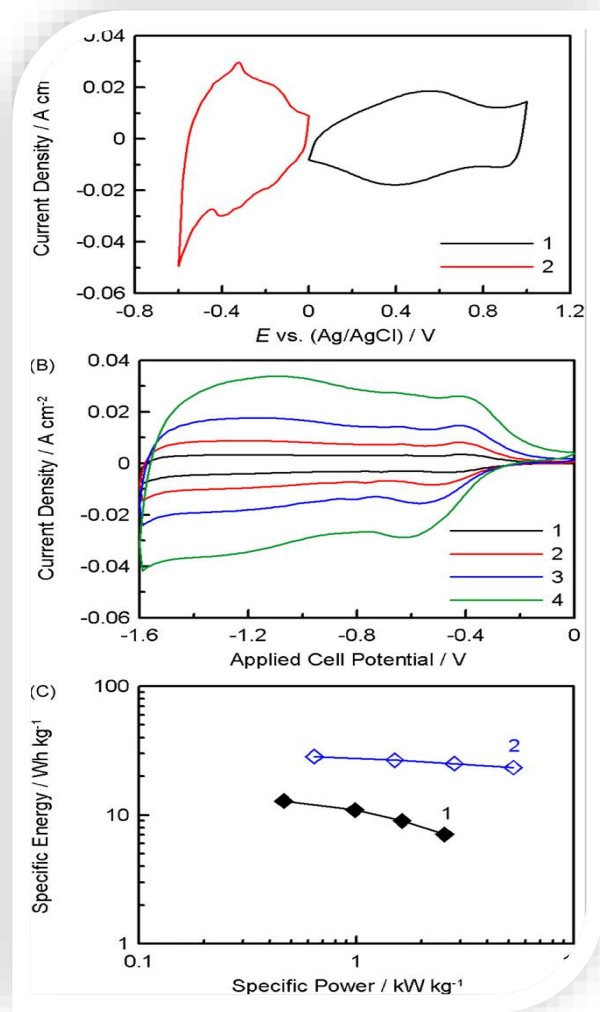


Fig. I-27. (a) Cyclic voltammograms of (1) RuO₂·xH₂O and (2) WO₃ measured at 25mVs⁻¹ in 0.5M H₂SO₄; (b) Cyclic voltammograms of a supercapacitor based on an asymmetric type consisting of a WO₃anode and a RuO₂·xH₂O cathode measured at (1) 10mVs⁻¹, (2) 25mVs⁻¹, (3) 50mVs⁻¹, and (4) 100mVs⁻¹ in 0.5M H₂SO₄; (c) The plots of specific energy vs. specific power for (1) symmetric (RuO₂–RuO₂) and (2) asymmetric (RuO₂–WO₃) capacitors. The total weight of all active materials (including cathode and anode) for both symmetric and asymmetric capacitors is equal to ca. 4mg cm⁻² [103].

(ii) EIS technique

Electrochemical impedance spectroscopy (EIS) is a classical electrochemical diagnostic tool which could bring useful information in terms of resistance and capacitance involved with electrodes designed for applications in supercapacitors. H.S. Nam et al. [74] proposed to use EIS in order to determine the electrochemical capacitive behavior in their synthesized nanoporous hydrous RuO₂. The EIS results of as-prepared and annealed RuO₂ electrodes with different hydrous contents are presented in figure I-28.

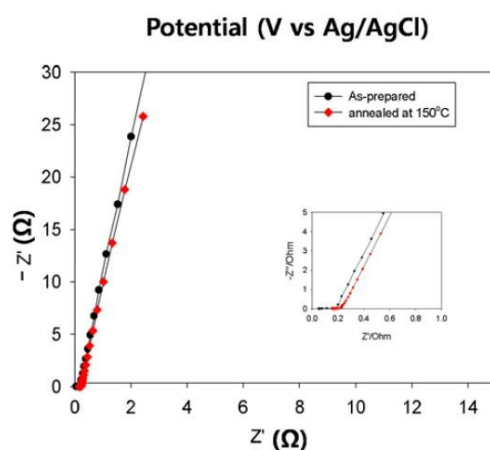


Fig I-28. Electrochemical Impedance measurements of nanoporous hydrous RuO_2 samples, for a frequency range from 100 kHz to 0.01 Hz at a potential of 1.0 V vs Ag/AgCl. The inset shows the magnification [74].

Both the $\text{RuO}_2 \cdot 3.38\text{H}_2\text{O}$ and $\text{RuO}_2 \cdot 2.56\text{H}_2\text{O}$ electrodes showed similar Nyquist plot curves with typical linear shape of electrochemical capacitors, where slope gradually changes from 45 to 90°, the imaginary part of impedance sharp increased and showed the vertical line of capacitive behavior. From these results it was concluded that both the $\text{RuO}_2 \cdot 3.38\text{H}_2\text{O}$ and $\text{RuO}_2 \cdot 2.56\text{H}_2\text{O}$ electrodes exhibited nearly pure electrochemical capacitive behavior. In another work [80] EIS was conducted to elucidate the electrochemical capacitive behavior of hybrid SWCNT/ WO_3 /PANI electrodes. Fig. I-29 shows the Nyquist plots of the electrodes measured within the range from 50 kHz to 50 mHz at 0 V vs Ag/AgCl.

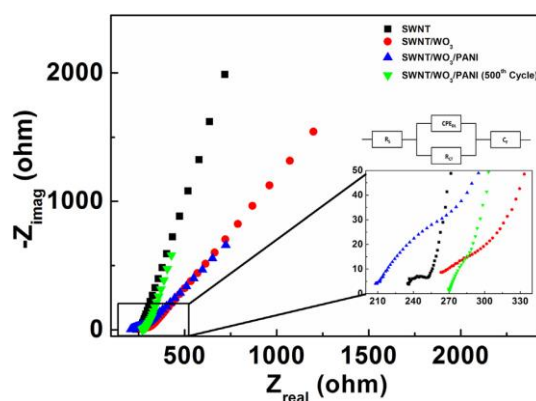


Fig. I-29. Impedance spectra of thin RuO_2 films measured within the range from 50 kHz to 50 mHz at a 0 V DC potential. Inset is magnified for the high frequency region of the impedance spectra [80].

Supercapacitor electrodes EIS responses look like a resistance at high frequency values and like a capacitance at low frequency values. In a theoretical Nyquist plot, there is a small semicircle in the high frequency region and a straight line in the low frequency region. The high frequency semicircle is attributed to the electrode-electrolyte interface, which is related to the double-layer capacitance in parallel with the charge-transfer

resistances. It was observed that bare SWCNT electrodes had the smallest semicircle, while those for the composite electrodes were too broad and unclear. The continuous line which appears in the low frequency region is due to the pseudocapacitance response: the steepest line was related to the SWCNT electrodes, while the slope decreased for the composites. It is also shown in figure I-29 that the resistance (not shown here) of ternary composites was smaller than the binary composite and bare SWCNT electrodes. This could be attributed to the protonated nature of PANI, which decreases the resistance. After 500 charge/discharge cycles, ternary nanocomposite was found to have an increased resistance with enhanced pseudocapacitance as observed in the figure I-29.

From these examples and also other available studies not presented here it could be concluded that EIS could bring information in terms of resistance of transfer and capacitance determined through an equivalent circuit approach. Nevertheless, it would describe globally the elements involved in this electrochemical system from a general point of view. However, this methodology lonely doesn't give that much of kinetics information necessary to understand the key reactions involved with ions and charge compensation at the interface of electrode/electrolyte.

(iii) Quartz Crystal Microbalance

Another methodology which could target ions intercalation/electroadsorption is quartz crystal microbalance (QCM). There have been various studies using quartz crystal microbalance as an in situ gravimetric probe to study the insertion and/or electroadsorption of ions in metal oxides or carbon based electrodes [104–107].

Electrochemical quartz crystal microbalance (EQCM) and cyclic voltammetry (CV) measurements (Fig. I-30) were used by P Simon et al. [104] to characterize ion electroadsorption involved with carbide-derived carbon (CDC) with two different average pore sizes, from neat and solvated EMI-TFSI electrolytes. Their EQCM study showed some key differences existing between EMI⁺ and TFSI⁻ ions during transport and electroadsorption into carbon nanopores.

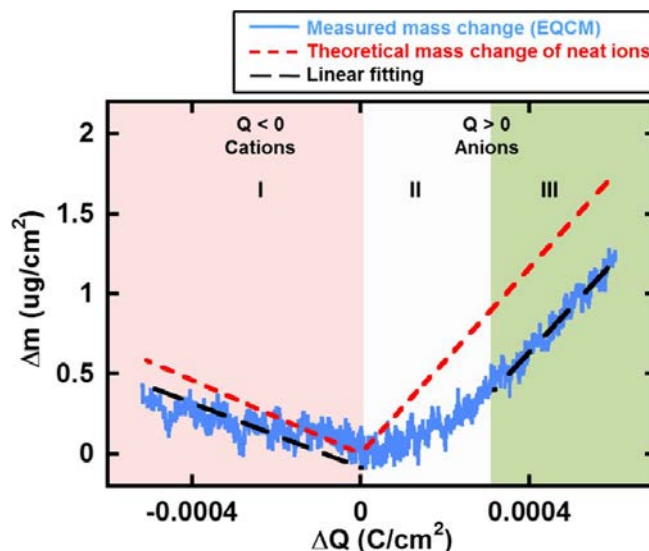


Fig. I-30. Electrode mass change vs charge during the polarization of CDC-1 nm in neat EMI-TFSI: Blue solid lines are measured mass change (EQCM), red dashed lines are the theoretical mass change of neat ions calculated from Faraday's law. The black dashed line shows the linear fitting of measured mass change [104].

Santos et al. [105] studied the Li^+ ion intercalation/adsorption behavior of dense WO_3 films in acetonitrile solution containing LiClO_4 by QCM measurements during cyclic voltammetry (EQCM). The mass-to-charge ratios were calculated from the EQCM data in LiClO_4 /acetonitrile electrolytes, which can be used to estimate the molar mass of the species inserted in the material. However, none of the values obtained from the MCR was in the order of the equivalent weight of either ion (Li^+ , or ClO_4^-) or solvent molecules (acetonitrile) of the study. The equivalent weight values, higher than that of Li^+ (7 g mol^{-1}) were simply attributed to the acetonitrile molecules, accompanying the Li^+ ions.

A similar study by Vondrak et al. [106] investigated the electrochemical insertion of H^+ , Li^+ , Na^+ ions into thin layers of WO_3 by EQCM in propylene carbonate. EQCM data of their work also detected molar mass values higher than that would correspond to the cation present in the electrolyte. Therefore, it was suggested that ions do not enter the space lattice alone but may be accompanied by propylene carbonate solvent molecules without any other pertinent explanation.

Despite useful information given by EQCM when it comes to describe the ion intercalation/electroadsorption mechanisms involved with charge storage in capacitive materials, there are also some limitations. EQCM gives a global response corresponding in fact to several possible pathways such that ions, ions with solvation shells and even indirectly free solvent molecules can be associated to the electrochemical process. Additionally, ions may lose a part of their solvation to access to the sites in smaller nanopores. These possible pathways,

and kinetic or dynamic aspects of the ion intercalation/electroadsorption processes have never been characterized in the previous mentioned EQCM studies due to the limitations of the classical technique.

An alternative characterization tool was proposed to overcome the limitations of the classical EQCM to study the ion intercalation/electro adsorption mechanisms in pseudocapacitive electrodes. This method, so-called *ac*-electrogravimetry consists of an in situ coupling of electrochemical impedance spectroscopy (EIS) and a fast quartz crystal microbalance (QCM). Although QCM exists more or less routinely in laboratories these days, this coupling has been developed in a limited number of laboratories worldwide. The *ac*-electrogravimetry simultaneously measures the electrochemical impedance, $\frac{\Delta E}{\Delta I}(\omega)$, and the mass/potential transfer functions, $\frac{\Delta m}{\Delta E}(\omega)$ during a sinusoidal potential perturbation with a small amplitude applied to the modified electrode. The mass/potential transfer functions allow the change in mass due to a unit charge passing through the electrode/film/electrolyte interfaces to be determined. It provides the access to the relevant information on (i) the kinetics of species transferred at the solid/ solution interfaces, and their transport in the bulk of the materials, (ii) the nature of these species as well as their relative concentration within the material. This coupling dominates over the limitations of QCM technique and has the ability to deconvolute the global mass changes provided by QCM measurements. Specifically, it detects the contribution of the charged or uncharged species and to identify anionic, cationic, and the free solvent contributions during various redox processes, and recently has been applied to study pseudo-capacitive charge storage mechanisms in Li-birnessite type MnO₂ electrodes [107].

V. The Scope and Principle Objectives of Thesis Project:

In the first section of this chapter the importance of investigating materials, with an emphasize on those which can be used for fabricating pseudocapacitive films for energy storage devices, was discussed. Furtherly several examples of capacitive metal oxides and various possibilities for their elaboration were categorized. Then, different structural and electrochemical diagnostic tools were employed in order to characterize them and therefore, to improve their performances. Since the key phenomena in all these examples of capacitive materials is the ion's exchange at the interface of electrode/electrolyte, it was clearly seen that none of mentioned diagnostic methods lonely provide information on the exact identification of the intercalated ionic species, their dynamics of transfer at the interfaces, as well as the role of electrolyte composition and

the effect of ions solvation on the various phenomena. The status of transferred ions is not a quite solved problem and the characterization of their transfer dynamics is not straightforward using conventional characterization tools. Therefore, the challenge is to find an eligible technique offering mechanistic solutions in a single body. This technique should allow the study of ion intercalation/electroadsorption phenomena in situ and in contact with an electrolyte. Consequently, it was concluded to focus on the special capability of *ac*-electrogravimetry as a powerful coupled electrochemical methodology in order to exploit information and to study the ion intercalation/extraction behavior of WO_3 , RuO_2 and TiO_2 metal oxides. Special attention is given to the poorly understood aspects, such as the nature of the ions involved in the charge compensation, solvation and the role of the electrolytes and the dynamic information of ions transfer at the electrode/electrolyte interfaces.

Another equally important discussion was the improvement of the performance of metal oxide based electrodes which is with no doubt attributed to their structure. Nanostructuring could procure materials with favorable morphologies, unique properties and functionalities that can effectively be exploited in electrochemical devices. As a consequent, the main objective of this thesis project is to provide an answer to the following questions:

- Do mesoporous films, with small pore sizes, and large surface area to volume ratios, facilitate the ion intercalation/electro adsorption process involved with each chosen synthesized MO_x ?
- What differences in behavior are mainly brought by procuring porosity within the film?
- How *ac*-electrogravimetry as the main non-classical methodology served in this project could be advantageous for our study?
- Is this technique able to extract subtleties unreachable with classical tools?
- In which way the obtained information could be helpful for the future design and optimization of electrode materials for energy storage systems?

VI. References:

- [1] K. Ozoemena, *Nanomaterials in Advanced Batteries and Electrochemical Capacitors*, Springer, 2016.
- [2] T. Brousse, F. Favier, P. Simon, *Carbon-based or Pseudocapacitive Materials Supercapacitors*, Wiley, 2016.
- [3] S.K. Tripathi, A. Jain, *Supercapacitors “Alternative Energy Storage System,”* LAP LAMBERT Academic Publishing, Saarbrücken, 2013.
- [4] P. Simon, Y. Gogotsi, *Materials for electrochemical capacitors*, *Nat. Mater.* 7 (2008) 845–854.
- [5] M. Beidaghi, Y. Gogotsi, *Capacitive energy storage in micro-scale devices: recent advances in design and fabrication of micro-supercapacitors*, *Energy Environ. Sci.* 7 (2014) 867–884.
- [6] M. Lazzari, *Electrode Materials for Ionic Liquid Based-Supercapacitors*, (2010). <http://amsdottorato.unibo.it/2718/> (accessed June 25, 2016).
- [7] R. Lin, *Formulation of electrolytes based on ionic liquids for supercapacitor applications*, Université de Toulouse, Université Toulouse III-Paul Sabatier, 2012. <http://thesesups.ups-tlse.fr/1895> (accessed June 25, 2016).
- [8] C. Péan, *Modélisation des processus dynamiques dans les supercondensateurs*, Paris 6, 2015. <http://www.theses.fr/2015PA066243> (accessed June 25, 2016).
- [9] C. Zhong, Y. Deng, W. Hu, J. Qiao, L. Zhang, J. Zhang, *A review of electrolyte materials and compositions for electrochemical supercapacitors*, *Chem. Soc. Rev.* 44 (2015) 7484–7539.
- [10] Y. Gogotsi, *Not just graphene: The wonderful world of carbon and related nanomaterials*, *MRS Bull.* 40 (2015) 1110–1121.
- [11] B.E. Conway, V. Birss, J. Wojtowicz, *The role and utilization of pseudocapacitance for energy storage by supercapacitors*, *J. Power Sources.* 66 (1997) 1–14.
- [12] B. Babakhani, D.G. Ivey, *Investigation of electrochemical behavior of Mn–Co doped oxide electrodes for electrochemical capacitors*, *Electrochimica Acta.* 56 (2011) 4753–4762.
- [13] S. Devaraj, N. Munichandraiah, *Effect of crystallographic structure of MnO₂ on its electrochemical capacitance properties*, *J. Phys. Chem. C.* 112 (2008) 4406–4417.
- [14] L. Kong, C. Zhang, S. Zhang, J. Wang, R. Cai, C. Lv, W. Qiao, L. Ling, D. Long, *High-power and high-energy asymmetric supercapacitors based on Li⁺-intercalation into a T-Nb₂O₅/graphene pseudocapacitive electrode*, *J. Mater. Chem. A.* 2 (2014) 17962–17970.

- [15] B.K. Kim, V. Chabot, A. Yu, Carbon nanomaterials supported Ni(OH)₂/NiO hybrid flower structure for supercapacitor, *Electrochimica Acta*. 109 (2013) 370–380.
- [16] A. Ferris, S. Garbarino, D. Guay, D. Pech, 3D RuO₂ Microsupercapacitors with Remarkable Areal Energy, *Adv. Mater.* 27 (2015) 6625–6629.
- [17] R.B. Rakhi, W. Chen, M.N. Hedhili, D. Cha, H.N. Alshareef, Enhanced rate performance of mesoporous Co₃O₄ nanosheet supercapacitor electrodes by hydrous RuO₂ nanoparticle decoration, *ACS Appl. Mater. Interfaces*. 6 (2014) 4196–4206.
- [18] S. Makino, T. Ban, W. Sugimoto, Towards implantable bio-supercapacitors: pseudocapacitance of ruthenium oxide nanoparticles and nanosheets in acids, buffered solutions, and bioelectrolytes, *J. Electrochem. Soc.* 162 (2015) A5001–A5006.
- [19] G.H. Jeong, H.-M. Lee, J. Kang, H. Lee, C.-K. Kim, J.-H. Lee, J.-H. Kim, S.-W. Kim, ZrO₂–SiO₂ Nanosheets with Ultrasmall WO₃ Nanoparticles and Their Enhanced Pseudocapacitance and Stability, *ACS Appl. Mater. Interfaces*. 6 (2014) 20171–20178.
- [20] M. Sasidharan, N. Gunawardhana, M. Yoshio, K. Nakashima, WO₃ hollow nanospheres for high-lithium storage capacity and good cyclability, *Nano Energy*. 1 (2012) 503–508.
- [21] Z. Chen, Y. Peng, F. Liu, Z. Le, J. Zhu, G. Shen, D. Zhang, M. Wen, S. Xiao, C.-P. Liu, others, Hierarchical Nanostructured WO₃ with Biomimetic Proton Channels and Mixed Ionic-Electronic Conductivity for Electrochemical Energy Storage, *Nano Lett.* 15 (2015) 6802–6808.
- [22] H. Yamada, K. Tagawa, M. Komatsu, I. Moriguchi, T. Kudo, High power battery electrodes using nanoporous V₂O₅/carbon composites, *J. Phys. Chem. C*. 111 (2007) 8397–8402.
- [23] S.B. Kondawar, *Conducting Polymer Nanocomposites for Supercapacitors*, 2016.
- [24] J. Zang, S.-J. Bao, C.M. Li, H. Bian, X. Cui, Q. Bao, C.Q. Sun, J. Guo, K. Lian, Well-aligned cone-shaped nanostructure of polypyrrole/RuO₂ and its electrochemical supercapacitor, *J. Phys. Chem. C*. 112 (2008) 14843–14847.
- [25] S.F. Shaikh, J.Y. Lim, O.-S. Joo, Electrochemical supercapacitors of electrodeposited PANI/H-RuO₂ hybrid nanostructure, *Curr. Appl. Phys.* 13 (2013) 758–761.
- [26] X. Li, Y. Wu, F. Zheng, M. Ling, F. Lu, Preparation and characterization of RuO₂/polypyrrole electrodes for supercapacitors, *Solid State Commun.* 197 (2014) 57–60.
- [27] V. Augustyn, P. Simon, B. Dunn, Pseudocapacitive oxide materials for high-rate electrochemical energy storage, *Energy Environ. Sci.* 7 (2014) 1597–1614.
- [28] M. Mallouki, F. Tran-Van, C. Sarrazin, P. Simon, B. Daffos, A. De, C. Chevrot, J.-F. Fauvarque, Polypyrrole-Fe₂O₃ nanohybrid materials for electrochemical storage, *J. Solid State Electrochem.* 11 (2007) 398–406.

- [29] M. Mallouki, F. Tran-Van, C. Sarrazin, C. Chevrot, J.F. Fauvarque, Electrochemical storage of polypyrrole-Fe₂O₃ nanocomposites in ionic liquids, *Electrochimica Acta*. 54 (2009) 2992–2997.
- [30] A. Mery, F. Ghamouss, C. Autret, D. Farhat, F. Tran-Van, Aqueous ultracapacitors using amorphous MnO₂ and reduced graphene oxide, *J. Power Sources*. 305 (2016) 37–45.
- [31] W.A. Christinelli, R. Gonçalves, E.C. Pereira, A new generation of electrochemical supercapacitors based on layer-by-layer polymer films, *J. Power Sources*. 303 (2016) 73–80.
- [32] Q. Wang, J. Yan, Z. Fan, Carbon materials for high volumetric performance supercapacitors: design, progress, challenges and opportunities, *Energy Environ. Sci.* 9 (2016) 729–762.
- [33] K. Fic, E. Frackowiak, F. Béguin, Unusual energy enhancement in carbon-based electrochemical capacitors, *J. Mater. Chem.* 22 (2012) 24213–24223.
- [34] Y. Gogotsi, Formulation of Ionic Liquid Electrolyte to Expand the Voltage Window of Supercapacitors, in: 228th ECS Meet. Oct. 2015.
- [35] R.R. Salunkhe, J. Tang, Y. Kamachi, T. Nakato, J.H. Kim, Y. Yamauchi, Asymmetric supercapacitors using 3D nanoporous carbon and cobalt oxide electrodes synthesized from a single metal-organic framework, *ACS Nano*. 9 (2015) 6288–6296.
- [36] R.R. Salunkhe, Y.-H. Lee, K.-H. Chang, J.-M. Li, P. Simon, J. Tang, N.L. Torad, C.-C. Hu, Y. Yamauchi, Nanoarchitected graphene-based supercapacitors for next-generation energy-storage applications, *Chem. Eur. J.* 20 (2014) 13838–13852.
- [37] X. Xiao, T. Li, Z. Peng, H. Jin, Q. Zhong, Q. Hu, B. Yao, Q. Luo, C. Zhang, L. Gong, others, Freestanding functionalized carbon nanotube-based electrode for solid-state asymmetric supercapacitors, *Nano Energy*. 6 (2014) 1–9.
- [38] A. Eftekhari, F. Molaei, Carbon nanotube-assisted electrodeposition. Part I: Battery performance of manganese oxide films electrodeposited at low current densities, *J. Power Sources*. 274 (2015) 1306–1314.
- [39] A. Eftekhari, F. Molaei, Carbon nanotube-assisted electrodeposition. Part II: Superior pseudo-capacitive behavior of manganese oxide film electrodeposited at high current densities, *J. Power Sources*. 274 (2015) 1315–1321.
- [40] B. You, N. Li, H. Zhu, X. Zhu, J. Yang, Graphene Oxide-Dispersed Pristine CNTs Support for MnO₂ Nanorods as High Performance Supercapacitor Electrodes, *ChemSusChem*. 6 (2013) 474–480.
- [41] H. Jiang, Y. Dai, Y. Hu, W. Chen, C. Li, Nanostructured ternary nanocomposite of rGO/CNTs/MnO₂ for high-rate supercapacitors, *ACS Sustain. Chem. Eng.* 2 (2013) 70–74.

- [42] L. Li, Z.A. Hu, N. An, Y.Y. Yang, Z.M. Li, H.Y. Wu, Facile synthesis of MnO₂/CNTs composite for supercapacitor electrodes with long cycle stability, *J. Phys. Chem. C*. 118 (2014) 22865–22872.
- [43] Q. Cheng, J. Tang, J. Ma, H. Zhang, N. Shinya, L.-C. Qin, Graphene and nanostructured MnO₂ composite electrodes for supercapacitors, *Carbon*. 49 (2011) 2917–2925.
- [44] F. Yang, L. Zhang, A. Zuzuarregui, K. Gregorczyk, L. Li, M. Beltrán, C. Tollan, J. Brede, C. Rogero, A. Chuvilin, others, Functionalization of defect sites in graphene with RuO₂ for high capacitive performance, *ACS Appl. Mater. Interfaces*. 7 (2015) 20513–20519.
- [45] F. Pico, E. Morales, J.A. Fernandez, T.A. Centeno, J. Ibáñez, R.M. Rojas, J.M. Amarilla, J.M. Rojo, Ruthenium oxide/carbon composites with microporous or mesoporous carbon as support and prepared by two procedures. A comparative study as supercapacitor electrodes, *Electrochimica Acta*. 54 (2009) 2239–2245.
- [46] H. Li, R. Wang, R. Cao, Physical and electrochemical characterization of hydrous ruthenium oxide/ordered mesoporous carbon composites as supercapacitor, *Microporous Mesoporous Mater*. 111 (2008) 32–38.
- [47] I.-H. Kim, J.-H. Kim, K.-B. Kim, Electrochemical characterization of electrochemically prepared ruthenium oxide/carbon nanotube electrode for supercapacitor application, *Electrochem. Solid-State Lett*. 8 (2005) A369–A372.
- [48] R.-R. Bi, X.-L. Wu, F.-F. Cao, L.-Y. Jiang, Y.-G. Guo, L.-J. Wan, Highly dispersed RuO₂ nanoparticles on carbon nanotubes: facile synthesis and enhanced supercapacitance performance, *J. Phys. Chem. C*. 114 (2010) 2448–2451.
- [49] Y. Su, W.U. Feng, L. Bao, Z. Yang, RuO₂/activated carbon composites as a positive electrode in an alkaline electrochemical capacitor, *New Carbon Mater*. 22 (2007) 53–57.
- [50] W. Wang, S. Guo, I. Lee, K. Ahmed, J. Zhong, Z. Favors, F. Zaera, M. Ozkan, C.S. Ozkan, Hydrous ruthenium oxide nanoparticles anchored to graphene and carbon nanotube hybrid foam for supercapacitors, *Sci. Rep*. 4 (2014) 4452.
- [51] X. Leng, J. Zou, X. Xiong, H. He, Hydrothermal synthesis and pseudo capacitance behavior of a highly homogeneous dispersed graphene sheets/ruthenium oxide nanocomposite, *RSC Adv*. 4 (2014) 61596–61603.
- [52] Z. Zhou, Y. Zhu, Z. Wu, F. Lu, M. Jing, X. Ji, Amorphous RuO₂ coated on carbon spheres as excellent electrode materials for supercapacitors, *RSC Adv*. 4 (2014) 6927–6932.
- [53] Z.R. Cormier, H.A. Andreas, P. Zhang, Temperature-dependent structure and electrochemical behavior of RuO₂/carbon nanocomposites, *J. Phys. Chem. C*. 115 (2011) 19117–19128.
- [54] C. Portet, P.L. Taberna, P. Simon, E. Flahaut, C. Laberty-Robert, High power density electrodes for carbon supercapacitor applications, *Electrochimica Acta*. 50 (2005) 4174–4181.

- [55] B. Daffos, P.-L. Taberna, Y. Gogotsi, P. Simon, Recent advances in understanding the capacitive storage in microporous carbons, *Fuel Cells*. 10 (2010) 819–824.
- [56] J. Tang, T. Wang, R.R. Salunkhe, S.M. Alshehri, V. Malgras, Y. Yamauchi, Three-Dimensional Nitrogen-Doped Hierarchical Porous Carbon as an Electrode for High-Performance Supercapacitors, *Chem. Eur. J.* 21 (2015) 17293–17298.
- [57] M. Zhu, W. Meng, Y. Huang, Y. Huang, C. Zhi, Proton-insertion-enhanced pseudocapacitance based on the assembly structure of tungsten oxide, *ACS Appl. Mater. Interfaces*. 6 (2014) 18901–18910.
- [58] J. Xu, T. Ding, J. Wang, J. Zhang, S. Wang, C. Chen, Y. Fang, Z. Wu, K. Huo, J. Dai, Tungsten oxide nanofibers self-assembled mesoscopic microspheres as high-performance electrodes for supercapacitor, *Electrochimica Acta*. 174 (2015) 728–734.
- [59] C. Yuan, H. Lin, H. Lu, E. Xing, Y. Zhang, B. Xie, Anodic deposition and capacitive property of nano-WO₃·H₂O/MnO₂ composite as supercapacitor electrode material, *Mater. Lett.* 148 (2015) 167–170.
- [60] J. Kang, S.-H. Wei, K. Zhu, Y.-H. Kim, First-principles theory of electrochemical capacitance of nanostructured materials: Dipole-assisted subsurface intercalation of lithium in pseudocapacitive TiO₂ anatase nanosheets, *J. Phys. Chem. C*. 115 (2011) 4909–4915.
- [61] T. Brezesinski, J. Wang, J. Polleux, B. Dunn, S.H. Tolbert, Templated nanocrystal-based porous TiO₂ films for next-generation electrochemical capacitors, *J. Am. Chem. Soc.* 131 (2009) 1802–1809.
- [62] X. Sun, M. Xie, J.J. Travis, G. Wang, H. Sun, J. Lian, S.M. George, Pseudocapacitance of amorphous TiO₂ thin films anchored to graphene and carbon nanotubes using atomic layer deposition, *J. Phys. Chem. C*. 117 (2013) 22497–22508.
- [63] J. Zhu, W. Shi, N. Xiao, X. Rui, H. Tan, X. Lu, H.H. Hng, J. Ma, Q. Yan, Oxidation-etching preparation of MnO₂ tubular nanostructures for high-performance supercapacitors, *ACS Appl. Mater. Interfaces*. 4 (2012) 2769–2774.
- [64] T. Brousse, D. Bélanger, J.W. Long, To be or not to be pseudocapacitive?, *J. Electrochem. Soc.* 162 (2015) A5185–A5189.
- [65] X. Zhang, X. Sun, H. Zhang, D. Zhang, Y. Ma, Microwave-assisted reflux rapid synthesis of MnO₂ nanostructures and their application in supercapacitors, *Electrochimica Acta*. 87 (2013) 637–644.
- [66] Y. Hu, J. Wang, X. Jiang, Y. Zheng, Z. Chen, Facile chemical synthesis of nanoporous layered δ-MnO₂ thin film for high-performance flexible electrochemical capacitors, *Appl. Surf. Sci.* 271 (2013) 193–201.

- [67] Q. Qu, P. Zhang, B. Wang, Y. Chen, S. Tian, Y. Wu, R. Holze, Electrochemical Performance of MnO₂ Nanorods in Neutral Aqueous Electrolytes as a Cathode for Asymmetric Supercapacitors, *J. Phys. Chem. C*. 113 (2009) 14020–14027. doi:10.1021/jp8113094.
- [68] C.-C. Hu, K.-H. Chang, M.-C. Lin, Y.-T. Wu, Design and tailoring of the nanotubular arrayed architecture of hydrous RuO₂ for next generation supercapacitors, *Nano Lett.* 6 (2006) 2690–2695.
- [69] C.-C. Hu, Y.-H. Huang, Effects of preparation variables on the deposition rate and physicochemical properties of hydrous ruthenium oxide for electrochemical capacitors, *Electrochimica Acta*. 46 (2001) 3431–3444.
- [70] C.-C. Hu, K.-H. Chang, Cyclic voltammetric deposition of hydrous ruthenium oxide for electrochemical supercapacitors: effects of the chloride precursor transformation, *J. Power Sources*. 112 (2002) 401–409.
- [71] J.P. Zheng, P.J. Cygan, T.R. Jow, Hydrous ruthenium oxide as an electrode material for electrochemical capacitors, *J. Electrochem. Soc.* 142 (1995) 2699–2703.
- [72] D.J. Suh, T.-J. Park, W.-I. Kim, I.-K. Hong, Synthesis of high-surface-area ruthenium oxide aerogels by non-alkoxide sol–gel route, *J. Power Sources*. 117 (2003) 1–6.
- [73] V. Subramanian, S.C. Hall, P.H. Smith, B. Rambabu, Mesoporous anhydrous RuO₂ as a supercapacitor electrode material, *Solid State Ion*. 175 (2004) 511–515.
- [74] H.-S. Nam, K.-S. Jang, J.M. Ko, Y.-M. Kong, J.-D. Kim, Electrochemical capacitance of nanoporous hydrous RuO₂ templated by anionic surfactant, *Electrochimica Acta*. 56 (2011) 6459–6463.
- [75] B.-X. Zou, Y. Liang, X.-X. Liu, D. Diamond, K.-T. Lau, Electrodeposition and pseudocapacitive properties of tungsten oxide/polyaniline composite, *J. Power Sources*. 196 (2011) 4842–4848.
- [76] P.-L. Taberna, G. Chevallier, P. Simon, D. Plée, T. Aubert, Activated carbon–carbon nanotube composite porous film for supercapacitor applications, *Mater. Res. Bull.* 41 (2006) 478–484.
- [77] H. Peng, G. Ma, K. Sun, J. Mu, M. Luo, Z. Lei, High-performance aqueous asymmetric supercapacitor based on carbon nanofibers network and tungsten trioxide nanorod bundles electrodes, *Electrochimica Acta*. 147 (2014) 54–61.
- [78] L. Ma, X. Zhou, L. Xu, X. Xu, L. Zhang, C. Ye, J. Luo, W. Chen, Hydrothermal preparation and supercapacitive performance of flower-like WO₃·H₂O/reduced graphene oxide composite, *Colloids Surf. Physicochem. Eng. Asp.* 481 (2015) 609–615.
- [79] Y.-H. Wang, C.-C. Wang, W.-Y. Cheng, S.-Y. Lu, Dispersing WO₃ in carbon aerogel makes an outstanding supercapacitor electrode material, *Carbon*. 69 (2014) 287–293.

- [80] R. Yuksel, C. Durucan, H.E. Unalan, Ternary nanocomposite SWNT/WO₃/PANI thin film electrodes for supercapacitors, *J. Alloys Compd.* 658 (2016) 183–189.
- [81] M. Li, F. Liu, J.P. Cheng, J. Ying, X.B. Zhang, Enhanced performance of nickel–aluminum layered double hydroxide nanosheets/carbon nanotubes composite for supercapacitor and asymmetric capacitor, *J. Alloys Compd.* 635 (2015) 225–232.
- [82] X. Liu, R. Wang, M. Liu, J. Luo, X. Jin, J. Sun, L. Gao, *Materials Chemistry A*, (2014).
- [83] F. He, Z. Hu, K. Liu, S. Zhang, H. Liu, S. Sang, In situ fabrication of nickel aluminum-layered double hydroxide nanosheets/hollow carbon nanofibers composite as a novel electrode material for supercapacitors, *J. Power Sources.* 267 (2014) 188–196.
- [84] W. Yang, Z. Gao, J. Wang, J. Ma, M. Zhang, L. Liu, Solvothermal one-step synthesis of Ni–Al layered double hydroxide/carbon nanotube/reduced graphene oxide sheet ternary nanocomposite with ultrahigh capacitance for supercapacitors, *ACS Appl. Mater. Interfaces.* 5 (2013) 5443–5454.
- [85] M. Li, J.P. Cheng, J.H. Fang, Y. Yang, F. Liu, X.B. Zhang, NiAl-layered double hydroxide/reduced graphene oxide composite: microwave-assisted synthesis and supercapacitive properties, *Electrochimica Acta.* 134 (2014) 309–318.
- [86] S. Musić, S. Popović, M. Maljković, K. Furić, A. Gajović, Influence of synthesis procedure on the formation of RuO₂, *Mater. Lett.* 56 (2002) 806–811.
- [87] S. Musić, S. Popović, M. Maljković, A. Šarić, Synthesis and characterization of nanocrystalline RuO₂ powders, *Mater. Lett.* 58 (2004) 1431–1436.
- [88] U.M. Patil, S.B. Kulkarni, V.S. Jamadade, C.D. Lokhande, Chemically synthesized hydrous RuO₂ thin films for supercapacitor application, *J. Alloys Compd.* 509 (2011) 1677–1682.
- [89] T.P. Gujar, V.R. Shinde, C.D. Lokhande, W.-Y. Kim, K.-D. Jung, O.-S. Joo, Spray deposited amorphous RuO₂ for an effective use in electrochemical supercapacitor, *Electrochem. Commun.* 9 (2007) 504–510.
- [90] Y.-Y. Liang, H.L. Li, X.-G. Zhang, Solid state synthesis of hydrous ruthenium oxide for supercapacitors, *J. Power Sources.* 173 (2007) 599–605.
- [91] C. Sassoie, C. Laberty, H. Le Khanh, S. Cassaignon, C. Boissiere, M. Antonietti, C. Sanchez, Block-Copolymer-Templated Synthesis of Electroactive RuO₂-Based Mesoporous Thin Films, *Adv. Funct. Mater.* 19 (2009) 1922–1929.
- [92] C. Sassoie, G. Muller, D.P. Debecker, A. Karelavic, S. Cassaignon, C. Pizarro, P. Ruiz, C. Sanchez, A sustainable aqueous route to highly stable suspensions of monodispersed nano ruthenia, *Green Chem.* 13 (2011) 3230–3237.

- [93] M.-C. Liu, L.-B. Kong, C. Lu, X.-M. Li, Y.-C. Luo, L. Kang, A sol-gel process for fabrication of NiO/NiCo₂O₄/Co₃O₄ composite with improved electrochemical behavior for electrochemical capacitors, *ACS Appl. Mater. Interfaces*. 4 (2012) 4631–4636.
- [94] J.P. Zheng, P.J. Cygan, T.R. Jow, Hydrous ruthenium oxide as an electrode material for electrochemical capacitors, *J. Electrochem. Soc.* 142 (1995) 2699–2703.
- [95] M. Kahram, M. Asnavandi, A. Dolati, Synthesis and electrochemical characterization of sol-gel-derived RuO₂/carbon nanotube composites, *J. Solid State Electrochem.* 18 (2014) 993–1003.
- [96] B.-O. Park, C.D. Lokhande, H.-S. Park, K.-D. Jung, O.-S. Joo, Performance of supercapacitor with electrodeposited ruthenium oxide film electrodes—effect of film thickness, *J. Power Sources*. 134 (2004) 148–152.
- [97] B.-O. Park, C.D. Lokhande, H.-S. Park, K.-D. Jung, O.-S. Joo, Cathodic electrodeposition of RuO₂ thin films from Ru(III)Cl₃ solution, *Mater. Chem. Phys.* 87 (2004) 59–66.
- [98] I. Zhitomirsky, L. Gal-Or, Ruthenium oxide deposits prepared by cathodic electrosynthesis, *Mater. Lett.* 31 (1997) 155–159.
- [99] V.D. Patake, C.D. Lokhande, O.S. Joo, Electrodeposited ruthenium oxide thin films for supercapacitor: Effect of surface treatments, *Appl. Surf. Sci.* 255 (2009) 4192–4196.
- [100] G. Wang, L. Zhang, J. Zhang, A review of electrode materials for electrochemical supercapacitors, *Chem. Soc. Rev.* 41 (2012) 797–828.
- [101] K.-H. Kim, K.S. Kim, G.-P. Kim, S.-H. Baeck, Electrodeposition of mesoporous ruthenium oxide using an aqueous mixture of CTAB and SDS as a templating agent, *Curr. Appl. Phys.* 12 (2012) 36–39.
- [102] D. Muñoz-Rojas, M. Casas-Cabanas, E. Baudrin, Effect of particle size and cell parameter mismatch on the lithium insertion/deinsertion processes into RuO₂, *Solid State Ion.* 181 (2010) 536–544.
- [103] K.-H. Chang, C.-C. Hu, C.-M. Huang, Y.-L. Liu, C.-I. Chang, Microwave-assisted hydrothermal synthesis of crystalline WO₃–WO₃·0.5H₂O mixtures for pseudocapacitors of the asymmetric type, *J. Power Sources*. 196 (2011) 2387–2392.
- [104] W.-Y. Tsai, P.-L. Taberna, P. Simon, Electrochemical quartz crystal microbalance (EQCM) study of ion dynamics in nanoporous carbons, *J. Am. Chem. Soc.* 136 (2014) 8722–8728.
- [105] V.C. Fernandes, M.C. Santos, L.O.S. Bulhões, Nanogravimetric studies of tungsten oxide thin films obtained by the polymeric precursor method, *Thin Solid Films*. 515 (2007) 7155–7161.

- [106] J. Vondrák, M. Sedlářiková, J. Velická, P. Špičák, V. Svoboda, J. Kazelle, Insertion of cations into WO_3 investigated by QCM techniques, *J. Solid State Electrochem.* 11 (2007) 1459–1462.
- [107] C.R. Arias, C. Debiemme-Chouvy, C. Gabrielli, C. Laberty-Robert, A. Pailleret, H. Perrot, O. Sel, New Insights into Pseudocapacitive Charge-Storage Mechanisms in Li-Birnessite Type MnO_2 Monitored by Fast Quartz Crystal Microbalance Methods, *J. Phys. Chem. C.* 118 (2014) 26551–26559.

Résumé du Chapitre II

Ce chapitre est consacré aux différentes techniques de mesures/caractérisation utilisées au cours de ce projet de thèse ainsi qu'aux bases théoriques associées et aux méthodes d'élaboration des différents matériaux examinés dans ce travail.

La première partie est consacrée à la description des différentes techniques de caractérisation structurale (**diffractométrie de rayons X, spectrométrie de photoélectrons induits par rayons X, microscopie électronique à transmission (haute résolution), microscopie électronique à balayage**) et électrogravimétriques (**électrogravimétrie cyclique, *ac*-électrogravimétrie**). L'ensemble de ces outils sera utilisé pour étudier l'influence des différentes méthodes de préparation électrochimiques et physiques utilisés pour la fabrication des électrodes de type MO_x avec différentes morphologies sur la réponse électrochimique de ces différents films.

La fabrication des films de TiO_2 amorphes a été faite selon trois types de morphologie, compacte, poreuse et très poreuse (résultats présentés dans le chapitre III) grâce à un dispositif de pulvérisation réactive de type magnétron au sein de notre laboratoire. Ceci a été possible en contrôlant un paramètre important qui est la pression d'argon et d'oxygène dans la chambre de pulvérisation pendant le dépôt. Cela permet de déposer des couches denses mais également poreuses qui présentent des porosités différentes. La question fondamentale qui doit être posée lors de la pulvérisation réactive est comment le gaz réactif qui se combine avec la cible métallique va modifier sa nature chimique. Ainsi les propriétés de surface de la cible métallique sont modifiées en fonctions des conditions de fonctionnement du réacteur de pulvérisation magnétron. Le taux de pulvérisation pour le nouveau matériau formé sur la cible, est en général nettement inférieur par rapport à celui du matériau cible métallique en particulier si ce composé est un semi-conducteur comme TiO_2 ou un isolant. L'objectif du champ magnétique est d'augmenter l'efficacité du phénomène d'ionisation du gaz noble employé en piégeant les électrons dans le plasma. En effet, cela permet de confiner le plasma au voisinage de la surface de la cible. Une source RF est plus efficace qu'une source de courant continu dans le cas de la pulvérisation cathodique réactive d'un matériau semi-conducteur en raison de l'accumulation de charges isolantes sur les surfaces dans ce dernier cas. Avant d'effectuer les analyses électrogravimétriques, la structure de ces films a été étudiée par MEB et MET à haute résolution.

La synthèse de films minces de WO_3 denses et mésoporeux (résultats présentés dans le chapitre IV) a été réalisée par voie électrochimique sans ou avec la présence de molécules de tensioactifs. Pour cette voie de préparation, les molécules tensioactives, du dodécylsulfate de sodium (SDS), ont été ajoutées à la solution de dépôt électrolytique en tant qu'agents structurants. L'incorporation de ces molécules dans les films électrogénérés résulte de l'auto-assemblage contrôlé d'agrégats de tensioactifs inorganiques aux interfaces solide-liquide. Lors de la formation électrochimique des films, ces agrégats sont piégés et de par leurs dimensions, ils remplissent des cavités. Après cette étape, ces agents tensioactifs peuvent être facilement éliminés par lavage avec un alcool approprié ce qui permet d'obtenir des pores de tailles contrôlées (~3-5 nm de diamètre). Ces nanostructures, avec des pores de petites dimensions et avec de plus un ratio surface sur volume très grand, sont censés faciliter le processus de transfert des ions. Ici, une importance particulière a été portée sur les matériaux amorphes plutôt que sur les matériaux cristallins pour évaluer les performances électrochimiques de ces premiers. La structure, la morphologie et la composition des films mésoporeux synthétisés par voie électrochimique ont été caractérisés (XPS, MEB et MET à haute résolution) et comparés avec leurs homologues denses.

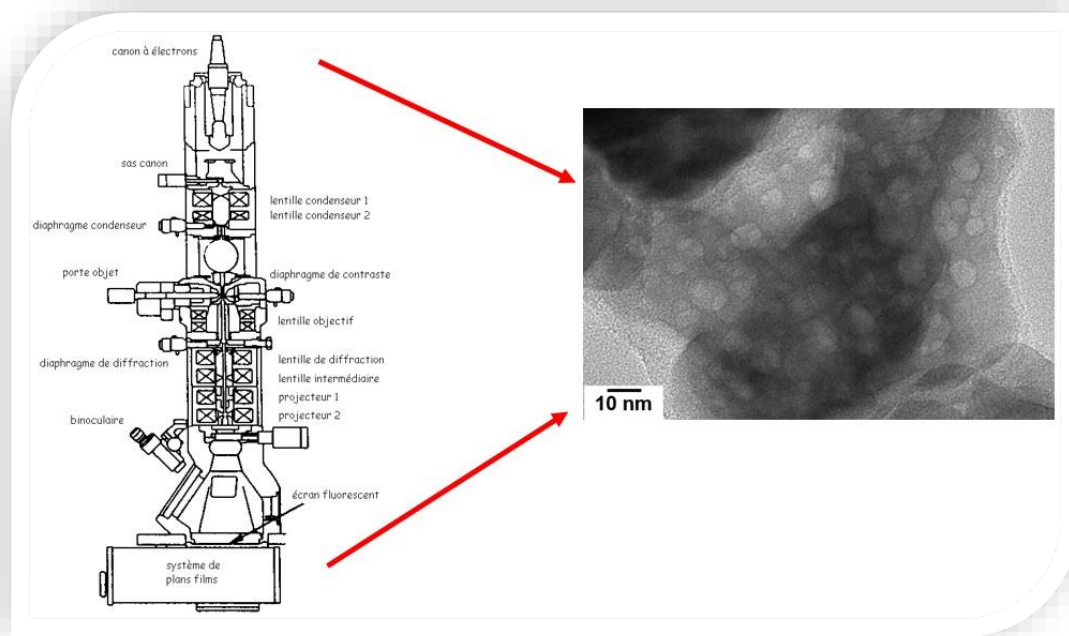


Schéma de principe de la microscopie électronique à transmission (à gauche) et image à haute résolution d'un film mésoporeux de trioxyde de tungstène (à droite).

La fabrication de films mésoporeux d'oxydes de ruthénium hydraté (résultats présentés dans le chapitre V), comme pour l'élaboration des films de WO_3 , est basée sur une électro-génération

en présence de tensioactifs. Ici, le CTAB (cetyltriméthylammonium bromide) a été utilisé comme agent tensio-actif ionique lors de la préparation électrochimique de films $\text{RuO}_2 \cdot x\text{H}_2\text{O}$. Cela conduit à la création de mésopores de $\sim 7\text{-}10$ nm de diamètre après le départ des micelles correspondants. Les films analogues denses ont été également synthétisés par voie électrochimique dans des conditions similaires mais en l'absence des molécules de CTAB. La structure, la morphologie et la composition des films électrosynthétisés mésoporeux ont été caractérisés un ensemble de techniques (DRX, XPS, MEB, MET et SAED) et comparés avec leurs homologues compacts.

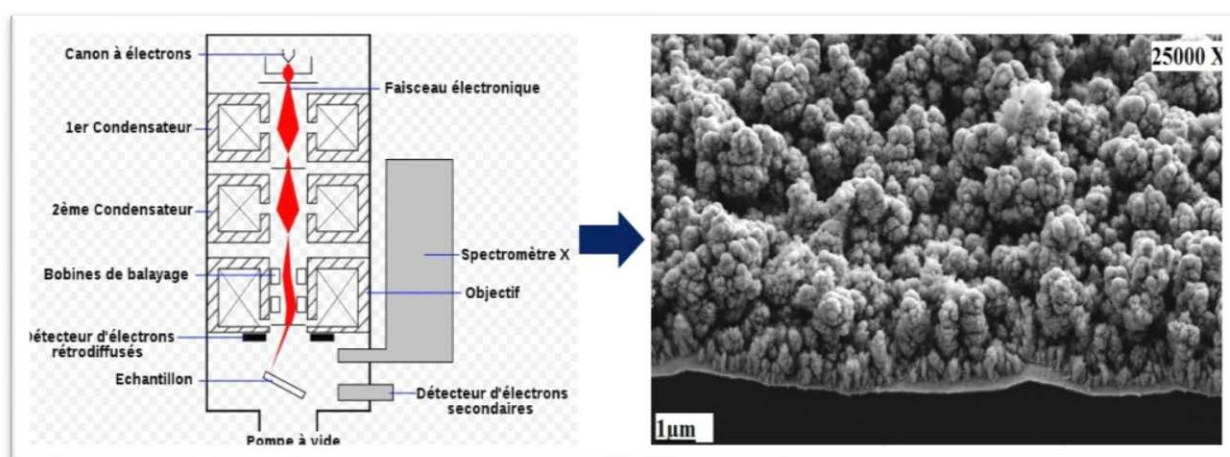


Schéma de principe de la microscopie électronique à balayage (à gauche) et image d'un film compact d'oxyde de ruthénium hydraté (à droite).

Enfin, des films composites à base de Nanotubes de Carbone (CNTs) et d'oxydes de ruthénium hydraté ont été réalisés. Tout d'abord, des films de nanotubes de carbone ont été déposés par la méthode de « drop casting » sur l'électrode d'or de la microbalance à partir d'une suspension de CNTs. Par la suite, une couche très fine d'oxyde de ruthénium hydraté a été électrodéposée sur ces films de CNTs. L'idée est de combiner les performances en termes de capacité du $\text{RuO}_2 \cdot x\text{H}_2\text{O}$ avec celles des films de nanotubes de carbone. La structure et la morphologie de ces films ont été caractérisées avec MEB et MET à haute résolution.

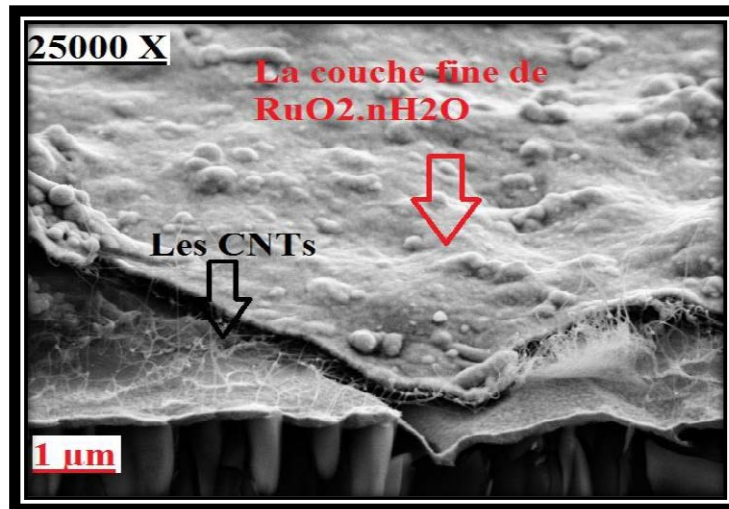


Image en coupe d'un film mince de l'oxyde de ruthénium hydraté électrodéposé sur des films de nanotubes de carbone.

Dans une deuxième partie, la méthode d'*ac*-électrogravimétrie est présentée sous une approche théorique en donnant les bases de calcul des différentes fonctions de transfert. En effet, l'*ac*-électrogravimétrie porte sur le couplage entre la spectroscopie d'impédance électrochimique et une microbalance à quartz rapide (QCM), utilisée en mode courant alternatif. La réponse en courant et en masse suite à une perturbation en potentiel de faible niveau, permet d'estimer simultanément la fonction de transfert électrochimique, $\frac{\Delta E}{\Delta I}(\omega)$ et la fonction de transfert masse/potentiel, $\frac{\Delta m}{\Delta E}(\omega)$. La combinaison de ces deux fonctions de transfert offre la possibilité d'une séparation des différents processus électrochimiques, au niveau des variations de masse et de charges.

➤ **Concentration/Potential TF**

$$\frac{\Delta C_i}{\Delta E}(\omega) = -\frac{G_i}{j\omega d_f + K_i}$$

➤ **Impedance TF**

$$\frac{\Delta E}{\Delta I}(\omega) = \frac{1}{j\omega d_f F \left[\frac{G_c}{j\omega d_f + K_c} - \frac{G_a}{j\omega d_f + K_a} \right]}$$

➤ **Charge/Potential TF**

$$\frac{\Delta q}{\Delta E}(\omega) = d_f F \left[\frac{G_c}{j\omega d_f + K_c} - \frac{G_a}{j\omega d_f + K_a} \right]$$

➤ **Mass/Potential TF**

$$\frac{\Delta m}{\Delta E}(\omega) = -d \left(m_c \frac{G_c}{j\omega d_f + K_c} + m_a \frac{G_a}{j\omega d_f + K_a} + m_s \frac{G_s}{j\omega d_f + K_s} \right)$$

Fonctions de transfert principales théoriques utilisées pour la partie ajustement des résultats expérimentaux d'*ac*-électrogravimétrie.

Chapter II: Theory and Experimental

I: Introduction

This chapter is dedicated to necessary theoretical and experimental basics used in this thesis project. The first part is attributed to the description of various structural and electrochemical characterization techniques applied as diagnostic tools to study the different electrochemical and physical preparation methods used for fabricating the MO_x electrodes with different morphologies. In the second part, the different components of the model used for *ac*-electrogravimetric fittings/simulations will be introduced; it will be shown how the different *ac*-electrogravimetric transfer functions for an electroactive film can help in a pertinent way to ion transfer investigations.

II: Experimental

II-1: Electrochemical and (Electro)gravimetric Characterization Techniques

II-1.1: Quartz Crystal Microbalance (QCM)

Principle of piezoelectricity:

The word piezoelectricity comes from the Greek and it means "electricity by pressure" (piezo means pressure in Greek); it was proposed by Hankel in 1881, a year after the discovery of this phenomenon by Jacques and Pierre Curie. The piezoelectric effect is the property of certain materials to polarize under the action of a mechanical force, and vice versa to be altered if an electric field is applied. Both effects are inseparable. The first is called direct piezoelectric effect, the second inverse piezoelectric effect. More generally, the direct effect can be utilized in the production of sensors (pressure sensor, microbalance) while the reverse effect can be used (piezo injectors in automotive, nano-manipulator, etc).

According to the definition of piezoelectricity, the quartz crystal is capable of converting a mechanical stress into an electrical signal. It can be used to make a transducer. In fact, the piezoelectric transducer is an entity capable of converting an interaction to the modified electrode / liquid interface in an easily measurable electrical signal. Piezoelectric transducers, more commonly called quartz microbalance, are increasingly used in electrochemistry for the study of interfaces [1-6]. Among the piezoelectric components existing in nature, quartz is the one most commonly used. Quartz is a crystal of silica (SiO₂) available in nature which is synthesized in industry. This crystal has a great hardness and it is chemically inert. Only

hydrofluoric acid might attack the crystal. Under ambient temperature and normal pressure, quartz solubility is almost zero in basic solution [7].

The AT-cut oriented $35^{\circ} 12'$ relative to the axis Z, is the one we use thereafter [8]. It is the mode of the microbalance the most commonly used. The crystal is shaped like a thin disc (Figure II-1), with a 14 mm diameter. The thickness of the quartz determines the resonant frequency. On each side of the disk, a gold electrode was deposited by vacuum evaporation. Each electrode is in the form of a key hole with a central disk of 5 mm diameter. Practically, a chromium under-layer is sandwiched between the crystal and the gold, this is due to the poor adhesion of the gold on the crystal. In general, the gold electrode has a thickness of 200 nm and the sub-layer of chromium is about ten times finer. The piezoelectric effect can only take place within the area defined by the two gold electrodes opposite from each other, so-called active surface area. Figure II-1 illustrates a quartz disk with its gold electrodes, front view (a) and sectional view (b). The arrow indicates the active area of the electrodes. The second arrow, circular cap shows the electrode legs used for making connections. When a sinusoidal voltage is applied between the two electrodes, the upper and lower sides of the active zone of the crystal vibrate parallel to each other in a thickness shear mode. An acoustic wave is thus generated in this volume and under resonant conditions, has a characteristic frequency called quartz resonant frequency or microbalance frequency. This electrical excitation frequency corresponds to a conversion between electrical energy and maximal mechanical energy (acoustic) upon application of an alternative voltage. The quartz provided and equipped with these electrodes is called piezoelectric resonator.

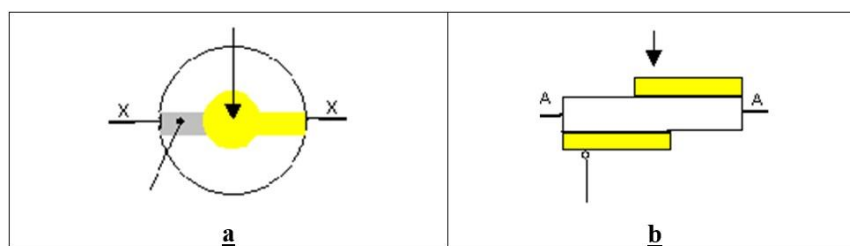


Fig. II-1. Quartz face's covered with two gold electrodes on each side. In a front view (a) and in a cross-sectional view (b).

II-1.1.1: Principle of QCM

According to the definition of piezoelectricity, the quartz crystal is capable of converting a mechanical stress or a mass load into an electrical signal. Indeed, this piezoelectric transducer is an entity capable of converting an interaction at the modified electrode / liquid interface to an easily measurable electrical signal. Piezoelectric transducers, more commonly called quartz microbalance, are increasingly used in electrochemistry for the study of interfaces. The quartz

crystal microbalance is a high precision instrument able to measure the mass changes at the surface of one of the quartz faces by measuring the change in frequency associated with the quartz resonator. The quartz crystal microbalance is made of a quartz crystal inserted in an electronic circuit which provides a stable signal over time. This set-up is called an oscillator and any perturbation applied to the quartz surface varies the oscillation frequency, with a measured quantity.

In 1959 Sauerbrey was the first to establish a simple equation relating mass variations to microbalance frequency [9]. When a rigid material, purely elastic, and thin, is deposited on the surface of one of the quartz faces, the relationship between the mass of material Δm and the translation of the microbalance frequency of quartz, Δf_m , is linear and can be expressed as:

$$\Delta f_m = -k_{th}^S \Delta m = -\left(\frac{2f_0^2}{Sn\sqrt{\mu\rho}} \right) \Delta m \quad (1)$$

Where Δf_m is the microbalance frequency variation (Hz), S is the surface of metal electrodes positioned on the quartz (cm^2), ρ is the quartz density ($2,648 \text{ g cm}^{-3}$), μ is the quartz shear modulus ($2,947 \cdot 10^{11} \text{ g. s}^{-2} \cdot \text{cm}^{-1}$), n is the harmonic number, f_0 is the frequency of the microbalance in the air and k_{th}^S is the theoretical sensitivity of the microbalance.

With a microbalance operating at 9 MHz, k_{th}^S is theoretically equal to $16,7 \times 10^{+7} \text{ Hz. g}^{-1} \cdot \text{cm}^{+2}$; for a microbalance frequency change of 1 Hz variation, a mass variation of 1 ng for $0,2 \text{ cm}^2$ of active surface is estimated theoretically. The calibration of the microbalance by copper galvanostatic deposition on the electrode gives a value of the sensitivity of the microbalance around $16,3 \cdot 10^{+7} \text{ Hz. g}^{-1} \cdot \text{cm}^{+2}$ for an imposed current of 0,5 mA, which is in good agreement with theory. Sauerbrey Equation (eq. 1) shows that an increase in mass at the electrode causes a decrease in the microbalance frequency. The sensitivity of the microbalance follows a constant value in the gravimetric regime or in other words, of the Sauerbrey equation is valid for a fine thickness of a purely rigid material deposited on the surface of the quartz. When electrochemical studies are performed in solution, the validity of the Sauerbrey equation is limited by the viscosity, the density of the solution and also by the viscoelasticity of the deposited film. To limit this effect, electrogenerated films with a sub-micron thickness could be considered as acoustically thin enough layers: the equation of Sauerbrey will be valid and the microbalance will operate in gravimetric regime.

II-1.1.2: Experimental Set-up

The quartz crystal and its electrodes constitute a piezoelectric resonator: the surface modifications (mass, mechanical stress, etc.) are transformed into measurable electrical signals. The quartz resonator, coupled with appropriate electronic to form an oscillator, experience its resonant frequency shift as a result of these surface modifications.

The experimental set-up used usually for our experiments is a microbalance fully fabricated at LISE laboratory. The quartz crystal with 9 MHz resonant frequency (RAKON, France or AWS, Spain) with its up layer gold electrode, is fixed on a printed circuit chip. A silver paste is used to ensure the electrical contacts and a silicone glue is then applied to isolate them from the solution contact. This device is connected to an oscillator associated with a 9 MHz electronic circuit developed in the laboratory (Fig. II-2). It is possible to receive the microbalance frequency changes, Δf_m , in real time via the FRQM software developed at LISE.

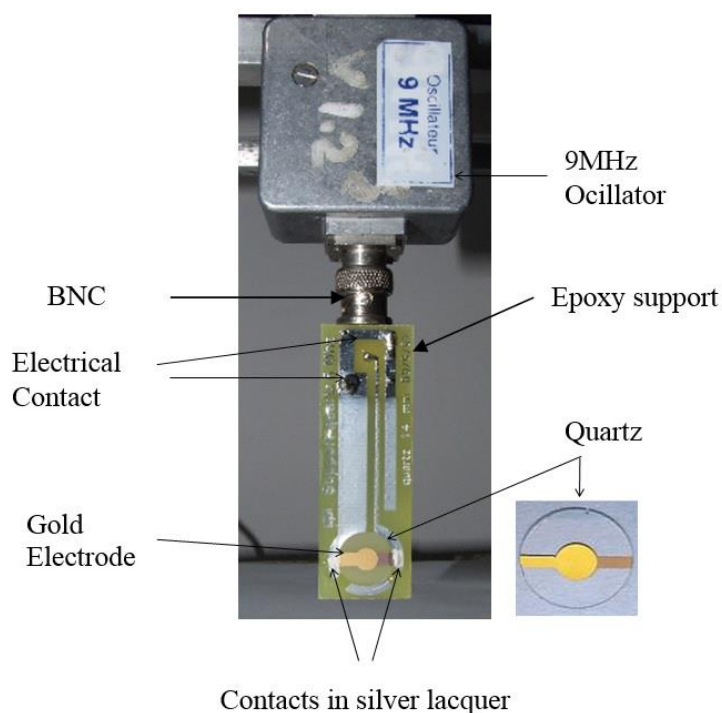


Fig. II-2. Quartz assembly coupled with its 9 MHz oscillator.

II-1.2: Cyclic Electrogravimetry (EQCM)

II-1.2.1: Principle

Cyclic voltammetry is a classic electrochemical characterization method. This technique is used in a first approach to study the electrochemical reactions mechanisms because of its simplicity

and rapidity. Cyclic voltammetry also allows to electrogenerate electroactive films on the surface of the working electrodes and in a second step, to determine the field of activity of these deposited films in a given electrolyte. The measurements are made with a classical three-electrode assembly. The principle is to impose two successive scans of potential in the opposite direction, the term cyclic, between the working electrode and a reference electrode and monitoring the change in current across the working electrode. By using the gold electrode of the microbalance as a working electrode, it is possible to follow concurrently the variation of the microbalance frequency, Δf_m , as a function of potential, and thus, to evaluate the mass variations within an electroactive film. As a matter of fact, the changes in the potential applied through the film, by the charge compensation process, lead to insertion/expulsion of charged or non-charged species at the interface of film/solution. These species movements procure changes in the mass of the film on the crystal's surface also in the microbalance frequency, f_m .

The experimental montage includes: a reference electrode either saturated calomel electrode (SCE) or saturated Ag/AgCl, a platinum counter electrode with a dimension of 2cm × 4cm, a gold working electrode deposited on the quartz resonators, with 0,5 cm diameter with an electrochemical active surface of 0,27 cm² and an effective surface area of 0,2 cm² (for mass). This electrochemical three-electrode cell is connected to a potentiostat specially modified to be compatible with our microbalance as our working electrode is grounded. The potentiostat is equipped with an additional acquisition data card (analog / digital or A / D) to measure, in parallel with the current, the microbalance frequency variation consecutive to voltage sweep. The assembly is controlled by a BioLogic software. Between 9 MHz oscillator and the potentiostat A/D input, a frequency meter (Yokogawa, TC110) is also intercalated. The latter operates for the conversion of microbalance frequency variations, Δf_m , using a 15-bits frequency/voltage converter: each change in f_m is converted to a voltage between 0 and 10 V, which is then received by the potentiostat. Thus, it is possible to measure both the current changes, i , and microbalance frequency variations, Δf_m , over potential scans (Figure II-3).

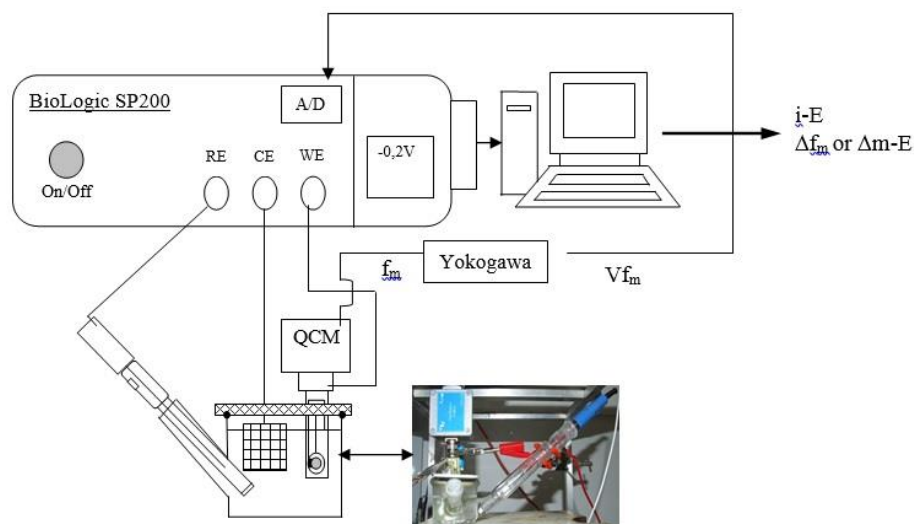


Fig. II-3. Experimental device for the cyclic electrogravimetry measurements.

II-1.3: Electrochemical Impedance Spectroscopy (EIS)

in the case of complex electrochemical reactions consisting of a series of elementary steps of different kinetics. But to better understand the different mechanisms of an electrochemical system, it is interesting to characterize each of these reactions. If the conventional techniques make it difficult to distinguish these basic steps of each other, the electrochemical impedance can provide the necessary information in this regard [10-12].

II-1.3.1: Principle

The basic principle of the electrochemical impedance is to apply on an electrochemical system a stationary potential accompanied with a sinusoidal perturbation of a small amplitude at a given frequency of modulation. The electrochemical system can be considered under stationary condition and this low level perturbation should help to separate the different reactions with different kinetics [12]. Most electrochemical systems have generally a non-linear current-voltage characteristic curve. However, working only on a small portion of this curve, it could be considered having a linear relationship between the different variables measured (Figure II-4). As a result, by applying to the system a sinusoidal perturbation of small amplitude ΔV around a stationary potential V_s , the current response will also be sinusoidal, with a small amplitude ΔI around a stationary value I_s .

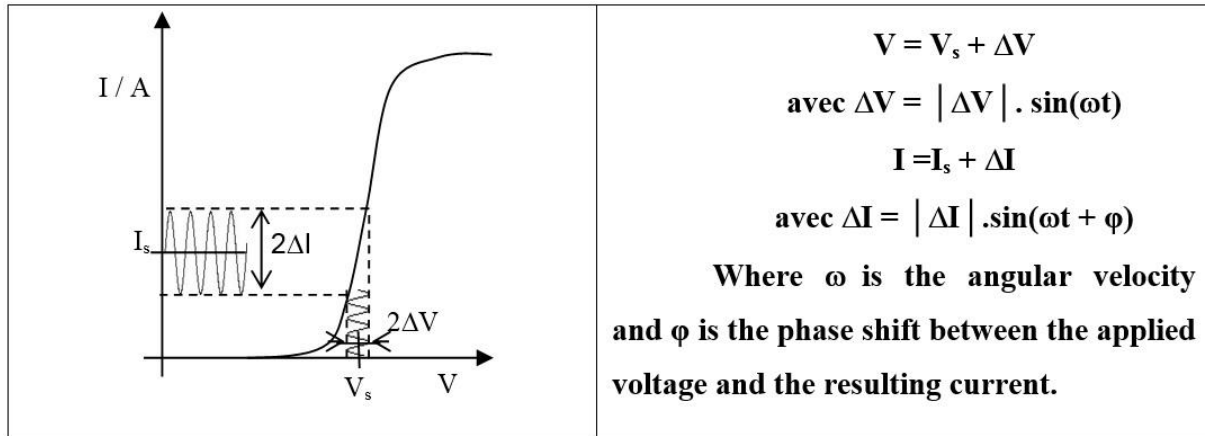


Fig. II-4. Linear current response to a sinusoidal potential perturbation of small amplitude around a stationary V_s value.

By definition for a linear system, there is a linear relationship between ΔV and ΔI . Then, we

can measure the $\frac{\Delta V}{\Delta I}(\omega)$ transfer function, called electrochemical impedance, where $\omega = 2\pi f$ is the pulsation.

The electrochemical impedance, $Z(\omega)$, is a complex number that can be represented either in polar $(|Z|, \varphi)$ or in cartesian coordinates $(\text{Re } Z, \text{Im } Z)$:

$$Z(\omega) = |Z| \exp j\varphi = \text{Re } Z + j \text{Im } Z \quad (2)$$

The relationship between these quantities are:

$$\text{Firstly,} \quad |Z|^2 = (\text{Re } Z)^2 + (\text{Im } Z)^2 \quad \text{and} \quad \varphi = \arctan \frac{\text{Im } Z}{\text{Re } Z} \quad (3)$$

$$\text{Then,} \quad \text{Re } Z = |Z| \cos \varphi \quad \text{and} \quad \text{Im } Z = |Z| \sin \varphi \quad (4)$$

Where $|Z|$ is the modulus, the ratio between the amplitudes of ΔV and ΔI ; j is the complex number (as $j^2 = -1$); φ is the phase, the representative phase difference between ΔV and ΔI ; $\text{Re } Z$ and $\text{Im } Z$ are the real and imaginary parts of $Z(\omega)$.

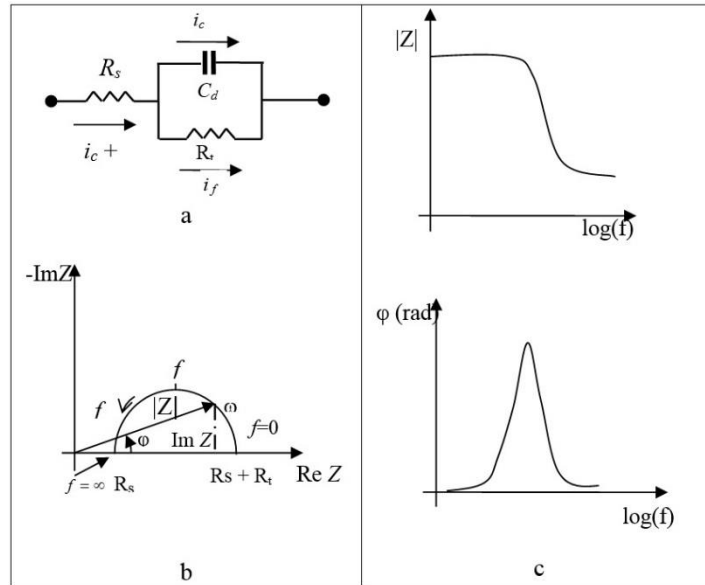


Fig. II-5. Equivalent electrical circuit (a) and plots of impedance of an electrochemical cell in the Nyquist plane (b) and in the Bode plane (c).

Two types of plots are used to describe these relationships. They are illustrated in figure II-5 regarding the equivalent circuit of an electrochemical cell which has the impedance

$$Z(\omega) = R_s + \frac{1}{\frac{1}{R_t} + j\omega C_d} \quad (5)$$

$Z(\omega)$ can be plotted in the Nyquist plan ($-Im Z$, $Re Z$) (Fig. II-5b) or in the Bode illustration (Fig. II-5c). This allows to observe changes in $|Z|$ and ϕ with frequency; $Re Z$ and $Im Z$ can be traced similarly. The electrochemical admittance, $Y(\omega) = Z^{-1}(\omega)$ can be similarly analyzed and used.

II-1.3.2: Experimental Set-Up

The experimental setup is shown in figure II-6. It consists of:

- ✓ A SOTELEM-PGSTAT100 potentiostat that works in potentiostatic mode, and imposes the stationary potential V_s ,
- ✓ A frequency generator that delivers the sinusoidal perturbation of small amplitude, ΔV .
- ✓ A three-electrode cell

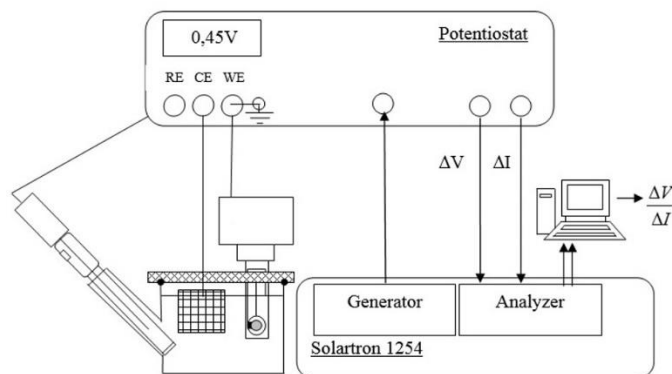


Fig. II-6. Experimental setup for measurements of the electrochemical impedance.

II-1.4: *Ac-electrogravimetry ; Fast Electrogravimetric Method*

II-1.4.1: *Principle*

The *ac*-electrogravimetry is similar to the electrochemical impedance technique. In fact, a ΔE sinusoidal perturbation signal of low amplitude, applied to the electrochemical system, may cause changes in the mass of the film, Δm , deposited on the microbalance allowing the measurement of a transfer function called mass/potential or electrogravimetric transfer function, $\frac{\Delta m}{\Delta E}(\omega)$. By using the gold electrode of the quartz crystal microbalance as a working electrode, we can simultaneously perform two distinct types of measures: The electrochemical impedance $\frac{\Delta E}{\Delta I}(\omega)$, and the electrogravimetric transfer function, $\frac{\Delta m}{\Delta E}(\omega)$.

The measurements are made with the same three-electrode cell described above in an aqueous medium. When a sinusoidal perturbation, ΔE , of small amplitude is applied to the electroactive film deposited on the gold quartz microbalance electrode, a certain number of charged species in the solution will participate in the charge compensation process within the material. This insertion or expulsion of species in/from the film is detected by the microbalance frequency variations, Δf_m . Moreover, due the high sensitivity of the microbalance, it measures mass changes, Δm , in the scale range of nanograms and with a very fast response time, less than a millisecond. The corresponding mass variation, Δm , is then estimated through the Sauerbrey's equation (Eq. (1)).

The modulation frequency of the perturbation signal provides additional information: it allows to separate the kinetics of different species involved in the charge compensation of electroactive film. The measurements are controlled by a computer via the FRACOM software, which was

also developed at LISE laboratory. Figure II-7 shows the principle of the electrogravimetric transfer function, $\frac{\Delta m}{\Delta E}(\omega)$, measurement.

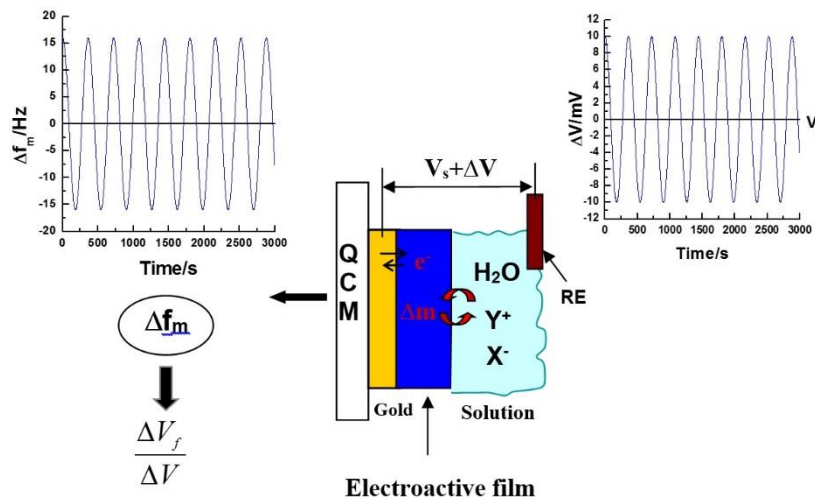


Fig. II-7. Principle of the electrogravimetric measurement.

For these measurements, it is necessary to use a multichannel analyzer (Solartron 1254) in order to determine, in parallel, the two main experimental transfer functions: the electrochemical impedance, $\frac{\Delta E}{\Delta I}(\omega)$, and an the $\frac{\Delta V_f}{\Delta V}(\omega)$ transfer function, which allows to calculate the electrogravimetric transfer function $\frac{\Delta m}{\Delta E}(\omega)$. Indeed, it is not possible to measure directly the electrogravimetric TF, $\frac{\Delta m}{\Delta E}(\omega)$. So, a lab-made frequency / voltage converter was used for transforming the signal of the microbalance Δf_m in a measurable voltage signal, ΔV_f , which can then be received by the analyzer 1254. Then, it is possible to extrapolate Δm from this signal, ΔV_f , for a configuration and a given type of measurement. This was achieved by calibrating the system before measurements.

III-1.4.2. Experimental Method

The experimental setup (Figure II-8) is composed of different elements:

- ✓ A three electrodes electrochemical cell: The reference electrode is usually a saturated calomel electrode (SCE) or Ag/AgCl, the counter electrode is made of platinum grid and the working electrode is the gold electrode deposited on the faces of the quartz resonator,

- ✓ A potentiostat SOTELEM PG-STAT100,
- ✓ An FRA-Solartron 1254 comprising a voltage generator, $\Delta V'$, and analyzer of the transfer functions,
- ✓ A reference frequency synthesizer, Marconi 2023,
- ✓ A frequency/voltage converter developed by LISE.

As shown in figure II-8, the 1254 generator delivers a sinusoidal perturbation of small amplitude, $\Delta V'$ at a given modulation frequency, f . This signal is superimposed on the bias potential supplied by the potentiostat, V_s .

The signal of the microbalance f_m is sent to a frequency-voltage converter which subtracts a reference signal f_r , near the frequency of the microbalance, issued by the frequency synthesizer Marconi-2023. The $f_m - f_r$ signal is then converted into a continuous voltage V_f . If f_m varies from Δf_m then, the converter delivers a voltage variation ΔV_f . This result is finally sent to the FRA 1254 analyzer. Since Solartron 1254 analyzer has four measurement channels, it is possible to recover the ΔI and ΔV values parallel to ΔV_f in order to measure the electrochemical impedance, $\frac{\Delta E}{\Delta I}(\omega)$. Consequently, we obtain the experimental transfer functions $\frac{\Delta V}{\Delta I}(\omega)$ and $\frac{\Delta V_f}{\Delta V}(\omega)$ as shown in Figure II-8. This is the reason for which this measurement is called "electrochemical impedance coupled with electrogravimetry" or *ac*-electrogravimetry.

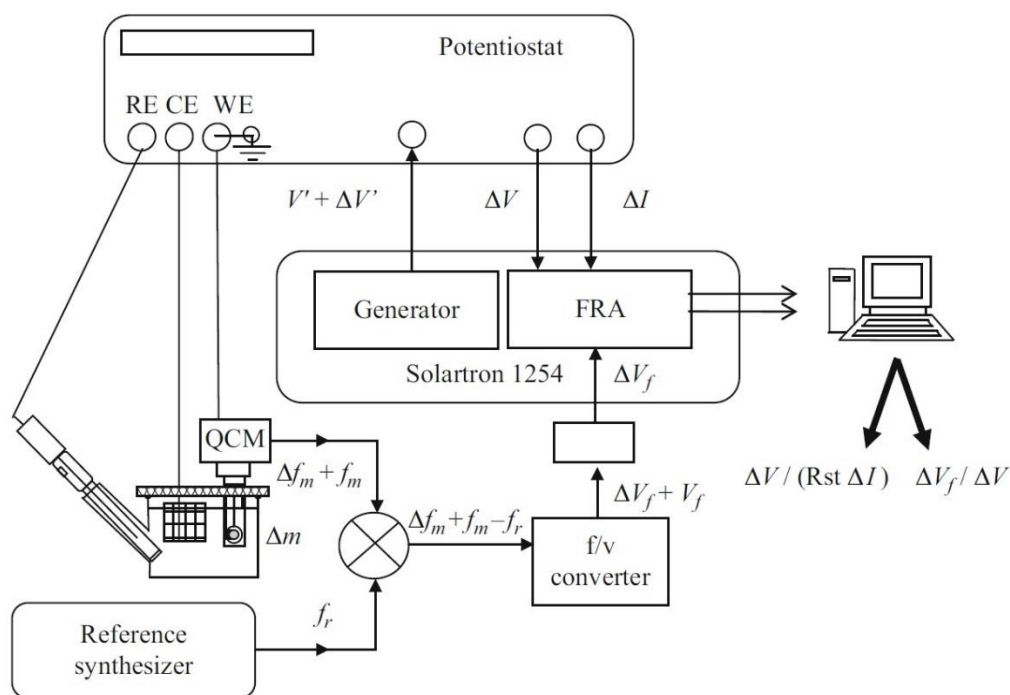


Fig. II-8. *Ac*-electrogravimetric and electrochemical impedance set-up.

II-1.4.3. Calibration and System Corrections

The purpose of the calibration is to measure the parasitic transfer function of the electronic part which distorts electrogravimetric transfer function. In reality, the calibration will give us a characterization of the electronic set-up used and then, it will be used to digitally correct the experimental files $\frac{\Delta V_f}{\Delta V}(\omega)$ to obtain $\frac{\Delta m}{\Delta E}(\omega)$ for each frequency modulation.

The relation between electrogravimetric transfer function $\frac{\Delta m}{\Delta E}(\omega)$ and various correction terms is described below:

$$\frac{\Delta m}{\Delta E} = \frac{\Delta m}{\Delta f_m}(\omega) \frac{\Delta f_m}{\Delta V_f}(\omega) \frac{\Delta V_f}{\Delta V}(\omega) \frac{\Delta V}{\Delta E}(\omega) \quad (6)$$

Where,

$\frac{\Delta m}{\Delta f_m}$ is the sensitivity of the microbalance obtained by calibration and it appears in the Sauerbrey equation (eq. 1). For a 9 MHz quartz [13], the experimental sensitivity value is $16.3 \cdot 10^{+7} \text{ Hz g}^{-1} \text{ cm}^{+2}$.

$\frac{\Delta f_m}{\Delta V_f}(\omega)$ is the inverse of the sensitivity of the frequency-voltage converter and it might be estimated by the equation:

$$\frac{\Delta f_m}{\Delta V_f}(\omega) = \frac{\Delta f_m}{\Delta e}(\omega) \frac{\Delta e}{\Delta V_f}(\omega) \quad (7)$$

Where $\Delta f_m / \Delta e(\omega) = \Delta f_s / \Delta e(\omega)$ is the sensitivity of the synthesizer that simulates the microbalance considering $\Delta f_m = \Delta f_s$. $\Delta e / \Delta V_f(\omega)$ is the inverse of the transfer function of the frequency / voltage converting device and it is obtained by calibration.

- $\frac{\Delta V_f}{\Delta V}(\omega)$ is the measurement obtained directly with FRA-1254 analyzer and FRACOM software.
- $\frac{\Delta V}{\Delta E}(\omega)$ is the term that allows the IR drop correction to be done. Using the electrolyte resistance, R_e , the expression can be taken:

$$\frac{\Delta V}{\Delta E}(\omega) = \frac{R_e}{(\Delta E / \Delta I)(\omega)} + 1.$$

It is observed that the voltage perturbation during a calibration is denoted $\Delta e = |\Delta e| \cdot \sin(\omega t)$. It should also be noted that the converter sensitivity is given by the value of $\frac{\Delta V_f}{\Delta f_s}$.

II-1.4.4. Transfer Function of the Frequency/Voltage Converter:

This transfer function is determined by replacing the microbalance by a frequency synthesizer, Agilent 33205A. The rest of the montage is identical to what was previously explained with the exception of the electrochemical part which disappears. The signal Δe , from the FRA 1254 generator, will allow to modulate the frequency of the synthesizer, Agilent 33205A, to be done and also to simulate the response of a microbalance on which sinusoidal mass variations are observed.

An example of calibration curve obtained is presented in the form of a Bode diagram in figure II-9. It is noted that for frequencies of modulation, f , less than 1 Hz, the phase shift is negligible and the modulus has a constant value in relation to the sensitivity of the converter used. This means that up to this frequency, a simple proportional correction can be performed on experimental measurements. Below 1 Hz, a frequency to frequency correction should be performed digitally in order to eliminate the electronic contribution to modulus and to phase of the $\frac{\Delta V_f}{\Delta V}(\omega)$ measurement.

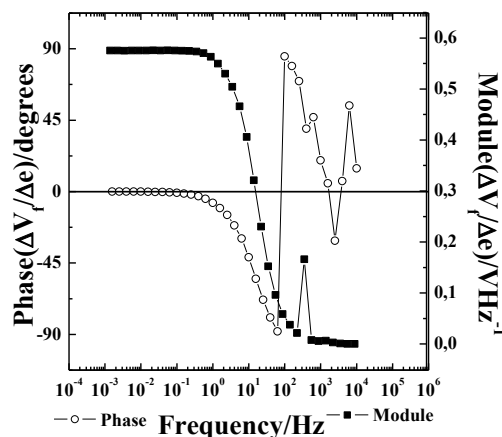


Fig. II-9. Calibration and determination of the frequency / voltage converter TF, $\frac{\Delta V_f}{\Delta e}$.

II-1.4.5. Calibration of the Synthesizer:

It is then to determine the $\frac{\Delta f_s}{\Delta e}$ transfer function of the Agilent 33250A synthesizer which was used to simulate a microbalance during the calibration process previously mentioned. To determine the transfer function of this synthesizer it should simply apply, via the FRA 1254 generator, a fixed sinusoidal perturbation of frequency f , which with a certain amplitude Δe . The Agilent synthesizer 33250A is adjusted to a 9.0 MHz carrier frequency equivalent to the frequency of microbalance used. Three levels of depth linked to the frequency carrier (FM mode) were tested. Three configurations of the Agilent 33250A, 10 Hz, 100 Hz and 300 Hz, were selected. Figure II-10 shows schematically the input and output signals of synthesizer for determining the module of the $\frac{\Delta f_s}{\Delta e}$ transfer function. The signals Δe and Δf_s are measured using respectively a Keithley-2000 voltmeter and a Fluke-PM6690 frequency meter. A plot in the Origin® software allows to determine Δe and Δf_s in a precise manner for adjusting the modulation depth of the given synthesizer.

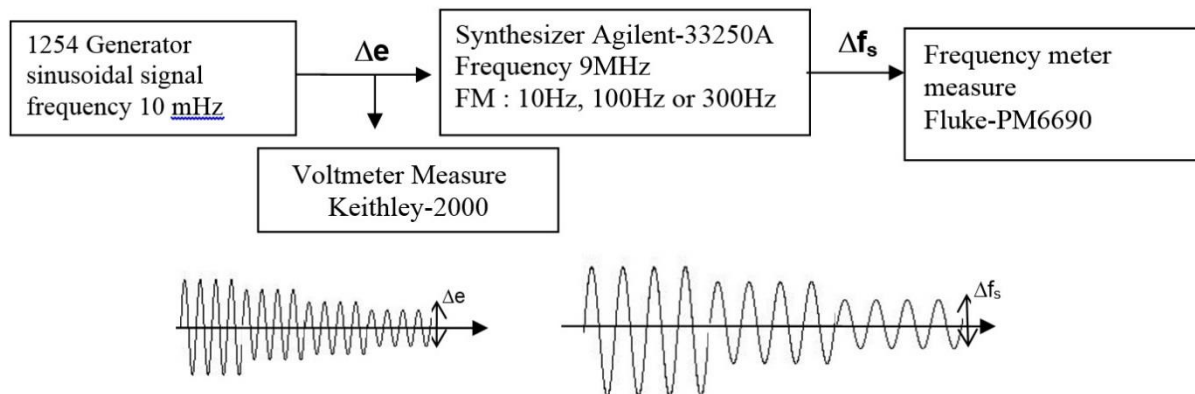


Fig. II-10. Calibration of Agilent 33250A synthesizer and determination of the frequency / voltage converter transfer function.

For three settings of modulation depth, the following values for the synthesizer function $\frac{\Delta f_s}{\Delta e}$ are obtained (Fig. II-11):

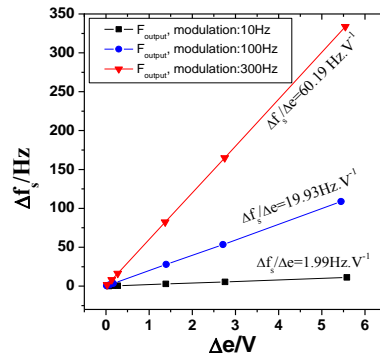


Fig. II-11. Synthesizer's transfer function $\frac{\Delta f_s}{\Delta e}$ (Agilent 33250A) for three modulation depth settings (FM): 10 Hz, 100 Hz, 300 Hz.

For the rest of the study, the work is performed with the FM setting = 100 Hz. So, to correct the measurements, the following table should be considered (Table II-1) to use the equations 2 and 6.

$\frac{\Delta m}{\Delta f_m}$ (g. cm ² . Hz ⁻¹)	$\left \frac{\Delta V_f}{\Delta e} \right _{\omega \rightarrow 0}$	$\frac{\Delta f_s}{\Delta e}$ (Hz V ⁻¹)
$-\frac{1}{16.3 \cdot 10^7}$	0.58	19.93

Table II-1. Values of various parameters used for the measurements correction.

II-2: Preparation of MO_x based Thin Films Electrodes

II-2.1: Elaboration of Compact, Porous and Highly Porous TiO₂ by RF Reactive Magnetron Sputtering

The deposition of compact, porous and highly porous TiO₂, was realized by reactive RF magnetron reactive sputtering at LISE laboratory. Optimal deposition conditions were chosen based on previous reports by H. Fakhouri et al. [14-16]. According to their reports, the basic issue that must be faced during reactive sputtering is that the reactive gas combines with the target material to form a new compound, in this way it will change the surface properties of the target [14]. Ideally, this reaction takes place on the surface of the substrate, but in reality it occurs not only at the substrate but also in the reactor volume, on chamber walls and even on the target surface. It is the reaction on the target surface that leads to the classic problem in

reactive sputtering called *“poisoning”* phenomena. The sputtering rate for the compound material, which forms on the target, is usually significantly less than the rate for the metallic target material especially if this compound is a semiconductor (TiO_2) or an insulator.

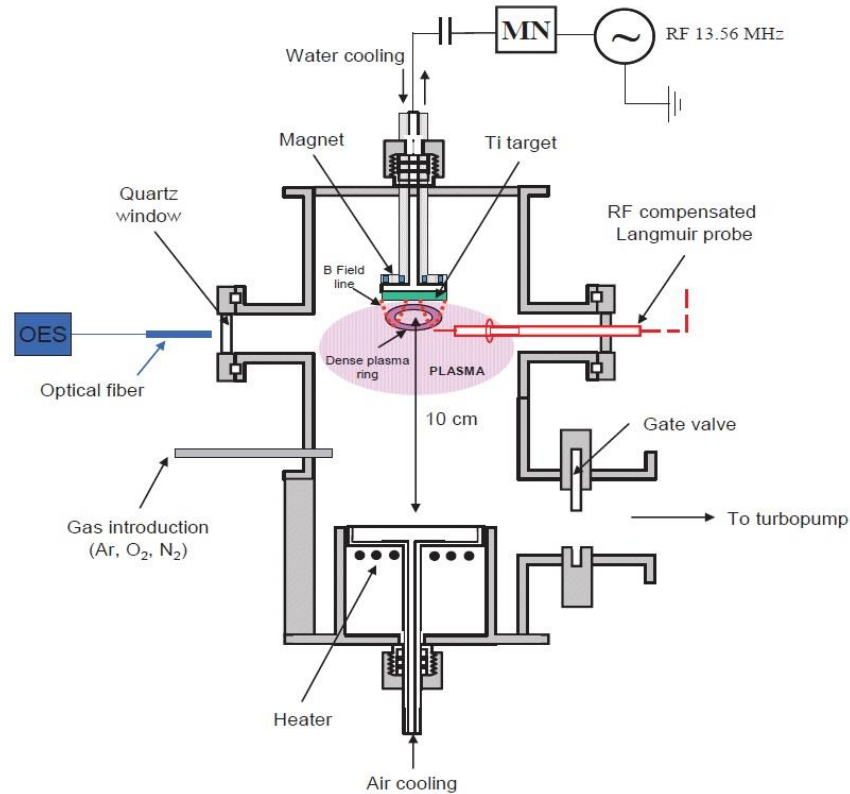


Fig. II-12. General illustration of the sputtering deposition system with diagnostic tools (Langmuir probe and OES).

The major components of the system are presented in fig. II-12. The objective of the magnetic field is to increase the ionization efficiency by trapping the electrons in the plasma. This allows plasma to be confined at the vicinity of the target surface. An RF source is more efficient than DC source in the case of the reactive sputtering of a semiconductor or insulating material because of charge accumulation on such surfaces in the case of the latter.

The thin films are deposited in a 13.56 MHz RF magnetron sputtering deposition chamber (SPT 120, Plasmionique, Canada), using a balanced magnetron cathode (MAGNION-B). The pumping system includes a turbo molecular pump (300 s^{-1} , Varian TV301 Navigator) and a mechanical pump (ULVAC) for backing the turbo. The SPT 120 magnetron sputtering reactor has two quartz windows used as vacuum viewports for optical spectra acquisition. To prevent any contamination on the windows, the viewports are mounted about 10 cm away from the reactor walls using special flanges with additional aluminum foils inside the reactor.

The background pressure for all depositions was about 5×10^{-6} Torr (6.7×10^{-4} Pa), while the total working pressure was adjusted between 2 to 20 mTorr (0.3 to 3 Pa). All films were deposited using a metallic Ti target (99.95% purity, 2-inch diameter, NEYCO). Prior to each deposition, the target was pre-sputtered in argon atmosphere for 10 minutes to remove any contaminations or “poisoned film” from the Ti surface. Then, the target was sputtered in a reactive gas atmosphere containing Ar + O₂ for TiO₂ films deposition. The typical RF power delivered by the generator was 200 W, corresponding to a typical DC bias ranging from -140 V to -160 V, depending on the target surface conditions (clean target or poisoned target).

Pure TiO₂ thin films of different morphologies were prepared by this methodology with the following details. A metallic Ti target of high purity (99.95%), was sputtered in a reactive gas atmosphere containing Ar and O₂ for the deposition of pure TiO₂ films. For that, the deposition pressure was controlled by the Ar flow rate in the deposition chamber, fabricating films at $p = 3, 6,$ and 14 mTorr with corresponding Ar flow rates of 30, 60, and 140 sccm (standard cubic centimeter) respectively. The O₂ gas flow rate was fixed at 1.9 -2.1 mtorr for all the samples. The fixed experimental conditions chosen were situated in the intermediate region between two stable sputtering modes, reactive and metallic. The substrate holder was maintained at low temperature below 100°C. The distance between the substrate holder and the target was fixed at 10 cm. The films were deposited on gold-patterned quartz substrates of 9 MHz. Before deposition, the substrates were ultrasonically cleaned with acetone, ethanol and then, deionized water for 20 min each.

II-2.2: Electrochemical Elaboration of Amorphous Compact and Amorphous Mesoporous WO₃

The electrodeposition solutions for the synthesis of dense and mesoporous WO₃ thin films were prepared as described elsewhere [17, 18]. Briefly, 0.9 g W powder (99.99%, Aldrich Chem, USA) was dissolved in 30 ml of 30% H₂O₂ (analytical reagent, Sigma-Aldrich Germany) which takes about 4 hours for complete dissolution. A small portion of Pt black was then added to remove the excess of H₂O₂. This removal process can be accelerated by heating the solution up to 70 °C to obtain a pale-yellow solution of H_xWO₃. The solution was diluted to 50 mM with a 50:50 water and isopropanol mixture. For the mesoporous thin film synthesis, the solution also contained 0.05 M sodium dodecyl sulfate (SDS) (ACS reagent, 99.0% Sigma-Aldrich, Japan). Gold-patterned quartz substrates of 9 MHz (RAKON, France) were used as working electrodes. A platinum grid and an Ag/AgCl (3M KCl saturated with AgCl) served as counter electrode

and reference electrode, respectively. The electrochemical WO_3 synthesis was performed by potentiostatic electrodeposition at -0.5 V vs Ag/AgCl . During electrodeposition, a salt-bridge junction equipped with a porous glass frit on the end was used to prevent the reference electrode to be contaminated by the media and vice versa. The electrodeposition was performed by using a potentiostat (Autolab PGSTAT100) and the deposition process was monitored by quartz crystal microbalance measurements. Film area is 0.25 cm^2 (gold electrode on the quartz resonator) and the film thickness was controlled by the electrodeposition time, typically for 15, 20 or 30 minutes. The SDS surfactant in the WO_3 thin films was extracted from the inorganic matrix by washing with ethanol/double distilled water mixture before the electrogravimetric studies.

For the electrochemical synthesis of the mesoporous WO_3 thin film, surfactant molecules (sodium dodecyl sulfate (SDS)) were added in the electrodeposition solution as templating agents. Typical current and microbalance frequency profiles, simultaneously measured on the quartz crystal during electrodeposition are presented in Fig. II-13. The frequency variations, Δf , are converted to the corresponding mass variations, Δm , by using the Sauerbrey equation (Eq. 30). The mass variation profiles during potentiostatic electrodeposition for both dense and mesoporous films are presented in Fig. II-13. The initial deposition current is higher for mesoporous thin films than that of dense WO_3 thin films. The deposition current density depends on both the sheet resistance of the working electrode and the electrical conductivity of the peroxotungstic acid (PTA) electrolyte solution [19]. Since identical substrates (gold coated quartz resonators) are used as working electrodes, the higher initial deposition current for the mesoporous WO_3 deposit (Fig. II-13b) is mainly due to the higher conductivity of the deposition solution resulting from the addition of the ionic surfactant molecules (SDS). In both cases, the deposition current initially decreases, finally approaching a steady value (Fig. II-13), which is consistent with previous reports [19]. The gold electrode is a conductor while the WO_3 is a semiconductor and the contributions of the two components determine the relative amount of the deposition current decrease. The time for stabilization of the deposition current is higher for the films synthesized in the presence of SDS surfactant (Fig. II-13) than that of a dense film electrodeposition. In the absence of SDS templates, impingement/percolation probably takes place at relatively lower thickness of the WO_3 deposits since larger grain formation may easily occur. But in the presence of SDS, the grain growth is limited due to the presence of SDS micellar structures on the gold electrode/solution interface. This may result in a slight delay in approaching a steady current value (Fig. II-13). Therefore, the differences in the deposition

current profiles in Fig. II-13 already give indications of the formation of different morphologies of WO_3 thin films in the presence and absence of SDS templating agents. In other words, the mechanism of electrogeneration appears strongly dependent on the bath composition.

The characteristic frequency of the quartz resonator decreases as a function of the electrodeposition time corresponding to a mass increase of the gold electrode of the quartz resonator. The mass variations calculated from the frequency variations are also presented in Figure II-13. The total deposited mass is higher for the films synthesized in the presence of SDS surfactant (Fig. II-13b), indicating the incorporation of the SDS surfactant molecules. These films are considered to be inorganic/organic hybrids composed of a WO_3 inorganic matrix surrounding the SDS surfactant micelles, and they are extracted from the inorganic matrix in a subsequent step following the electrodeposition.

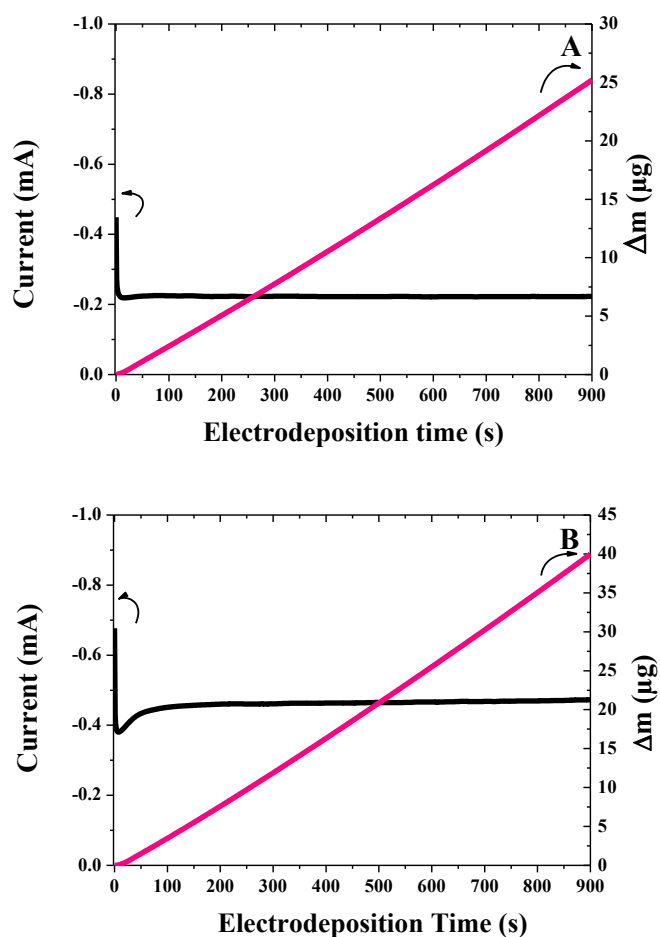
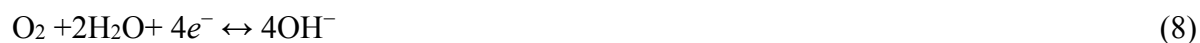


Fig. II-13. Synthesis of WO_3 thin films: typical electropotentiostatic deposition data and simultaneous QCM characterization (mass variation of the quartz crystal during electrodeposition) of (A) dense and (B) mesoporous WO_3 thin films (deposited at -0.5 V vs Ag/AgCl during 15 min).

II-2.3: Electrochemical Elaboration of Compact and Mesoporous $RuO_x \cdot nH_2O$

In our approach, the following reactions are considered to generate base on the electrode surface:



These reactions consume H_2O , generate OH^- and high pH values at the cathode are observed. In cathodic deposition, metal ions or complexes are hydrolyzed by electrogenerated base to form oxide, hydroxide or peroxide deposits on cathodic substrates. Hydroxide and peroxide deposits can be converted in to corresponding oxides by thermal treatment.

Electrodeposition can appear as an appropriate method for the deposition of RuO_2 films. The mechanism of RuO_2 deposition is not fully understood [20-24]. Hydrated ruthenium chloride, the salt used in this application, is a heterogeneous ionic material with an average ruthenium oxidation state between 3 and 4, close to 4. For this reason, the mechanism of formation of RuO_2 from $RuCl_3 \cdot nH_2O$ precursor is rather complex. The ruthenium species are most likely to precipitate as hydrated ruthenic oxide ($RuO_2 \cdot nH_2O$) or ruthenic hydroxide $Ru(OH)_4$. This process consumes the electrochemically generated OH^- ions. As the deposition process progresses, an insulating layer forms, which in turn prevents OH^- generation, and therefore, further deposition is stopped. However, ruthenium oxide exhibits metallic conductivity so deposition of high thickness of ruthenium oxide is possible. It has been reported elsewhere [20-24] that the initial pH of the deposition bath strongly influences the RuO_2 deposition process. This effect was considered to be due to the chemical conversion of the dissolved $RuCl_3 \cdot nH_2O$ into $Ru(OH)_y 3Cl_{3-y} \cdot cH_2O$ structure. Since the pH of the precursor solution $RuCl_3$ varies with storage time; in the present study, attempt was made to maintain the pH of $RuCl_3$ solution at about 2.0 (± 0.1) with addition of diluted HCl solution and making fresh solution of $RuCl_3$ before deposition.

I. Zhitomirsky et al. [20] was the first to synthesis of RuO_2 by a cathodic electrodeposition process on Ni, Ti, Pt foils and Si wafers. Following the same concept B.O. Park et al. [21, 22] reported the synthesis of Ruthenium oxide (RuO_2) films of different thicknesses by cathodic electrodeposition on titanium substrates from aqueous acidic $Ru(III)Cl_3$ solution. The author indicates that electrodeposition is an advantageous preparation route, mainly because: (i) it is a low temperature method of preparation and (ii) the resulted thin film presents high porosity.

Inspired from these primary reports on RuO₂ electrodeposition, we have chosen the same pathway for synthesizing hydrated RuO₂ or more correctly RuO_x.nH₂O. The typical experimental set-up is illustrated in figure II-14. More precisely, the electrodeposition solutions were prepared from a freshly 10 mM electrolyte containing 0.1037 g of RuCl₃.xH₂O as precursor (ReagentPlus, Sigma-Aldrich, USA) dissolved in 50:50 v/v mixture of two solutions: 10⁻¹ M KCl and 10⁻¹ M HCl solutions. The pH of the solution was adjusted to ~2.15-2.5 by few drops of 10⁻¹ M KOH. For the mesoporous thin film synthesis, the CTAB/precursor [25] ratio was 0.32 and the solution contained 0.116 g of cetyltrimethylammonium bromide (BioXtra, 99.0% Sigma-Aldrich, China).

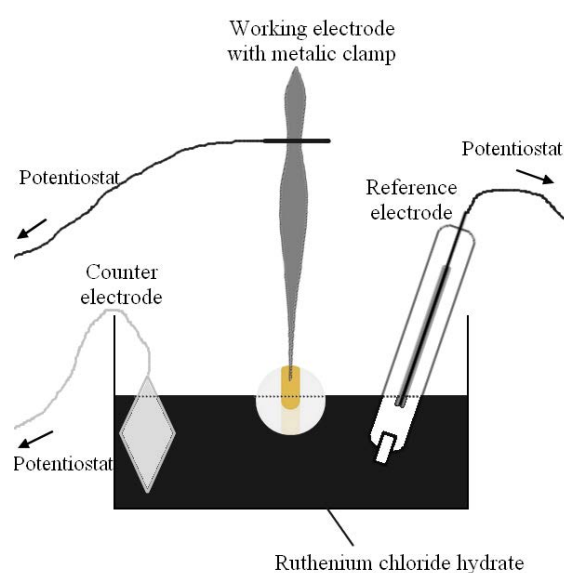


Fig. II-14. Typical set-up used for the electrodeposition.

Gold-patterned quartz substrates of 9 MHz (RAKON, France) were used as working electrodes. A platinum grid and an Ag/AgCl (3M KCl saturated with AgCl) served as counter electrode and reference electrode, respectively. The electrochemical RuCl₃.xH₂O synthesis was performed by potentiostatic electrodeposition at -0.6 V vs Ag/AgCl. The electrodeposition was performed using a potentiostat (BioLogic SP-200) and the deposition process was monitored by quartz crystal microbalance measurements. The film area is 0.2 cm² (gold electrode on the quartz resonator) and the film thickness was controlled by the electrodeposition time, typically for 15, 20 or 30 minutes. The CTAB surfactant in the as-prepared mesoporous thin films was extracted from the inorganic matrix after deposition by washing with ethanol/water mixture and heating the sample up to 150°C for 1h maximum, before the different studies.

II-2.4: Elaboration of CNTs/RuO_x.nH₂O Films

CNT deposition: The carbon nanotube CNT film deposition includes a direct deposition of a CNT suspension droplets on the gold-covered quartz substrates. To do so, the CNT solution should be prepared before procedure is as follows [26]:

First, 32 mg of CNT (90 %, Sigma-Aldrich, Belgium) (single wall) are mixed with 2 mg of acetylene black (99.9%, Alfa Aesar, USA) (which is added to improve the electrical conductivity of the composite electrode), 4 mg of polyvinylidene fluoride which is the polymeric binder (PVDF-HFP, Solvay, Belgium), and 10 mL of N-methyl-2-pyrrolidone (99.5%, Sigma Aldrich, Germany). Then, the resulting suspension is placed in an ultrasonic bath. The homogenisation of this suspension takes quite a time (at least two days) and when the solution is ready, a very fine micropipette is used to cover the substrate with 4 μ L of this suspension. A mask is used in order to drop the suspension properly only on the gold surface. The prepared samples are then kept for 12 hours in a silica gel desiccator and finally heated in a tubular ceramic furnace at 130°C for \sim 30-45 minutes [26]. In a second step, the metal oxide deposition is performed as previously explained by varying the deposition time (between 5 to 15 minutes).

II-3: Structural and Morphological Investigation Methods:

II-3.1: Scanning Electron Microscopy (SEM) and Energy Dispersive X-rays (EDX)

A **scanning electron microscope (SEM)** [27-29] is a type of electron microscope that produces images of a sample by scanning it with a focused beam of electrons. The electrons interact with atoms in the sample, producing various signals that contain information about the sample's surface topography and composition. The electron beam is generally scanned in a raster scan pattern, and the beam's position is combined with the detected signal to produce an image. Specimens can be observed in high vacuum, in low vacuum, in wet conditions (in environmental SEM), and at a wide range of cryogenic or elevated temperatures. The most common SEM mode is detection of secondary electrons emitted by atoms excited by the electron beam. The number of secondary electrons that can be detected depends, among other things, on the angle at which beam meets surface. By scanning the sample and collecting the

passes through it. An image is formed from the interaction of the electrons transmitted through the specimen; the image is magnified and focused on an imaging device, such as a fluorescent screen, on a layer of photographic film, or to be detected by a sensor such as a CCD camera (fig II-16). This enables the instrument's user to examine fine detail—even as small as a single column of atoms, which is thousands of times smaller than the smallest resolvable object in a light microscope.

At smaller magnifications TEM image contrast is due to absorption of electrons in the material, to the thickness and composition of the material. At higher magnifications complex wave interactions modulate the intensity of the image, requiring expert analysis of observed images. Alternate modes of use allow for the TEM to observe modulations in chemical identity, crystal orientation, electronic structure and sample induced electron phase shift as well as the regular absorption based imaging.

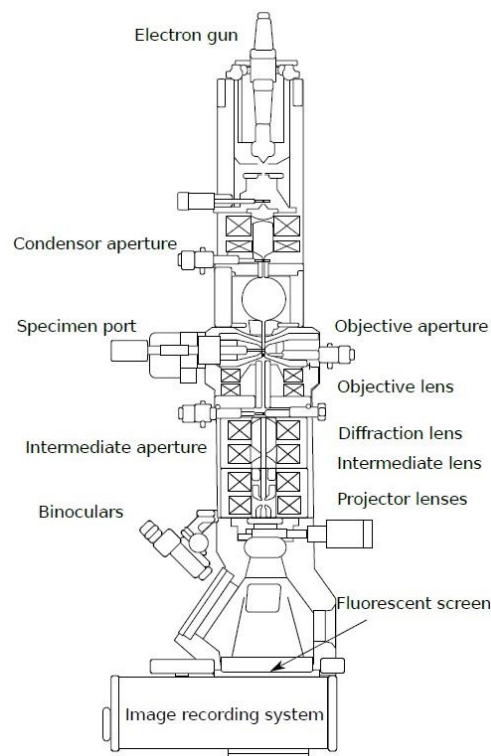


Fig. II-16. Layout of optical components in a basic TEM [27].

II-3.3: High-Resolution Transmission Electron Microscopy (HR-TEM)

High-resolution transmission electron microscopy (HRTEM) [27, 30] is an imaging mode of the transmission electron microscope (TEM) that allows direct imaging of the atomic structure of the sample to be done. HRTEM is a powerful tool to study properties of materials on the atomic scale. HRTEM is often also used to refer to high resolution scanning TEM. For

disambiguation, the technique is also often referred to as phase contrast TEM. At present, the highest point resolution realized in phase contrast with the new generation of TEM is around 0.5 ångströms (0.050 nm). At these small scales, individual atoms of a crystal and its defects can be resolved. For 3-dimensional crystals, it may be necessary to combine several views, taken from different angles, into a 3D map. This technique is called electron tomography.

The microscope uses an electron beam at a high voltage, issued by the electron gun. The electromagnetic lenses focus the electrons on the sample. The electron beam produces different types of radiation by coming through the atoms of the sample. Finally, only the transmitted electrons are analyzed by the detector which converts the signal in a contrasted image.

The sample could be analysed either in directly in powder form or scratched from the surface:

- ✓ Powder: the powder is dismissed in ethanol, then, a drop of the solution is laid on the sample holder (which is a 3 mm copper grid).
- ✓ Electrodeposited films on a substrate: The deposit is scraped off the gold foil by a razor and collected by ethanol droplets. The solution is then pumped into a micropipette and deposited on the Cu grid.

The proper sample is then positioned in the microscope chamber and then, analysed by observing every tile of the grid (about 100), focusing on each nano-agglomerate. Images are taken at various magnifications, prior to image acquisition, an elemental analysis could assure the nature of metal oxide. For HR-TEM studies of the electrochemically prepared WO_3 and $\text{RuO}_x \cdot n\text{H}_2\text{O}$ by surfactant assisted electrodeposition, the thin films were deposited on gold substrates (gold foil, 0.05 mm thickness, 99.95% purity (Goodfellow)) followed by thermal treatment at different temperatures. The samples were scraped off from the gold substrates and ultrasonically dispersed in ethanol. For TiO_2 films, the samples were directly deposited on the copper grids. Our analyses were performed using a JEOL JEM 2010 UHR with a LaB_6 filament microscope operating at 200 kV equipped with a CCD camera (GATAN). The chemical analyses were obtained by selected Energy-Dispersive X-Ray Spectroscopy (EDX) associated to a microanalyser (PGI_IMIX PC) mounted in the microscope.

II-3.4: Selected Area Electron Diffraction (SAED)

Selected area (electron) diffraction (abbreviated as **SAD** or **SAED**) [31], is a crystallographic experimental technique that can be performed inside a transmission electron microscope (**TEM**). In a TEM, a thin crystalline specimen is subjected to a parallel beam of high-energy

electrons. As TEM specimens are typically ~100 nm thick, and the electrons typically have an energy of 100–400 KeV, the electrons pass easily through the sample. In this case, electrons are treated as wave-like, rather than particle-like. Because the wavelength of high-energy electrons is a few thousands of nanometer and the spacing between atoms in a solid is about a hundred times larger, the atoms act as a diffraction grating to the electrons, which are diffracted. That is, some fraction of them will be scattered to particular angles, determined by the crystal structure of the sample, while others continue to pass through the sample without deflection. As a result, the image on the screen of the TEM will be a series of spots, the **selected area diffraction pattern**, and each spot corresponding to a satisfied diffraction condition of the sample's crystal structure. If the sample is tilted, the same crystal will stay under illumination, but different diffraction conditions will be activated, and different diffraction spots will appear or disappear.

SAD is referred to as “selected” because the user can easily choose from which part of the specimen to obtain the diffraction pattern. Located below the sample holder on the TEM column is a **selected area aperture**, which can be inserted into the beam path. This is a thin strip of metal that will block the beam. It contains several different sized holes, and can be moved by the user. The effect is to block all of the electron beam except for the small fraction passing through one of the holes; by moving the aperture hole to the section of the sample the user wishes to examine. This particular area is *selected* by the aperture, and only this section will contribute to the SAED on the screen. This is important, for example, in polycrystalline specimens. If more than one crystal contributes to the SAED, it can be difficult or impossible to analyze. As such, it is useful to select a single crystal for analysis at a time. It may also be useful to select two crystals at a time, in order to examine the crystallographic orientation between them. As a diffraction technique, SAED can be used to identify crystal structures and examine crystal defects. It is similar to X-ray diffraction, but samples as small as several hundred nanometers in size can be examined, whereas X-ray diffraction typically can only examined samples areas with several centimeters in size. In our studies, the crystallinity of the synthesized as-prepared hydrated ruthenium oxide, as well the structural evolution of heated samples (at 150°C and 450°C) was investigated by SAED during TEM analyzes. This operation has been conducting in a JEOL JEM 100CX UHR microscope equipped with a CCD camera Keenview.

II-3.5: X-ray Diffraction (XRD)

XRD [31-33] is a tool used for identifying the atomic and molecular structure of a crystal, in which the crystalline atoms cause a beam of incident X-rays to diffract into many specific directions (the elements of X-ray are shown in figure II-17). By measuring the angles and intensities of these diffracted beams, a crystallographer can produce a three-dimensional picture of the density of electrons within the crystal. From this electron density, the mean positions of the atoms in the crystal can be determined, as well as their chemical bonds, their disorder and various other information.

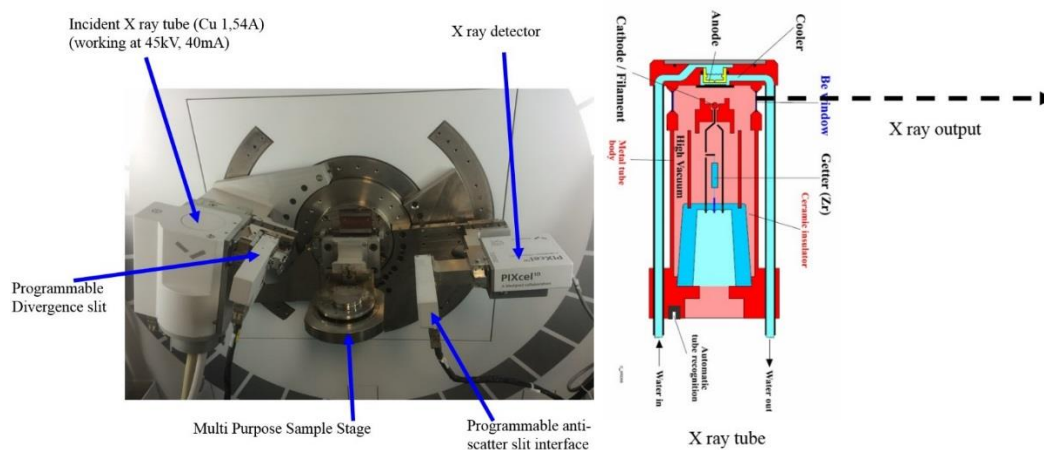


Fig. II-17. The schema of X-ray chamber, and the inside view of the X-ray tube (LISE Lab).

In a single-crystal X-ray diffraction measurement, a crystal is mounted on a goniometer. The goniometer is used to position the crystal at selected orientations. The crystal is illuminated with a finely focused monochromatic beam of X-rays, producing a diffraction pattern of regularly spaced spots known as *reflections* (see Fig. II-17). The two-dimensional images taken at different orientations are converted into a three-dimensional model of the density of electrons within the crystal using the mathematical method of Fourier transforms, combined with chemical data known for the sample. Poor resolution (fuzziness) or even errors may result if the crystals are too small, or not uniform enough in their internal makeup.

X-ray crystallography is related to several other methods for determining atomic structures. Similar diffraction patterns can be produced by scattering electrons or neutrons, which are likewise interpreted by Fourier transformation. If single crystals of sufficient size cannot be obtained, various other X-ray methods can be applied to obtain less detailed information; such methods include fiber diffraction, powder diffraction and (if the sample is not crystallized) small-angle X-ray scattering (SAXS). If the material under investigation is only available in the

form of nanocrystalline powders or suffers from poor crystallinity, the methods of electron crystallography can be applied for determining the atomic structure.

The diffractometer used for the XRD results (of $\text{RuO}_x \cdot n\text{H}_2\text{O}$) was a Panalytical Xpert Pro MPD equipped with a copper anode. A Bragg Brentano configuration with a Göbel mirror was used to parallelize the beam and measure the sample at grazing incidence ($\omega = 3^\circ$). The Soller slits of 0.04° sides incident. The measured angular range was 25 to 95° in 2θ with a step of 0.067° and a total acquisition time of 1h.

II-3.6: X-ray Photoelectron Spectroscopy (XPS)

X-ray photoelectron spectroscopy (XPS) [27, 34] is a surface-sensitive quantitative spectroscopic technique that measures the elemental composition the chemical state and electronic state of the elements that exist within a material. XPS spectra are obtained by irradiating a material with a beam of X-rays while simultaneously measuring the kinetic energy and number of electrons that escape from the top 0 to 10 nm of the material analyzed (as shown in figure II-18). XPS requires high vacuum ($P \sim 10^{-8}$ millibar) or ultra-high vacuum (UHV; $P < 10^{-9}$ millibar) conditions. XPS can be used to analyze the surface chemistry of a material in its as-received state, or after some treatment. These treatments may include: fracturing, cutting or scraping in air or UHV to expose the bulk chemistry, ion beam etching to clean off some or all of the surface contamination or to intentionally expose deeper layers of the sample in depth profiling XPS, exposure to heat to study the changes due to heating, exposure to reactive gases or solutions, exposure to ion beam implant, exposure to ultraviolet light. In principle XPS detects all elements. In practice, using typical laboratory-scale X-ray sources, XPS detects all elements with an atomic number (Z) of 3 (lithium) and above. It cannot easily detect hydrogen ($Z = 1$) or helium ($Z = 2$). Detection limits for most of the elements (on a modern instrument) are in the parts per thousand range. Detection limits of parts per million (ppm) are possible, but require special conditions: concentration at top surface or very long collection time (overnight).

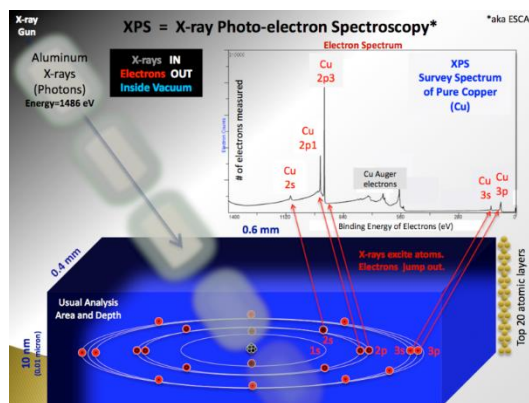


Fig. II-18. Basic components of a monochromatic XPS system.

XPS is used to measure:

- ✓ elemental composition of the surface (top 0–10 nm usually)
- ✓ empirical formula of pure materials
- ✓ elements that contaminate a surface
- ✓ chemical or electronic state of each element in the surface
- ✓ uniformity of elemental composition across the top surface (or line profiling or mapping)
- ✓ uniformity of elemental composition as a function of ion beam etching (or depth profiling)

XPS can be performed using a commercial XPS system, a lab made XPS system, or a synchrotron based light source combined with a custom-designed electron energy analyzer. Commercial XPS instruments in the year 2005 used either a focused 20- to 500- micrometer-diameter beam of monochromatic Al $K\alpha$ X-rays, or a broad 10- to 30-mm diameter beam of non-monochromatic (polychromatic) Al $K\alpha$ X-rays or Mg $K\alpha$ X-rays. A few specially designed XPS instruments can analyze volatile liquids or gases, or materials at pressures of roughly 1 torr (1.00 torr = 1.33 millibar), but there are relatively few of these types of XPS systems. The ability to heat or cool the sample during or prior to analysis is relatively common.

Because the energy of an X-ray with particular wavelength is known (for Al $K\alpha$ X-rays, $E_{photon} = 1486.7$ eV), and because the emitted electrons' kinetic energies are measured, the electron binding energy of each of the emitted electrons can be determined by using an equation that is based on the work of Ernest Rutherford (1914):

$$E_{binding} = E_{photon} - (E_{kinetic} + \phi) \quad (10)$$

where $E_{binding}$ is the binding energy (BE) of the electron, E_{photon} is the energy of the X-ray photons being used, $E_{kinetic}$ is the kinetic energy of the electron as measured by the instrument

and ϕ is the work function dependent on both the spectrometer and the material. This equation is essentially a conservation of energy equation. The work function term ϕ is an adjustable instrumental correction factor that accounts for the few eV of kinetic energy given up by the photoelectron as it becomes absorbed by the instrument's detector. It is a constant that rarely needs to be adjusted in practice.

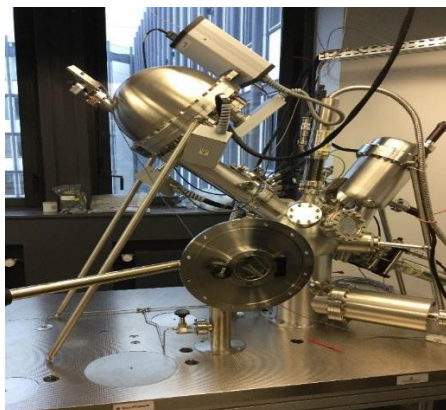


Fig. II-19. General view of the XPS montage used in for our studies (LRS laboratory, UPMC).

The composition of the studied MO_x films were determined by X-ray photoelectron spectroscopy (XPS) with the same montage shown in figure II-19 (on a VG ESCALAB 250i-XL spectrometer using monochromatic Al $K\alpha$ radiation as the X-ray source).

III: Theory of *ac*-electrogravimetry

III-1. A Three Species Model with a Cation, an Anion and a Free Solvent Contribution

The *ac*-electrogravimetric methodology and theoretical background were precisely discussed by Gabrielli *et al.* [35-40]. Briefly, *ac*-electrogravimetry consists of coupling electrochemical impedance spectroscopy (EIS) with a fast quartz crystal microbalance (QCM) used in *ac*-mode.

It allows the response in current, $\frac{\Delta E}{\Delta I}(\omega)$, electrochemical transfer function, and in mass,

$\frac{\Delta m}{\Delta E}(\omega)$, mass-potential transfer function to be simultaneously obtained owing to a sinusoidal potential perturbation with a small amplitude (ΔE). The combination of such transfer functions provides the possibility of a fair separation of different electrochemical processes, which involves concomitantly mass and charge changes.

III-2. Electrochemical reactions and kinetics

The transfer of two cations (c1 and c2), and an anion (a) in the electroactive films incorporating three different sites, P1, P2, and P3 during the redox reaction of the host material $\langle P \rangle$ where a single electronic transfer takes place in three independent sites can be expressed as:



where $\langle P1c1 \rangle$ and $\langle P2c2 \rangle$ are the film matrices doped with cations, and $\langle P3a \rangle$ is the film matrices doped with anions. The cation and anion transfers at the film solution interface are only taken into account as rate-limiting steps since the ionic transports inside the thin film and in the solution are supposed to be fast enough through thin films or in sufficiently concentrated electrolytes. In case of electroadsorption reactions, a similar approach will be used without any potential dependence of the kinetics rate of transfer (k_i and k_i').

The net instantaneous molar flux change of each cation, ΔJ_{c1} and ΔJ_{c2} and anion ΔJ_a can be written as follows taking into account the various concentrations and kinetic rate of transfer:

$$J_{c1}(d_f) = -d_f \frac{dC_{c1}}{dt} = k_{c1}' (C_{c1} - C_{c1min}) - k_{c1} (C_{c1max} - C_{c1}) C_{c1sol} \quad (14)$$

$$J_{c2}(d_f) = -d_f \frac{dC_{c2}}{dt} = k_{c2}' (C_{c2} - C_{c2min}) - k_{c2} (C_{c2max} - C_{c2}) C_{c2sol} \quad (15)$$

$$J_a(d_f) = -d_f \frac{dC_a}{dt} = k_a (C_a - C_{amin}) - k_a' (C_{amax} - C_a) C_{asol} \quad (16)$$

By using the Hillman solvation model [41] the same relationship can be used for the solvent flux:

$$J_s(d_f) = -d_f \frac{dC_s}{dt} = k_s' (C_s - C_{smin}) - k_s (C_{smax} - C_s) \quad (17)$$

where (α) d_f is the film thickness; (β) C_i is the concentration of species i in the film associated to P_i site, C_{isol} is the concentration of species i in the solution by assuming that the diffusion of

the ions in solution does not limit the global kinetics; (γ) the term $(C_{imax} - C_i)$ is the concentration in free sites for species i at time t , where C_{imax} is the maximum concentration of the free sites in the film for species i ; (δ) the term $(C_i - C_{imin})$ is the concentration of species i in the film bulk at time t , where C_{imin} is the minimum concentration of species i in the film. In case of a redox process, the kinetic constants which appear here depend on the potential under the classical form:

$$k'_i = k'_{i0} e^{\left[b'_i (E - E_i^\circ) \right]} \quad (18)$$

$$k_i = k_{i0} e^{\left[b_i (E - E_i^\circ) \right]} \quad (19)$$

where E is the potential, E_i° is the apparent normal potential, $(E - E_i^\circ)$ is the overvoltage, k_{i0} , k'_{i0} , b_i and b'_i are constants.

III-3. Dynamic regime and flux of each species

Under the effect of a sinusoidal potential perturbation with low amplitude, ΔE , imposed to the electrode/film/electrolyte system, sinusoidal fluctuations of concentration, ΔC_i , and flux, ΔJ_i , are observed such as:

$$\Delta J_i = -d_f \frac{dC_i}{dt} = -j\omega d_f \Delta C_i \quad (20)$$

The expression of the global insertion/expulsion flux, ΔJ_i , which depends on the concentration and potential perturbations, at the film/electrolyte interface is:

$$\Delta J_i = \left(\frac{\partial J_i}{\partial C_i} \right)_E \Delta C_i + \left(\frac{\partial J_i}{\partial E} \right)_{C_i} \Delta E = K_i \Delta C_i (d_f) + G_i \Delta E \quad (21)$$

where $j = \sqrt{-1}$, $\omega = 2\pi f$ is the pulsation, f is the perturbation frequency and K_i and G_i are the partial derivatives of the flux, J_i , with respect to the concentration and the potential respectively,

$K_i = \left(\frac{\partial J_i}{\partial C_i} \right)_E$ and $G_i = \left(\frac{\partial J_i}{\partial E} \right)_{C_i}$, where J_i stands for the flux of the species i crossing the

film/electrolyte interface. More precisely, K_i is the kinetics rate of transfer and G_i is the inverse of the transfer resistance, Rt_i , of the species at the film/electrolyte interface (where i is the cation c1, cation c2, anion a, or the free solvent s). Therefore, the characteristic frequency, f_i , of the transfer can be estimated through the following equation:

$$f_i = \frac{K_i}{\pi d_f} \quad (22)$$

The transfer resistance, Rt_i , can be calculated taking into account the values of G_i :

$$Rt_i = \frac{1}{FG_i} \quad (23)$$

For each transferred species, the ionic transfer resistance, Rt_i , is a good estimation of the ease of the transfer.

Also, under the effect of a sinusoidal potential perturbation with low amplitude, ΔE , imposed to the electrode/film/electrolyte system, sinusoidal fluctuations of concentration, ΔC_i , are observed. In the present case, for electroactive metal oxide thin films, the change of the concentration, ΔC_i , of each species (cation 1 (c1), cation 2 (c2), anion (a), and free solvent (s)) with potential ΔE can be calculated.

$\left. \frac{\Delta C_{c1}}{\Delta E} \right _{th} (\omega) = -\frac{G_{c1}}{(j\omega d_f) + K_{c1}} \quad (24)$	$\left. \frac{\Delta C_{c2}}{\Delta E} \right _{th} (\omega) = -\frac{G_{c2}}{(j\omega d_f) + K_{c2}} \quad (25)$
$\left. \frac{\Delta C_a}{\Delta E} \right _{th} (\omega) = -\frac{G_a}{(j\omega d_f) + K_a} \quad (26)$	$\left. \frac{\Delta C_s}{\Delta E} \right _{th} (\omega) = -\frac{G_s}{(j\omega d_f) + K_s} \quad (27)$

III-4. Charge/potential transfer function, $\left. \frac{\Delta q}{\Delta E} \right|_{th}$

The charge/potential transfer function, $\left. \frac{\Delta q}{\Delta E} \right|_{th} (\omega)$, is calculated for the insertion/expulsion of the two cations, c1 and c2 and an anion, a and by using the Faraday number, F , and the film thickness, d_f :

$$\left. \frac{\Delta q}{\Delta E} \right|_{th} (\omega) = -Fd_f \left(\left. \frac{\Delta C_{c1}}{\Delta E} \right|_{th} + \left. \frac{\Delta C_{c2}}{\Delta E} \right|_{th} - \left. \frac{\Delta C_a}{\Delta E} \right|_{th} \right) \quad (28)$$

Then, for the two cations, c1 and c2, and an anion it comes using equations 24-27:

$$\left. \frac{\Delta q}{\Delta E} \right|_{th} (\omega) = Fd_f \left(\frac{G_{c1}}{j\omega d_f + K_{c1}} + \frac{G_{c2}}{j\omega d_f + K_{c2}} - \frac{G_a}{j\omega d_f + K_a} \right) \quad (29)$$

III-5. Electrochemical impedance, $\left. \frac{\Delta E}{\Delta I} \right|_{th}$

Then, the Faradaic impedance, $Z_F(\omega)$, relative to the global ionic transfer of the electroactive film for three charged species, cations (c1 and c2) and anion (a) involved in the charge compensation is:

$$Z_F|_{th}(\omega) = \left. \frac{\Delta E}{\Delta I_F} \right|_{th}(\omega) = \frac{1}{j\omega \left. \frac{\Delta q}{\Delta E} \right|_{th}(\omega)} \quad (30)$$

And using Eq. (29), we can obtain for the Faradaic impedance, $Z_F(\omega)$:

$$Z_F|_{th}(\omega) = \left. \frac{\Delta E}{\Delta I_F} \right|_{th}(\omega) = \frac{1}{j\omega d_f F \left[\frac{G_{c1}}{(j\omega d_f) + K_{c1}} + \frac{G_{c2}}{(j\omega d_f) + K_{c2}} - \frac{G_a}{(j\omega d_f) + K_a} \right]} \quad (31)$$

Finally, the electrochemical impedance can be estimated incorporating the electrolyte resistance, R_{el} and the interfacial capacitance, C_{dl} :

$$\left. \frac{\Delta E}{\Delta I} \right|_{th}(\omega) = R_{el} + \frac{1}{j\omega C_{dl} + \frac{1}{Z_F|_{th}(\omega)}} \quad (32)$$

or with the K_i and G_i parameters related to the two cations and an anion:

$$\left. \frac{\Delta E}{\Delta I} \right|_{th}(\omega) = R_{el} + \frac{1}{j\omega C_{dl} + j\omega d_f F \left[\frac{G_{c1}}{(j\omega d_f) + K_{c1}} + \frac{G_{c2}}{(j\omega d_f) + K_{c2}} - \frac{G_a}{(j\omega d_f) + K_a} \right]} \quad (33)$$

When the response of the electrochemical system is perturbed at low frequencies with a parasitic electrochemical reaction, characterized by a parasitic impedance ($Z_{par}(\omega)$) described in equation (34), in parallel with the ionic transfer, the global electrochemical impedance becomes as shown in equation 35.

$$Z_{par}(\omega) = R_{par} + \frac{1}{j\omega C_{par}} \quad (34)$$

$$\frac{\Delta E}{\Delta I}(\omega) = R_{el} + \frac{1}{j\omega C_{dl} + \frac{\Delta I}{\Delta E} \Big|_{ions}(\omega) + \frac{1}{Z_{par}(\omega)}} \quad (35)$$

III-6. Mass/potential transfer function, $\frac{\Delta m}{\Delta E} \Big|_{th}(\omega)$

The electrogravimetric transfer function, $\frac{\Delta m}{\Delta E} \Big|_{th}(\omega)$, can be calculated theoretically, taking into account the uncharged species contribution (solvent molecules in some cases) through the two parameters K_s and G_s :

$$\frac{\Delta m}{\Delta E} \Big|_{th}(\omega) = -d_f \left(m_{c1} \frac{G_{c1}}{(j\omega d_f) + K_{c1}} + m_{c2} \frac{G_{c2}}{(j\omega d_f) + K_{c2}} + m_a \frac{G_a}{(j\omega d_f) + K_a} + m_s \frac{G_s}{(j\omega d_f) + K_s} \right) \quad (36)$$

where m_{c1} , m_{c2} , m_a and m_s are the atomic weight of involved species.

Partial mass/potential TF are also estimated either by removing the c2 contribution, calculating

$$\frac{\Delta m}{\Delta E} \Big|_{th}^{c1as}(\omega) ; \text{ or the c1 contribution, calculating } \frac{\Delta m}{\Delta E} \Big|_{th}^{c2as}(\omega) ; \text{ or the anion contribution,}$$

calculating $\frac{\Delta m}{\Delta E} \Big|_{th}^{c1c2s}(\omega)$. For that, the following equations are used:

In the case of cation c1, anion and solvent, the following equation is defined:

$$\frac{\Delta m}{\Delta E} \Big|_{th}^{c1as}(\omega) = d_f \left((m_{c1} - m_{c2}) \frac{\Delta C_{c1}}{\Delta E} + (m_a + m_{c2}) \frac{\Delta C_a}{\Delta E} + m_s \frac{\Delta C_s}{\Delta E} \right) \quad (37)$$

Similarly, in case of cation c2, anion and solvent, it comes:

$$\frac{\Delta m}{\Delta E} \Big|_{th}^{c2as}(\omega) = d_f \left((m_{c2} - m_{c1}) \frac{\Delta C_{c2}}{\Delta E} + (m_a + m_{c1}) \frac{\Delta C_a}{\Delta E} + m_s \frac{\Delta C_s}{\Delta E} \right) \quad (38)$$

Endly, for cation c1, cation c2, and solvent, it is written:

$$\frac{\Delta m}{\Delta E} \Big|_{th}^{c1c2s}(\omega) = d_f \left((m_{c1} + m_a) \frac{\Delta C_{c1}}{\Delta E} + (m_{c2} + m_a) \frac{\Delta C_{c2}}{\Delta E} + m_s \frac{\Delta C_s}{\Delta E} \right) \quad (39)$$

IV. References

- [1] H.M. French, M.J. Henderson, A.R. Hillman, E. Vieil, Ion and solvent transfer discrimination at a nickel hydroxide film exposed to LiOH by combined electrochemical quartz crystal microbalance (EQCM) and probe beam deflection (PBD) techniques, *J. Electroanal. Chem.* 500 (2001) 192–207.
- [2] R. Roto, A. Yamagishi, G. Villemure, Electrochemical quartz crystal microbalance study of mass transport in thin film of a redox active Ni–Al–Cl layered double hydroxide, *J. Electroanal. Chem.* 572 (2004) 101–108.
- [3] B.I. Lemon, F. Liu, J.T. Hupp, Electrochemical, spectral, and quartz crystal microgravimetric assessment of conduction band edge energies for nanocrystalline zirconium dioxide/solution interfaces, *Coord. Chem. Rev.* 248 (2004) 1225–1230.
- [4] B.I. Lemon, J.T. Hupp, EQCM Investigations of Dye-Functionalized Nanocrystalline Titanium Dioxide Electrode/Solution Interfaces: Does Luminescence Report Directly on Interfacial Electron Transfer Kinetics?, *J. Phys. Chem. B.* 103 (1999) 3797–3799.
- [5] K. Mech, P. Żabiński, R. Kowalik, K. Fitzner, EQCM, SEC and voltammetric study of kinetics and mechanism of hexaamminecobalt (III) electro-reduction onto gold electrode, *Electrochimica Acta.* 81 (2012) 254–259.
- [6] P.R. Bueno, R.C. Faria, L.O.S. Bulhões, EQCM study during lithium insertion/deinsertion processes in Nb₂O₅ films prepared by polymeric precursor method, *Solid State Ion.* 176 (2005) 1175–1180.
- [7] W. MASON, *Physicals acoustics, Principales and Methods*, 1964, vol 1, part A, New York, Academic Press, n.d.
- [8] L.T.T. Kim, *Etude de films électroactifs par couplage de techniques électrochimique et gravimétrique. Application à la caractérisation de membranes à conduction protonique.*, Université Pierre et Marie Curie, 2009. <https://hal.archives-ouvertes.fr/tel-01086589/> (accessed June 27, 2016).
- [9] G.Z. Sauerbrey, Use of quartz vibration for weighing thin films on a microbalance, *J Phys.* 155 (1959) 206–212.
- [10] C. Gabrielli, M. Keddou, Contribution of electrochemical impedance spectroscopy to the investigation of the electrochemical kinetics, *Electrochimica Acta.* 41 (1996) 957–965.
- [11] A. Rouis, R. Mlika, J. Davenas, H.B. Ouada, I. Bonnamour, N. Jaffrezic, Impedance spectroscopic investigations of ITO modified by new Azo-calix [4] arene immobilised into electroconducting polymer (MEHPPV), *J. Electroanal. Chem.* 601 (2007) 29–38.
- [12] M.E. Orazem, B. Tribollet, *Electrochemical impedance spectroscopy*, John Wiley & Sons, 2011.
- [13] K. Bizet, C. Gabrielli, H. Perrot, Immunodetection by quartz crystal microbalance, *Appl. Biochem. Biotechnol.* 89 (2000) 139–149.
- [14] H. Abdullber Fakhouri, Thin film deposition of pure and doped TiO₂ by RF magnetron sputtering for visible light photocatalytic and optoelectronic applications, Paris 6, 2012. <http://www.theses.fr/2012PAO66343> (accessed June 27, 2016).
- [15] H. Fakhouri, F. Arefi-Khonsari, A.K. Jaiswal, J. Pulpytel, Enhanced visible light photoactivity and charge separation in TiO₂/TiN bilayer thin films, *Appl. Catal. Gen.* 492 (2015) 83–92.

- [16] H. Fakhouri, J. Pulpytel, W. Smith, A. Zolfaghari, H.R. Mortaheb, F. Meshkini, R. Jafari, E. Sutter, F. Arefi-Khonsari, Control of the visible and UV light water splitting and photocatalysis of nitrogen doped TiO₂ thin films deposited by reactive magnetron sputtering, *Appl. Catal. B Environ.* 144 (2014) 12–21.
- [17] S.-H. Baeck, K.-S. Choi, T.F. Jaramillo, G.D. Stucky, E.W. McFarland, Enhancement of photocatalytic and electrochromic properties of electrochemically fabricated mesoporous WO₃ thin films, *Adv. Mater.* 15 (2003) 1269–1273.
- [18] W.L. Kwong, A. Nakaruk, P. Koshy, C.C. Sorrell, Tunable Photoelectrochemical properties by nanostructural control in WO₃ thin films prepared by carboxylic acid-assisted electrodeposition, *J. Phys. Chem. C.* 117 (2013) 17766–17776.
- [19] W.L. Kwong, N. Savvides, C.C. Sorrell, Electrodeposited nanostructured WO₃ thin films for photoelectrochemical applications, *Electrochimica Acta.* 75 (2012) 371–380.
- [20] I. Zhitomirsky, L. Gal-Or, Ruthenium oxide deposits prepared by cathodic electrosynthesis, *Mater. Lett.* 31 (1997) 155–159.
- [21] B.-O. Park, C.D. Lokhande, H.-S. Park, K.-D. Jung, O.-S. Joo, Performance of supercapacitor with electrodeposited ruthenium oxide film electrodes—effect of film thickness, *J. Power Sources.* 134 (2004) 148–152.
- [22] B.-O. Park, C.D. Lokhande, H.-S. Park, K.-D. Jung, O.-S. Joo, Cathodic electrodeposition of RuO₂ thin films from Ru(III)Cl₃ solution, *Mater. Chem. Phys.* 87 (2004) 59–66. doi:10.1016/j.matchemphys.2004.04.023.
- [23] K.-H. Kim, K.S. Kim, G.-P. Kim, S.-H. Baeck, Electrodeposition of mesoporous ruthenium oxide using an aqueous mixture of CTAB and SDS as a templating agent, *Curr. Appl. Phys.* 12 (2012) 36–39.
- [24] V.D. Patake, C.D. Lokhande, O.S. Joo, Electrodeposited ruthenium oxide thin films for supercapacitor: Effect of surface treatments, *Appl. Surf. Sci.* 255 (2009) 4192–4196.
- [25] A. Walcarius, E. Sibottier, M. Etienne, J. Ghanbaja, Electrochemically assisted self-assembly of mesoporous silica thin films, *Nat. Mater.* 6 (2007) 602–608.
- [26] M.D. Levi, G. Salitra, N. Levy, D. Aurbach, J. Maier, Application of a quartz-crystal microbalance to measure ionic fluxes in microporous carbons for energy storage, *Nat. Mater.* 8 (2009) 872–875.
- [27] D. Brune, R. Hellborg, H.J. Whitlow, O. Hunderi, *Surface characterization: a user's sourcebook*, John Wiley & Sons, 2008.
- [28] J. Goldstein, D.E. Newbury, P. Echlin, D.C. Joy, A.D. Romig Jr, C.E. Lyman, C. Fiori, E. Lifshin, *Scanning electron microscopy and X-ray microanalysis: a text for biologists, materials scientists, and geologists*, Springer Science & Business Media, 2012.
- [29] S.L. Flegler, J.W. Heckman Jr, K.L. Klomparens, *Scanning and transmission electron microscopy: an introduction*, Oxf. Univ. Press. 1993. (1993) 225.
- [30] L. Reimer, *Transmission electron microscopy: physics of image formation and microanalysis*, Springer, 2013.
- [31] V.A. Drits, E. Silvester, A.I. Gorshkov, A. Manceau, Structure of synthetic monoclinic Na-rich birnessite and hexagonal birnessite: I. Results from X-ray diffraction and selected-area electron diffraction, *Am. Mineral.* 82 (1997) 946–961.

- [32] C. Hammond, C. Hammond, *The basics of crystallography and diffraction*, Oxford University Press Oxford, 2009. <http://oldwww.iucr.org/iucr-top/journals/bookreviews/by0141.html> (accessed June 27, 2016).
- [33] C. Suryanarayana, M.G. Norton, *X-ray diffraction: a practical approach*, Springer Science & Business Media, 2013.
- [34] J.F. Watts, J. Wolstenholme, *An introduction to surface analysis by XPS and AES*, *Introd. Surf. Anal. XPS AES John F Watts John Wolstenholme* Pp 224 ISBN 0-470-84713-1 Wiley-VCH May 2003. (2003) 224.
- [35] R. Torres, Y. Jimenez, A. Arnau, C. Gabrielli, S. Joiret, H. Perrot, T.K.L. To, X. Wang, High frequency mass transfer responses with polyaniline modified electrodes by using new ac-electrogravimetry device, *Electrochimica Acta*. 55 (2010) 6308–6312.
- [36] C. Gabrielli, J.J. García-Jareño, M. Keddám, H. Perrot, F. Vicente, Ac-electrogravimetry study of electroactive thin films. I. Application to Prussian Blue, *J. Phys. Chem. B*. 106 (2002) 3182–3191.
- [37] C. Gabrielli, J.J. Garcia-Jareño, M. Keddám, H. Perrot, F. Vicente, Ac-electrogravimetry study of electroactive thin films. II. Application to polypyrrole, *J. Phys. Chem. B*. 106 (2002) 3192–3201.
- [38] J. Agrisuelas, C. Gabrielli, J.J. Garcia-Jareño, H. Perrot, F. Vicente, Ionic and free solvent motion in poly (azure A) studied by ac-electrogravimetry, *J. Phys. Chem. C*. 115 (2011) 11132–11139.
- [39] L.T.T. Kim, C. Gabrielli, H. Perrot, J. Garcia-Jareno, F. Vicente, Redox switching of Prussian blue thin films investigated by ac-electrogravimetry, *Electrochimica Acta*. 84 (2012) 35–48.
- [40] R.E. White, *Modern Aspects of Electrochemistry* 45, Springer Science & Business Media, 2009.
- [41] A. Jackson, A.R. Hillman, S. Bruckenstein, I. Jureviciute, Modelling mobile species population changes in electroactive films under thermodynamically and kinetically controlled conditions, *J. Electroanal. Chem.* 524 (2002) 90–102.

Résumé du Chapitre III

TiO₂ est un matériau polyvalent utilisé dans de nombreux domaines technologiques importants et divers [1-3]. En tant que matériau particulièrement stable, peu coûteux, non toxique, et abondant, TiO₂ a attiré beaucoup d'attention dans les applications de stockage d'énergie, en particulier dans le domaine des batteries lithium-ion et des supercondensateurs [4-9]. Avec le succès de TiO₂ comme matériaux d'anode pour les batteries Li-ion, il est aussi intéressant d'étudier son utilisation pour les batteries Na-ion.

Des films minces d'oxydes de métaux sont des matériaux idéaux pour le stockage électrochimique de l'énergie. En effet, les distances de diffusion requises pour le stockage des ions sont beaucoup plus courtes et ainsi, il est possible de travailler avec des coefficients de diffusion assez faibles. Le transfert lent d'ions dans les matériaux MO_x restreint considérablement la cinétique électrochimique [10]. Par conséquent, il est primordial de créer les structures dans lesquelles une meilleure accessibilité est prévue pour le transfert des espèces chargées. L'*ac*-électrogravimétrie a la capacité de détecter la contribution des espèces chargées ou non chargées, au cours des différents processus faradiques ou (pseudo)capacitif.

Dans ce chapitre, et pour la première fois, cette méthodologie originale a été utilisée afin d'étudier le transfert des ions entre un film de TiO₂ et l'électrolyte. Différentes morphologies de TiO₂ amorphe ont été évaluées : forme compacte, forme poreuse et très poreuse. Elles ont été déposées par pulvérisation réactive magnétron RF. Cette technique de préparation permet de synthétiser à basse température différents matériaux avec différentes morphologies à l'échelle nanométrique. Les conditions de dépôt de haute pureté sont fournies sous une atmosphère d'Ar.

Les couches minces de TiO₂ amorphes ont été étudiées dans deux milieux différents, LiClO₄ et NaClO₄, afin d'identifier les espèces qui participent au processus de compensation de charge. En effet, *ac*-électrogravimétrie peut servir comme sonde gravimétrique afin d'étudier les mécanismes complexes de stockage de charge et extraire des subtilités inaccessibles avec des outils classiques d'investigation.

Les courbes d'électrogravimétrie montrent une réponse quasiment capacitive dans la région anodique. La densité de courant cathodique et anodique des films de TiO₂ avec la morphologie très poreuse est beaucoup plus élevée que celle observée pour les films poreux et denses. Cela indique une cinétique plus rapide de transfert des ions. Les valeurs de densité de courant mesurées sont presque cent fois supérieures à celle obtenue pour le film moins poreux. Les variations de masse sont également influencées par la présence des pores, la réponse de la

microbalance est amplifiée dans le cas du film très poreux. Cette meilleure réponse est attribuée à une meilleure surface spécifique grâce à la présence de pores.

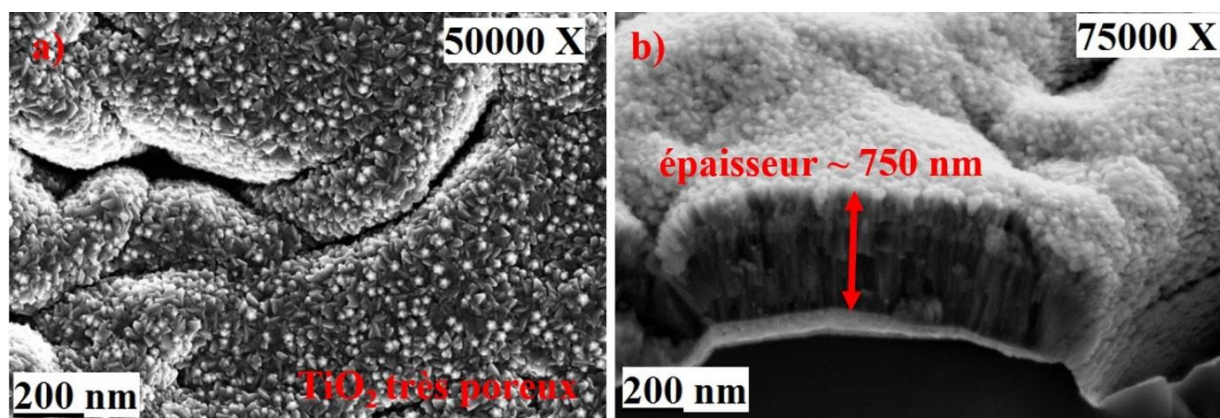
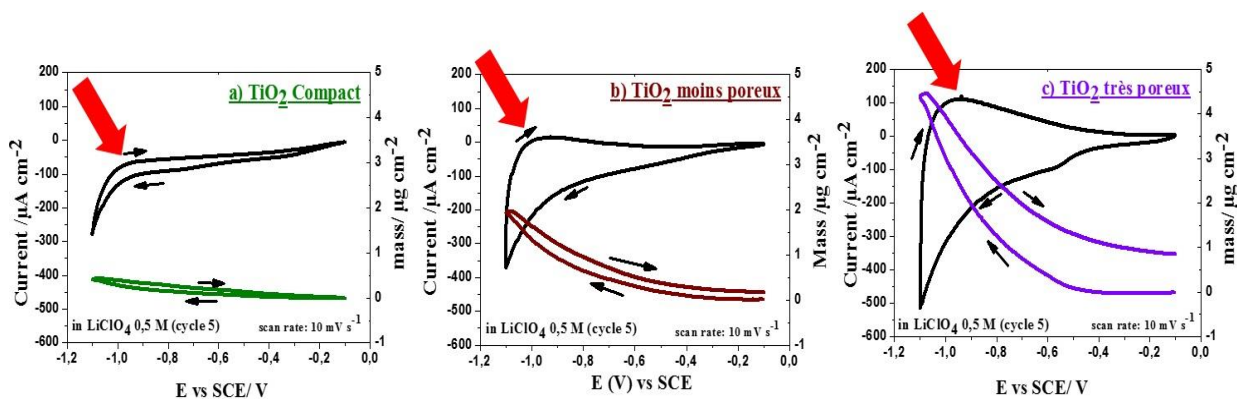


Image de la surface d'un film très poreux de TiO_2 (a) et image en coupe avec estimation de l'épaisseur (b).

Les résultats présentés dans ce chapitre pour les films minces de TiO_2 amorphes poreux et très poreux établissent que les mécanismes de stockage de charge pseudo-capacitif peuvent être examinés par *ac*-électrogravimétrie. La technique fournit l'identification exacte des espèces chargées et non-chargées et des informations cinétiques à ce propos, ce qui est impossible avec des mesures d'EQCM classique. Le comportement électrochimique des films minces de TiO_2 poreux et très poreux dans les solutions aqueuses de LiClO_4 et NaClO_4 implique les ions Li^+ , les ions Na^+ ainsi que les formes hydratées de ces ions. Il est à noter que des anions ont aussi été détectés par notre étude d'*ac*-électrogravimétrie.

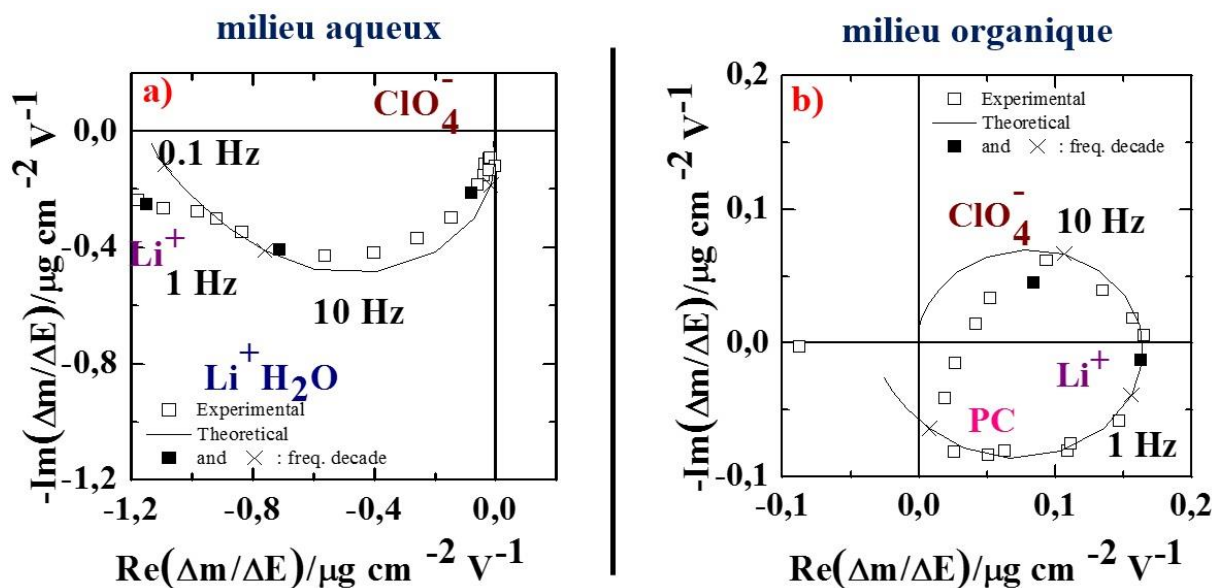


Variations de courant et de masse obtenues simultanément lors du cyclage électrochimique de films de TiO_2 (a) dense, (b) poreux, et (c) très poreux, déposés sur l'électrode d'or d'un résonateur à quartz. Les mesures sont en solution aqueuse de LiClO_4 0,5M avec une vitesse de balayage de 10 mV s^{-1} .

Les résultats de nos études dans une solution aqueuse de LiClO_4 ont révélé que la contribution des espèces chargées a été amplifiée dans les films de TiO_2 très poreux par rapport aux films moins poreux. Cette étude qualitative et quantitative de la contribution des espèces ioniques et non ioniques dans le processus de compensation de charge, ainsi que des informations dynamiques sur le transfert interfacial a encore prouvé la nature avantageuse des structures poreuses des films de TiO_2 . Celle-ci est probablement liée à une meilleure accessibilité fournie aux deux espèces cationiques Li^+ et $\text{Li}^+ \cdot \text{H}_2\text{O}$. En particulier, l'espèce lithium hydraté, $\text{Li}^+ \cdot \text{H}_2\text{O}$ a été transférée rapidement et facilement à l'interface électrode/électrolyte, dans le cas des films TiO_2 très poreux. De plus, les variations relatives de la concentration des ions dans l'électrode de TiO_2 très poreuse sont significativement plus élevées par rapport à celles de leurs homologues moins poreuses.

Pour NaClO_4 en milieu aqueux et pour le film de TiO_2 poreux, en raison d'une porosité intergranulaire réduite, la seule contribution majeure appartient au sodium hydraté. Dans ce cas, le transfert des espèces anioniques se révèle difficile. D'autre part, la surface active optimisée dans le cas du TiO_2 très poreux conduit à un transfert ionique du sodium hydraté encore plus facile.

La dernière section est dédiée à la comparaison entre deux électrolytes l'un aqueux et l'autre organique. Il s'agit d'étudier l'impact du solvant organique sur la dynamique du transfert des différentes espèces à la fois d'un point de vue cinétique et thermodynamique, et cela pour la première fois. Globalement, les résultats obtenus sont plus satisfaisants lorsque l'électrolyte à base de LiClO_4 est aqueux. Par exemple, la capacité instantanée des espèces ioniques transférées à l'interface électrode très poreuse de TiO_2 /électrolyte, est beaucoup plus élevée lorsque l'électrolyte est aqueux. Cela peut être lié à la viscosité dynamique plus élevée du solvant organique par rapport au milieu aqueux. Il en est de même pour les résistances de transfert ioniques plus importantes en milieu organique. Dans le cas des mesures en solvant organique, l'eau libre n'apparaît pas mais le solvant organique oui. Celui-ci accompagne le transfert des ions Li^+ . Ceci influence indirectement la dynamique de transfert ionique qui est du coup ralentie.



Fonctions de transfert de masse/potentiel, pour un film de TiO_2 très poreux dans (a) électrolyte aqueux de LiClO_4 0.5 M (comprenant trois espèces, en particulier Li^+ , $\text{Li}^+ \cdot \text{H}_2\text{O}$ et ClO_4^-) et (b) électrolyte organique de LiClO_4/PC 0,5M (comprenant trois espèces, en particulier Li^+ , PC et ClO_4^-). Les mesures sont effectuées à -0,9 V vs SCE (les courbes expérimentales et théoriques sont indiquées).

Enfin, à notre connaissance, c'est la première fois que les mécanismes d'échanges ont été examinés de manière in-situ et détaillés entre différentes morphologies de TiO_2 amorphe et deux types d'électrolyte, aqueux et organiques. Ces résultats sont très intéressants et originaux, grâce à la combinaison entre une QCM rapide et la spectroscopie d'impédance électrochimique. Cela permet une meilleure compréhension des mécanismes de transfert d'ions et de mieux comprendre l'impact des molécules de solvant sur ceux-ci dans le cas de matériaux à porosité variable. Ces avancées sont impossibles à déterminer en utilisant des EQCM simples. Par conséquent, la mise en place de caractérisations par *ac*-électrogravimétrie dans le domaine des matériaux liés à l'énergie est importante. Cela devra permettre de les optimiser pour créer une nouvelle génération de supercondensateurs à haute densité d'énergie.

Chapter III: TiO₂

I. Introduction

TiO₂ is a versatile material used in numerous important and diverse technological areas [1-3]. As an exceptionally stable, inexpensive, nontoxic, and abundant material, TiO₂ has garnered significant attention in energy-storage applications, in particular, in lithium-ion batteries and supercapacitor devices [4-9]. TiO₂ is one of a few transition metal oxide materials that intercalates Li ions at reasonably low voltage (~ 1.5 V vs Li/Li⁺) with comparable capacities to the dominant graphite anodes. With the success of TiO₂ as anode materials for Li-ion batteries, it is also interesting to investigate its utilization for Na-ion batteries.

Nanometric metal oxides for electrochemical energy storage have much shorter diffusion distances required for ion storage and they can overcome low diffusion coefficients. The slow insertion/expelling of ions in bulk metal oxide materials significantly restricts the electrochemical kinetics [10]. Therefore, it is primordial to create the structures in which a better accessibility is provided for the transfer of charged species. Various nanostructures, in the form of nanowires, nanosheets, and nanoparticles, decrease the ion diffusion distance and thus, increase the rate capability even further. A major concern with these materials is that nanostructured forms, which show higher capacity and rate capability than the bulk, exhibit irreversible capacity loss during cycling [10].

In a recent work done by T. Brezesinski et al. [11], a considerable enhancement of the electrochemical properties of self-organized TiO₂ was resulted when the films were both made from nanocrystals and mesoporous (called bimodal nanoporous) architecture. Such materials show high levels of capacitive charge storage. Indeed, when nanocrystal-based films were formed without mesoscale porosity the total capacity value was low, likely because most of the film was not accessible to the electrolyte/solvent. Nevertheless, when mesoscale porosity was created in a material with “dense” walls (rather than porous walls derived from the aggregation of nanocrystals), insertion capacities comparable to templated nanocrystal materials can be achieved. This remark underscores the importance of pseudocapacitive behavior that develops in high surface area mesoporous oxide films. High pseudocapacitance behavior in TiO₂ was also observed in porous TiO₂ films and when the TiO₂ particle sizes were below 10 nm. Through this porous structure, it might become possible to attain greater power densities while maintaining high levels of energy density in next-generation electrochemical capacitors that utilize this bimodal nanoporous architecture.

Nanoscale amorphous TiO₂ electrode is also a very appealing material to develop Na ion batteries, due to enhanced ion diffusion. The nanostructured materials could propose improved power and energy densities compared with their bulk counterparts due to enhanced kinetics and large surface area. But it has also been shown that increased concentration of interfacial regions in amorphous materials may form percolation pathways to facilitate the ion diffusion [4, 12, 13]. On the basis of these reasons, H. Xiong et al. [4] have investigated amorphous TiO₂ NT electrode as anode materials for Na-ion batteries. X. Sun et al. [14] investigated the pseudocapacitance of TiO₂ thin films anchored to CNTs. According to their investigation it was observed that amorphous TiO₂ films exhibited superior charge storage capability than crystalline TiO₂ films. The morphology dependent performance and ion intercalation behaviour of TiO₂ thin films have been investigated by several *in situ* or *ex situ* characterization techniques, including electrochemical methods [6, 8,9, 14], X-ray diffraction spectroscopy [6, 8,9, 14], X-ray photoelectron spectroscopy [6, 8,9, 14]. However, none of these methods alone provide the information on the exact identification of the transferred ionic species, their dynamics of transfer at the interfaces, as well as the role of electrolyte composition and the effect of ions solvation on the intercalation/capacitive phenomena. The status of transferred ions is not a quite solved problem and the characterization of their transfer dynamics is not straightforward using conventional characterization tools. The main challenge is to find a powerful technique offering mechanistic solutions in a unique set-up that can be used to study ion transfer *in-situ* and in contact with an electrolyte. There have been studies using quartz crystal microbalance (QCM) as an *in situ* gravimetric probe to study the intercalation/electroadsorption of ions in metal oxide or carbon based electrodes. Conducting electrodes coated on the QCM resonator surface are used as working electrodes in an electrochemical cell, and thus, the electrodeposition process can be monitored. Materials of interest deposited are studied in terms of mass changes during the electrochemical processes [15-18]. Nevertheless, EQCM gives a global response corresponding in fact to several possible pathways such that ions, ions with solvation shells and even, indirectly free solvent molecules can contribute indirectly to the electrochemical process [19]. Additionally, ions may lose a part of their solvation shell to access to the sites which could be corresponded to confined nanopores. These possible pathways, and kinetic or dynamic aspects of the ion intercalation/electroadsorption processes have never been characterized in the previous EQCM studies due to the limitations of the technique. In spite of its great relevance, fast electrogravimetric methods, i.e., coupling fast quartz crystal microbalance (QCM) and electrochemical impedance spectroscopy (EIS) (*ac*-electrogravimetry), have not yet been used

for studying transfer and transport phenomena in materials for charge storage (except for the use of QCM along with cyclic voltammetry experiments (EQCM)).

In this chapter and for the first time this original methodology was used in order to investigate ions intercalation/electroadsorption of two different morphologies related to amorphous porous TiO₂ deposited by reactive magnetron RF Sputtering

Among possible routine MO_x film preparation methods such as hydrothermal pathway [7, 8], or sol-gel [11], the reactive RF sputtering method could serve as an appealing alternative fabrication route. This preparation route allows a low-temperature synthesizing process of various materials with variable morphologies in nano-metric scale to be realized. The high purity deposition conditions are provided under argon atmosphere. This method has been used by H. Fakhouri et al. [20-21] to produce photocatalytic TiO₂ electrodes.

Ac-electrogravimetry has the ability to detect the contribution of the charged or uncharged species and to separate the anionic, cationic, and free solvent contributions during the various faradaic or (pseudo)capacitive processes. The amorphous porous TiO₂ thin films were studied in two different media, LiClO₄ and NaClO₄, to understand the charge-storage mechanisms and to identify the species contributions to the charge compensation process. It has been demonstrated herein that the *ac*-electrogravimetry responses of the porous TiO₂ thin films can serve as a gravimetric probe for studying the complex charge-storage mechanisms and extracting subtleties unreachable with classical tools.

II. Structure and Morphology Study of Dense, Porous and Highly porous Thin TiO₂ Films

The morphology of the synthesized TiO₂ thin films was characterized by FEG-SEM and HR-TEM. Based on their preparation details when the operating pressure monitored by the Ar flow rate in the reactor was low i.e. 3 mtorr for 30 sccm of Ar, a fairly dense film with some distinct cracks observed on some parts of the sample is obtained (fig. III-1a). The average film thickness is ~ 300 nm and could be tailored by varying the deposition time or the pressure used for their fabrication [20-21]. An advantageous aspect of deposition based on reactive RF sputtering is the possibility to obtain different morphologies simply by varying the argon pressure in the reactor (already discussed in the experimental section). In order to procure more porous structures, an intermediate Ar pressure (60 sccm) was used. The morphological impact, is presented in fig III-1c where the image shows a crack-free film which is composed of sphere-like shape nanoparticles of TiO₂. The cross-section image (fig III-1d) gives a 600 nm average film thickness. This coating is chosen to be called porous TiO₂ for the following discussions.

Furtherly, when the maximum Ar pressure (140 sccm) was applied, a completely different morphology was procured as shown in figure III-1e. The corresponding TiO₂ film which consists of nanosize TiO₂ particles, curiously grown with a columnar structure, with a rough surface. The estimated film thickness is now ~700 nm (fig. III-1f). For further discussions, this deposition is referred to highly porous TiO₂.

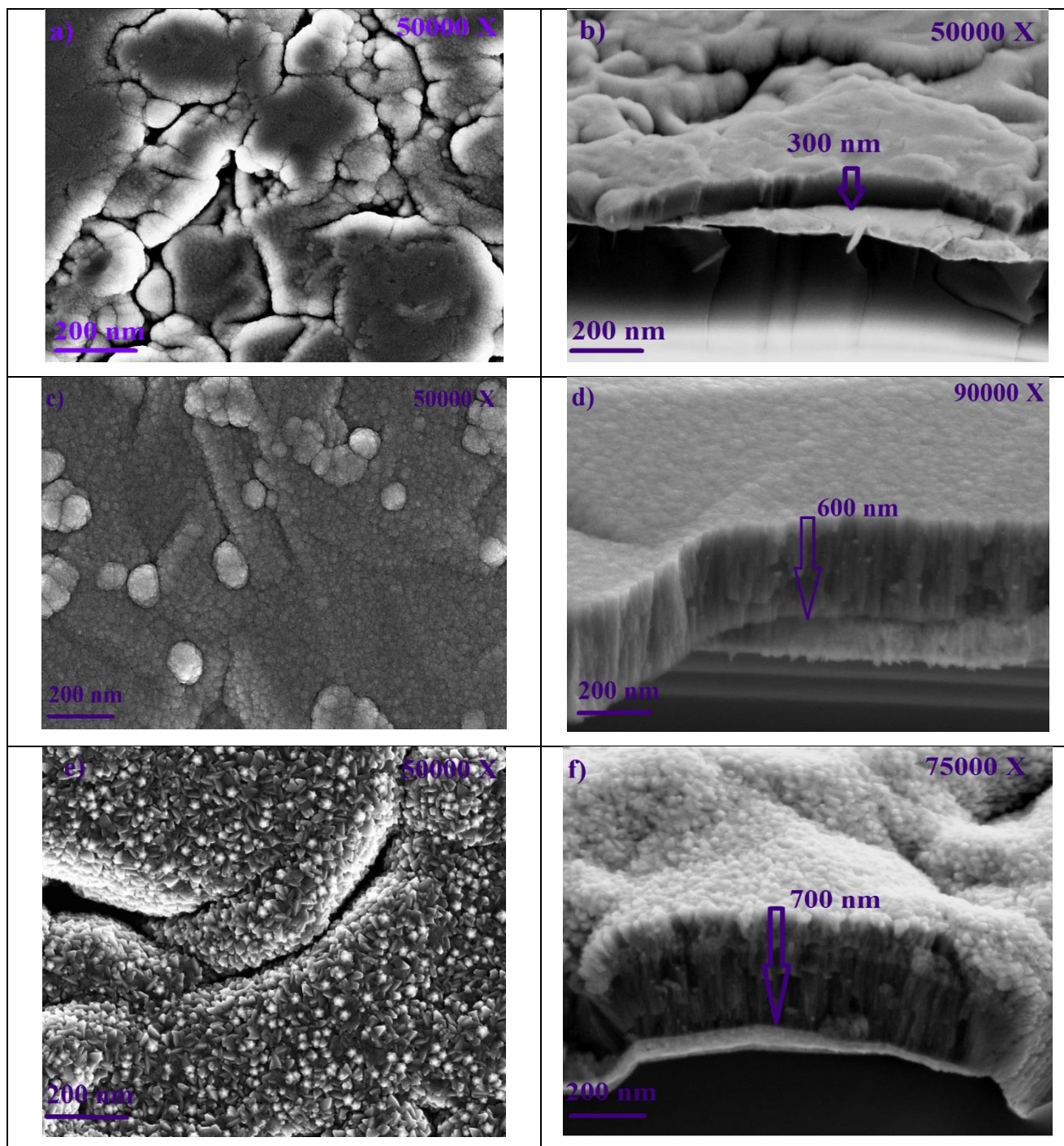


Fig. III-1. FEG-SEM images showing the top view and the cross-section of deposited dense (a, b), porous (c, d) and highly porous (e, f) TiO₂ thin film deposited on the Au coated electrode of quartz resonators by RF reactive sputtering (reactor conditions: RF power 200 W, 0.2 mtorr O₂ pressure, pressure: 3 mtorr for compact TiO₂, 6 mtorr for less porous TiO₂, 14 mtorr for highly porous TiO₂).

The EDX analysis coupled with FEG-SEM observations indicates the presence of Ti and O in all the deposited thin films (Fig. III-2a-c). A small contribution of Au is also detected due to the gold coated electrode of the quartz crystal substrate.

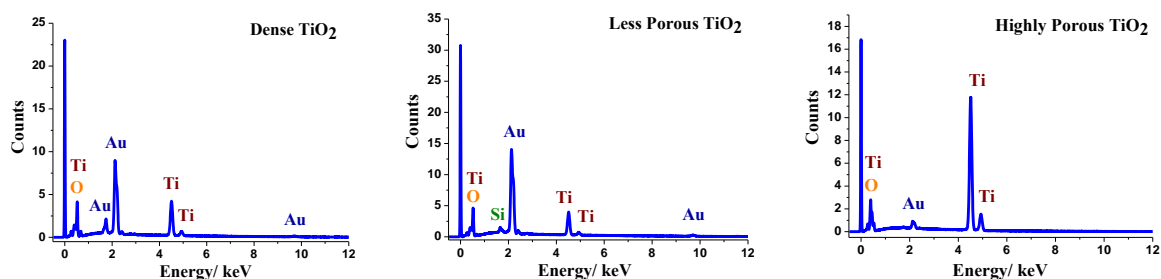


Fig. III-2. Compositional analysis by energy dispersive X-ray (EDX) spectroscopy of a dense (a), porous (b) and highly porous (c) TiO_2 films (obtained by FEG-SEM equipped with an EDX detector) (substrate: gold electrode of the quartz resonator).

In order to estimate the pore morphology of the TiO_2 thin films, as now on called ‘porous’ and ‘highly porous’, they were investigated by HR-TEM (Fig. III-3). Coherent to what was previously shown by SEM-FEG, the image corresponding to porous TiO_2 reveals a film with interconnected narrow cracks between TiO_2 isolated grain islands of ~ 8 - 10 nm. This provides slight intergrain porosity which is dispersed all over the film as illustrated in figures III-3a and III-3c with two different magnifications. By looking the images of ‘highly porous’ TiO_2 (fig. III-3b, III-3d), the growth of the intergrain spaces is easily distinguished: pore volumes of ~ 6 - 8 nm are estimated. Due to the high operating pressure which is applied for their fabrication a well-developed network of intergrain porosity is created which is quite well dispersed all over the films. During the HR-TEM imagery, SAED (selected area (electron) diffraction) was performed to follow the crystallographic state of the film. Since the atomic plan rings, not shown here, were so faint no distance was measurable, this proved the amorphousness of both analysed films.

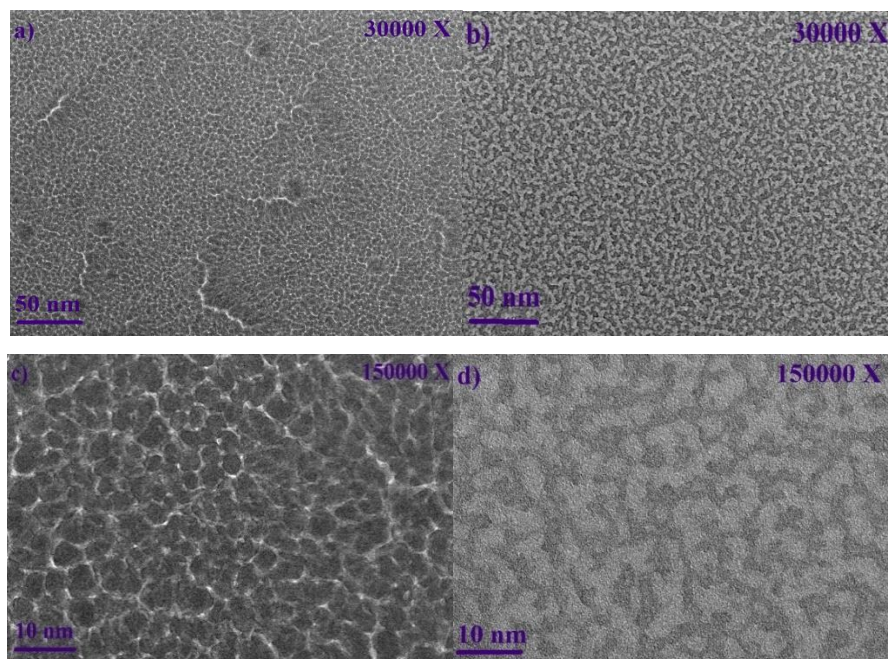


Fig. III-3. HR-TEM images of porous (a, c) and highly porous (b, d) TiO₂ thin films with 30000X and 150000X magnifications.

III. Electrochemical Study of Dense, Porous and Highly Porous TiO₂ Thin Films

The EQCM is a simultaneous measurement of the resonant frequency variations of a quartz resonator determined by QCM during CV measurements. A typical EQCM curve gives the current profile vs potential as well as the simultaneous QCM frequency variation. The quartz resonant frequency variations are converted into mass changes of the electrodes by Sauerbrey relation, i.e. the mass variations of the prepared TiO₂ electrodes during reduction bias and oxidation bias can be monitored.

III-1. Cyclic voltammetry and EQCM study in LiClO₄

The EQCM results of a dense, porous and highly porous TiO₂ film tested at room temperature in 0.5M LiClO₄ aqueous electrolyte are presented in Fig. III-4. The CV curves show a capacitive response in the anodic region whereas the intercalation reaction is observed in the potential range from -0.1 V to -1.1 V vs ECS. An asymmetric voltammogram is obtained with a broad anodic response corresponding to the cation extraction slower than their cathodic insertion at this scan rate value and for the two porous films (Fig. III-4). The capacitive behaviour grows gradually and becomes very well pronounced in the CV response of the highly porous TiO₂ film when compared with the current values of dense and porous films (Fig. III-4). This suggests that the high contribution of surface electroadsorption process which is also

accompanied with the faradaic response (shown by red arrows in Fig. III-4) corresponds to highly porous TiO₂ thin films. Both cathodic and anodic current density of the highly porous film (Fig. III-4c) are higher than those observed for the dense and porous films (Fig. III-4a and III-4b), this may indicate faster cation transfer kinetics. The current values measured are obviously amplified for the very porous films as compared to those obtained for dense and less porous films. The mass variations are also influenced by the presence of the pores (Fig. III-4), and the QCM response is amplified (~ 4 times) in the case of highly porous films. This enhanced behaviour can probably be attributed to the increased specific surface provided by the porous structure, as a result, the pores network provides a better accommodation of the electroactive sites and have an advantageous effect on the species exchange process. The mass responses shown in the reduction branches (Fig. III-4) correspond to the resonant frequency drops of the modified quartz resonators due to the mass increases of the films during reduction bias. In a reverse process, during oxidation bias, the inserted species are expelled out from the film, resulting in a decrease of the electrode mass.

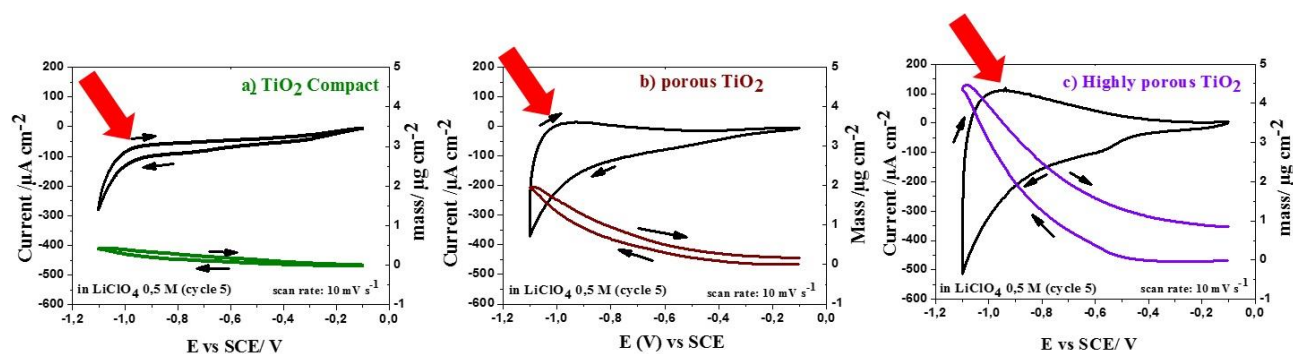


Fig. III-4. Cyclic voltammograms and mass responses obtained simultaneously during the electrochemical cycling for (a) dense, (b) porous and (c) highly porous TiO₂ films deposited on the gold coated electrode of the quartz resonator. Measurements are in 0.5M LiClO₄ aqueous solution with a scan rate of 10 mV s⁻¹.

III-2. Molecular Mass Estimation

The molecular mass of the species involved in the charge compensation process can be calculated roughly. For that, the $F \times \frac{\Delta m}{\Delta q}$ function was estimated $F \times \frac{\Delta m}{\Delta q} = F \frac{\Delta m / \Delta t}{\Delta Q / \Delta t}$ from the

EQCM data. Fig. III-5 depicts the $F \times \frac{\Delta m}{\Delta q}$ variations as a function of the applied potential for

dense, porous and highly porous TiO₂ thin films. According to this calculation, the only close estimation was obtained for the highly porous TiO₂. In this case, a molecular mass value of ~ 6-7 g mol⁻¹ is measured in 0.5 M LiClO₄ aqueous solutions with a scan rate of 10 mV s⁻¹, which is close to the molecular weight of Li⁺. On the contrary, the results of the same calculation give

a mass value of $\sim 1\text{-}2 \text{ g mol}^{-1}$ for dense and $\sim 4 \text{ g mol}^{-1}$ for porous TiO_2 . In these latter cases, the values do not correspond to any of the present species in the electrolyte.

In fact, if there is strictly one species involved, the $F \times \frac{\Delta m}{\Delta q}$ function should be equivalent to the molecular mass of the species transferred. However, for a complex electrochemical system which is in general the case, these values correspond to an average molecular weight related to the various species. Therefore, at this point, it is arguably observed that at this scan rate (10 mV s^{-1}), Li^+ ions are exclusively involved in the charge compensation process for the highly porous TiO_2 films. However, it cannot guarantee neither (i) the absence of any other species involved in the charge compensation process for dense and porous TiO_2 , nor (ii) the absence of any other species aside from Li^+ which cannot be detected at this scan rate for highly porous TiO_2 electrode (such as heavier ions including ClO_4^- , hydrated forms of lithium ions, or free water molecules). Thus, these results show the limitations of the classical EQCM technique: it gives a global response, and does not provide unambiguous information on which of the possible scenarios which can take place. In order to investigate the details which cannot be touched by the classical EQCM method, *ac*-electrogravimetric studies were performed on the different analogues of TiO_2 films.

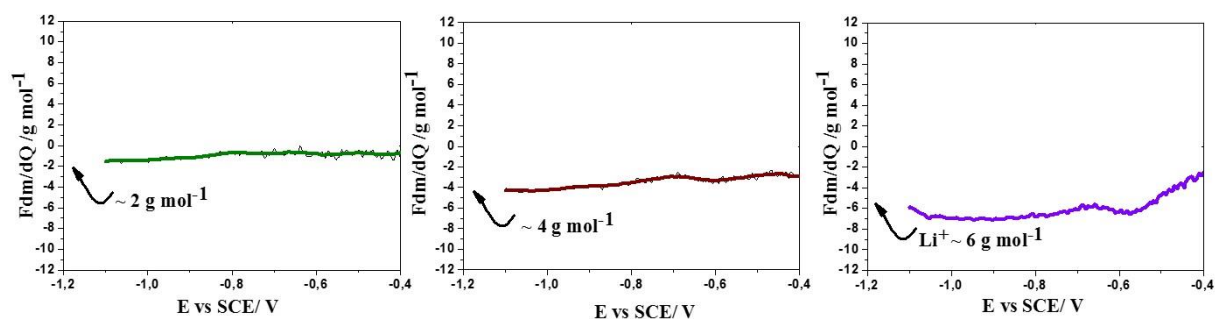


Fig. III-5. $F \times \frac{\Delta m}{\Delta q}$ values corresponding to the average molecular weight of the species involved in the charge compensation process as a function of the potential for (a) dense, (b) porous and (c) highly porous TiO_2 films cycled in 0.5 M aqueous LiClO_4 solutions (obtained from the reduction branch of the EQCM results at a scan rate of 10 mV s^{-1}).

IV. ac-electrogravimetric studies of TiO_2 Thin Films

To be able to have a resolution at the temporal level to deeply explore the intercalation/electroadsorption mechanism, *ac*-electrogravimetry (electrochemical impedance spectroscopy (EIS) coupled with fast QCM) was used to characterize our different TiO_2 films.

In the case of dense TiO₂ films, the response in terms of $\frac{\Delta m}{\Delta E}(\omega)$ transfer function was not sufficient to fairly exploit the experimental results. The reason was attributed to a limited electro activity (both in terms of current and mass responses) and probably a very compact morphological structure which may acts as an efficient barrier against facile exchange of charge species. Consequently, the results presented in the following parts include a comparative study between porous and highly porous TiO₂.

Ac-electrogravimetry measurements were performed in 0.5 M LiClO₄ aqueous solution, 0.5 M NaClO₄ aqueous solution and also in 0.5 M LiClO₄ prepared by propylene carbonate solution. Since the most effective electroactive behaviour was observed for the cathodic potentials (see the pronounced electrochemical response and also the mass variation slope in fig. III-4) stationary potential values from -0.7 V to -1 V vs SCE were chosen for this study.

IV-1. ac-electrogravimetric studies of Porous and Highly Porous TiO₂ Thin Films in 0.5M LiClO₄ aqueous solution

The results of the *ac*-electrogravimetric study of porous and highly porous TiO₂ thin films at -0.9 V vs SCE are summarized from figures III-6 to III-8 and the corresponding parameters in Table III-1.

The charge/potential transfer functions (TFs), $\frac{\Delta q}{\Delta E}(\omega)$ (Fig. III-6a and III-b) permit to separate the ionic contribution without any possibility to identify the ionic species involved. Here, it should be mentioned that the contribution of the parasitic reaction, occurring at low frequencies, was removed for keeping only the ionic transfer response. A large and somehow suppressed loop was obtained for both porous and highly porous TiO₂ thin films without a fair separation. The theoretical functions in Fig. III-6 indicates that there are more than one charged species involved in both analyzed cases (Fig. III-6a and III-b). Actually, the time constants corresponding to each ionic transfer seem to be very close to each other. It is to be noted that the $\frac{\Delta q}{\Delta E}(\omega)$ response of the highly porous film is clearly magnified (2 times) (Fig. III-6b), compared to the response of a porous TiO₂ film (Fig. III-6a). At this level, it is impossible to distinguish between the anion and the cation contributions and to determine the nature of the ionic species involved. Nevertheless, the K_i and G_i constants were determined for three ions in each of these films (Table III-1) and were used in the following fittings.

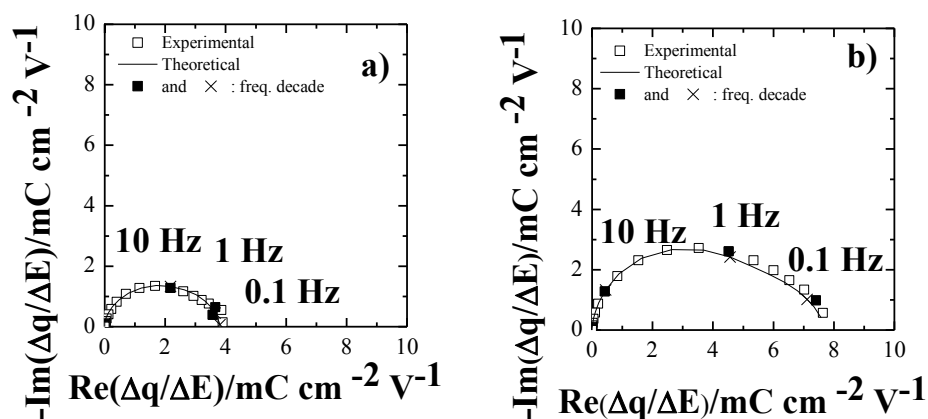


Fig. III-6. Charge/potential transfer functions, $\frac{\Delta q}{\Delta E}(\omega)$ for (a) porous TiO_2 and (b) highly porous TiO_2 films measured in 0.5 M LiClO_4 aqueous electrolyte at -0.9 V vs SCE (both experimental and theoretical curves are given).

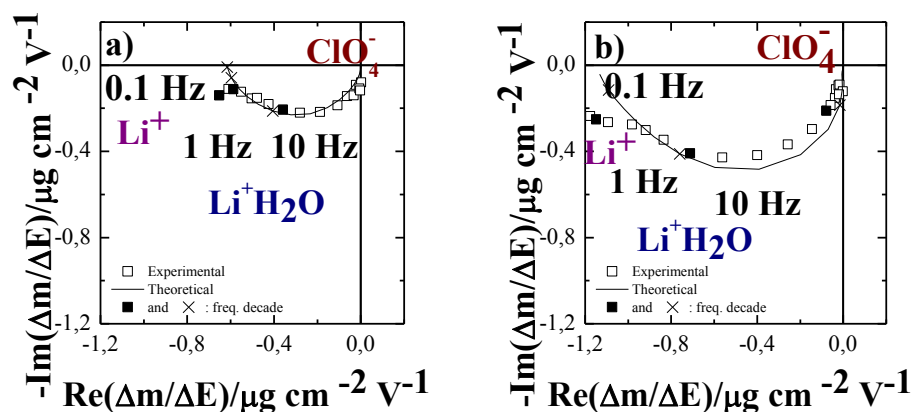


Fig. III-7. Mass/potential transfer functions, $\frac{\Delta m}{\Delta E}(\omega)$ for (a) porous TiO_2 (involving three species, specifically Li^+ , $\text{Li}^+\cdot\text{H}_2\text{O}$ and ClO_4^-) and (b) highly porous TiO_2 films (involving the same three species). The measurements are performed in 0.5 M LiClO_4 aqueous electrolyte at -0.9 V vs SCE (both experimental and theoretical curves are given).

Furtherly, to identify and clarify the contribution of the charged and also the uncharged species (*i.e.* free electrolyte molecules), the mass/potential transfer functions, $\frac{\Delta m}{\Delta E}(\omega)$ are scrutinized.

In the mass/potential TF, $\frac{\Delta m}{\Delta E}(\omega)$, (Fig. III-7a and III-7b), one big loop appears in the third quadrant at medium and low frequencies (MF and LF). This loop can be attributed to either two or three species with time constants which are not sufficiently different from each other. The loops in the third quadrant are usually characteristic for cation contributions or free solvent molecules following the same flux direction. For the exact identification of these loops several

configurations were tested using theoretical functions (theoretical chapter) to determine the exact contribution of each species. The mass response of both porous and highly porous TiO₂ thin films were fitted by considering three species: cation 1 ($c_1 = Li^+.H_2O$), cation 2 ($c_2 = Li^+$) and the anion ($a = ClO_4^-$).

The slight contribution of the anion appears at relatively HF, followed by $Li^+.H_2O$ at MF. Here, Li^+ are the slowest species transferred in both porous films since they are detected at lower frequency region in Fig. III-7a or III-b. It is important to note that the corresponding theoretical equation involves the molecular weight of the ionic and/or nonionic species, providing their identification by their molecular weight. Therefore, cations or their hydrated forms can be detected with an estimation of the hydration level (e.g. cation 1 ($c_1 = Li^+.H_2O$ n = 1), cation 2 ($c_2 = Li^+$)). Since the bulk hydration numbers for Li^+ ions is high, $n \sim 7-8$ [22], the cation 1 ($c_1 = Li^+.H_2O$ n = 1) detected in our study can be considered as partially dehydrated.

	f_i (Hz)	Cap_i (mF cm ⁻²)	K_i (s cm ⁻¹)	G_i (mol s ⁻¹ cm ⁻² V ⁻¹)	$Rt_i = \frac{1}{FG_i}$ (Ω cm ²)	$\frac{\Delta C_i}{\Delta E}(\omega) = -\frac{G_i}{K_i}$ (mol cm ⁻³ V ⁻¹)
Porous TiO₂						
c_1 (cation 1) : $Li^+. H_2O$ $7+18 \text{ g mol}^{-1}$	6	2,55	$22,6 \times 10^{-4}$	$9,95 \times 10^{-7}$	10,41	$-4,4 \times 10^{-4}$
c_2 (cation 2): Li^+ 7 g mol^{-1}	1	1,16	$3,77 \times 10^{-4}$	$0,75 \times 10^{-7}$	137,44	-2×10^{-4}
a (anion): ClO_4^- 96 g mol^{-1}	12.5	0,12	$47,1 \times 10^{-4}$	$-0,99 \times 10^{-7}$	104,72	$0,21 \times 10^{-4}$
Highly Porous TiO₂						
c_1 (cation 1) : $Li^+. H_2O$ $7+18 \text{ g mol}^{-1}$	3.5	5	$15,4 \times 10^{-4}$	11.5×10^{-7}	8,98	$-7,5 \times 10^{-4}$
c_2 (cation 2): Li^+ 7 g mol^{-1}	0,25	2,36	$1,1 \times 10^{-4}$	0.38×10^{-7}	269,27	$-3,5 \times 10^{-4}$
a (anion): ClO_4^- 96 g mol^{-1}	12.5	0,32	55×10^{-4}	$-2,64 \times 10^{-7}$	39,27	0.48×10^{-4}

Table III-1. Estimated values for K_i (kinetics of transfer), G_i (inverse of the transfer resistance), Rt_i (transfer resistance) and $-G_i/K_i$ (the concentration change measured per potential unit) parameters extracted from the fitting results of *ac*-electrogravimetry measurements in 0.5M LiClO₄ at -0.9 V vs. SCE for porous and highly porous TiO₂ films.

The partial mass/potential TFs were analyzed to validate our previous hypothesis involving three different species for porous and highly porous films. Partial mass/potential TFs are estimated for these films as shown in figure III-8, by removing the c2 contribution, calculating $\frac{\Delta m}{\Delta E} \Big|_{th}^{c1a}$ (fig. III-8a and III-d) or by removing the c1 contribution, calculating $\frac{\Delta m}{\Delta E} \Big|_{th}^{c2a}$ (fig. III-8b and III-e) or by removing the anion contribution, calculating $\frac{\Delta m}{\Delta E} \Big|_{th}^{c1c2}$ (fig. III-8c and III-f). All these partial mass/potential TFs exhibited a good agreement between the theoretical and experimental data. These TFs provide a crosscheck for validating the hypothesis involving multiple species and for obtaining a better separation of the various contributions.

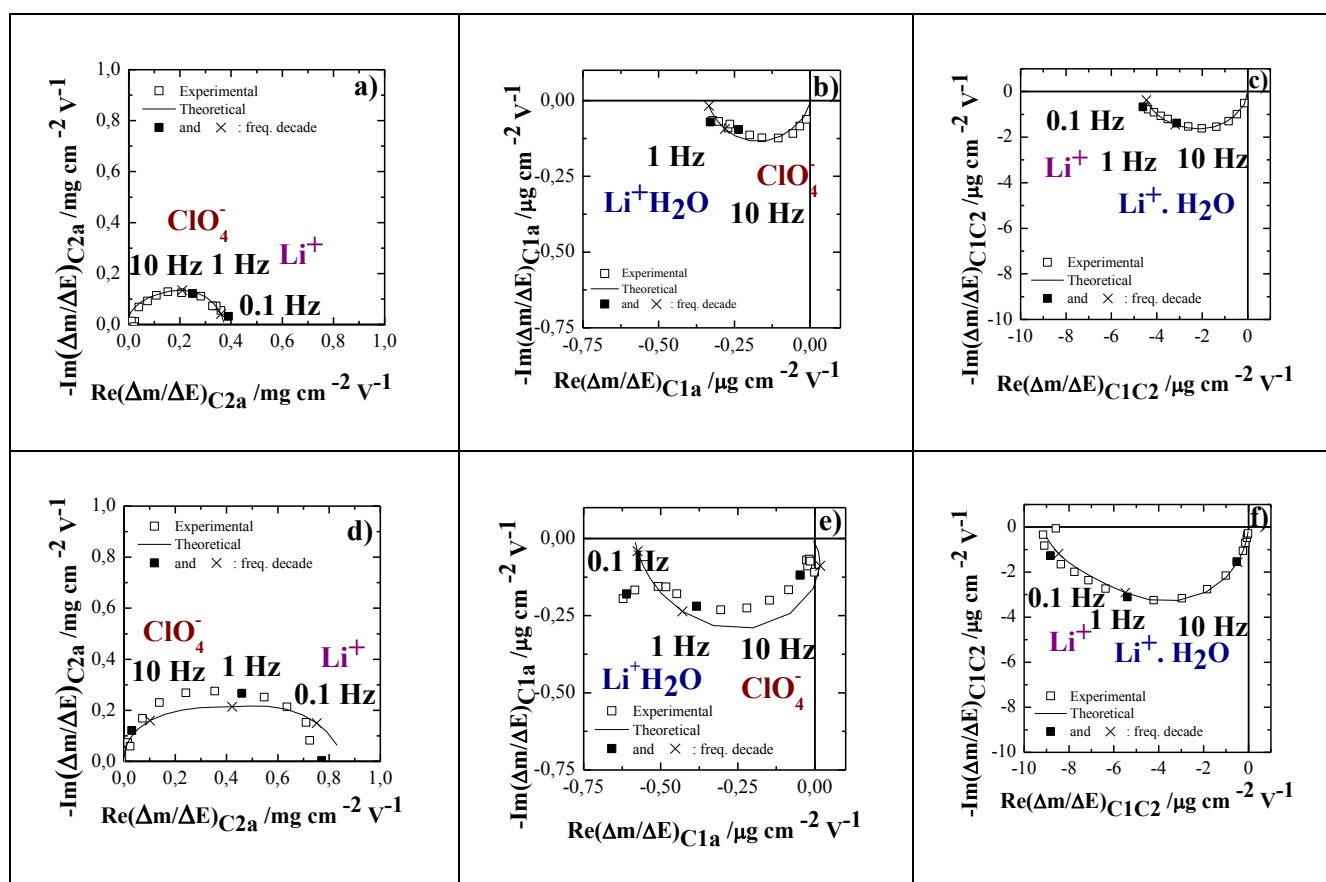


Fig. III-8. Three partial mass/potential transfer functions, for porous (a, b and c) and highly porous (d, e and f) TiO₂ films, measured in 0.5 M LiClO₄ aqueous electrolyte at -0.9 V vs SCE (both experimental and theoretical curves are given).

The K_i and the G_i constants are determined by fitting the experimental data using the theoretical functions for $\frac{\Delta q}{\Delta E}(\omega)$, $\frac{\Delta E}{\Delta I}(\omega)$, and $\frac{\Delta m}{\Delta E}(\omega)$ with the criteria of achieving a good agreement between the experimental and theoretical data (strictly for all of the TFs, including partial mass/potential TFs). The equivalent weight of the charged and uncharged species is determined by the electrogravimetric TF, $\frac{\Delta m}{\Delta E}(\omega)$ which provide the identification of the species by

estimating the molar weight, m_i (Table III-1). The G_i parameters permit to calculate the transfer resistance, Rt_i , for each species (theoretical chapter). The kinetic constants, K_i , obtained from *ac*-electrogravimetry at -0.9V vs SCE reveal the transfer rates of species at the electrode/electrolyte interfaces. For porous and highly porous TiO₂ thin films, similarly: (i) ClO_4^- species contribute at high frequencies (the fastest species), (ii) $Li^+.H_2O$ appear at the intermediate frequencies, and (iii) Li^+ appears at low frequencies (the slowest species). It is to be noted that the G_i sign for the anion is negative this means that they are involved in the opposite flux of the two cations. Here, it could be hypothesized that the surface is initially positively charged (in a basic pH), so the negatively charged anions are predominantly adsorbed at the surface, these anions are then expelled so that positively charged cations could be exchanged at the interface.

The G_i values determined from the *ac*-electrogravimetry study are related to the transfer resistance, ($Rt_i = \frac{1}{FG_i}$) which can explain the ease or the difficulty of the ionic/non-ionic transfer at the electrode/electrolyte interface. The transfer resistance, Rt_i , values follow the order which is the inverse of that observed for the kinetics parameters of transfer, K_i (Table III-1). In particular, for both porous and highly porous TiO₂ films, it pursues the order: $Rt_i (Li^+) > Rt_i (ClO_4^-) > Rt_i (Li^+.H_2O)$.

There are two cationic species (Li^+ and $Li^+.H_2O$) detected in both types of films. The kinetic parameters and resistance values for their interfacial transfer can be compared in Table III-1. One of the noticeable differences is that the $Rt_i (ClO_4^-)$ value for porous TiO₂ films is much higher than that for a highly porous film. This suggests that the transfer of perchlorate species at the interfaces is relatively easier in highly porous TiO₂ thin films than in porous counterparts. Thus, the transfer of large anions is favored when TiO₂ thin films are more porous. Based on the K_i values, the Li^+ species are transferred slowly in both types of films. This could be related to the ease of dehydration, the hydrated Li^+ transfer is easier compared to fully dehydrated Li^+ as the latter needs more energy to lose its solvation shell. The easiest species to transfer is $Li^+.H_2O$ and its transfer is slightly slower in porous films. These results indicate that highly porous films facilitate both ClO_4^- and $Li^+.H_2O$ transfer compared to porous TiO₂ thin films.

Another important parameter to compare is the $\frac{\Delta C_i}{\Delta E} (\omega \rightarrow 0) = -\frac{G_i}{K_i}$ value which can be considered as the quantity of species transferred per potential unit at low frequencies of

modulation. It is evident that the quantity of the cationic species transferred per potential unit is clearly higher in highly porous TiO₂ thin films than in porous films, a factor two is obtained in this case. Yet, the two films are similar in a way that for both porous and highly porous films, the higher capacitance related to the cations is obtained for $Li^+.H_2O$. Also, the quantity of the Li^+ transferred per potential unit is remarkably higher for porous films, which is relevant by the fact that the pore volume is increased. The contribution of anions is rather small based on the quantity transferred per potential unit (see Table III-1) ten times less compared to Li^+ contribution. This observation is contradictory with the kinetical information obtained for the anion. Despite the fact that the anions are more rapid compared to the cationic species in this study, only a small quantity of them are transferred at the interface. This is probably due to the large ionic radius of ClO_4^- anions that prohibit their involvement in the charge compensation process of these films in a large quantity. It could be speculated that anions are rapidly transferred as they interact only with the film surface and for this reason, a saturation state is rapidly reached. Key parameters were also obtained for each potential as presented in figure III-10.

The characteristic frequencies, f_i , extracted from *ac*-electrogravimetric results reveal the transfer rates of species at the electrode/electrolyte interfaces (fig III-10a and III-10e). Both for porous and highly porous TiO₂ thin films, similarly: (i) ClO_4^- species contribute at high frequencies (the fastest species), the results of our study for highly porous film show the presence of anions only at two potentials (ii) hydrated lithium ion ($Li^+.H_2O$), appear at the intermediate frequencies, and (iii) Li^+ appear at low frequencies (the slowest species).

A very useful information that could be obtained is the instantaneous capacitance, Cap_i , of each species shown in Fig. III-10b and III-10f. This parameter could indeed be defined as the capacity of the film to accommodate each of the previously involved species as a consequence of a potential perturbation given at each applied potential. Based on these values porous TiO₂ film have the highest capacitance for transferring the cationic species (Li^+ and $Li^+.H_2O$) specially $Li^+.H_2O$ and only a small capacitance corresponds to the anions (fig. III-10b). Similarly, in highly porous TiO₂ the highest capacitance values are attributed to both Li^+ and $Li^+.H_2O$. Moreover, compared to less porous film, the capacitances of these cationic species are relatively higher. This could be attributed to the larger surface area created by the pore volumes. Also, similar to porous TiO₂ the smallest capacitance belongs to ClO_4^- anions (fig. III-10f).

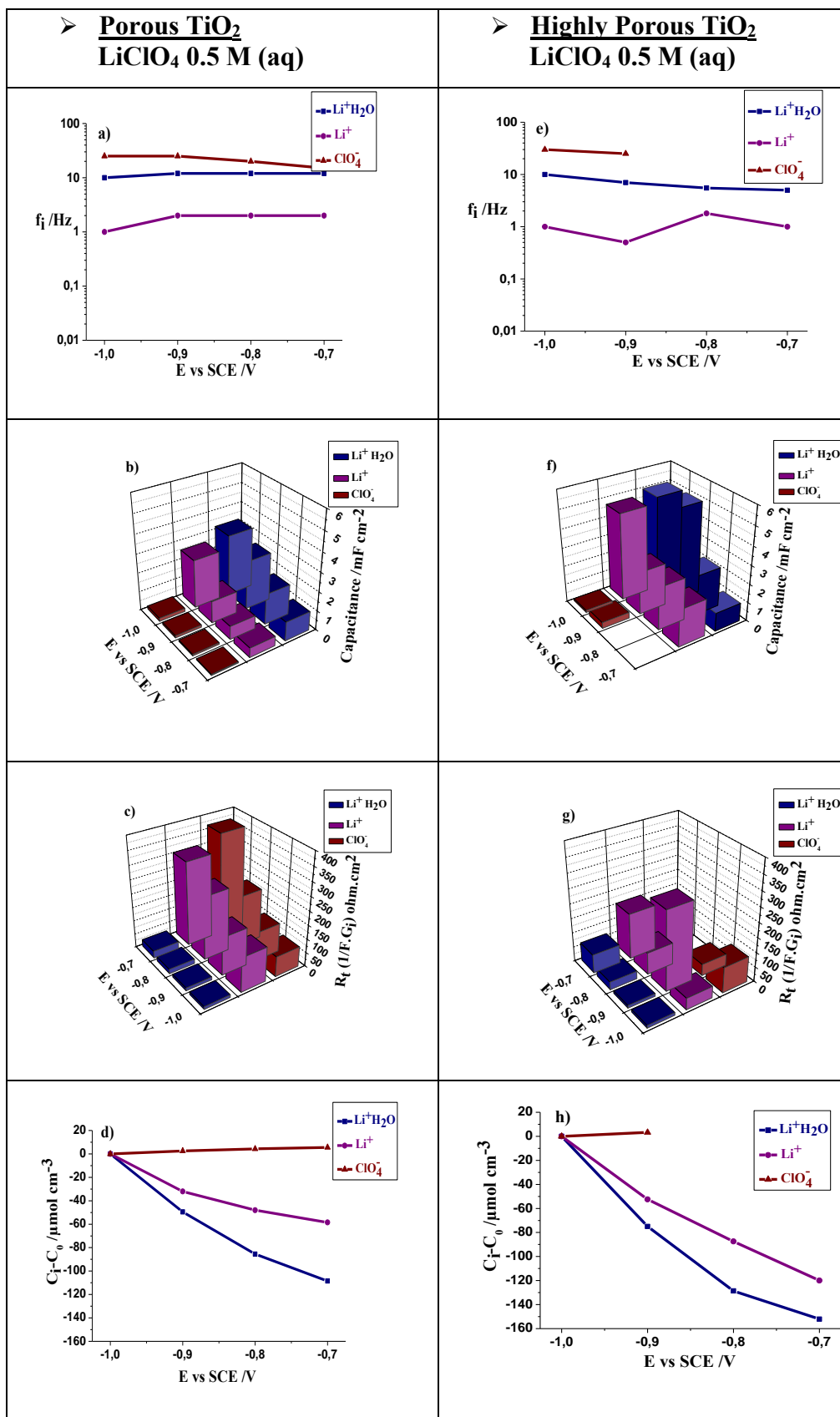


Fig. III-10. Evolution of different parameters as a function of potential including: the characteristic frequency of species, f_i , the instantaneous capacitance of species, Cap_i , the transfer resistance of species, R_{ti} , and the relative concentration of species ($C_i - C_0$) for porous (a-d) and highly porous (e-h) TiO₂ films in aqueous 0.5M LiClO₄.

The evolution of the transfer resistance, Rt_i , as a function of the potential is shown in fig. III-10c and III-10g. The observation could be classified as the following: (i) in both types of films studied, the lowest transfer resistance belongs to $Li^+.H_2O$, contrary to (ii) the transfer of the sole Li^+ is more difficult compared to $Li^+.H_2O$, this could suggest that the transfer of small Li^+ ions is facilitated when they are hydrated. (iii) Large ClO_4^- anions are the most difficult ions to be transferred at the interface of porous TiO_2 electrode, their transfer resistance decreases in highly porous TiO_2 . This suggests that the developed surface area due to the accumulated pores in this latter film favors a larger charged species transfer.

To quantify the role of each species, $\left. \frac{\Delta C_i}{\Delta E} \right|_{\omega \rightarrow 0} = -\frac{G_i}{K_i}$ has been estimated as a function of the

applied potential. The integration of $\left. \frac{\Delta C_i}{\Delta E} \right|_{\omega \rightarrow 0}$ against potential gives the insertion isotherm.

Figure III-10d and III-10h present the relative concentration change, $C_i - C_0$, as a function of E for Li^+ , $Li^+.H_2O$ and ClO_4^- species for porous and highly porous TiO_2 films. A significant difference is observed in the relative concentration change of the species when TiO_2 films are highly porous. Both the $(C_i - C_0)$ values for Li^+ and $Li^+.H_2O$ cations are magnified for highly porous TiO_2 films. The $(C_i - C_0)$ values for Li^+ present quite a difference between the two films, it is actually ~ 2 times higher in highly porous film compared to the porous TiO_2 . It is important to note that the kinetics of transfer values for Li^+ species were slower in the studied films compared to $Li^+.H_2O$, also their transfer resistance was higher compared to other species. This point underlines the differences between kinetics and thermodynamics related to the transferred species. However, their final concentration variation is ~ 2 times higher in highly porous films than that in the porous films. Despite the differences in their dynamics of transfer, the final amplified concentration variations in highly porous TiO_2 thin films corresponds to cationic species. It should be noticed that these subtleties are underlined for the very first time for these two different morphologies of amorphous TiO_2 films. The $Li^+.H_2O$ ions are transferred easily and in higher quantities when TiO_2 films are more porous. The $(C_i - C_0)$ value for ClO_4^- anions remains low compared with the cationic species in both types of films. Thus, only a small quantity of the anions are transferred, even if the kinetics of transfer is fast. To conclude this section, the contribution of the charged species is certainly magnified in highly porous TiO_2 films compared to the porous films. This qualitative and quantitative study of ionic and non-ionic species contribution in the charge compensation process, together with dynamic

information of their interfacial transfer further proves the advantageous nature of porous structure TiO₂ films for storage applications. The beneficial aspect of highly porous TiO₂ films is more likely related to the better accommodation of both Li⁺ and Li⁺.H₂O cations. Particularly, hydrated lithium species Li⁺.H₂O are transferred rapidly and easily at the highly porous electrode/electrolyte interfaces, and their concentration variations in the electrode is significantly increased with respect to that in their porous analogues.

IV-2. ac-electrogravimetry studies of Porous and Highly Porous TiO₂ Thin Films in 0.5M aqueous solution of NaClO₄

Ac-electrogravimetry measurements were then performed in 0.5 M NaClO₄ aqueous solution at the stationary potential values from -0.7 V to -1 V vs SCE. Prior to discussing the ac-electrogravimetry results in this section, the classical EQCM results of porous and highly porous TiO₂ film tested at room temperature in aqueous 0.5M NaClO₄ electrolytes are presented in Fig. III-11. Similar to the CV curves observed in LiClO₄, the CVs presented in figure III-11 show a capacitive response in the anodic region whereas the redox reaction which is observed in the potential range from -0.1 V to -1.1 V vs ECS. The same asymmetric pattern for the CV is obtained with a broad anodic response.

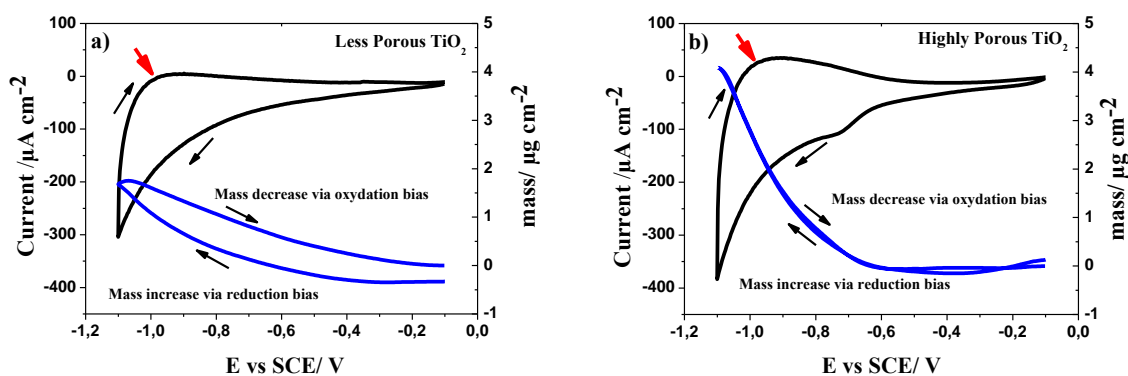


Fig. III-11. Electrogravimetric responses obtained simultaneously during the electrochemical cycling of (a) porous and (b) highly porous TiO₂ films deposited on the gold electrode of a quartz resonator. Measurements are in 0.5M NaClO₄ aqueous solution with a scan rate of 10 mV s⁻¹.

The capacitive behaviour is more pronounced in the CV curve of the highly porous TiO₂ film compared with that for porous films (Fig. III-11). This proposes a high contribution of surface electroadsorption process which is also accompanied with a faradaic response (shown by red arrows in Fig. III-11) in the case of highly porous TiO₂ thin films. Both cathodic and anodic current density of the higher porous film are higher than those observed for less porous films, this indicates faster ions transfer kinetics. The mass variations are also influenced by the

presence of the pores (blue curves in Fig. III-11), and the QCM response is amplified (~ 2 times) in the case of highly porous film. Moreover, in highly porous TiO_2 , the mass response is completely superimposed in the two directions which indicates a completely reversible process. This enhanced behaviour can probably be attributed to the increased specific surface area and the porous structure. The network of the pores provides a wide accessibility of electroactive sites and has an advantageous effect on the species exchange process. The results of the *ac*-electrogravimetry study of porous and highly porous TiO_2 thin films at -0.9 V vs SCE in aqueous 0.5 M NaClO_4 electrolyte are summarized in figures III-12, III-13 and Table III-2.

The charge/potential transfer functions (TFs), $\frac{\Delta q}{\Delta E}(\omega)$, (Fig. III-12a and III-12b) permit to separate the ionic contribution without any possibility to identify the ionic species involved. Here, the contribution of the parasitic reaction, occurring at low frequencies, was removed for keeping only the ionic transfer response. Similar to what was previously observed in aqueous 0.5 M LiClO_4 , a large and quite suppressed loop was observed specially in the case of highly porous TiO_2 thin films without an easy separation. The theoretical functions in Fig. III-12 indicated that there are more than one charged species involved in both cases (Fig. III-12a and III-12b). Indeed, the time constants corresponding to each ionic transfer seem to be very close to each other. It is to be noted that the $\frac{\Delta q}{\Delta E}(\omega)$ response of the highly porous film is magnified almost 3 times (Fig. III-12b), compared to $\frac{\Delta q}{\Delta E}(\omega)$ of a porous film. At this level, it is impossible to distinguish between the anion and the cation contributions and to determine the nature of the ionic species involved. Furtherly, the K_i and G_i constants were determined for two species in case of porous and three species in case of highly porous TiO_2 (Table III-2) and they were used in the following fittings.

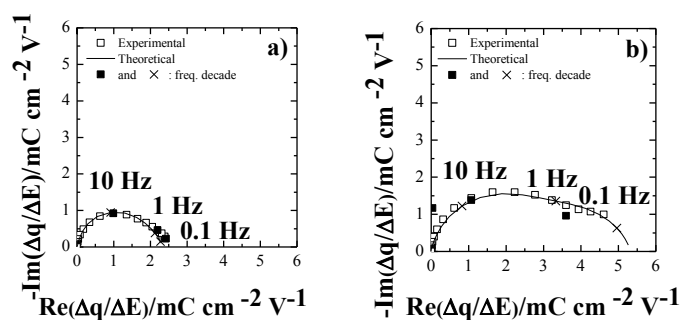


Fig. III-12. Charge/potential transfer functions, $\frac{\Delta q}{\Delta E}(\omega)$ for (a) porous TiO_2 and (b) highly porous TiO_2 films measured in 0.5 M NaClO_4 aqueous electrolyte at -0.9 V vs SCE (both experimental and theoretical curves are given).

Furtherly, to identify and clarify the contribution of the charged and also the uncharged species (*i.e.* free electrolyte molecules), the mass/potential transfer functions, $\frac{\Delta m}{\Delta E}(\omega)$ are determined.

In the mass/potential TF, $\frac{\Delta m}{\Delta E}(\omega)$, Fig. III-13a and III-13b, one loop appears in the third quadrant at medium and low frequencies (MF and LF). This loop can be attributed to either two species or to three species where their time constants are not sufficiently different from each other. Mostly, the loops in the third quadrant are characteristic for cation contributions or free solvent molecules in the same flux direction. For the exact identification of these loops several configurations were tested using theoretical functions (theoretical chapter) to determine the exact contribution of each species. The mass response of porous TiO₂ were fitted by considering only two species including a cation ($c1 = Na^+.H_2O$), and an anion ($a = ClO_4^-$). In the case of highly porous TiO₂, the mass responses were fitted by considering three species cation 1 ($c1 = Na^+.H_2O$), cation 2 ($c2 = Na^+$) and also free solvent molecule ($s = H_2O$).

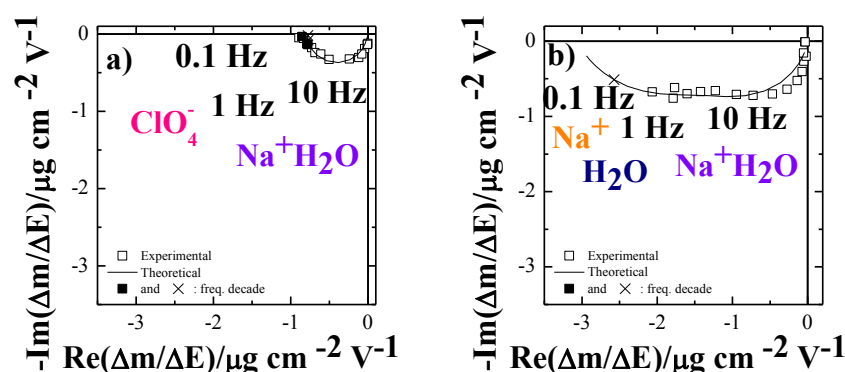


Fig. III-13. The mass/potential transfer functions, $\frac{\Delta m}{\Delta E}(\omega)$ for (a) less porous TiO₂ (involving two species, specifically $Na^+.H_2O$ and ClO_4^-) and (b) highly porous TiO₂ films (involving three species, specifically Na^+ , $Na^+.H_2O$ and ClO_4^-), respectively. The measurements are performed in aqueous 0.5 M NaClO₄ electrolyte at -0.9 V vs SCE (both experimental and theoretical curves are given).

According to f_i values presented in table III-2, in porous TiO₂ the hydrated sodium appears at MF and the anion is the slowest species appearing at relatively LF. For highly porous TiO₂, the $Na^+.H_2O$ is identified at MF and both Na^+ and H_2O appear only at LF.

For highly porous TiO₂, the partial mass/potential TFs were analyzed to validate our previous hypothesis involving three different species for these films, respectively. Partial mass/potential TFs were estimated for these films (not presented here), by removing the $c2$ contribution,

calculating $\left. \frac{\Delta m}{\Delta E} \right|_{th}^{c1s}$ or by removing the $c1$ contribution, calculating $\left. \frac{\Delta m}{\Delta E} \right|_{th}^{c2s}$. These partial

mass/potential TFs exhibited a good agreement between the theoretical and experimental data. These TFs validate the hypothesis involving multiple species and they help to obtain a better separation of the various contributions.

	f_i (Hz)	Cap_i (mF cm ⁻²)	K_i (s cm ⁻¹)	G_i (mol s ⁻¹ cm ⁻² V ⁻¹)	$Rt_i = \frac{1}{FG_i}$ (Ω cm ²)	$\frac{\Delta C_i}{\Delta E}(\omega) = -\frac{G_i}{K_i}$ (mol cm ⁻³ V ⁻¹)
Porous TiO₂						
c_1 (cation 1) : $Na^+ \cdot H_2O$ $23+18 \text{ g mol}^{-1}$	6	2,2	$22,6 \times 10^{-4}$	$8,6 \times 10^{-7}$	12	$-3,8 \times 10^{-4}$
a (anion): ClO_4^- 96 g mol^{-1}	1	0,14	$3,77 \times 10^{-4}$	$-0,094 \times 10^{-7}$	1100	$0,25 \times 10^{-4}$
Highly Porous TiO₂						
c_1 (cation 1) : $Na^+ \cdot H_2O$ $23+18 \text{ g mol}^{-1}$	6	3,17	$26,4 \times 10^{-4}$	$12,4 \times 10^{-7}$	8,35	$-4,7 \times 10^{-4}$
(cation 2): Na^+ 23 g mol^{-1}	0,35	2,16	$1,54 \times 10^{-4}$	$0,49 \times 10^{-7}$	210,37	$-3,2 \times 10^{-4}$
s (solvent): H_2O 18 g mol^{-1}	0,2	-	$0,88 \times 10^{-4}$	$0,83 \times 10^{-7}$	124	$-9,5 \times 10^{-4}$

Table III-2. Estimated values for K_i (kinetics of transfer), G_i (inverse of the transfer resistance), Rt_i (transfer resistance) and $-G_i/K_i$ (the quantity transferred per potential unit) parameters extracted from the fitting results of *ac*-electrogravimetric measurements in 0.5M NaClO₄ aqueous electrolyte at -0.9 V vs. SCE for porous and highly porous TiO₂ films.

The K_i and G_i constants are determined by fitting the experimental data using the theoretical functions for $\frac{\Delta q}{\Delta E}(\omega)$, $\frac{\Delta E}{\Delta I}(\omega)$, and $\frac{\Delta m}{\Delta E}(\omega)$. The kinetic constants of transfer, K_i , obtained from *ac*-electrogravimetry at -0.9V vs SCE reveal the transfer rates of species at the electrode/electrolyte interfaces. For porous TiO₂ thin film, similarly: (i) $Na^+ \cdot H_2O$ species are faster, they appear at the intermediate frequencies (ii) ClO_4^- species contribute at low frequencies (the slowest species) and for highly Porous TiO₂ films: (i) $Na^+ \cdot H_2O$ is relatively fast and appear at the intermediate frequencies, (ii) both Na^+ and free solvent molecules appear at low frequencies.

The G_i values determined from the *ac*-electrogravimetric study are correlated to the transfer resistance, ($Rt_i = \frac{1}{FG_i}$). The transfer resistance Rt_i values follow the order which is the inverse

of that observed for the kinetics parameters (K_i) (Table III-2). Specifically, for the porous film $Rt_i (ClO_4^-) \gg Rt_i (Na^+.H_2O)$, this clearly suggests that $Na^+.H_2O$ are the easiest species to be exchanged at the interface contrary to the high transfer resistance of the anions. In the case of highly porous TiO_2 , the following order persists: $Rt_i (Na^+) > Rt_i (H_2O) > Rt_i (Na^+.H_2O)$. This suggests that the Na^+ species are not easily transferred slowly in this film and that $Na^+.H_2O$ are transferred easily. Their transfer is facilitated compared to porous TiO_2 .

The instantaneous capacitance values, Cap_i , are also presented in table III-2. For porous TiO_2 the major capacity is attributed to $Na^+.H_2O$ and in the case of highly porous TiO_2 both cationic species $Na^+.H_2O$ and Na^+ have high capacitances. At this potential, the instantaneous capacitance attributed to the $Na^+.H_2O$ ions is higher when TiO_2 film is highly porous: a factor 1.5 times is estimated here.

Another important parameter to compare is the $\frac{\Delta C_i}{\Delta E} (\omega \rightarrow 0) = -\frac{G_i}{K_i}$ value which can be

considered as the quantity of the species transferred per potential unit at low frequencies of modulation. As previously explained, it is related to the capability to store charged or uncharged species. Particularly in highly porous TiO_2 the quantity of both cationic species and free solvent molecules transferred per potential unit are much higher. In porous TiO_2 , only a minor quantity of anions can be transferred and the hydrated sodium is the major quantity of charged species stored. Then, pertinent parameters, listed previously, were estimated over the potential as shown in figure III-14.

The characteristic frequencies, f_i , extracted from *ac*-electrogravimetric results reveal the transfer rates of species at the electrode/electrolyte interfaces (fig III-14a and III-14e). For porous TiO_2 : (i) $Na^+.H_2O$ are considered to be fast with a middle frequency contribution, (ii) ClO_4^- are the slowest species appearing at low frequencies. In highly porous TiO_2 , the anions do not participate but: (i) hydrated sodium ions $Na^+.H_2O$, appear at the intermediate frequencies, (ii) Na^+ ions are followed closely by H_2O molecules as the slowest species, appearing at low frequencies.

It is also interesting to look into the variation of the instantaneous capacitance, Cap_i , of each species as shown in Fig. III-14b and III-14f. For porous TiO_2 films, the high capacitance value belongs to $Na^+.H_2O$ contrary to minor values obtained for ClO_4^- . In the case of high porous TiO_2 films, given in figure III-14f, both of the involved cationic species including Na^+ and

$Na^+ \cdot H_2O$ have high capacitance values. For $Na^+ \cdot H_2O$ in highly porous TiO_2 , the capacitance values stand relatively higher compared to porous TiO_2 .

The evolution of transfer resistance, R_{ti} , as a function of potential is shown in fig. III-14c and III-14g. In porous TiO_2 (i) the lowest transfer resistance belongs to $Na^+ \cdot H_2O$ and (ii) the highest to ClO_4^- . In highly porous TiO_2 , (i) the easiest transfer happens for $Na^+ \cdot H_2O$ (ii) the transfer of Na^+ ions is also considered to be relatively easy and (iii) the highest resistance of transfer in this films is related to the free solvent molecules. This demonstrates the preferable transfer of cationic species.

The relative concentration change, $(C_i - C_0)$ as a function of potential for porous TiO_2 is shown in figure III-14d in which an important quantity of $Na^+ \cdot H_2O$ are favorably transferred while the quantity of perchlorate anions remains negligible. Therefore, in this film both kinetics (f_i vs E), (R_{ti} vs E) and thermodynamics ($C_i - C_0$ vs E) aspects are in relatively good agreement. The same concentration profile for highly porous TiO_2 shows the important and close quantity of all the involved species being transferred. While from a kinetics point of view the free solvent molecules are slower and their transfer resistance values are higher than those of Na^+ or $Na^+ \cdot H_2O$, the concentration profile shows a large contribution of the free solvent molecules (Fig. III-14h). This observation reveals that free solvent molecules even indirectly contribute in the charge compensation process and they are probably transferred by an electrodragging process. At this point, it is interesting to note the main differences between the two studied electrolytes. More precisely, by comparing first the porous TiO_2 in both electrolytes one could notice the kinetical differences, while ClO_4^- anions are the rapidest species in $LiClO_4$ electrolyte they are the slowest in $NaClO_4$ medium, furthermore, both solvated and desolvated cations participate in $LiClO_4$ although the presence of only solvated cations are detected in $NaClO_4$. Also thermodynamically, from the concentration variation profiles it is noted that the main population of species transferred belongs to both Li^+ and $Li^+ \cdot H_2O$ while in $NaClO_4$ the major species transferred at the interface are uniquely $Na^+ \cdot H_2O$. Then, with an overview through the results obtained for highly porous TiO_2 in $LiClO_4$ the involvement of fast anionic species is detected along with Li^+ and $Li^+ \cdot H_2O$ which participate more slowly, on the other hand, in $NaClO_4$ there is no trace of anions the rapidest species are $Na^+ \cdot H_2O$ and there is also the participation of Na^+ and free solvent molecules each separately. Thermodynamically, the concentration variation profiles in $LiClO_4$ show that the most population of species willing to be transferred at the interface are $Li^+ \cdot H_2O$ when in $NaClO_4$ medium both Na^+ and $Na^+ \cdot H_2O$ along with independent H_2O molecules are transferred in close quantities to each other.

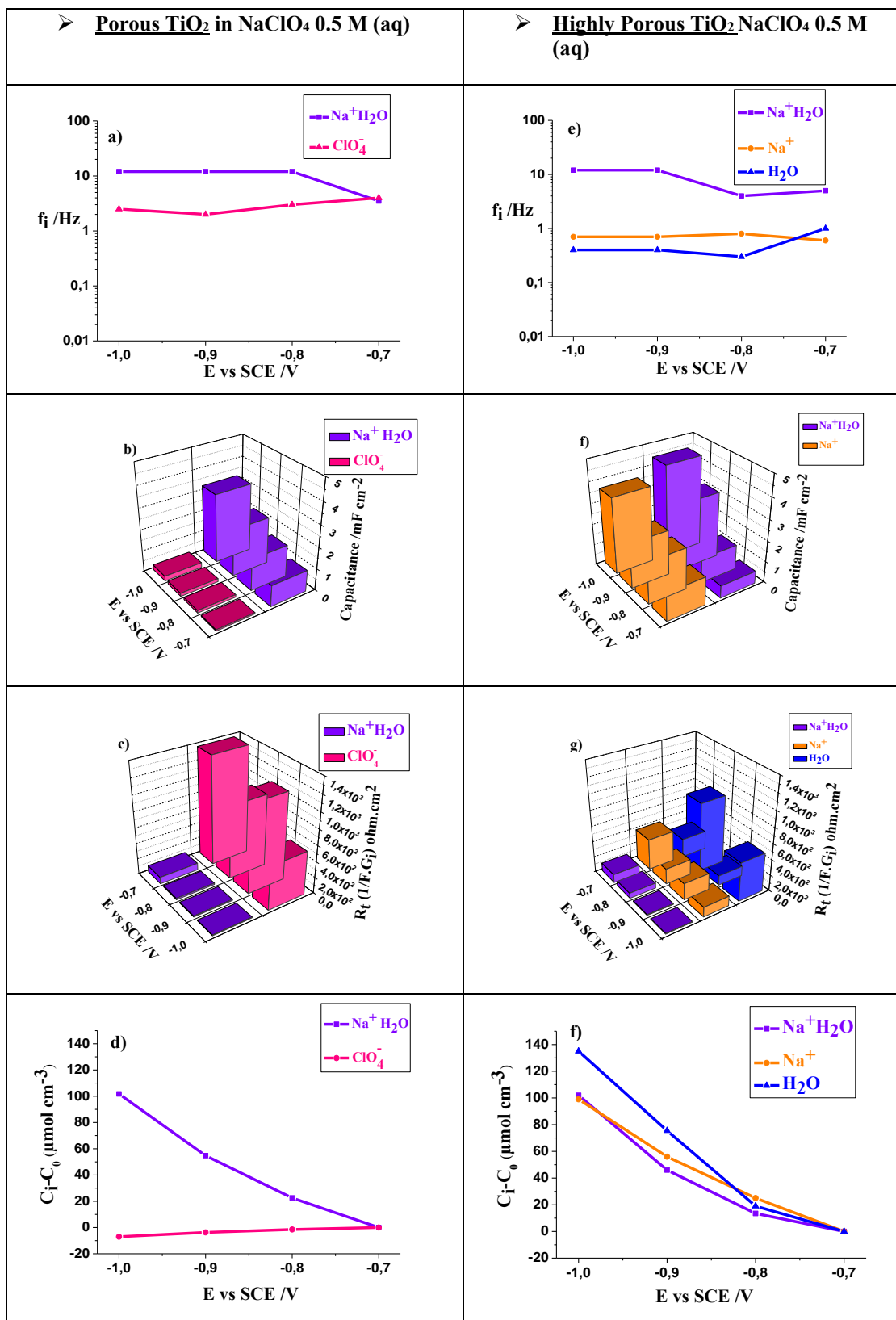


Fig. III-14. Evolution of different key parameters as a function of potential including: the characteristic frequency of species, f_i , the instantaneous capacitance of species, Cap_i , the transfer resistance, R_{ti} and the relative concentration of species, $C_i - C_0$, for porous (a-d) and highly porous (e-h) TiO₂ films in 0.5M NaClO₄ aqueous electrolyte.

Overall, it is concluded that in porous TiO₂ due to the confined intergrain porosity the only major contribution belongs to hydrated sodium and that the transfer of anionic species is

difficult and unfavourable. On the other hand, the enlarged surface area provided by accumulation of pore volumes in highly porous TiO₂ provides enough space and relatively facile transfer. As a consequent all the species involved contribute fairly in the charge compensation process at the interface of this electrode.

IV-3. ac-electrogravimetric studies of Highly Porous TiO₂ Thin Films in 0.5M LiClO₄. Comparison between Aqueous LiClO₄ (aq) and Organic LiClO₄ (PC) Solutions

In some reports, typical electrochemical studies were performed in organic solvents [13, 17]. No clear explanation are discussed regarding this choice in the regular reports except the solvent degradation or the potential window offered. Sometimes, the reason is related to the fact that organic solvents have bigger molecular mass compared to water molecules, this could minimize the possibility of their interference with ions dynamic.

So, to better study the ambiguous impact of an organic medium on the ions dynamics, a comparative investigation was performed. In the previous sections, it was observed that a large contribution of species were involved with highly porous TiO₂ and it was concluded that the porous morphology of TiO₂ could be advantageous. Therefore, here, *ac*-electrogravimetric measurements previously discussed for highly porous TiO₂ in 0.5 M LiClO₄ aqueous solution are compared when the same electrode is studied in 0.5 M LiClO₄/propylene carbonate from -0.7 V to -1 V vs SCE. Before the *ac*-electrogravimetric discussions, the classical EQCM results of highly porous TiO₂ film tested at room temperature for both types of electrolytes and are presented in Fig. III-15.

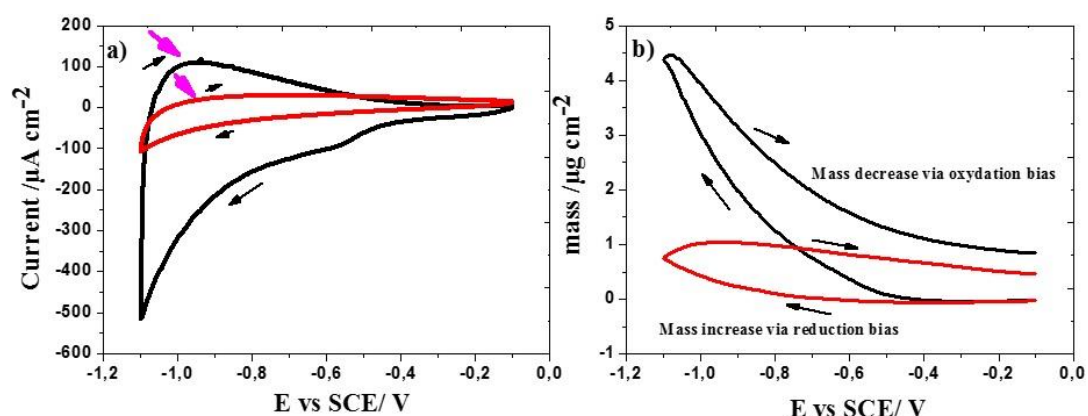


Fig. III-15. Electrogravimetric responses obtained simultaneously during the electrochemical cycling of highly porous TiO₂ films deposited on the gold coated electrode of the quartz resonator. Measurements are in 0.5M LiClO₄ aqueous solution (black curves) and 0.5 M LiClO₄ organic electrolyte (red curves, with a scan rate of 10 mV s⁻¹).

Based on the CV curves presented in figure III-15a, the capacitive response obtained in LiClO₄/PC electrolyte is too small compared to the response in LiClO₄ aqueous solution. The

noticeable asymmetric voltammogram with a broad anodic response which was observed in aqueous medium do not exist in *PC* organic medium. The peak current observed at the reverse anodic scan at -1 V vs SCE is almost over hundred μA higher compared to the negligible anodic current in organic medium. This suggests a higher contribution of the surface electroadsorption process which is also accompanied with the faradaic response (shown by pink arrows in Fig. III-15a) for highly porous TiO_2 thin films in organic medium.

The mass variations are also influenced by the nature of the electrolyte (Fig. III-15b), and the QCM response is magnified ~ 4 times in aqueous solution. This enhanced behaviour in aqueous medium suggests the involvement of large number of species in LiClO_4 (aq). However, at this level their identification is not possible, so the *ac*-electrogravimetric studies were performed.

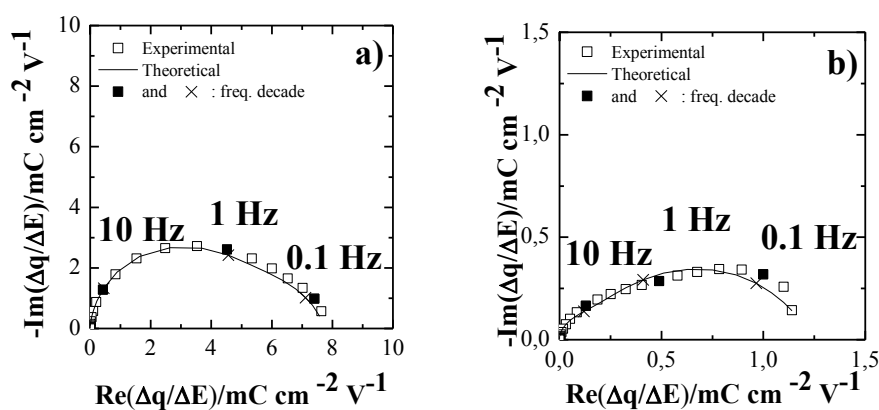


Fig. III-16. Charge/potential transfer functions, $\frac{\Delta q}{\Delta E}(\omega)$, for highly porous TiO_2 films measured in (a) 0.5 M LiClO_4 aqueous electrolyte and (b) 0.5 M LiClO_4 organic electrolyte at -0.9 V vs SCE (both experimental and theoretical curves are given).

The charge/potential transfer functions (TFs), $\frac{\Delta q}{\Delta E}(\omega)$, (Fig. III-16a and III-16b) allow to separate the ionic contribution without any possibility to identify the ionic species involved. In both studied cases a large suppressed loop was observed. Based on their theoretical functions (in Fig. III-16), there are more than one charged species involved in both cases for which the time constants corresponding to each ionic transfer are very close to each other. It is to be noted that the $\frac{\Delta q}{\Delta E}(\omega)$ response of the highly porous film in aqueous solution is remarkably magnified 8 times (Fig. III-16a), compared to $\frac{\Delta q}{\Delta E}(\omega)$ in *PC* medium. With $\frac{\Delta q}{\Delta E}(\omega)$ it is impossible to distinguish between the anion and the cation contributions and to determine the nature of the ionic species involved. In a further step, the K_i and G_i constants were determined

for three species in both studied electrolytes (Table III-3) and they were used in the following fittings.

Furtherly, to identify and clarify the contribution of the charged and also the uncharged species (*i.e.* free electrolyte molecules), the mass/potential transfer functions, $\frac{\Delta m}{\Delta E}(\omega)$ were measured.

In the mass/potential TF of highly porous TiO₂ in aqueous LiClO₄ ($\frac{\Delta m}{\Delta E}(\omega)$, Fig. III-17a) as previously discussed one big loop appears in the third quadrant. As already mentioned, the ClO₄⁻ appears at relatively HF, followed by Li⁺.H₂O at MF and Li⁺ at very low frequencies. The mass/potential transfer function of highly porous TiO₂ in organic medium, consists of two well separated demi-circles, one in the first quadrant corresponding to an anion (a= ClO₄⁻) and another one in the second quadrant which is attributed to (c = Li⁺) and (s = PC) in the same flux direction. The anion appears to be rapid and present at relatively HF, then, followed by Li⁺ and PC detected (fig. III-17b).

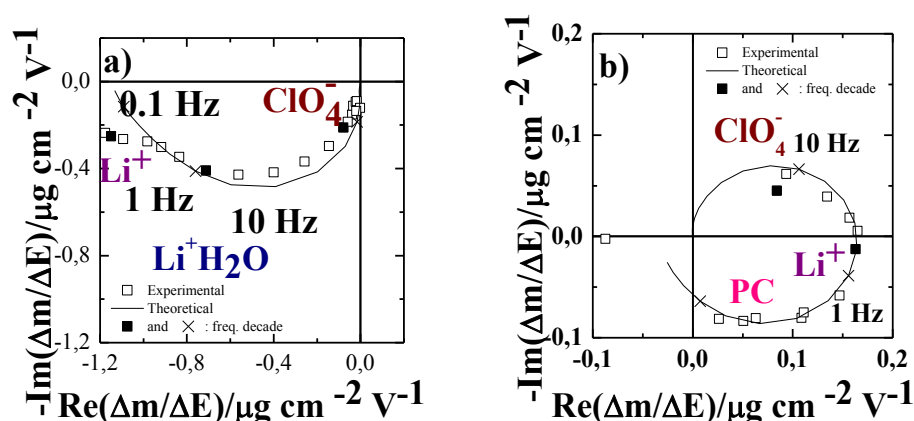


Fig. III-17. Mass/potential transfer functions, $\frac{\Delta m}{\Delta E}(\omega)$, for highly porous TiO₂ in (a) 0.5 M LiClO₄ aqueous electrolyte (involving three species, specifically Li⁺, Li⁺.H₂O and ClO₄⁻) and (b) 0.5 M LiClO₄ organic electrolyte (involving three species, specifically Li⁺, PC and ClO₄⁻). The measurements were performed at -0.9 V vs SCE (both experimental and theoretical curves are given).

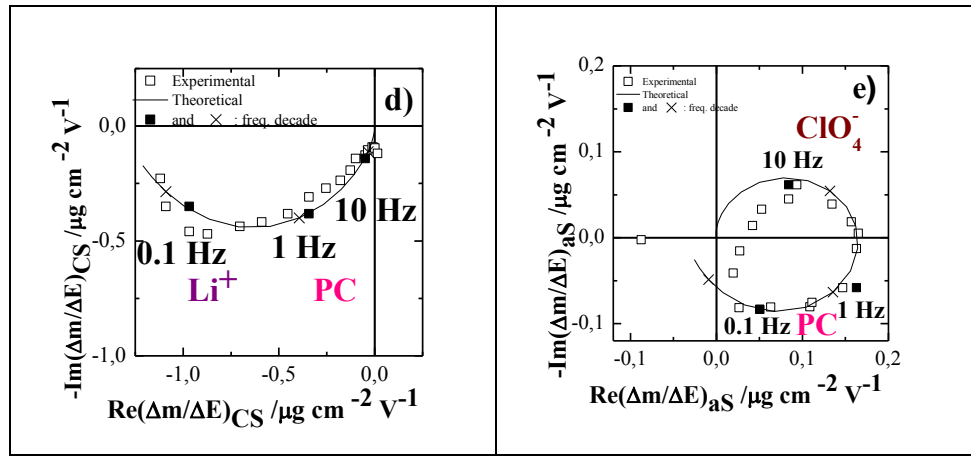
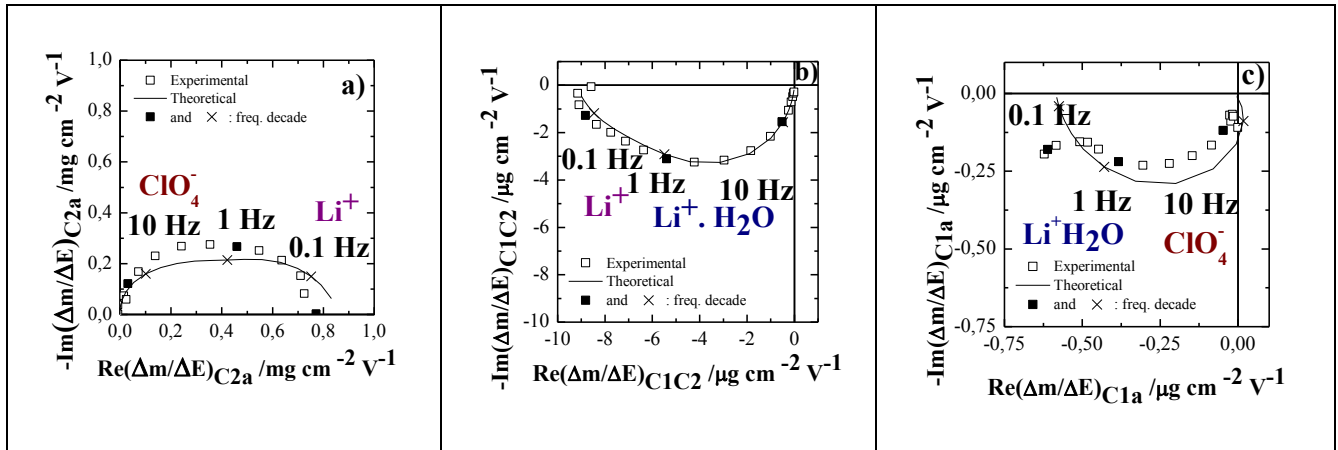


Fig. III-18. Partial electrogravimetric transfer functions, for highly porous TiO_2 in 0.5 M LiClO_4 aqueous electrolyte (a, b and c) and in 0.5 M LiClO_4 organic electrolyte (d and e) films measured at -0.9 V vs SCE (both experimental and theoretical curves are given).

The partial mass/potential TFs were analyzed to validate the hypothesis involving three different species in both electrolyte types. Partial mass/potential TFs are estimated for porous TiO_2 electrode in aqueous LiClO_4 solution (figure III-18a-c), by removing the c1 contribution,

calculating $\frac{\Delta m}{\Delta E} \Big|_{th}^{c2a}$ (fig. III-18a), by removing the anion contribution, calculating $\frac{\Delta m}{\Delta E} \Big|_{th}^{c1c2}$

(fig. III-18b) or by removing the c2 contribution, calculating $\frac{\Delta m}{\Delta E} \Big|_{th}^{c1a}$ (fig. III-18c). The partial

mass/potential TFs in PC medium were estimated similarly (fig. III-18d and III-18e). All these partial mass/potential TFs exhibited a good agreement between the theoretical and experimental

data. This provides a double check for validating the hypothesis involving multiple species and for obtaining a better separation of the various contributions.

<i>Porous TiO₂</i>	<i>f_i</i> (Hz)	<i>Cap_i</i> (mF cm ⁻²)	<i>K_i</i> (s cm ⁻¹)	<i>G_i</i> (mol s ⁻¹ cm ⁻² V ⁻¹)	$Rt_i = \frac{1}{FG_i}$ (Ω cm ²)	$\frac{\Delta C_i}{\Delta E}(\omega) = -\frac{G_i}{K_i}$ (mol cm ⁻³ V ⁻¹)
In LiClO₄ (aq)						
<i>c₁</i> (cation 1) : <i>Li⁺. H₂O</i> <i>7+18 g mol⁻¹</i>	3,5	5	15,4×10 ⁻⁴	11,5×10 ⁻⁷	8.98	-7,5×10 ⁻⁴
<i>c₂</i> (cation 2): <i>Li⁺</i> <i>7 g mol⁻¹</i>	0,25	2,36	1,1×10 ⁻⁴	0,38×10 ⁻⁷	269,27	-3,5×10 ⁻⁴
<i>a</i> (anion): <i>ClO₄⁻</i> <i>96 g mol⁻¹</i>	12,5	0,32	55×10 ⁻⁴	-2,64×10 ⁻⁷	39,27	0,48×10 ⁻⁴
In LiClO₄ (PC)						
<i>c</i> (cation): <i>Li⁺</i> <i>7 g mol⁻¹</i>	0,18	1	0,46×10 ⁻⁴	0,12×10 ⁻⁷	825	-2,7×10 ⁻⁴
<i>solvent: PC</i> <i>102 g mol⁻¹</i>	0,2	-	0,49×10 ⁻⁵	0.022×10 ⁻⁷	4700	0,5×10 ⁻⁴
<i>a</i> (anion): <i>ClO₄⁻</i> <i>96 g mol⁻¹</i>	7,5	0,2	18,9×10 ⁻⁴	0,98×10 ⁻⁷	105,7	-0,45×10 ⁻⁴

Table. III-3. Estimated values for K_i (kinetics of transfer), G_i (inverse of the transfer resistance), R_{ti} (transfer resistance) and $-G_i/K_i$ (quantity transferred per potential unit) parameters extracted from the fitting results of *ac*-electrogravimetric measurements in 0.5M LiClO₄ aqueous and organic electrolyte at -0.9 V vs. SCE for highly porous TiO₂ films.

The K_i and G_i constants are determined by fitting the experimental data using the theoretical functions for $\frac{\Delta q}{\Delta E}(\omega)$, $\frac{\Delta E}{\Delta I}(\omega)$, and $\frac{\Delta m}{\Delta E}(\omega)$ with the criteria of achieving a good agreement between the experimental and theoretical data (strictly for all of the TFs, including partial mass/potential TFs). The equivalent weight of the charged and uncharged species is determined by the electrogravimetric TF, $\frac{\Delta m}{\Delta E}(\omega)$ which provide the identification of the species (Table III-3). As previously discussed for highly porous TiO₂ thin films in aqueous solution: (i) ClO_4^- species contribute at high frequencies (the fastest species), (ii) $Li^+.H_2O$ appear at the intermediate frequencies, and (iii) Li^+ appears at low frequencies (the slowest species). In *PC* electrolyte (i) ClO_4^- species are slower compared to aqueous solution, they contribute at middle frequencies, (iii) Li^+ and *PC* free solvent molecules are the slowest species appearing at low frequencies.

From the G_i values, the transfer resistance, ($R_{t_i} = \frac{1}{FG_i}$) was determined. In aqueous solution, it pursues the order: $R_{t_i} (Li^+) > R_{t_i} (ClO_4^-) > R_{t_i} (Li^+.H_2O)$. In organic medium, the different order appears: $R_{t_i} (PC) > R_{t_i} (Li^+) > R_{t_i} (ClO_4^-)$. The PC free solvent transfer resistance is much higher when compared with the R_{t_i} values of the other species (see the values in Table III-3). Even the R_{t_i} values of Li^+ and ClO_4^- in organic medium are noticeably higher than their resistances in aqueous solution. Therefore, globally it could be concluded that the transfer of charged species is much easier in aqueous solutions.

Another parameter to examine is the $\frac{\Delta C_i}{\Delta E} (\omega \rightarrow 0) = -\frac{G_i}{K_i}$ value which can be considered as the quantity of the species transferred per potential unit at low frequencies. The quantity of the Li^+ transferred per potential unit is higher in aqueous solution compared to the contribution of anions which is similar, but rather small, in both types of electrolytes (Table III-3). Despite the fact that the characteristic frequency of the anion (in each of the studied electrolytes) is higher than other species, their transfer resistance is higher than cationic species. More importantly, the film doesn't show a remarkable instantaneous capacitance for these negatively charged species.

The results obtained from the measurements at -0.9 V vs SCE, when first indicates the absence of hydrated lithium ions ($Li^+.H_2O$) in organic medium and it is the free PC molecules that contribute. The following results presented in figure III-18 summarize the evolution of key parameters as a function of the applied potential.

The characteristic frequencies, f_i , extracted from *ac*-electrogravimetric results reveal (shown in figure III-18a and III-18e) that for highly porous TiO_2 thin film in both electrolytes: (i) ClO_4^- species contribute at high frequencies (the fastest species), even if the presence of the anion is shown only at two potentials in aqueous solution (ii) hydrated lithium ion ($Li^+.H_2O$) appears only in aqueous electrolyte at the intermediate frequencies, and (iii) Li^+ appears at low frequencies (the slowest species).

The instantaneous capacitance of each species, Cap_i , both in aqueous and organic electrolyte are illustrated in Fig. III-18b and III-18f. This shows that the capacity of the highly porous TiO_2 to accommodate the positively charged species as following a potential step is much higher when the electrolyte was aqueous. While the capacitance of the anion remains small in both cases, the capacitance of positively charged lithium ions are magnified over ~ 5 times in aqueous solution.

The evolution of the transfer resistance, R_{ti} , as a function of potential are shown in fig. III-18c and III-18g. Indeed, in organic medium the transfer resistance of all the included species are much higher than what is estimated in aqueous solution.

This involves $R_{ti}(Li^+)_{PC} > R_{ti}(Li^+)_{aq}$ and $R_{ti}(ClO_4^-)_{PC} > R_{ti}(ClO_4^-)_{aq}$. Specially, the transfer resistance of *PC* is very high. This could be related to the fact that the dynamic viscosity of *PC* (0.042 Pa. s) is almost 47 times more than water (8.9×10^{-4} Pa. s) and this would clearly influence on the transfer resistance of the species.

The relative concentration change, $(C_i - C_0)$ as a function of applied potential (presented in fig III-18d and III-18f) quantifies the contribution of the species. In aqueous solution the major contribution belongs to both cationic species: Li^+ and $Li^+.H_2O$, the number of anions in $\mu\text{mole per cm}^3$ transferred at the interface being negligible. In organic *PC* solution, the only noticeable ions transferred at the interface are Li^+ , compared to this, the contribution of *PC* and ClO_4^- are small. When both $LiClO_4$ (aq) and $LiClO_4$ (*PC*) electrolytes are compared, the amount of the anions contribution in both types of medium is similarly minor, but the small Li^+ ions contribute more (almost 2 times) in aqueous solution since the electrolyte is less viscous.

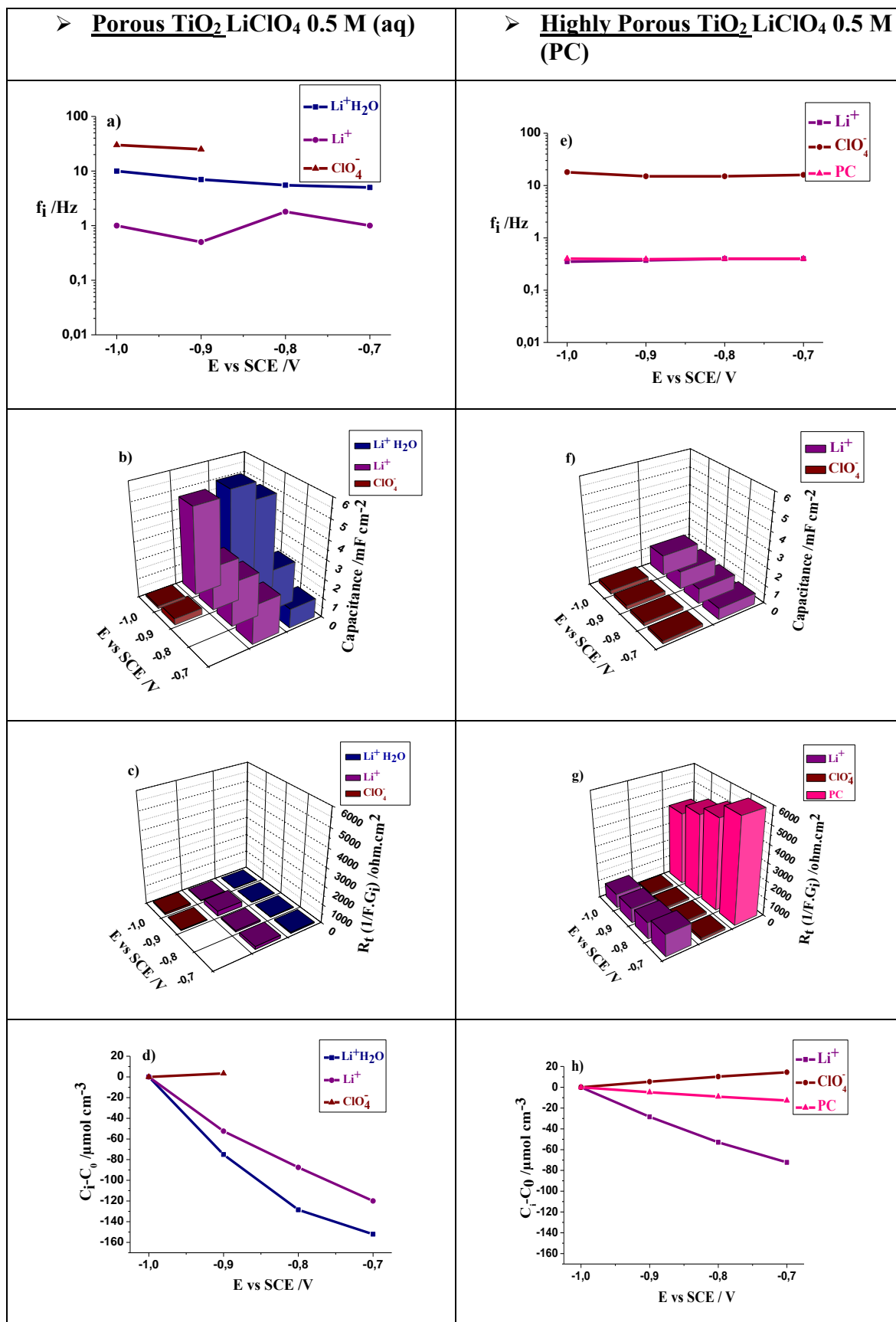


Fig. III-18. Evolution of key parameters as a function of potential including: the characteristic frequency of species (f_i), the instantaneous capacitance of species (Cap_i), the transfer resistance of species (R_{ti}) and the relative concentration of species ($C_i - C_0$) for highly porous TiO₂ film in 0.5M LiClO₄ (a-d) aqueous and 0.5 M LiClO₄ organic electrolyte (e-h).

Overall, in this section for the first time the impact of an organic solvent on the dynamics of transferred species was investigated both kinetically and thermodynamically. In a global point of view, these results are more satisfactory when the LiClO_4 electrolyte is aqueous for the following reasons: i) the value of the anodic capacitive current (CV curves) is higher in aqueous solution, ii) the instantaneous capacitance of the species willing to be transferred at the interface of highly porous TiO_2 electrode, are much higher when the electrolyte is aqueous, iii) due to the high dynamic viscosity of organic solvents the transfer resistances of species are more difficult in *PC* electrolyte, iv) more amount of charged species are transferred in porous TiO_2 electrode when the electrolyte is aqueous. The free water molecules are not directly involved in the charge compensation process but *PC* molecules participate as free solvent at very low frequencies.

V. Conclusion

The results presented in this chapter for amorphous porous TiO_2 thin films establish that the pseudocapacitive charge-storage mechanisms can be monitored in a deep manner by *ac*-electrogravimetry. The technique provides the exact identification and kinetic information on the charged and uncharged species involved in the charge storage process, which is not possible with classical EQCM measurements. Electrochemical behavior of porous and highly porous TiO_2 thin films in LiClO_4 and NaClO_4 aqueous solutions involves Li^+ ions, Na^+ ions, their respective hydrated ionic species as well as ClO_4^- anions which were detected by our *ac*-electrogravimetric studies. A detailed comparison was then performed in both aqueous and organic solution of LiClO_4 to investigate precisely the impact organic solvent on the ion dynamics transfer. The kinetics, f_i , the transfer resistance, R_{ti} , the instantaneous capacitance of the involved species, Cap_i , and the variation of the relative concentration of the species ($C_i - C_0$) of the different species transferred at the electrode/electrolyte interfaces were estimated for each studied case from our *ac*-electrogravimetric study.

In LiClO_4 aqueous electrolyte, the contribution of the charged species is magnified for high porous TiO_2 films compared to the porous films. This qualitative and quantitative study of ionic and non-ionic species contribution in the charge compensation process, together with dynamic information of their interfacial transfer further proved the advantageous nature of porous structures of TiO_2 films for storage applications. The beneficial aspect of more porous TiO_2 films was more likely related to the better accommodation of both Li^+ and $\text{Li}^+ \cdot \text{H}_2\text{O}$ cations. Particularly, hydrated lithium species $\text{Li}^+ \cdot \text{H}_2\text{O}$ were transferred rapidly and easily for highly

porous films, and their concentration variations in the electrode were significantly higher with respect to that in their less porous analogues.

From the results obtained in NaClO₄ aqueous electrolyte, it has been concluded that in porous TiO₂, because of the confined intergrain porosity, the only major contribution belonged to hydrated sodium and that the transfer of anionic species are difficult and unfavourable. On the other hand, the enlarged surface area provided by accumulation of pore volumes in highly porous TiO₂ provides enough space and facilitate a relatively easy transfer. Consequently, all the species involved contributed fairly well in the charge compensation process at the interface of the highly porous electrode.

The last section is dedicated to a comparison between aqueous and organic electrolytes. The impact of organic solvent on the dynamics of transfer of the species was investigated for the first time both kinetically and thermodynamically. Globally, the obtained electrochemical results were more satisfactory when the LiClO₄ electrolyte was aqueous. The instantaneous capacitance values of the species willing to be transferred at the interface of highly porous TiO₂ electrode, were much higher when the electrolyte was aqueous. These results may be due to the high dynamic viscosity of organic solvent. In the same way, the transfer resistance of the species were more difficult in the organic solvent as more charged species were transferred in porous TiO₂ electrode. On the one hand, the free water molecules were not directly involved in the charge compensation process, and the $Li^+.H_2O$ ions were hypothesized to be partially dehydrated. On the other hand, in organic electrolyte, PC molecules participate only as free solvent molecules. This indirectly influenced on the Li ions dynamics and slowed down their transfer.

Finally, to our knowledge, this is the first time that a fair and in situ determination of as-described parameters has been clearly demonstrated for different morphologies of amorphous TiO₂.

These results are exciting, and the combination of fast QCM with electrochemical impedance spectroscopy offers a great opportunity for a better understanding of the ions transfer and extent of solvent molecules impact on porous materials which is not possible with single EQCM measurements. Therefore, the establishment of the *ac*-electrogravimetric characterization in the energy materials domain is significant for designing optimized materials for the next-generation of high energy density supercapacitors.

VI. References

- [1] A. Fujishima, X. Zhang, D.A. Tryk, TiO₂ photocatalysis and related surface phenomena, *Surf. Sci. Rep.* 63 (2008) 515–582.
- [2] T. Paunesku, T. Rajh, G. Wiederrecht, J. Maser, S. Vogt, N. Stojićević, M. Protić, B. Lai, J. Oryhon, M. Thurnauer, others, Biology of TiO₂–oligonucleotide nanocomposites, *Nat. Mater.* 2 (2003) 343–346.
- [3] E.A. Rozhkova, I. Ulasov, B. Lai, N.M. Dimitrijevic, M.S. Lesniak, T. Rajh, A high-performance nanobio photocatalyst for targeted brain cancer therapy, *Nano Lett.* 9 (2009) 3337–3342.
- [4] H. Xiong, M.D. Slater, M. Balasubramanian, C.S. Johnson, T. Rajh, Amorphous TiO₂ nanotube anode for rechargeable sodium ion batteries, *J. Phys. Chem. Lett.* 2 (2011) 2560–2565.
- [5] G. Wang, L. Zhang, J. Zhang, A review of electrode materials for electrochemical supercapacitors, *Chem. Soc. Rev.* 41 (2012) 797–828.
- [6] P. Yu, C. Li, X. Guo, Sodium storage and pseudocapacitive charge in textured Li₄Ti₅O₁₂ thin films, *J. Phys. Chem. C.* 118 (2014) 10616–10624.
- [7] J. Qu, J. Ding, N. Yuan, The Synthesis of four Morphologies of TiO₂ through Temperature Control and Their Electrochemical Performance, *Int J Electrochem Sci.* 10 (2015) 8385–8394.
- [8] M. Lübke, J. Shin, P. Marchand, D. Brett, P. Shearing, Z. Liu, J.A. Darr, Highly pseudocapacitive Nb-doped TiO₂ high power anodes for lithium-ion batteries, *J. Mater. Chem. A.* 3 (2015) 22908–22914.
- [9] Y. Qin, J. Zhang, Y. Wang, X. Shu, C. Yu, J. Cui, H. Zheng, Y. Zhang, Y. Wu, Supercapacitive performance of electrochemically doped TiO₂ nanotube arrays decorated with Cu₂O nanoparticles, *RSC Adv.* 6 (2016) 47669–47675.
- [10] J. Kang, S.-H. Wei, K. Zhu, Y.-H. Kim, First-principles theory of electrochemical capacitance of nanostructured materials: Dipole-assisted subsurface intercalation of lithium in pseudocapacitive TiO₂ anatase nanosheets, *J. Phys. Chem. C.* 115 (2011) 4909–4915.
- [11] T. Brezesinski, J. Wang, J. Polleux, B. Dunn, S.H. Tolbert, Templated nanocrystal-based porous TiO₂ films for next-generation electrochemical capacitors, *J. Am. Chem. Soc.* 131 (2009) 1802–1809.
- [12] P. Heitjans, S. Indris, Diffusion and ionic conduction in nanocrystalline ceramics, *J. Phys. Condens. Matter.* 15 (2003) R1257.
- [13] P. Heitjans, E. Tobschall, M. Wilkening, Ion transport and diffusion in nanocrystalline and glassy ceramics, *Eur. Phys. J. Spec. Top.* 161 (2008) 97–108.
- [14] X. Sun, M. Xie, J.J. Travis, G. Wang, H. Sun, J. Lian, S.M. George, Pseudocapacitance of amorphous TiO₂ thin films anchored to graphene and carbon nanotubes using atomic layer deposition, *J. Phys. Chem. C.* 117 (2013) 22497–22508.
- [15] C. Benmouhoub, J. Agrisuelas, N. Benbrahim, F. Pillier, C. Gabrielli, A. Kadri, A. Pailleret, H. Perrot, O. Sel, Influence of the Incorporation of CeO₂ Nanoparticles on the Ion Exchange Behavior of Dodecylsulfate Doped Polypyrrole Films: Ac-Electrogravimetry Investigations, *Electrochimica Acta.* 145 (2014) 270–280.
- [16] P.M. Dziewoński, M. Grzeszczuk, Impact of the electrochemical porosity and chemical composition on the lithium ion exchange behavior of polypyrroles (ClO₄⁻, TOS⁻, TFSI⁻) prepared electrochemically in propylene carbonate. Comparative EQCM, EIS and CV studies, *J. Phys. Chem. B.* 114 (2010) 7158–7171.

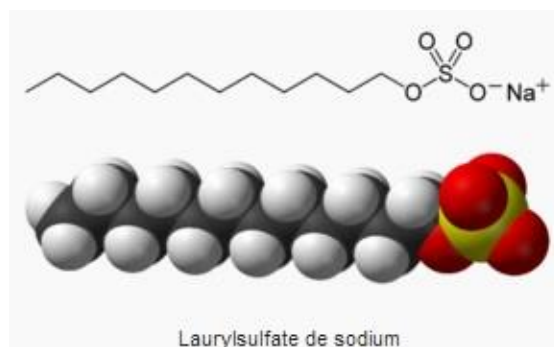
- [17] C.R. Arias, C. Debiemme-Chouvy, C. Gabrielli, C. Laberty-Robert, A. Pailleret, H. Perrot, O. Sel, New Insights into Pseudocapacitive Charge-Storage Mechanisms in Li-Birnessite Type MnO₂ Monitored by Fast Quartz Crystal Microbalance Methods, *J. Phys. Chem. C.* 118 (2014) 26551–26559.
- [18] B.I. Lemon, J.T. Hupp, EQCM Investigations of Dye-Functionalized Nanocrystalline Titanium Dioxide Electrode/Solution Interfaces: Does Luminescence Report Directly on Interfacial Electron Transfer Kinetics?, *J. Phys. Chem. B.* 103 (1999) 3797–3799.
- [19] J. Vondrák, M. Sedlaříková, J. Velická, P. Špičák, V. Svoboda, J. Kazelle, Insertion of cations into WO₃ investigated by QCM techniques, *J. Solid State Electrochem.* 11 (2007) 1459–1462.
- [20] H. Fakhouri, F. Arefi-Khonsari, A.K. Jaiswal, J. Pulpytel, Enhanced visible light photoactivity and charge separation in TiO₂/TiN bilayer thin films, *Appl. Catal. Gen.* 492 (2015) 83–92.
- [21] H. Fakhouri, J. Pulpytel, W. Smith, A. Zolfaghari, H.R. Mortaheb, F. Meshkini, R. Jafari, E. Sutter, F. Arefi-Khonsari, Control of the visible and UV light water splitting and photocatalysis of nitrogen doped TiO₂ thin films deposited by reactive magnetron sputtering, *Appl. Catal. B Environ.* 144 (2014) 12–21.
- [22] J. Mähler, I. Persson, A study of the hydration of the alkali metal ions in aqueous solution, *Inorg. Chem.* 51 (2011) 425–438.

Résumé du Chapitre IV

L'utilisation de films minces d'oxyde métallique avec une porosité à l'échelle nanométrique est devenue un sujet d'intérêt croissant pour diverses applications électrochimiques, par exemple, dans le domaine du stockage d'énergie, pour les dispositifs électrochromes, etc. Parmi ces matériaux, le trioxyde de tungstène, WO_3 , est un oxyde métallique qui peut offrir une large gamme d'applications technologiques comme décrit dans le chapitre I. Par conséquent, les nouveaux développements et les approches pour améliorer les performances de ces systèmes peuvent avoir un impact technologique direct.

L'insertion électrochimique réversible ou l'intercalation d'ions de l'électrolyte dans un matériau présente le principe fondamental de fonctionnement de dispositifs électrochimiques à base de WO_3 . Par conséquent, il est essentiel d'optimiser les interactions entre les ions de l'électrolyte et ces matériaux d'électrodes. Afin d'optimiser les performances d'une électrode à base de WO_3 , l'attention principale a été portée sur la nanostructuration de celle-ci. Les propriétés uniques qui en sont issues ainsi que les fonctionnalités peuvent être exploitées pour mettre au point des dispositifs électrochimiques originaux. Comme il a été discuté précédemment dans le chapitre expérimental, la synthèse électrochimique reste une technique simple, peu coûteuse et rapide à basse température qui peut également conduire à la formation de films nanométriques homogènes avec les qualités souhaitées. Cette approche utilise des molécules tensio-actives spécifiques qui adsorbées aux interfaces et sous génération électrochimique du film engendre la formation de films nanostructurés. Après dépôt, les agents tensioactifs utilisés peuvent être facilement éliminés par lavage avec un alcool approprié. Cela conduit à la formation de pores ou de cavités dues aux phases tensio-actives insérées dans le film électrogénéré. Ces nanostructures, avec des pores de petite taille et des grands rapports surface sur volume, sont censés faciliter les processus de transfert/transport d'ions à l'interface films/électrolyte.

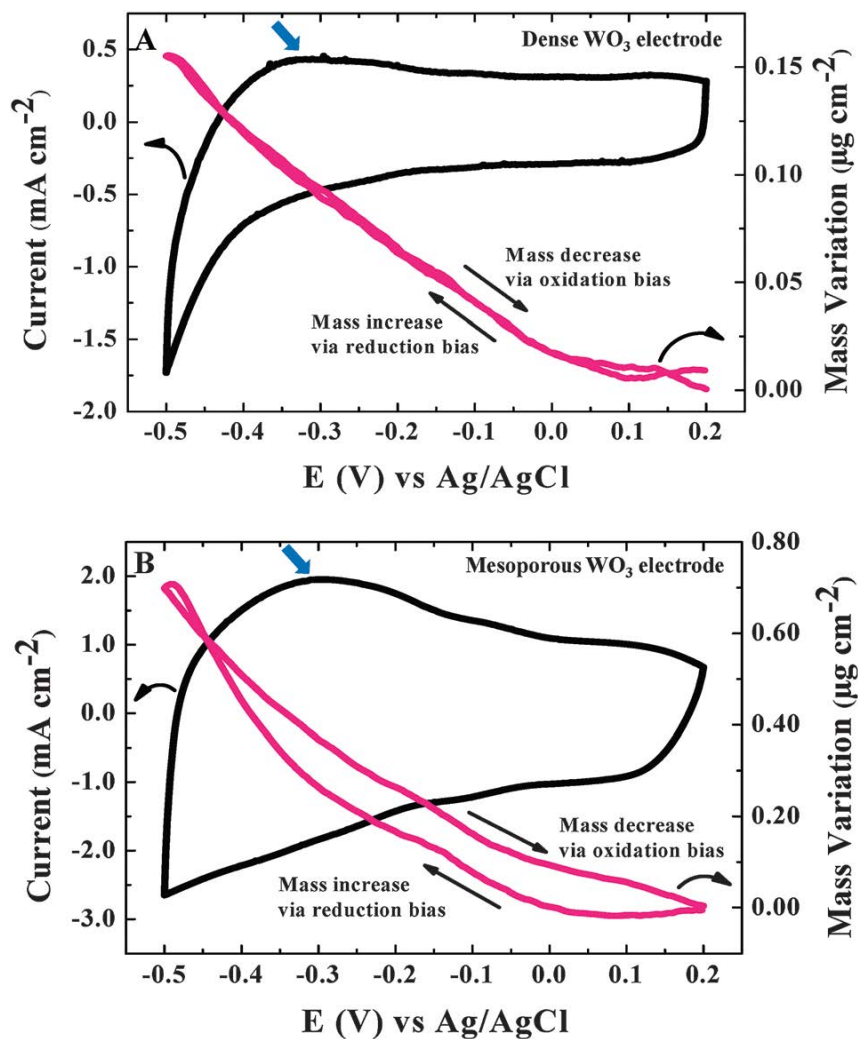
Pour suivre cette idée, le présent chapitre fournit une étude approfondie des processus d'intercalation/d'électroadoption des ions au sein de films de WO_3 mésoporeux. Ici, nous nous concentrons particulièrement sur les matériaux amorphes plutôt que cristallisés dans le but de souligner le rôle de cette structuration sur les performances électrochimiques des films de WO_3 . Ces films minces mésoporeux de WO_3 ont été préparés par voie électrochimique en utilisant un tensioactif ionique, le SDS, lors de l'électrosynthèse.



Représentation de la topographie de la molécule tensio-active utilisée en tant que porogène dans la présente étude.

La structure, la morphologie et la composition des films mésoporeux de WO₃ synthétisés ont été étudiées et comparées à leurs analogues denses. Les propriétés électrochimiques de ces films sont ensuite examinées. Les mécanismes d'électroadsorption/intercalation ont été regardés dans une solution aqueuse de LiClO₄ par des méthodes électrogravimétriques (EQCM et *ac*-électrogravimétrie).

Les courbes d'électrogravimétrie montrent une réponse quasiment capacitive dans la région anodique. En accord avec les données de la littérature dans des conditions similaires, un voltamogramme asymétrique est obtenu avec le film dense. La densité de courant cathodique et anodique des films mésoporeux est plus élevée que celle observée pour les films denses, ce qui peut indiquer une cinétique plus rapide de transfert des ions. Les valeurs de densité de courant mesurées sont presque quatre fois supérieures à celle obtenue pour un film dense. Les variations de masse sont également influencées par la présence des mésopores, la réponse de la microbalance est amplifiée environ 4 fois dans le cas de film mésoporeux. Ce meilleur comportement est attribué à une meilleure surface spécifique. En effet, un meilleur accès aux sites électroactifs est fourni et c'est un effet avantageux pour la réponse électrochimique d'électrodes poreuses à base de WO₃.



Electrogravimétrie cyclique lors de la réaction électrochimique (A) de couches minces de WO_3 dense et (B) de couches minces de WO_3 mésoporeux déposés sur l'électrode d'or d'un résonateur à quartz 9MHz. Les mesures sont en solution aqueuse 0,5 M LiClO_4 avec une vitesse de balayage de 50 mV s^{-1} .

Des analyses d'*ac*-electrogravimétrie permettent de détecter la contribution des espèces chargées ou non-chargé pendant les différents processus électrochimiques. Plus précisément, notre étude identifie clairement et de manière indiscutable l'implication de plusieurs espèces chargées (Li^+ , $\text{Li}^+ \cdot \text{H}_2\text{O}$) lors de la compensation de la charge, ainsi que les molécules libres de solvant qui contribuent indirectement au processus. D'une manière surprenante, une légère contribution des ions ClO_4^- a été détectée dans le cas des films mésoporeux de WO_3 . Les résultats de l'étude indiquent aussi que les résistances de transfert de Li^+ et $\text{Li}^+ \cdot \text{H}_2\text{O}$ diminuent lorsque les films de WO_3 sont mésoporeux. Une différence significative est surtout observée pour les ions les plus grands comme $\text{Li}^+ \cdot \text{H}_2\text{O}$ partiellement déshydratés. Cela suggère une augmentation de la surface en raison du volume des pores créé par la morphologie mésoporeuse ce qui facilite le transfert d'espèces chargées d'une manière tout à fait remarquable. Les

changements des concentrations relatives des ions sont également amplifiés dans ces films amorphes et structurés.

Ion insertion in Mesoporous WO_3 by electrogravimetry

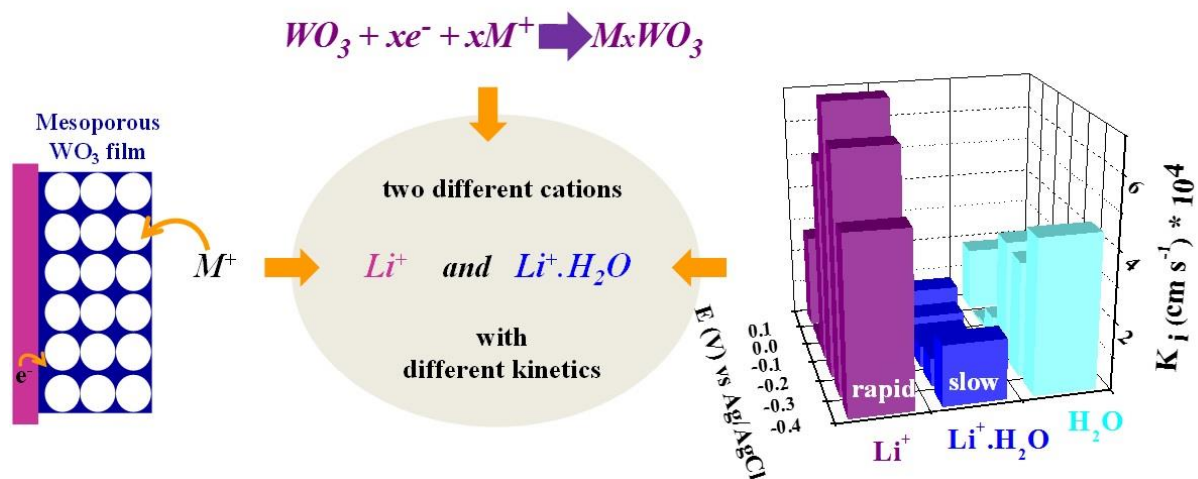


Schéma illustratif de l'étude effectuée par *ac*-électrogravimétrie.

Les variations de la concentration finale des cations sont beaucoup plus élevées dans les films mésoporeux que celles des films denses; environ 4 fois plus élevé pour Li^+ et environ 10 fois plus élevé pour $Li^+.H_2O$. Dans la littérature, il n'est pas fait mention de cette identification sans ambiguïté des différentes espèces. En effet, il est en général indiqué que seuls les cations déshydratés comme par exemple les ions Li^+ sont impliqués. De plus, notre stratégie permet d'obtenir des informations sur la dynamique de transfert et la quantification des espèces impliquées, point qui n'a jamais été trop abordé dans la littérature pour décrire le processus de compensation de charge du WO_3 .

I. Introduction

The use of metal oxide thin films with nanoscale porosity for diverse electrochemical applications, *e.g.* energy storage, electrochromic devices, *etc.* has become a subject of growing interest [1-4]. Among these materials, tungsten (VI) oxide (WO₃) is a particular metal oxide which can offer a wide range of technological applications. It is a representative metal oxide of a group of chromogenic materials due to the coloration effects associated with various processes. Aside from its potential applications including Li-ion batteries [5-7], supercapacitors [8-19], photoelectrochemical and solar [20-23], and fuel cells [24-26], WO₃ has been extensively studied as a promising electrochromic material. Meanwhile, WO₃ has already been integrated in low-voltage electrochromic devices for smart windows, which emphasizes the high technological relevance of this kind of material. Thus, new developments and approaches to improve such systems may have a direct technological impact.

The reversible electrochemical insertion or intercalation of electrolyte ions into an electrode material is the fundamental operation principle of WO₃ based electrochemical devices, this includes the simultaneous insertion of cations and electrons into the inorganic matrix during the reduction step (W⁺⁶/W⁺⁵), and the subsequent formation of coloring centers (W⁺⁵). Therefore, it is crucial to optimize the interactions between electrolyte ions and electrode materials.

For the improvement of the performance of metal oxide based electrodes, main attention has been attributed to their nanostructuration with various morphologies due to the unique properties and functionalities that can effectively be exploited in electrochemical devices. As previously discussed in the experimental chapter, electrochemical synthesis remains to be a fast, simple, low-cost and low-temperature technique which may also lead to the formation of homogenous nanoscale films with desirable qualities [27-31]. This approach manipulates surfactant-inorganic assemblies only in the thin interfacial region by electrochemically controlling surface interactions, which allows the formation of nanostructured films from dilute surfactant solutions. After deposition, surfactants can be easily removed from the pores by washing with a suitable alcohol, leading to the porous inorganic replicas of the surfactant phases [21]. These nanostructures, with small sizes, and large surface area to volume ratios, are expected to facilitate the ion intercalation/extraction process. These improvements are often attributed to (i) a facilitated transfer and short diffusion length for ions transport, (ii) a high

electrode/electrolyte contact area, and (iii) a better stress/strain management of the material during ion intercalation/extraction.

The morphology dependent performance and ion intercalation behaviour of WO_3 thin films have been investigated by several *in situ* or *ex situ* characterization techniques [32-33], including electrochemical and optical methods [34, 35, 22], wide-angle X-ray scattering combined with electrochemical studies [37], Raman spectroscopy [26], and X-ray photoelectron spectroscopy studying electrochromic materials before and after cation intercalation [34, 38]. However, none of these methods alone provide the information on the exact identification of the intercalated ionic species, their dynamics of transfer at the interfaces, as well as the role of electrolyte composition and the effect of ions solvation on the intercalation/extraction phenomena. The status of inserted ions is not a quite solved problem and the characterization of their transfer dynamics is not straightforward using conventional characterization tools. There is always a challenge to find an eligible technique offering mechanistic solutions in a single body that can be used to study ion intercalation phenomena *in-situ* and in contact with an electrolyte. There have been studies using quartz crystal microbalance (QCM) as an *in situ* gravimetric probe to study the insertion and/or electroadsorption of ions in metal oxide or carbon based electrodes [39-44]. These deposited materials are then studied in terms of mass changes during the electrochemical processes. EQCM gives a global response corresponding in fact to several possible pathways such that ions, ions with solvation shells and even indirectly free solvent molecules which can contribute to the electrochemical process. Additionally, ions may lose a part of their solvation to access to the sites in smaller nanopores [44]. These possible pathways, and kinetic or dynamic aspects of the ion intercalation/extraction processes have never been characterized in the previous EQCM studies due to the limitations of the technique.

As a consequence, based on what was previously explained in the introduction part of previous chapter regarding to the originality of *ac*-electrogravimetry for the investigation of TiO_2 , in the previous chapter, this coupled methodology is exploited to study the ion intercalation/extraction behaviour of mesoporous WO_3 films. Here, we particularly focus on the amorphous materials rather than crystalline ones to emphasize its role on the electrochemical performance of WO_3 films [5, 36]. For their fabrication, previously introduced electrochemical pathway so-called surfactant-assisted electrodeposition was chosen [21, 27, 29, 30], which provides a facile, low temperature and rapid alternative to the mesoporous thin film synthesis. The structure, morphology and the composition of the mesoporous electrochemically synthesized films were

characterized, and compared with their dense counterparts. The electrochemical performance and ion intercalation/extraction mechanisms were studied in aqueous LiClO_4 electrolytes by electrogravimetric methods (EQCM, and *ac*-electrogravimetry). Special attention was given to the poorly understood aspects, such as the nature of the ions involved in the charge compensation, solvation and the role of the electrolytes and the dynamic information of ions transfer at the electrode/electrolyte interfaces. It has been demonstrated herein that the *ac*-electrogravimetry responses of the electrodeposited WO_3 thin films can serve as a gravimetric probe to study the complex Li^+ intercalation/extraction mechanisms and to extract subtleties unreachable with classical tools.

II: Structure and Morphology Study of Dense and Mesoporous Thin Films

The morphology of the electrochemically synthesized WO_3 thin films was characterized by FEG-SEM and HR-TEM. In the absence of the surfactant molecules, fairly dense thin films composed of sphere-like shape nanoparticles of WO_3 are obtained, which is consistent with previous reports (Fig. IV-1) [21, 45]. Similar morphologies are obtained for the mesoporous counterparts on the scale of FEG-SEM observations. The average film thickness is ~ 300 nm under these experimental conditions (Fig. IV-1B), and it can be tailored by changing the electrodeposition time.

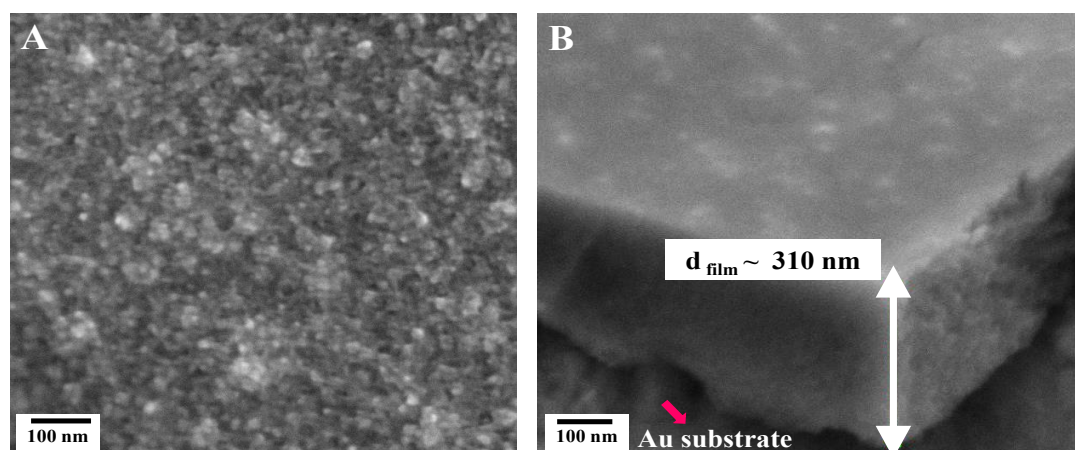


Fig. IV-1. FEG-SEM images showing the top view (A) and the cross-section (B) of an as deposited dense WO_3 thin film (electrodeposited on the Au electrode of a quartz resonator at -0.5 V vs Ag/AgCl during 20 min).

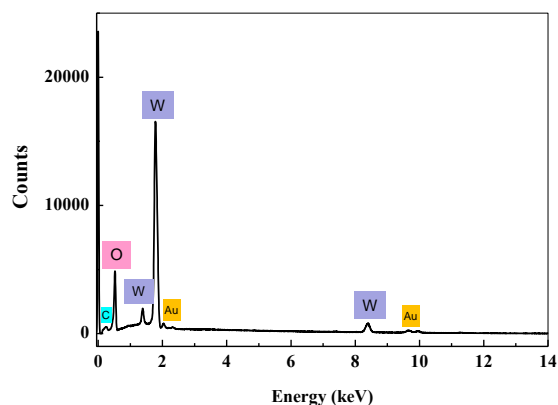


Fig. IV-2. Compositional analysis by energy dispersive X-ray (EDX) spectroscopy of a dense WO_3 thin film (obtained by FEG-SEM equipped with an EDX detector) (substrate: gold electrode of the quartz resonator).

The EDX analysis coupled with FEG-SEM observations indicates the presence of W and O in as-deposited dense thin films (Fig. IV-2). A small contribution of Au also appears which is due to the gold electrode of the quartz crystal substrate. The EDX spectrum of films synthesized in the presence of SDS templates (not given here) showed additional peaks corresponding to Na element, indicating the successful incorporation of the SDS templates in the inorganic/organic hybrids. The contribution of Na peak is substantially decreased after the extraction of the SDS templates, signifying the facile removal of the SDS templates (discussed in experimental section).

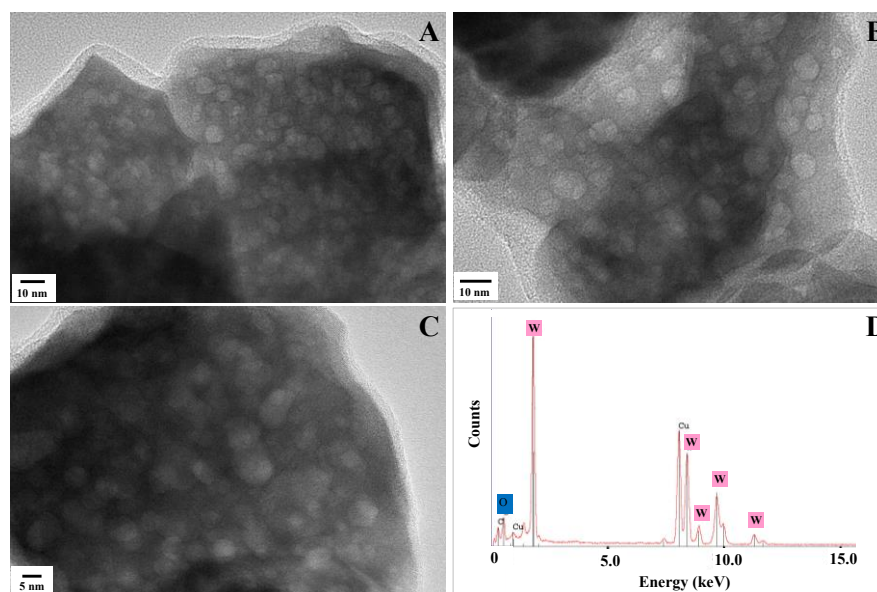


Fig. IV-3. HR-TEM images (A, B, C) and the EDX pattern (D) of mesoporous WO_3 thin films deposited by surfactant assisted electrodeposition (using SDS) at -0.5 V vs Ag/AgCl for 30 min, sample is thermally treated at 450°C for 2h.

The pore morphology of the WO_3 thin films electrodeposited in the presence of SDS templates was investigated by HR-TEM (Fig. IV-3) which revealed spherical mesopores of around 2-5 nm. The mesopores in the present films are randomly ordered and have certain dispersity in their pore size but fairly homogeneous domains expand within the film. Compared with the mesoporous thin film preparations based on the evaporation induced self-assembly (EISA), surfactant assisted electrodeposition method employs more dilute surfactant solutions. The main principle is based on the potential-controlled self-assembly of surfactant-inorganic aggregates at solid-liquid interfaces [21]. The concentration increases at the electrode surface leads to the formation of surfactant micelles, and the electrodeposition process occurs around these template structures. The subsequent removal of surfactant micelles leads to the formation of mesoporous films which are inverse replicas of the micellar structures, as shown in Fig. IV-3. Elemental composition analysis of the mesoporous WO_3 thin films was also obtained by EDX analysis coupled with HR-TEM observations. The main contributions in the EDX spectrum in Fig. IV-3D are attributed to the presence of W and O elements (Cu peaks in Fig. IV-3D are originated from TEM grids).

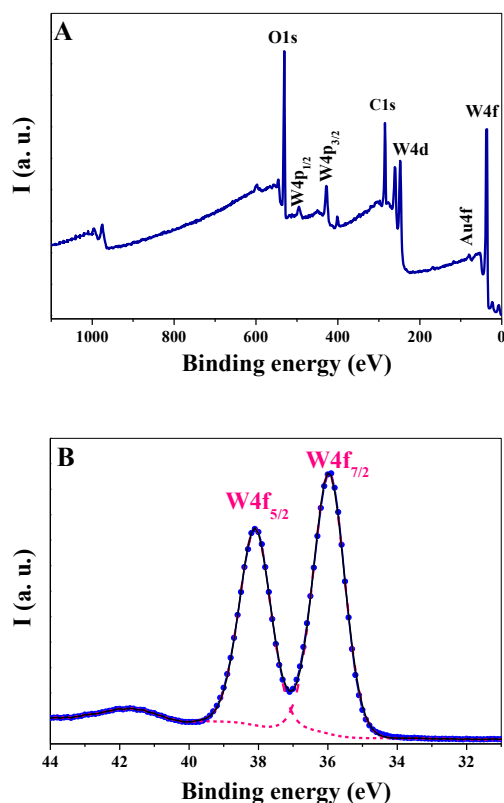
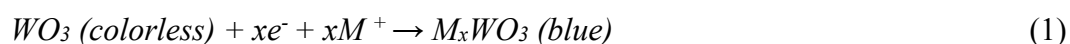


Fig. IV-4. X-ray Photoelectron Spectroscopy (XPS) survey spectrum (A) and the corresponding W 4f core level spectrum (B) of as-prepared dense WO_3 film electrosynthesized at -0.5 V vs Ag/AgCl for 20 min.

To determine the exact composition and the oxidation state of the W species, as-deposited thin films were characterized by X-ray photoelectron spectroscopy (XPS) and the results are shown in Fig. IV-4. All peaks can be indexed to W and O elements (except the presence of Au peaks due to the substrate) indicating the high purity of as-synthesized sample. A fitting curve of the W 4f level is presented in Fig. IV-4B. The peaks at binding energies of 35.6 and 37.7 eV match greatly well with the reported values for the W⁶⁺ oxidation state, indicating that the synthesized WO₃ is stoichiometric [38].

III: Electrochemical studies Study of Dense and Mesoporous WO₃ Thin Films

The optical variation of the WO₃ can be controlled by the application of a reversible voltage based on the double intercalation/extraction of cations and electrons into/out from the material. The general coloration process of WO₃, which is a cathodic coloring electrochromic material, is often presented in the literature by the following equation:



where M^+ refers to a non-solvated cation such as H^+ , Li^+ , Na^+ . This simplified intercalation/extraction mechanism is based on the charge compensation process by cations. When applying a negative voltage on WO₃ layer, electrons and cations are inserted, and the electrons reduce the W⁶⁺ ions to W⁵⁺. Whereas by applying a positive voltage, electrons and cations are extracted, and W⁵⁺ ions are oxidized to W⁶⁺. The general view in the literature is that the integrated cathodic current density over time equates to the amount of cation intercalated to form tungsten bronze M_xWO₃ (Eq. 1), indicating that a higher current density means faster cation intercalation kinetics [46]. However, this simplified scheme does not take into account of (i) the ion solvation effect, (ii) the possible presence of more than one ionic species which may favour/disfavour the kinetics of the electrochromism and charge/discharge rates, and (iii) the influence of free electrolyte molecules that can interact, indirectly, with porous electrodes. Although often stated as a paradigm, to the best of our knowledge, the indirect effect of the solvent molecules on the charge compensation mechanisms has not been thoroughly studied. In the following part, these aspects of the intercalation/extraction mechanism will be discussed in detail by EQCM and *ac*-electrogravimetric characterizations for both dense and mesoporous amorphous WO₃ thin films in aqueous LiClO₄ electrolytes.

III.1. The cyclic voltammetry and EQCM study

The EQCM is a simultaneous measurement of the resonant frequency variation of a quartz resonator determined by QCM during CV measurements. A typical EQCM curve gives the potential vs current profile, simultaneous to the frequency variation vs potential response. The quartz resonant frequency variations are converted into mass changes of the electrodes by Sauerbrey relation (Eq. 1 chapter II), e.g. the mass variations of the WO₃ electrodes during coloration (reduction bias) and bleaching (oxidation bias) can be monitored.

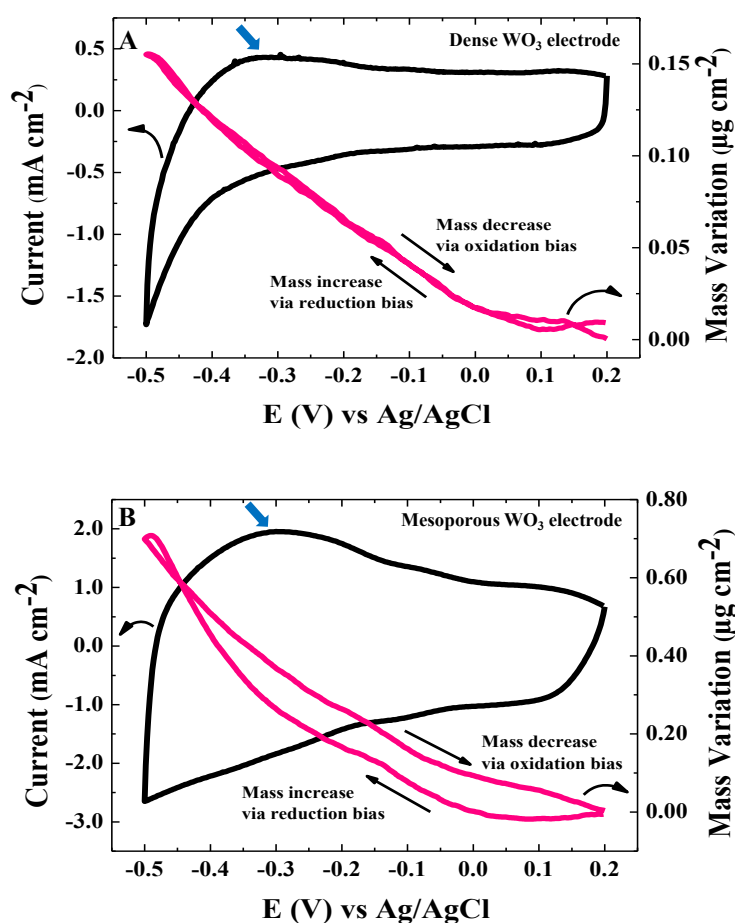


Fig. IV-5. Cyclic voltammograms and mass responses obtained simultaneously during the electrochromic response of (A) dense and (B) mesoporous WO₃ thin films deposited on the gold electrode of the quartz resonator. Measurements are in 0.5M aqueous solution of LiClO₄ with a scan rate of 50 mV s⁻¹.

The EQCM results of a dense and mesoporous WO₃ film tested at room temperature in aqueous 0.5M LiClO₄ electrolytes are presented in Fig. IV-5. The CV curves show a quasi-capacitive response in the anodic region whereas the coloration reaction is observed in the potential range of -0.15 V to -0.5 V vs Ag/AgCl. In agreement with the literature data under similar dynamic

conditions, an asymmetric voltammogram is obtained with a broad anodic loop displaying an extraction of cationic species that is slower than its cathodic insertion at this scan rate (Fig. IV-5). The capacitive behaviour is somehow more pronounced in the CV response of the dense films compared with that for a mesoporous film (Fig. IV-5). This suggests a higher contribution of surface electroadsorption process, compared with the faradaic response (shown by blue arrows in Fig. IV-5) in the case of dense WO₃ thin films. The cathodic and anodic current density of the mesoporous films (Fig. IV-5B) are higher than those observed for the dense films (Fig. IV-5A), which may indicate faster cation transfer kinetics, as mentioned in Ref. [46]. The current values measured are almost four times higher than that obtained for a dense film. The mass variations are also influenced by the presence of the mesopores (Fig. IV-5), as indicated by the QCM response amplified more or less four times in the case. This enhanced behaviour can probably be attributed to the increased specific surface area and pore volume. The mesopores provide a better accommodation of the electroactive sites and have an advantageous effect on the coloration process. The mass responses shown in the reduction branches (Fig. IV-5) correspond to the resonance frequency drops of the modified quartz resonators due to the mass increases of the films during reduction bias (coloration). In a reverse process, during oxidation bias (bleaching), the inserted species are expelled out from the film, resulting in a decrease of the electrode mass.

The molecular mass of the species (cations and/or the other ionic/non-ionic species if present) involved in the charge compensation can be obtained roughly with further calculation. To do so, $F \times \frac{\Delta m}{\Delta q}$ function was determined ($F \times \frac{\Delta m}{\Delta q} = F \frac{\Delta m / \Delta t}{\Delta Q / \Delta t}$) from the EQCM data. Fig. IV-6 depicts the variation of $F \times \frac{\Delta m}{\Delta q}$ values as a function of the applied potential for a dense and a mesoporous WO₃ thin film. According to this calculation, an absolute molecular mass value of $\sim 5-6 \text{ g mol}^{-1}$ was obtained for dense or mesoporous films measured in 0.5 M aqueous solutions of LiClO₄ with a scan rate of 50 mV s⁻¹, which is close to the molecular weight of Li⁺.

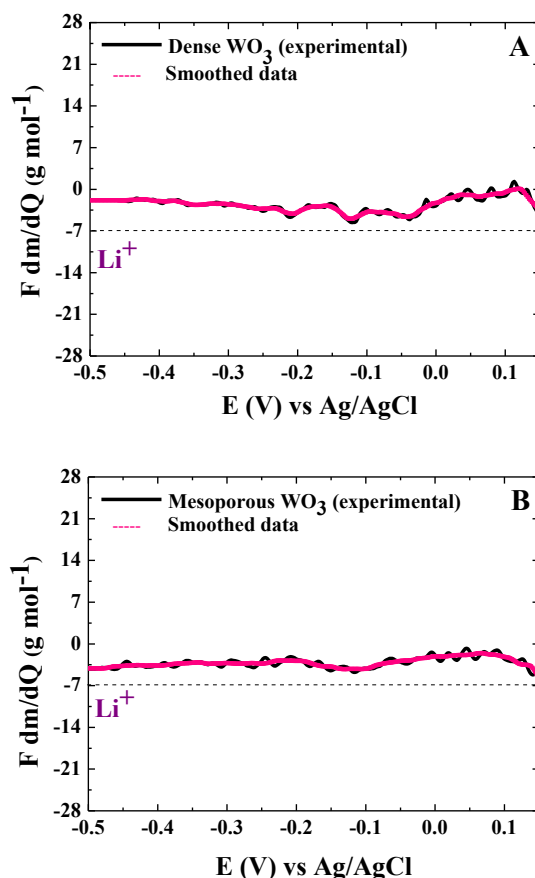


Fig. IV-6. $F \times \frac{\Delta m}{\Delta q}$ values corresponding to the average molecular weight of the species involved in the charge compensation as a function of the potential for a dense (A) and a mesoporous (B) WO_3 film cycled in 0.5 M aqueous LiClO_4 solutions (obtained from the reduction branch of the EQCM results at a scan rate of 50 mV s^{-1}).

If there is strictly one species involved, the $F \times \frac{\Delta m}{\Delta q}$ function should be equivalent to the molecular mass of the species transferred. However, for a complex electrochemical system, these values correspond to an average molecular weight related to the various species, and it is actually an average in terms of mass and kinetics. Therefore, at this point, one can arguably discuss that at this fast scan rate (50 mV s^{-1}), Li^+ ions are exclusively involved in the charge compensation process. However, it cannot guarantee the absence of any other species which may have different time constants and cannot be detected at this scan rate (such as heavier ions including ClO_4^- , hydrated forms of lithium ions, or free water molecules). Indeed, these results show the limitations of the classical EQCM technique. The EQCM gives a global response, and does not provide unambiguous information on which of the possible scenarios actually takes place. To investigate the subtleties that cannot be reachable by EQCM method, an *ac-*

electrogravimetric study was performed on mesoporous WO₃ films and compared with their dense analogues.

III-2. *ac*-electrogravimetric study of dense and mesoporous WO₃ films

To be able to have a resolution at the temporal level in the intercalation/expulsion mechanism, *ac*-electrogravimetry was used to characterize WO₃ films. *Ac*-electrogravimetric measurements were performed in aqueous 0.5 M LiClO₄ solution, at stationary potential values in the range of 0.1 V to -0.4 V vs Ag/AgCl.

(i) *Ac*-electrogravimetric exploration at -0.3V vs Ag/AgCl:

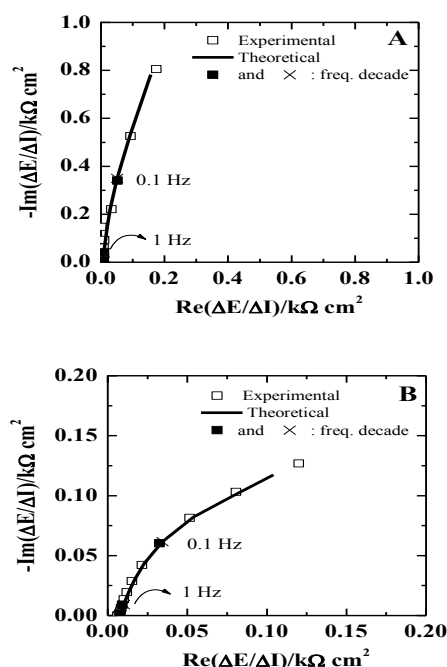


Fig. IV-7. The electrochemical impedances, $\frac{\Delta E}{\Delta I}(\omega)$ for a dense (A) and a mesoporous (B) WO₃ thin film, measured in aqueous 0.5 M LiClO₄ electrolyte at -0.3 V vs Ag/AgCl (both experimental and theoretical curves are given).

Fig. IV-7 exhibits the electrochemical impedance spectroscopy, $\frac{\Delta E}{\Delta I}(\omega)$, of a dense and mesoporous thin film, at a selected potential, specifically at -0.3 V vs Ag/AgCl. This potential value is presented because it corresponds to a situation where the electrodeposited film is in the reduced state. The $\frac{\Delta E}{\Delta I}(\omega)$ responses (Fig. IV-7A and IV-7B) have the usual shape, when dealing with an ion-blocking electrode, from which it is difficult to easily extract information. The low frequency trend was related to a parasitic response which is more pronounced in the

mesoporous films (Fig. IV-7B), and was fitted by using the corresponding equation in the theoretical section. The experimental transfer function and the fitted data from the model (see theoretical part), are reported on the same graphs; a good agreement between the two sets of data is evident in term of shape and frequency distribution (Fig. IV-7). It should be noted that there is no evident part with a slope equals to 45° or below in the electrochemical impedance response; therefore, the rate limiting step is not the mass transport in the films or in the solution but rather ionic transfer between the solution and the film [42].

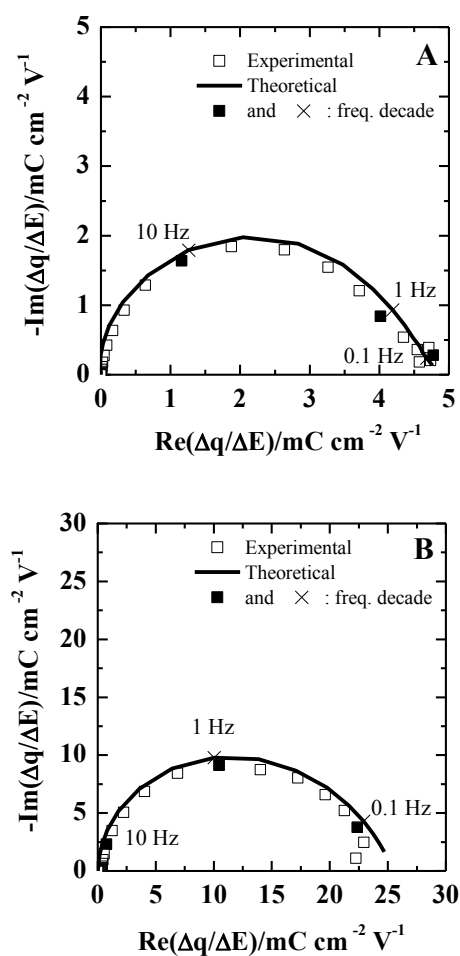


Fig. IV-8. Charge/potential transfer functions, $\frac{\Delta q}{\Delta E}(\omega)$ for a dense (A) and mesoporous (B) WO_3 thin film measured in aqueous 0.5 M LiClO_4 electrolyte at -0.3 V vs Ag/AgCl (both experimental and theoretical curves are given).

The charge/potential transfer functions (TFs), $\frac{\Delta q}{\Delta E}(\omega)$, (Fig. IV-8A, and IV-8B) permit to separate the ionic contribution without any possibility to identify the ionic species involved. It should be indicated here that the contribution of the parasitic reaction, occurring at low frequencies, was removed for keeping only the ionic transfer response. A large and slightly suppressed loop was obtained for both dense and mesoporous WO_3 thin films without a fair separation between different loops. In fact, the theoretical functions in Fig. IV-8 indicated that there are more than one charged species involved in both cases (Fig. IV-8A and IV-8B) where the time constants corresponding to each ionic transfer appear to be very close to each other. It is important to note that the $\frac{\Delta q}{\Delta E}(\omega)$ response of the mesoporous film is magnified (~ 5 times) (Fig. IV-8 B), compared to the response of a dense film (Fig. IV-8 A). At this stage, it is impossible to distinguish between the anion and the cation contributions and to determine the nature of the ionic species involved. Nevertheless, the K_i and G_i constants were determined for two ions (for dense) and three ions (for mesoporous) WO_3 thin films (see Table IV-I for the K_i and G_i values) and were used in the following fittings.

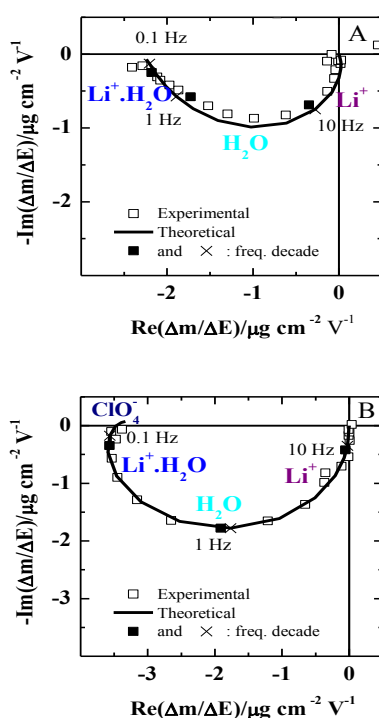


Fig. IV-9. The mass/potential transfer functions, $\frac{\Delta m}{\Delta E}(\omega)$, for a dense (A) (involving three species, specifically Li^+ , $\text{Li}^+\cdot\text{H}_2\text{O}$ and H_2O) and a mesoporous WO_3 thin films (B) (involving four species, specifically Li^+ , $\text{Li}^+\cdot\text{H}_2\text{O}$, ClO_4^- and H_2O), respectively. The measurements are performed in aqueous 0.5 M LiClO_4 electrolyte at -0.3 V vs Ag/AgCl (both experimental and theoretical curves are given).

	f_i (Hz)	Cap_i (mF cm ⁻²)	K_i (s cm ⁻¹)	G_i (mol s ⁻¹ cm ⁻² V ⁻¹)	$Rt_i = \frac{1}{FG_i}$ (Ω cm ²)	$\frac{\Delta C_i}{\Delta E}(\omega) = -\frac{G_i}{K_i}$ (mol cm ⁻³ V ⁻¹)
Dense WO₃						
c_2 (cation 2): Li^+, H_2O $7+18 \text{ g mol}^{-1}$	0.275	0.5	5.2×10^{-5}	0.01×10^{-6}	1175.6	1.1×10^{-4}
s (solvent): $H_2O 18 \text{ g mol}^{-1}$	3	-	57.8×10^{-5}	1.96×10^{-6}	5.3	10.7×10^{-4}
c_1 (cation 1): $Li^+ 7 \text{ g mol}^{-1}$	9.5	4.36	179×10^{-5}	2.69×10^{-6}	3.9	3.9×10^{-4}
Mesoporous WO₃						
c_2 (cation 2) : Li^+, H_2O $7+18 \text{ g mol}^{-1}$	0.425	6.5	8.0×10^{-5}	0.18×10^{-6}	57.5	18.6×10^{-4}
s (solvent): $H_2O 18 \text{ g mol}^{-1}$	1.75	-	33.0×10^{-5}	1.32×10^{-6}	7.9	15.6×10^{-4}
c_1 (cation 1): $Li^+ 7 \text{ g mol}^{-1}$	3.6	18	67.4×10^{-5}	4.10×10^{-6}	2.5	12.7×10^{-4}
a (anion): $ClO_4^- 96 \text{ g mol}^{-1}$	0.15	1.8	2.8×10^{-5}	-0.02×10^{-6}	592.2	-1.6×10^{-4}

Table IV-1. Estimated values for f_i , Cap_i , K_i (kinetics of transfer), G_i (inverse of the transfer resistance), Rt_i (transfer resistance) and $-G_i/K_i$ (the quantity transferred per potential unit) parameters extracted from the fitting results of *ac*-electrogravimetric measurements in aqueous 0.5M LiClO₄ at -0.3 V vs. Ag/AgCl for dense and mesoporous WO₃ films.

Then, to identify and clarify the contribution of the charged/uncharged species (*i.e.* free electrolyte molecules), the mass/potential transfer functions, $\frac{\Delta m}{\Delta E}(\omega)$ are scrutinized. In the mass/potential TF ($\frac{\Delta m}{\Delta E}(\omega)$, Fig. IV-9 A and IV-9 B), one big loop appears in the third quadrant at medium and low frequencies (MF and LF). This loop can be attributed to either one species or to two species where their time constants are not sufficiently different from each other. The loops in the third quadrant are characteristic for cation contributions or free solvent molecules in the same flux direction. Another contribution also appears in Fig. IV-9B (for the mesoporous WO₃ thin film) at very low frequencies in the fourth quadrant (either anions or water molecules with opposite flux direction compared to cations) highlighting the challenge in obtaining an exact identification of these two or three loops. Therefore, several configurations were tested using theoretical functions to determine the exact contribution of each species (given in chapter II).

The mass response of a dense WO₃ thin film was fitted by considering three species cation 1 ($c1 = Li^+$), free solvent molecules ($s = H_2O$) and cation 2 ($c2 = Li^+.nH_2O$) (Fig. IV-9 A). In the case of a mesoporous WO₃ film, a similar response is obtained, but with an additional contribution from another charged species, the anion ($a = ClO_4^-$). They appear characteristically in the fourth quadrant. Here, they are the slowest species transferred in the mesoporous films as they are detected at lower frequency region in Fig. IV-8 or IV-9B. It is important to note that Eq. 36 (theoretical section chapter II) involves the molecular weight of the ionic and/or nonionic species, providing their identification by their molecular weight. Therefore, cations or their hydrated forms can be detected with an estimation of the hydration level e.g. cation 1 ($c1 = Li^+$), cation 2 ($c2 = Li^+.nH_2O, n = 1$). Since the bulk hydration numbers for Li^+ ions is high, $n \sim 7-8$ [55], the cation 2 ($c2 = Li^+.nH_2O, n = 1$) detected in our study can be considered as partially dehydrated.

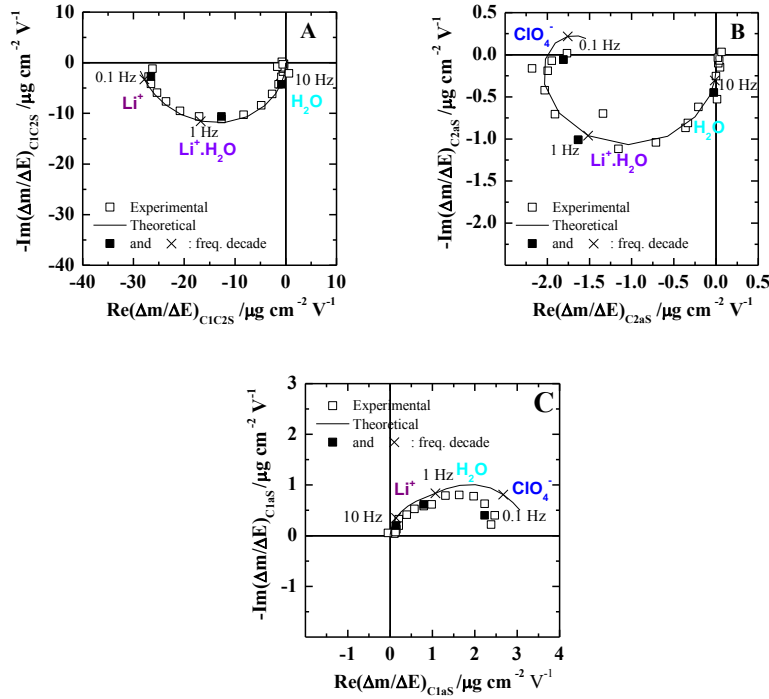


Fig. IV-10. Three partial transfer functions, for a mesoporous WO_3 thin film, (A) $\left. \frac{\Delta m}{\Delta E} \right|^{c1c2s}(\omega)$, (B) $\left. \frac{\Delta m}{\Delta E} \right|^{c2as}(\omega)$, and (C) $\left. \frac{\Delta m}{\Delta E} \right|^{c1as}(\omega)$, measured in aqueous 0.5 M LiClO_4 electrolyte at -0.3 V vs Ag/AgCl (both experimental and theoretical curves are given).

In addition, the partial mass/potential TFs were analyzed to validate our previous hypothesis involving three and four different species for dense and mesoporous films, respectively. Partial mass/potential TFs are estimated for mesoporous films (Fig. IV-10), for example by removing

the c2 contribution, calculating $\left. \frac{\Delta m}{\Delta E} \right|_{th}^{c1s}$ or by removing the c1 contribution, calculating $\left. \frac{\Delta m}{\Delta E} \right|_{th}^{c2s}$

as only three species are involved in the case of a dense film. The partial TFs for mesoporous

films were also analyzed, specifically $\left. \frac{\Delta m}{\Delta E} \right|_{th}^{c1c2s}$, $\left. \frac{\Delta m}{\Delta E} \right|_{th}^{c1as}$, and $\left. \frac{\Delta m}{\Delta E} \right|_{th}^{c2as}$ and all exhibited a good

agreement between the theoretical and experimental data as given in Fig. IV-10. These partial mass/potential TFs provide a crosscheck for validating the hypothesis involving multiple species and for obtaining a better separation of the various contributions. The K_i and the G_i constants are determined by fitting the experimental data using the theoretical functions for

$\frac{\Delta q}{\Delta E}(\omega)$, $\frac{\Delta E}{\Delta I}(\omega)$, and $\frac{\Delta m}{\Delta E}(\omega)$ with the criteria of achieving a good agreement between the experimental and theoretical data (strictly for all of the TFs, including partial mass/potential TFs).

The G_i parameters permit to calculate the transfer resistance (R_{ti}) for each species. The kinetic constants (K_i) obtained from *ac*-electrogravimetry at -0.3V vs Ag/AgCl reveal the transfer rates

of species at the electrode/electrolyte interfaces. Both for dense and mesoporous WO_3 thin films: (i) Li^+ species contribute at high frequencies (the fastest species), (ii) free water molecules appear at the intermediate frequencies, and (iii) $\text{Li}^+.\text{H}_2\text{O}$ appears at low frequencies (the slowest species). In the case of mesoporous WO_3 thin films, an additional contribution is observed at the lowest frequency range corresponding to the anions transfer (ClO_4^-) and their transfer kinetics is slower than cationic species and free water molecules (see values in Table IV-1). The G_i values determined from the *ac*-electrogravimetric study are related to the transfer resistance, ($Rt_i = \frac{1}{FG_i}$) which can explain the ease or the difficulty of the transfer of the ionic or nonionic species at the electrode/electrolyte interface. The transfer resistance, Rt_i , follow the order which is the inverse of that observed for the kinetics parameters (K_i) (Table IV-1). Specifically, for dense films, it pursues the order: $Rt_i (\text{Li}^+.\text{H}_2\text{O}) > Rt_i (\text{H}_2\text{O}) > Rt_i (\text{Li}^+)$, and for mesoporous films the same order persists: $Rt_i (\text{ClO}_4^-) > Rt_i (\text{Li}^+.\text{H}_2\text{O}) > Rt_i (\text{H}_2\text{O}) > Rt_i (\text{Li}^+)$, except the presence of additional ClO_4^- anions exhibiting the highest transfer resistance.

There are two cationic species (Li^+ and $\text{Li}^+.\text{H}_2\text{O}$) detected in both dense and mesoporous thin films. The kinetic parameters and resistance values for their interfacial transfer can be compared in Table IV-1. One of the most remarkable differences is that the $Rt_i (\text{Li}^+.\text{H}_2\text{O})$ value for dense films is much higher than that for a mesoporous film. This strongly suggests that the transfer of hydrated lithium species ($\text{Li}^+.\text{H}_2\text{O}$) at the interfaces is much easier in mesoporous WO_3 thin films than in dense counterparts. Thus, the transfer of larger hydrated lithium species ($\text{Li}^+.\text{H}_2\text{O}$) is favored when WO_3 thin films are mesoporous. Based on the K_i (or f_i) values, the species are transferred slightly slower in the case of mesoporous films but their transfer resistance, Rt_i , is in the same order of magnitude, or even slightly lower than that in dense films. These results indicate that mesoporous films facilitate both (Li^+ and $\text{Li}^+.\text{H}_2\text{O}$) transfer compared to dense WO_3 thin films. The ClO_4^- anions contribution was detected in mesoporous films, but their transfer is slow and more difficult compared to other species.

These observations are well harmonized with the estimated instantaneous capacitances, Cap_i , which is the capacity of the film to accommodate each involved charged species as a consequence of a potential jump. Here, they were estimated at a chosen applied potential of $E = -0.3 \text{ V}$ vs. Ag/AgCl for both dense and mesoporous WO_3 (see table IV-1). This transparent criterion shows an advantageous aspect of the mesoporous film. In fact, by comparing the values, it could be easily noticed that this instantaneous capacitance is magnified over 4 times

for small Li^+ ions and remarkably ~ 13 times for hydrated lithium ions ($Li^+.H_2O$) in the case of mesoporous films compared to dense films.

The transfer kinetics and the resistance of H_2O molecules are somehow similar to those Li^+ of species in both dense and mesoporous films, suggesting that these are the water molecules accompanying the transfer of Li^+ species most likely due to the electrodragging (Table IV-1). The quantity of the water molecules transferred per potential unit is slightly higher for mesoporous films, which is in agreement with the increased pore volume.

The results obtained from the measurements at $E = -0.3 V$ vs. Ag/AgCl, first of all indicate that there are other species than only Li^+ ions which intervene in the electrochemical process; such as hydrated lithium ions ($Li^+.H_2O$), free electrolyte molecules (water in the present case) or even anionic species present in the electrolyte which may contribute to the charge compensation but only in the case of mesoporous WO_3 thin films. In the following, the kinetic parameters (K_i) and the transfer resistance (R_{ti}) of the species are investigated as a function of the applied potential.

(ii) Ac-electrogravimetric measurements versus potential:

Figure IV-11 shows the evolution of the kinetic parameters, K_i , and the transfer resistance, R_{ti} , of the species as a function of the potential applied. This potential range corresponds to the conditions where the electrochemical process of the WO_3 thin films is observed. Based on the K_i values presented in Fig. IV-11 A and IV-11 B, Li^+ ions are persistently the fastest species transferred both in dense and mesoporous WO_3 thin films.

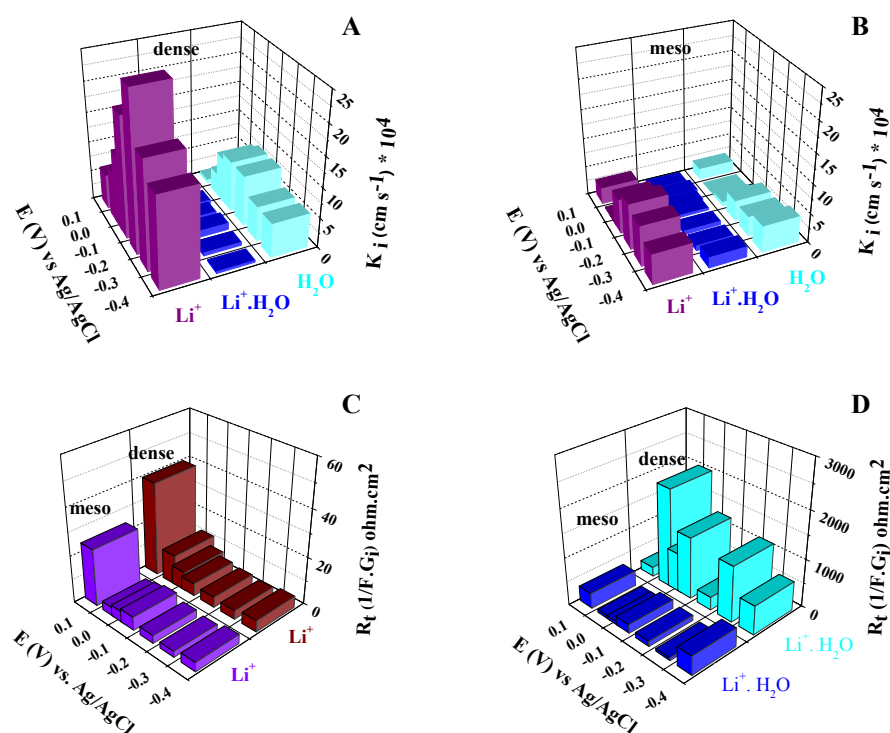


Fig. IV-11. Evolution of kinetic parameters, K_i , for a dense (A) and mesoporous (B) WO_3 thin films, and the comparative curve of the transfer resistance values, R_t , for cationic species in dense and mesoporous WO_3 thin films, Li^+ ions (C), and $\text{Li}^+.\text{H}_2\text{O}$ ions (D), presented as a function of applied potential.

There are two different cation populations (Li^+ and $\text{Li}^+.\text{H}_2\text{O}$) for both dense and mesoporous films at all the potentials studied. Compared to the dense films, the kinetics of transfer for Li^+ ions is slower in the mesoporous films and this could be related to the morphology of the films. The hydrated lithium ions $\text{Li}^+.\text{H}_2\text{O}$ in the electrolyte lose their hydration shell and get transferred at the interface, (bulk electrolyte/dense WO_3 film interface). But if this transfer happens at an electrode/electrolyte interface of a confined pore wall (as in the case of a mesoporous WO_3 film), the dehydration of the hydrated lithium ions in a small confined space may occur slower than that may happen in the bulk of the electrolyte. Therefore, one can arguably discuss that the different dehydration kinetics may be responsible for the differences in the $K_i(\text{Li}^+)_{\text{meso}}$ and $K_i(\text{Li}^+)_{\text{dense}}$ values shown in Fig. IV-11. The transfer kinetics of the larger, partially dehydrated $\text{Li}^+.\text{H}_2\text{O}$ is in the same order of magnitude in both mesoporous and dense films (Fig. IV-11 A and B). The transfer kinetics of free water molecules are somehow close to the values of the Li^+ ions in Fig. IV-11A and IV-11B. Additionally, these water molecules have the same flux directions with the cations, suggesting that they might be the water molecules accompanying the transfer of Li^+ species most likely due to an electrodragging

process. At all potential values studied, independent from the film morphology there are two types of cations, specifically fully dehydrated and partially dehydrated lithium species.

However, the transfer resistance values reveal significant differences between mesoporous and dense WO_3 thin films (Fig. IV-11C and IV-11D). Both Li^+ and $\text{Li}^+.\text{H}_2\text{O}$ have lower transfer resistance, indicating the ease of their transfer at the electrode/electrolyte interfaces when the WO_3 films are mesoporous. A more significant difference is observed for the larger and partially dehydrated $\text{Li}^+.\text{H}_2\text{O}$ ions, suggesting that increased surface area and pore volume, created by the mesoporous morphology, favor the larger charged species transfer.

To quantify the role of each species, $\left. \frac{\Delta C_i}{\Delta E} \right|_{\omega \rightarrow 0} = -\frac{G_i}{K_i}$ has been estimated as a function of the

applied potential. The integration of the $\left. \frac{\Delta C_i}{\Delta E} \right|_{\omega \rightarrow 0}$ against potential gives the insertion

isotherm. Fig. IV-12 presents the calculated relative concentration changes, $(C_i - C_0)$ for Li^+ , $\text{Li}^+.\text{H}_2\text{O}$, H_2O and ClO_4^- species for dense (Fig. IV-12 A) and mesoporous WO_3 (Fig. IV-12B) thin films. A significant difference is observed when WO_3 thin films are mesoporous. Both the $(C_i - C_0)$ values for Li^+ and $\text{Li}^+.\text{H}_2\text{O}$ cations are magnified for mesoporous films. It is important to note that the kinetics of transfer values for Li^+ species were higher (faster kinetics) in dense films compared to that in mesoporous films, and their ease of transfer was in the same order of magnitude (Fig. IV-11A, B and C). This point underlines the differences between kinetics and thermodynamics related to the transferred species. However, the final concentration variation is ~ 4 times higher in mesoporous films than that in the dense films. Despite of the differences in their dynamics of transfer, the final concentration variations are magnified in the mesoporous WO_3 thin films. It should be noticed that these subtleties can be only underlined and for the very first time for both dense and mesoporous WO_3 films.

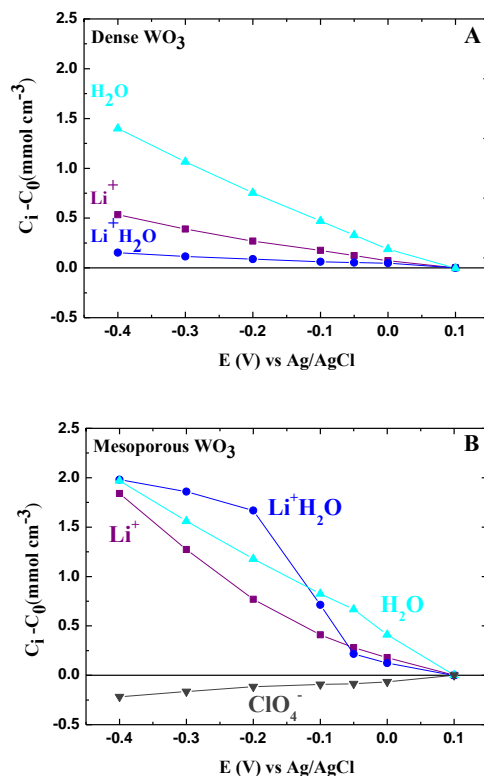


Fig. IV-12. Evolution of the relative concentration, $C_i - C_0$, of each species over the potential applied, for a dense (A) and a mesoporous (B) WO_3 thin film, measured in 0.5 M LiClO_4 aqueous electrolyte.

The $(C_i - C_0)$ values for $\text{Li}^+ \cdot \text{H}_2\text{O}$ present a drastic difference between the two films, and it is ~ 10 times higher in mesoporous films compared to the dense WO_3 . Their transfer resistance at the interfaces was also significantly smaller in mesoporous films (Fig. IV-11D), indicating that these large and partially dehydrated $\text{Li}^+ \cdot \text{H}_2\text{O}$ species are much easier transferred. In other words, $\text{Li}^+ \cdot \text{H}_2\text{O}$ ions are easily transferred in higher quantities when WO_3 films are mesoporous. The $(C_i - C_0)$ values for water molecules are in the same order of magnitude, or no significant difference is observed. The $(C_i - C_0)$ value for ClO_4^- anions is low compared with the cationic species, thus only a small quantity is transferred. Their kinetics of transfer was also very slow and difficult as it was shown in Table IV-1.

Overall, the contribution of all the charged species is magnified in mesoporous WO_3 films compared to dense films. This qualitative and quantitative study of ionic and non-ionic species contribution in the charge compensation process, together with dynamic information of their interfacial transfer further proves the advantageous nature of nanostructuring of WO_3 films for potential applications. For most of these application (e.g. in electrochromism), it is important to have a fast switching during the coloration/decoloration process which is related to the charge compensation of the redox reaction between $\text{W}^{6+} / \text{W}^{5+}$. The beneficial aspect of

mesoporous WO_3 films is more likely related to the better accommodation of both Li^+ and $\text{Li}^+.\text{H}_2\text{O}$ cations. Particularly, hydrated lithium species $\text{Li}^+.\text{H}_2\text{O}$ are transferred rapidly and easily at the mesoporous electrode/electrolyte interfaces, and their concentration variations in the electrode is significantly higher with respect to that in their dense analogues.

IV. Conclusion

Mesoporous WO_3 thin films were synthesized by surfactant assisted electrodeposition method. The idea of using an ionic surfactant (SDS) during the electrochemical preparation of WO_3 films led to the creation of ~ 5 nm spherical mesopores which are templated by the corresponding spherical micelles. The dense analogues were also electrochemically synthesized under similar conditions but in the absence of SDS templates.

The electrochromic behavior related to the cation intercalation/extraction in amorphous mesoporous and dense WO_3 thin films was investigated by coupled time resolved characterization methods (fast QCM/electrochemical impedance spectroscopy). The chemical nature and the role of each species (ions, solvated ions, and free solvent molecules), directly or indirectly involved in the electrochemical processes were estimated for the very first time.

Our study identifies the involvement of several charged species (Li^+ , $\text{Li}^+.\text{H}_2\text{O}$) in the charge compensation, and H_2O molecules indirectly contribute to the process in both dense and mesoporous WO_3 thin films. Even a slight contribution of ClO_4^- ions was detected in the case of mesoporous analogues.

Compared to the dense films, the kinetics of transfer for Li^+ ions are slower in the mesoporous films. This surprising result can be attributed to the transfer of ions occurring at different sites in the films. This transfer probably happens at an electrode/electrolyte interface of a confined pore wall (as in the case of a mesoporous WO_3 film), the dehydration of the hydrated lithium ions in a small confined space may occur slower than that may happen in the bulk of the electrolyte. Therefore, the different dehydration kinetics may be responsible for the differences in the $K_i(\text{Li}^+)_{\text{meso}}$ and $K_i(\text{Li}^+)_{\text{dense}}$. The transfer kinetics of the larger, partially dehydrated $\text{Li}^+.\text{H}_2\text{O}$ is in the same order of magnitude in both mesoporous and dense films, indicating that these larger ions interact with the surface or close to surface sites of the mesoporous WO_3 films.

Contrary to the kinetics of transfer, both Li^+ and $\text{Li}^+.\text{H}_2\text{O}$ have lower transfer resistance, indicating the ease of their transfer at the electrode/electrolyte interfaces when the WO_3 films

are mesoporous. Also, the instantaneous capacitance of both Li^+ and $Li^+.H_2O$ are noticeably magnified in mesoporous WO_3 . A more significant difference is observed for the larger and partially dehydrated $Li^+.H_2O$ ions, suggesting that increased surface area and pore volume created by mesoporous morphology facilitate the larger charged species transfer.

The relative concentration changes of Li^+ and $Li^+.H_2O$ cations are also magnified for the mesoporous films. The final concentration variation for Li^+ species is ~ 4 times higher in mesoporous films than that in the dense films. For $Li^+.H_2O$, this value is ~ 10 times higher in mesoporous films compared to the dense WO_3 .

This qualitative and quantitative study of ionic and nonionic species contribution in the charge compensation process, together with dynamic information of their interfacial transfer further proves the advantageous nature of nanostructuring of WO_3 films for potential applications. The results of the study indicate that the transfer resistances of the cations are much lower when the WO_3 films are mesoporous. This observation is probably in agreement with the previous reports in the literature indicating a fast switching during the coloration/decouration process of the mesoporous films. Another beneficial aspect of mesoporous WO_3 films is related to the better accommodation of both Li^+ and $Li^+.H_2O$ cations. Particularly, hydrated lithium species $Li^+.H_2O$ are transferred rapidly and easily at the mesoporous electrode/electrolyte interfaces, and their concentration variations in the electrode is significantly higher with respect to that occurs in their dense analogues. To the best of our knowledge, an unambiguous identification of species other than Li^+ ions, the information on their transfer dynamics and quantification of the transferred species have never been reported in the literature.

This study particularly focuses on the investigation of amorphous mesoporous and dense WO_3 thin films. The fact that crystalline materials increase the energy barrier for lithium ions, and thus, their electrochemical capacity may be inferior compared to their amorphous analogues has been discussed in the literature [36]. The aspect of crystallinity of the films can also be studied when WO_3 thin films thermally treated at different temperatures, thus possessing different degree of crystallinity. However, such an electrogravimetric study requires the utilization of the resonators as substrates that have better thermal resistance than quartz crystals, and will be the subject of a further study.

Our exiting results suggest that the establishment of the *ac*-electrogravimetry characterization in the nanostructured, ion-insertion materials is significant for designing optimized materials for the next generation electrochromic and energy storage devices.

V. References

- [1] W.J. Gomes, D.M. Araújo, A.J. Carvalho, S.P. Campana-Filho, F. Huguenin, High Lithium Ion Electroinsertion Rate into Self-Assembled Films Formed from TiO₂, *J. Phys. Chem. C*. 117 (2013) 16774–16782.
- [2] R. Ostermann, B. Smarsly, Does mesoporosity enhance thin film properties? A question of electrode material for electrochromism of WO₃, *Nanoscale*. 1 (2009) 266–270.
- [3] C. Sanchez, C. Boissiere, D. Grosso, C. Laberty, L. Nicole, Design, synthesis, and properties of inorganic and hybrid thin films having periodically organized nanoporosity†, *Chem. Mater.* 20 (2008) 682–737.
- [4] W. Wang, Y. Pang, S.N. Hodgson, Design and fabrication of bimodal meso-mesoporous WO₃ thin films and their electrochromic properties, *J. Mater. Chem.* 20 (2010) 8591–8599.
- [5] H. Wei, X. Yan, S. Wu, Z. Luo, S. Wei, Z. Guo, Electropolymerized polyaniline stabilized tungsten oxide nanocomposite films: electrochromic behavior and electrochemical energy storage, *J. Phys. Chem. C*. 116 (2012) 25052–25064.
- [6] M. Sasidharan, N. Gunawardhana, M. Yoshio, K. Nakashima, WO₃ hollow nanospheres for high-lithium storage capacity and good cyclability, *Nano Energy*. 1 (2012) 503–508.
- [7] W.-J. Li, Z.-W. Fu, Nanostructured WO₃ thin film as a new anode material for lithium-ion batteries, *Appl. Surf. Sci.* 256 (2010) 2447–2452.
- [8] B.-X. Zou, Y. Liang, X.-X. Liu, D. Diamond, K.-T. Lau, Electrodeposition and pseudocapacitive properties of tungsten oxide/polyaniline composite, *J. Power Sources*. 196 (2011) 4842–4848.
- [9] C. Yuan, H. Lin, H. Lu, E. Xing, Y. Zhang, B. Xie, Anodic deposition and capacitive property of nano-WO₃·H₂O/MnO₂ composite as supercapacitor electrode material, *Mater. Lett.* 148 (2015) 167–170.
- [10] G.H. Jeong, H.-M. Lee, J. Kang, H. Lee, C.-K. Kim, J.-H. Lee, J.-H. Kim, S.-W. Kim, ZrO₂–SiO₂ Nanosheets with Ultrasmall WO₃ Nanoparticles and Their Enhanced Pseudocapacitance and Stability, *ACS Appl. Mater. Interfaces*. 6 (2014) 20171–20178.
- [11] H. Peng, G. Ma, K. Sun, J. Mu, M. Luo, Z. Lei, High-performance aqueous asymmetric supercapacitor based on carbon nanofibers network and tungsten trioxide nanorod bundles electrodes, *Electrochimica Acta*. 147 (2014) 54–61.
- [12] J. Xu, T. Ding, J. Wang, J. Zhang, S. Wang, C. Chen, Y. Fang, Z. Wu, K. Huo, J. Dai, Tungsten oxide nanofibers self-assembled mesoscopic microspheres as high-performance electrodes for supercapacitor, *Electrochimica Acta*. 174 (2015) 728–734.
- [13] K. Brezesinski, J. Wang, J. Haetge, C. Reitz, S.O. Steinmueller, S.H. Tolbert, B.M. Smarsly, B. Dunn, T. Brezesinski, Pseudocapacitive contributions to charge storage in highly

ordered mesoporous group V transition metal oxides with iso-oriented layered nanocrystalline domains, *J. Am. Chem. Soc.* 132 (2010) 6982–6990.

[14] K.-H. Chang, C.-C. Hu, C.-M. Huang, Y.-L. Liu, C.-I. Chang, Microwave-assisted hydrothermal synthesis of crystalline $\text{WO}_3\text{-WO}_3 \cdot 0.5\text{H}_2\text{O}$ mixtures for pseudocapacitors of the asymmetric type, *J. Power Sources.* 196 (2011) 2387–2392.

[15] L. Ma, X. Zhou, L. Xu, X. Xu, L. Zhang, C. Ye, J. Luo, W. Chen, Hydrothermal preparation and supercapacitive performance of flower-like $\text{WO}_3 \cdot \text{H}_2\text{O}$ /reduced graphene oxide composite, *Colloids Surf. Physicochem. Eng. Asp.* 481 (2015) 609–615.

[16] M. Zhu, W. Meng, Y. Huang, Y. Huang, C. Zhi, Proton-insertion-enhanced pseudocapacitance based on the assembly structure of tungsten oxide, *ACS Appl. Mater. Interfaces.* 6 (2014) 18901–18910.

[17] R. Yuksel, C. Durucan, H.E. Unalan, Ternary nanocomposite SWNT/ WO_3 /PANI thin film electrodes for supercapacitors, *J. Alloys Compd.* 658 (2016) 183–189.

[18] R.D. Kumar, Y. Andou, S. Karuppuchamy, Synthesis and characterization of nanostructured Ni- WO_3 and NiWO_4 for supercapacitor applications, *J. Alloys Compd.* 654 (2016) 349–356.

[19] Y.-H. Wang, C.-C. Wang, W.-Y. Cheng, S.-Y. Lu, Dispersing WO_3 in carbon aerogel makes an outstanding supercapacitor electrode material, *Carbon.* 69 (2014) 287–293.

[20] V. Cristino, S. Caramori, R. Argazzi, L. Meda, G.L. Marra, C.A. Bignozzi, Efficient photoelectrochemical water splitting by anodically grown WO_3 electrodes, *Langmuir.* 27 (2011) 7276–7284.

[21] S.-H. Baeck, K.-S. Choi, T.F. Jaramillo, G.D. Stucky, E.W. McFarland, Enhancement of photocatalytic and electrochromic properties of electrochemically fabricated mesoporous WO_3 thin films, *Adv. Mater.* 15 (2003) 1269–1273.

[22] H. Zheng, Y. Tachibana, K. Kalantar-zadeh, Dye-sensitized solar cells based on WO_3 , *Langmuir.* 26 (2010) 19148–19152.

[23] K. Hara, Z.-G. Zhao, Y. Cui, M. Miyauchi, M. Miyashita, S. Mori, Nanocrystalline electrodes based on nanoporous-walled WO_3 nanotubes for organic-dye-sensitized solar cells, *Langmuir.* 27 (2011) 12730–12736.

[24] C. Laberty-Robert, K. Valle, F. Pereira, C. Sanchez, Design and properties of functional hybrid organic–inorganic membranes for fuel cells, *Chem. Soc. Rev.* 40 (2011) 961–1005.

[25] W. Zhao, Y. Yang, H. Zhang, Electrodeposition preparation of highly dispersed Pt/ H_xWO_3 composite catalysts for PEMFCs, *Electrochimica Acta.* 99 (2013) 273–277.

[26] A.J. Martín, A.M. Chaparro, L. Daza, Single cell study of electrodeposited cathodic electrodes based on Pt- WO_3 for polymer electrolyte fuel cells, *J. Power Sources.* 196 (2011) 4187–4192.

- [27] S.H. Baeck, T. Jaramillo, G.D. Stucky, E.W. McFarland, Controlled electrodeposition of nanoparticulate tungsten oxide, *Nano Lett.* 2 (2002) 831–834.
- [28] N.R. de Tacconi, C.R. Chenthamarakshan, K. Rajeshwar, T. Pauporté, D. Lincot, Pulsed electrodeposition of WO₃–TiO₂ composite films, *Electrochem. Commun.* 5 (2003) 220–224.
- [29] E.A. Meulenkaamp, Mechanism of WO₃ Electrodeposition from Peroxy-Tungstate Solution, *J. Electrochem. Soc.* 144 (1997) 1664–1671.
- [30] W.L. Kwong, A. Nakaruk, P. Koshy, C.C. Sorrell, Tunable Photoelectrochemical properties by nanostructural control in WO₃ thin films prepared by carboxylic acid-assisted electrodeposition, *J. Phys. Chem. C* 117 (2013) 17766–17776.
- [31] Z. Chen, Y. Peng, F. Liu, Z. Le, J. Zhu, G. Shen, D. Zhang, M. Wen, S. Xiao, C.-P. Liu, others, Hierarchical Nanostructured WO₃ with Biomimetic Proton Channels and Mixed Ionic-Electronic Conductivity for Electrochemical Energy Storage, *Nano Lett.* 15 (2015) 6802–6808.
- [32] L. Bobics, L. Sziraki, G.G. Lang, The impedance related to the electrochemical hydrogen insertion into WO₃ films—On the applicability of the diffusion-trapping model, *Electrochem. Commun.* 10 (2008) 283–287.
- [33] L.V. Kondrachova, R.A. May, C.W. Cone, D.A. Vanden Bout, K.J. Stevenson, Evaluation of Lithium Ion Insertion Reactivity via Electrochromic Diffraction-Based Imaging, *Langmuir*. 25 (2009) 2508–2518.
- [34] D.S. Dalavi, R.S. Devan, R.A. Patil, R.S. Patil, Y.-R. Ma, S.B. Sadale, I. Kim, J.-H. Kim, P.S. Patil, Efficient electrochromic performance of nanoparticulate WO₃ thin films, *J. Mater. Chem. C*. 1 (2013) 3722–3728.
- [35] S. Sallard, T. Brezesinski, B.M. Smarsly, Electrochromic stability of WO₃ thin films with nanometer-scale periodicity and varying degrees of crystallinity, *J. Phys. Chem. C*. 111 (2007) 7200–7206.
- [36] R.S. Vemuri, K.K. Bharathi, S.K. Gullapalli, C.V. Ramana, Effect of structure and size on the electrical properties of nanocrystalline WO₃ films, *ACS Appl. Mater. Interfaces*. 2 (2010) 2623–2628.
- [37] D. Chatzikyriakou, N. Krins, B. Gilbert, P. Colson, J. Dewalque, J. Denayer, R. Cloots, C. Henrist, Mesoporous amorphous tungsten oxide electrochromic films: a Raman analysis of their good switching behavior, *Electrochimica Acta*. 137 (2014) 75–82.
- [38] X. Chang, S. Sun, L. Dong, Y. Dong, Y. Yin, Large-scale production of tungsten trioxide nanoparticles for electrochromic application, *RSC Adv.* 4 (2014) 8994–9002.
- [39] V.C. Fernandes, M.C. Santos, L.O.S. Bulhões, Nanogravimetric studies of tungsten oxide thin films obtained by the polymeric precursor method, *Thin Solid Films*. 515 (2007) 7155–7161.

- [40] J. Vondrák, M. Sedlaříková, J. Velická, P. Špičák, V. Svoboda, J. Kazelle, Insertion of cations into WO_3 investigated by QCM techniques, *J. Solid State Electrochem.* 11 (2007) 1459–1462.
- [41] O. Bohnke, B. Vuillemin, C. Gabrielli, M. Keddám, H. Perrot, H. Takenouti, R. Torresi, An electrochemical quartz crystal microbalance study of lithium insertion into thin films of tungsten trioxide I. Modeling of the ionic insertion mechanism, *Electrochimica Acta.* 40 (1995) 2755–2764.
- [42] O. Bohnke, B. Vuillemin, C. Gabrielli, M. Keddám, H. Perrot, An electrochemical quartz crystal microbalance study of lithium insertion into thin films of tungsten trioxide II. Experimental results and comparison with model calculations, *Electrochimica Acta.* 40 (1995) 2765–2773.
- [43] P.R. Bueno, R.C. Faria, L.O.S. Bulhões, EQCM study during lithium insertion/deinsertion processes in Nb_2O_5 films prepared by polymeric precursor method, *Solid State Ion.* 176 (2005) 1175–1180.
- [44] W.-Y. Tsai, P.-L. Taberna, P. Simon, Electrochemical quartz crystal microbalance (EQCM) study of ion dynamics in nanoporous carbons, *J. Am. Chem. Soc.* 136 (2014) 8722–8728.
- [45] W.L. Kwong, N. Savvides, C.C. Sorrell, Electrodeposited nanostructured WO_3 thin films for photoelectrochemical applications, *Electrochimica Acta.* 75 (2012) 371–380.
- [46] Z. Xie, L. Gao, B. Liang, X. Wang, G. Chen, Z. Liu, J. Chao, D. Chen, G. Shen, Fast fabrication of a $\text{WO}_3 \cdot 2\text{H}_2\text{O}$ thin film with improved electrochromic properties, *J. Mater. Chem.* 22 (2012) 19904–19910.
- [47] J. Mähler, I. Persson, A study of the hydration of the alkali metal ions in aqueous solution, *Inorg. Chem.* 51 (2011) 425–438.

Résumé du Chapitre V

L'importance des condensateurs électrochimiques à base de RuO_2 a déjà été discutée dans le chapitre bibliographique. En bref, RuO_2 présente une capacité spécifique beaucoup plus élevée que tous les autres oxydes de métaux ou de différents types de carbone. Ce matériau présente également une conductivité métallique élevée et une faible résistance interne, ce qui peut provoquer un processus de charge-décharge rapide [1-4]. Cependant, de façon similaire aux films WO_3 et TiO_2 précédemment étudiés, la majorité des travaux récents ne proposent que de nouveaux modes de synthèse pour atteindre une capacité spécifique plus élevée. Il est notable qu'il y a un manque de techniques de diagnostic puissantes capable d'apporter des informations essentielles sur l'apport positif de cette nanostructuration de ces oxydes métalliques [5-7].

Dans la première partie de ce chapitre, les deux techniques classiques (EQCM) et non-classiques (*ac*-électrogravimétrie) ont été exploitées pour étudier les mécanismes de transfert d'ions à l'interface film $\text{RuO}_x \cdot n\text{H}_2\text{O}$ mésoporeux/électrolyte. Pour leur fabrication, similairement aux résultats discutés précédemment pour WO_3 , l'électrogénération en présence de tensioactifs a été choisie. L'utilisation de CTAB comme agent tensio-actif ionique pendant la préparation électrochimique de films $\text{RuO}_x \cdot n\text{H}_2\text{O}$ a conduit à la création de mésopores de $\sim 7\text{-}10$ nm qui sont organisés autour des micelles correspondantes. Les analogues denses ont été également synthétisés par la voie électrochimique dans les conditions similaires mais en l'absence des molécules de CTAB. La structure, la morphologie et la composition des films électrosynthétisés mésoporeux ont été caractérisés et comparés avec leurs homologues compacts.

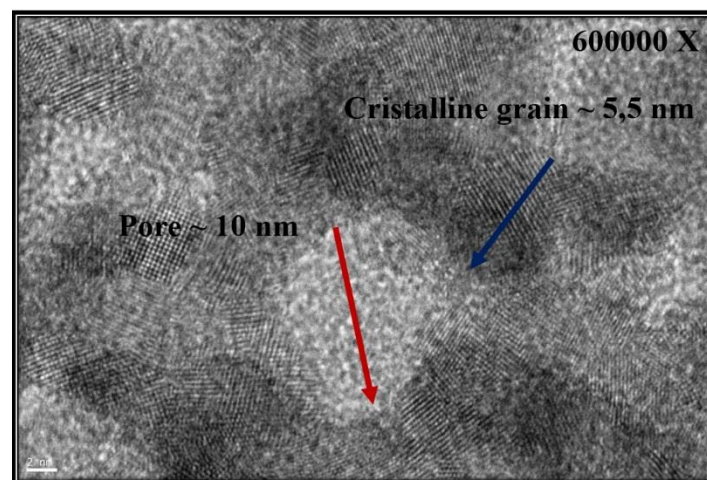


Image HR-TEM d'un film mésoporeux de RuO_2 ; effet de CTAB sur la porosité et la taille des grains du matériau électrogénéré.

La perméabilité de ces films d'oxydes de ruthénium hydratés compacts et mésoporeux vis-à-vis des ions (intercalation / electroadsorption) a été étudiée par *ac*-électrogravimétrie. La nature chimique et le rôle de chaque espèce (ions, ions solvatés et molécules de solvant libre), directement ou indirectement impliquées dans les processus électrochimiques a été estimée pour la première fois. L'influence de la nanostructuration sur la dynamique du transfert des ions et l'impact de la taille des cations de l'électrolyte ont été examinés dans deux électrolytes aqueux, H₂SO₄ et Na₂SO₄.

Les résultats de nos études en solution aqueuse de H₂SO₄ ont conduit à l'identification de plusieurs espèces chargées (H^+ et H_3O^+) impliquées dans le processus de compensation de charge ; molécules d'eau contribuent indirectement au processus dans les deux films de RuO_x.nH₂O compacts et mésoporeux. Même une légère contribution des ions SO_4^{2-} a été détectée dans le cas des films mésoporeux. La contribution de l'espèce chargée a été amplifiée dans les films de RuO_x.nH₂O mésoporeux par rapport aux homologues compacts. Cette étude qualitative et quantitative de la contribution des espèces ioniques dans le processus de compensation de charge, ainsi que des informations dynamiques du transfert interfacial prouve encore le caractère avantageux des films RuO_x.nH₂O structurés pour des applications énergétiques. Il a été prouvé que le film mésoporeux RuO_x.nH₂O accueille mieux les espèces cationiques. Les ions H^+ en particulier, sont transférés rapidement à l'interface électrode mésoporeux / électrolyte, et leur profil de concentration relative en fonction du potentiel est significativement plus élevé par rapport aux valeurs obtenues pour leurs analogues compacts. L'étude a aussi été développée en solution aqueuse de Na₂SO₄, pour étudier à la fois l'impact de la taille du cation et du pH. A partir des profils cinétiques et thermodynamiques obtenus (i vs E , R_{st} vs E , Cap vs E et $C_i - C_0$ vs E), il a été conclu que les films mésoporeux ne présentent aucun avantage. En effet, nos études ont confirmé que les résultats les plus notables de RuO_x.nH₂O sont obtenus dans une solution de H₂SO₄.

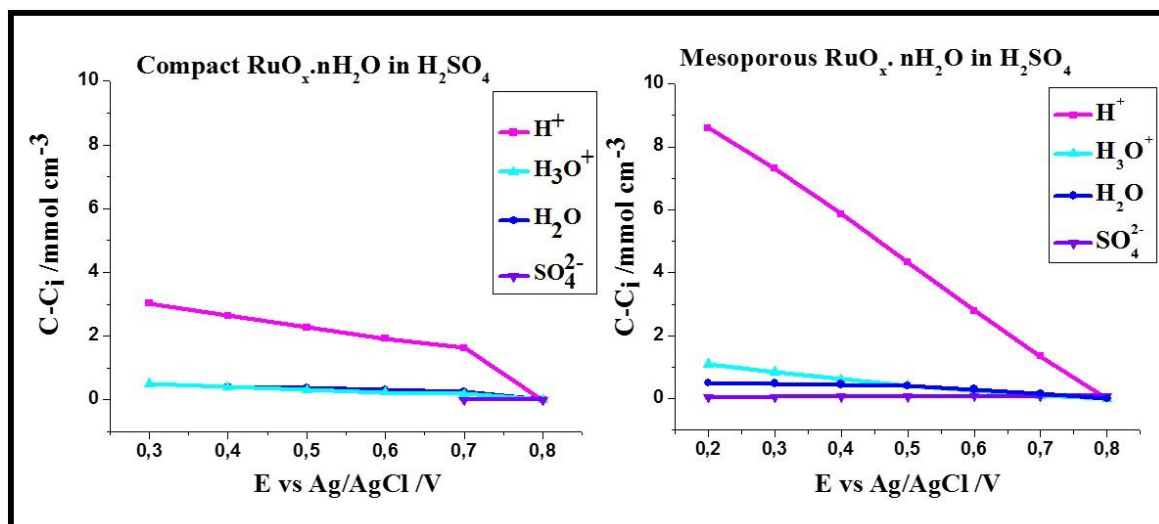


Schéma comparatif de la variation de concentration des espèces intervenant pour un film dense (image à gauche) et un film mésoporeux (à droite).

Un autre aspect intéressant qui a été discuté concerne l'impact de CNTs lors de l'élaboration des films de RuO₂. Ainsi, une approche intéressante pour augmenter la capacité consiste à déposer un matériau pseudo-capacitif sur un support structuré de grande surface spécifique. Par conséquent, la deuxième partie de ce chapitre porte sur l'investigation électrogravimétrique de films composites de type de CNTs/ RuO_x.nH₂O.

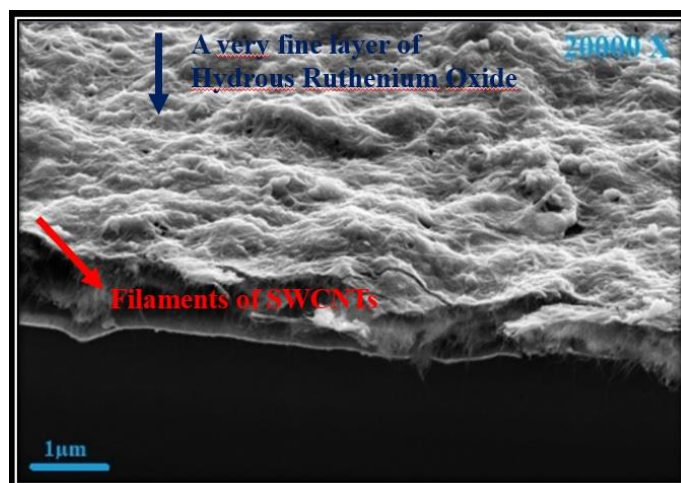


Image MEB de la coupe d'une fine couche d'oxyde de ruthénium couvrant les nanotubes de carbones.

Le film composite a été synthétisé à partir d'une couche très fine d'oxyde de ruthénium hydraté électrodéposée sur un film de CNTs dans le but de combiner les performances pseudocapacitives de RuO_x.nH₂O avec la grande surface spécifique de films de CNTs [8 -11]. De cette façon, les électrodes même recouvertes avec une faible quantité de RuO_x.nH₂O, montrent des capacités spécifiques plus élevées que celles des CNTs nus. En outre, l'évolution

des paramètres cinétiques précédemment introduits sont également présentés pour des films de CNTs et des films de $\text{RuO}_x \cdot n\text{H}_2\text{O}$ pour permettre une comparaison complète afin d'obtenir une meilleure compréhension des différentes réponses en fonction de la nature des trois films.

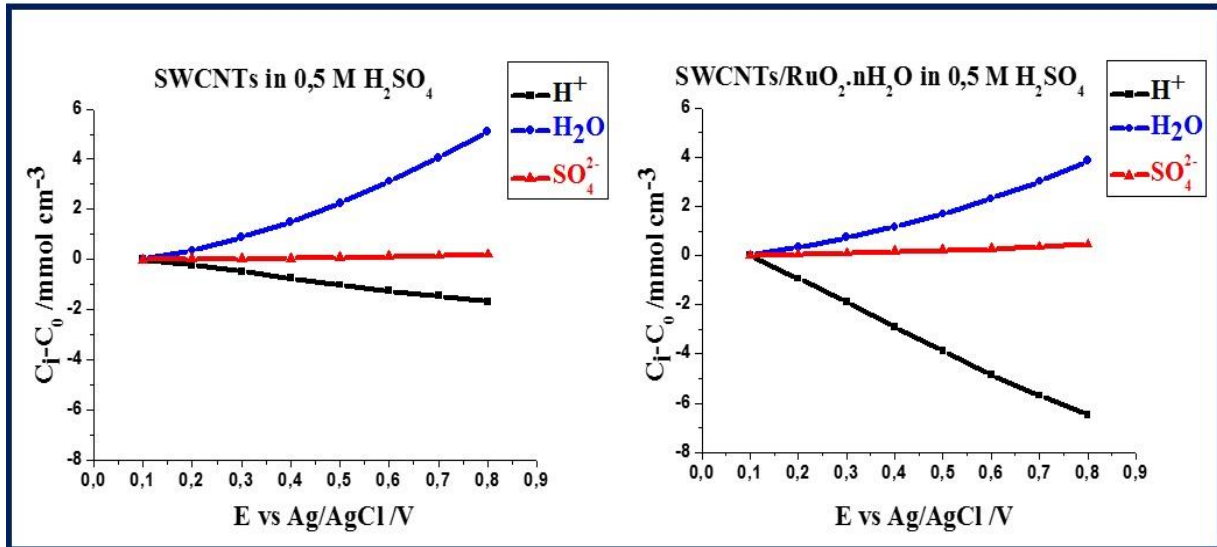


Schéma comparatif de la variation de la concentration des espèces pour un film CNTs pur (image à gauche) et un film composite CNTs/ $\text{RuO}_x \cdot n\text{H}_2\text{O}$ (à droite).

Le comportement des films composites montre, comparativement aux autres films, une amélioration notable en termes de capacité instantanée ainsi qu'un nombre amplifié de cations transférés au sein de ces films. Cette nouvelle structure composite combine plusieurs avantages comme la haute conductivité et la grande surface spécifique des CNTs ainsi que le caractère pseudo-capacitif des couches minces de $\text{RuO}_x \cdot n\text{H}_2\text{O}$ composées de grains nanométriques.

I. Introduction:

The importance of the electrochemical capacitors based on RuO_2 was previously discussed in bibliographic chapter. Briefly, RuO_2 exhibits a much higher specific capacitance than any other metal oxide or various types of carbon materials. Such a superior energy-storage property is believed to be due to pseudocapacitance properties via reversible redox/capacitive reactions. This material has also a high metallic conductivity and a low internal resistance, which can cause a rapid charge-discharge process [1–4]. However, similarly to previously studied MO_x films (WO_3 and TiO_2), the majority of reports propose only new synthesis possibilities for reaching higher specific capacitance and one could feel the lack of powerful diagnostic techniques being able to bring information about the essential factors for which these new nanostructures are preferable [5–7]. For our better understanding in the first section of this chapter, both classical EQCM and EIS techniques were exploited to study the ion transfer behaviour of as-prepared mesoporous hydrous $RuO_x.nH_2O$ films. For their fabrication, similar to previously discussed WO_3 chapter, surfactant-assisted electrodeposition was chosen which provides a facile, low temperature and rapid alternative to the mesoporous thin film synthesis. The structure, the morphology and the composition of these mesoporous electrochemically synthesized films were characterized, and compared with their compact counterparts. The electrochemical performance and ion intercalation/electroadsorption mechanisms were studied in aqueous H_2SO_4 and Na_2SO_4 electrolytes by electrogravimetric methods (EQCM and *ac*-electrogravimetry). A particular attention was paid to some ambiguous aspects, such as the nature of the ions involved in the charge compensation process, the solvation effects and the role of the electrolytes associated to the dynamic of ions transfer at the electrode/electrolyte interface. It has been demonstrated herein that the *ac*-electrogravimetric responses of the electrodeposited $RuO_x.nH_2O$ thin films can serve as an attractive probe to study the complex H^+ and Na^+ transfer mechanisms and to extract subtleties unreachable with classical tools. So, the first part is attributed to the influence of nanostructuration on the dynamics of ions transfer. Furtherly, the studies are completed by investigating the impact of the electrolyte's cation size. Another interesting aspect that would be discussed is the impact of CNTs as a supporting electrode. A 3D array of electrode allows more active materials to be loaded per unit area. An attractive approach to increase the capacitance is to deposit a pseudo-capacitive material onto a high surface area structured support. So, the second part of this chapter includes the

electrogravimetric investigations of CNTs/RuO_x·nH₂O composite electrode by using the previously mentioned classical and non-classical diagnostic tools in order to pursue the ion's kinetics evolution involved with this 3D structure. The composite film is made from a very thin layer of hydrous ruthenium oxide RuO_x·nH₂O electrodeposited onto CNTs layers for the purpose to combine the high pseudocapacitance (also called redox-type capacitance) of RuO_x·nH₂O with the double-layer capacitance of carbon layers [8–11]. By this way, electrodes with low contents in RuO_x·nH₂O were prepared with the instruction already explained in the experimental section. Also, the evolution of different key parameters, already seen, are also investigated for bare CNTs and bare RuO_x·nH₂O which will provide a complete comparison for our better understanding. To do so, a composite of SWCNTs/RuO_x·nH₂O prepared simply via the electrodeposition of a fine layer of RuO_x·nH₂O onto SWCNTs/Au/AT-cut 9MHz quartz crystal is studied to understand the synergic effects of CNTs.

II. Structural Characterizations:

Prior to electrochemical characterizations, the as-prepared hydrous ruthenium oxide, partially dehydrated ruthenium oxide (heated at 150°C) and anhydrous ruthenium oxide (heated at 450°C), were studied by different structural characterization techniques including XRD, XPS, SEM-FEG, TEM, SAED and HR-TEM. In order to easily distinguish the terminology used for studied hydrous and anhydrous films, the RuO_x·nH₂O formula is used whenever hydrous as-prepared and hydrous 150°C heated ruthenium oxide films are investigated. The RuO₂ formula is employed only when the sample is heated up to 450°C and therefore completely anhydrous.

II-1. XRD Characterization of as-prepared RuO₂·xH₂O and RuO₂ heated at 450 °C:

Both as-prepared RuO_x·nH₂O and anhydrous RuO₂ films crystallinity were analyzed using X-ray diffraction. The films were prepared at different deposition times on large-surface Au substrates as described in chapter II. The X-ray diffraction spectra are shown in Fig. V-1. In order to minimize the peak intensities of Au substrate the results of a thick film deposited during 60 min were chosen. Nevertheless, the presence of pronounced peaks at 38°, 45° and 65° coming from Au substrate are inevitable. The apparition of peaks at 58° and 70°, indicates clearly that the as-deposited film is not amorphous, contradicting the observations made by Zhitomirsky et al. [12] and Hu et al. [13,14]. Based on previous XRD analysis for RuO₂, the presence of peaks at 58°, 70° could be attributed to the both hexagonal ruthenium oxide and also metallic

ruthenium [12,14,15]. The broadening of RuO_2 peaks suggests that the deposited films consist of grains with nanometer size. The crystallographic state of as-prepared $\text{RuO}_x \cdot n\text{H}_2\text{O}$ is not clearly the same as annealed RuO_2 and this is mainly due to the presence of structural water. Therefore, it could be concluded that in as-prepared samples both RuO_2 and Ru peaks exist, the structural evolution happens when the sample is annealed in air up to 450°C , as a result the appearance of peaks at 28° , 35° and 54.4° correspond to rutile RuO_2 . Also the hidden low intensity peak at 42° in both cases is related to hexagonal structure of Ru.

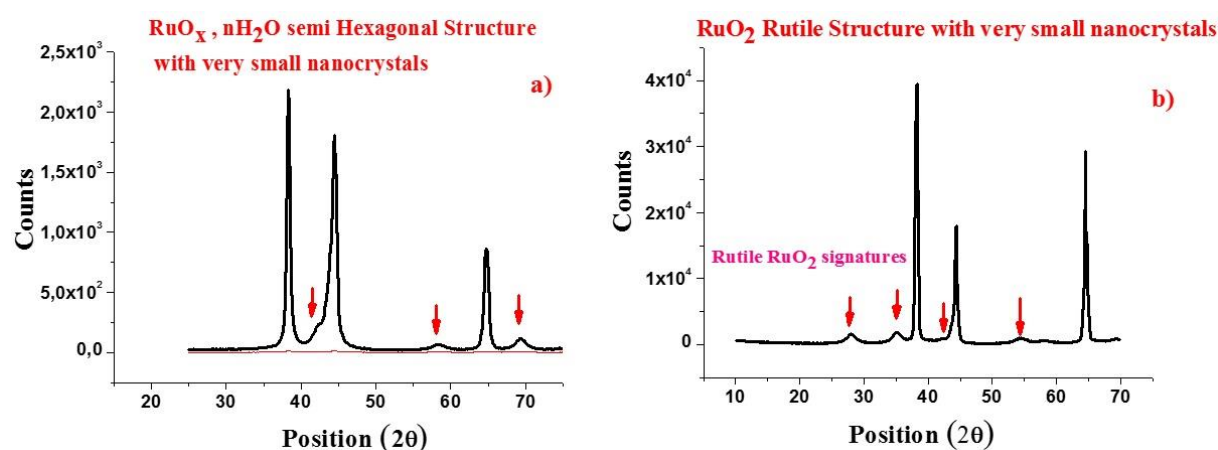


Fig. V-1. The X-ray diffraction patterns of as-prepared $\text{RuO}_x \cdot n\text{H}_2\text{O}$ and RuO_2 films electrodeposited on Au substrate at -0.6V vs Ag/AgCl for 1h (a) as-prepared sample (b) annealed sample at 450°C for 2h.

II-2. SEM-FEG Characterization:

(i) Compact and Mesoporous $\text{RuO}_x \cdot n\text{H}_2\text{O}$:

All $\text{RuO}_x \cdot n\text{H}_2\text{O}$ deposits were examined by SEM to examine the film morphologies. It should be noted that in compact $\text{RuO}_x \cdot n\text{H}_2\text{O}$ (figure V-2a and V-2b), the surface morphology seems quite different than that of mesoporous $\text{RuO}_x \cdot n\text{H}_2\text{O}$ prepared by surfactant assisted deposition (as shown in figure V-2c and V-2d). Network-like morphology with a forest like branches in as-prepared $\text{RuO}_x \cdot n\text{H}_2\text{O}$ give their place to attached-spherical like grains with larger domains of intergrain porosity in mesoporous counterparts. This could be related to the impact of surfactant CTAB molecules in order to procure controlled porosity.

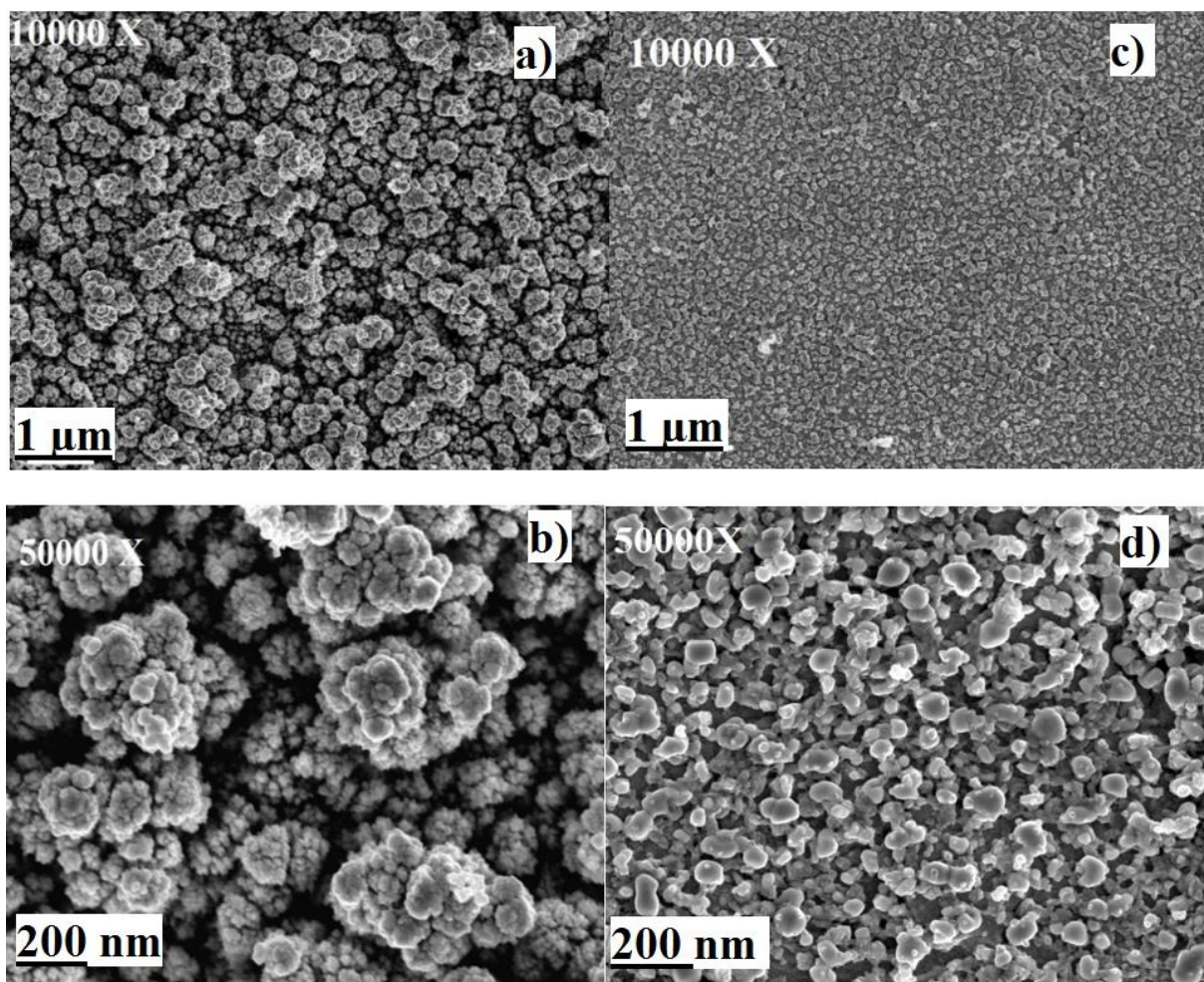


Fig. V-2. SEM-FEG characterization of as-prepared compact (a, b) and mesoporous (c, d) RuO_x·nH₂O. (The samples are electrodeposited at -0,5 V for 30 min).

The SEM-FEG results highlight that morphologies of RuO_x·nH₂O are also affected by the rate of deposition. In the absence of CTAB molecules this rate is very high and the film thickness continues to grow fast (based on EQCM results not show here) (figure V-2a and V-2b). On the other hand, in the presence of CTAB the formation of cationic spherical micelles at the interface forms an inhibitor layer so that the electrodeposition slows down as it could only take place around these spherical micelles [16,17]. After the deposition, when the sample is rinsed properly and dried in air for CTAB removal, a porous morphology is obtained. These obtained three-dimensional (3D) porous RuO_x·nH₂O are known to enable the ions transport by providing pathways between the material and the electrolyte for the sake of enhancing the pseudo-capacitance.

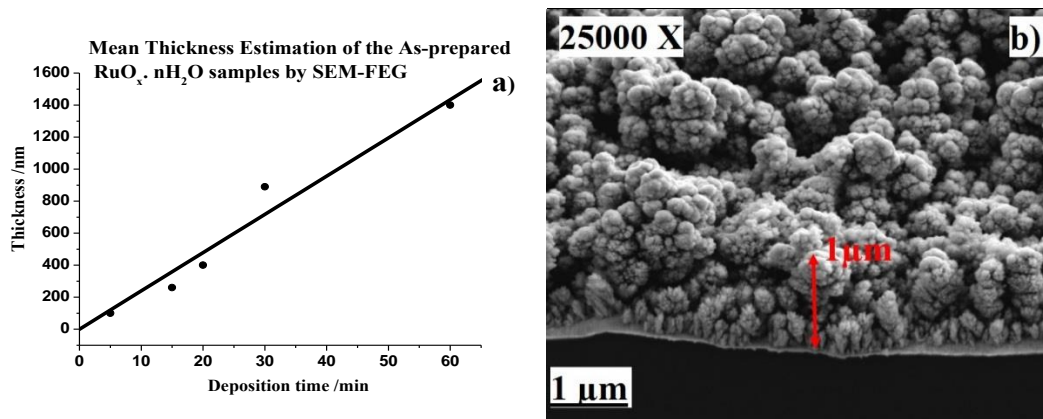


Fig. V-3. Mean changes electrodeposited $\text{RuO}_x \cdot n\text{H}_2\text{O}$ film thickness at different deposition times determined through SEM-FEG measurements (left) cross-section image of the as-prepared $\text{RuO}_x \cdot n\text{H}_2\text{O}$ (right) (prepared potentiostatically at $-0,5 \text{ V}$ during 1h).

As it could be seen in figure V-3, the film thickness estimation of as-prepared $\text{RuO}_x \cdot n\text{H}_2\text{O}$ is not easy since the film is not homogenous, the average thickness is estimated for different deposition times revealing the spontaneous growth of the film (figure V-3).

(ii) SWCNTs / $\text{RuO}_x \cdot n\text{H}_2\text{O}$:

The preparation of the composite film was previously explained in the experimental section. Fig. V-4 shows the morphological state of the surface of SWCNTs covered by a thin layer of $\text{RuO}_x \cdot n\text{H}_2\text{O}$ electrodeposited with three different magnifications. The surface of virgin fine chains of carbon nanotubes is protected with a grey like coverage of hydrated ruthenium oxide film.

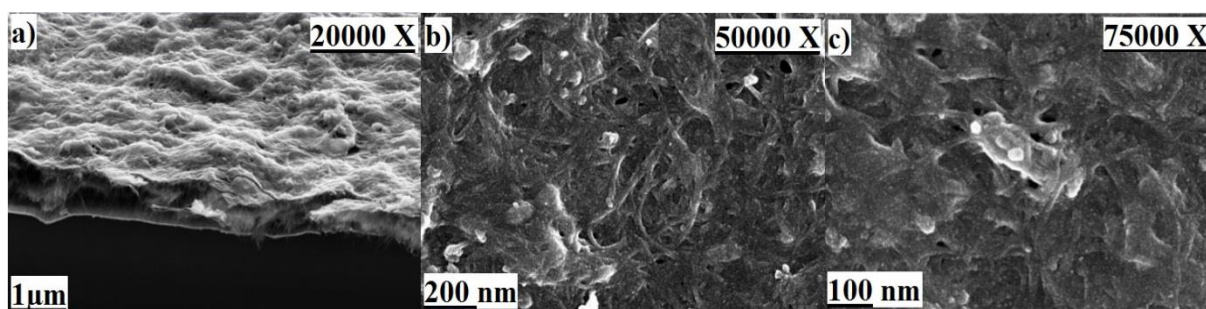


Fig. V-4. SEM-FEG images of SWCNTs electrode covered by thin layer of hydrated ruthenium oxide.

II-3. Targeting Evolution of Morphology and Crystallography by TEM & SAED: The effect of calcination

The XRD results do not give a clear idea of amorphous and/or crystalline properties for as-prepared $\text{RuO}_x \cdot n\text{H}_2\text{O}$. However, contradicting what is reported in several publications about the amorphousness of $\text{RuO}_x \cdot n\text{H}_2\text{O}$ [12–14], the appearance of even small peaks in previously

discussed XRD results proves the existence of crystalline domains. Therefore, SAED studies are pursued for further investigation of this aspect.

(i) **The Effect of Heat Treatment on Compact Ruthenium oxide:**

Figure V-5a illustrates the morphology of the compact as-prepared $\text{RuO}_x \cdot n\text{H}_2\text{O}$ film consisting of dense dark branches. The SAED (fig. V-5c) reveals a certain crystallinity with the presence of faint rings. The as-prepared film is indexed as metallic Ru (hcp). In Figure V-5b different morphologies are observed after annealing at 450°C during 2h. In this image small grains, bigger grains and also compact branches co-exist together, but with exactly the same diffraction pattern. At 450°C , the SAED pattern is modified. It exhibits the polycrystalline nature of tetragonal RuO_2 : the RuO_2 rutile structure.

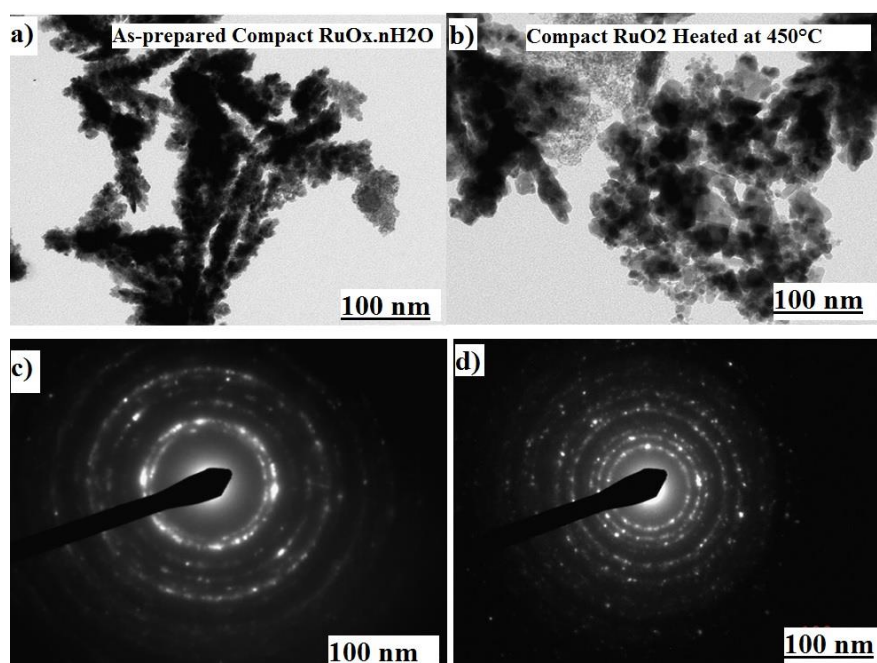


Fig. V-5. TEM images and corresponding SAED for compact as-prepared $\text{RuO}_x \cdot n\text{H}_2\text{O}$ (a, c) and (b, d) RuO_2 heated at 450°C .

(ii) **The Effect of Heat Treatment on Porous Ruthenium oxide:**

TEM images with corresponding SAEDs for mesoporous $\text{RuO}_x \cdot n\text{H}_2\text{O}$ are now illustrated in figure V-6. Here, CTAB molecules were used to create porosity in the film and the mesoporous samples were heated up to 150°C in order to ensure CTAB removal. As a consequence, the comparison is made between as prepared $\text{RuO}_x \cdot n\text{H}_2\text{O}$ samples heated at 150°C and annealed RuO_2 at 450°C .

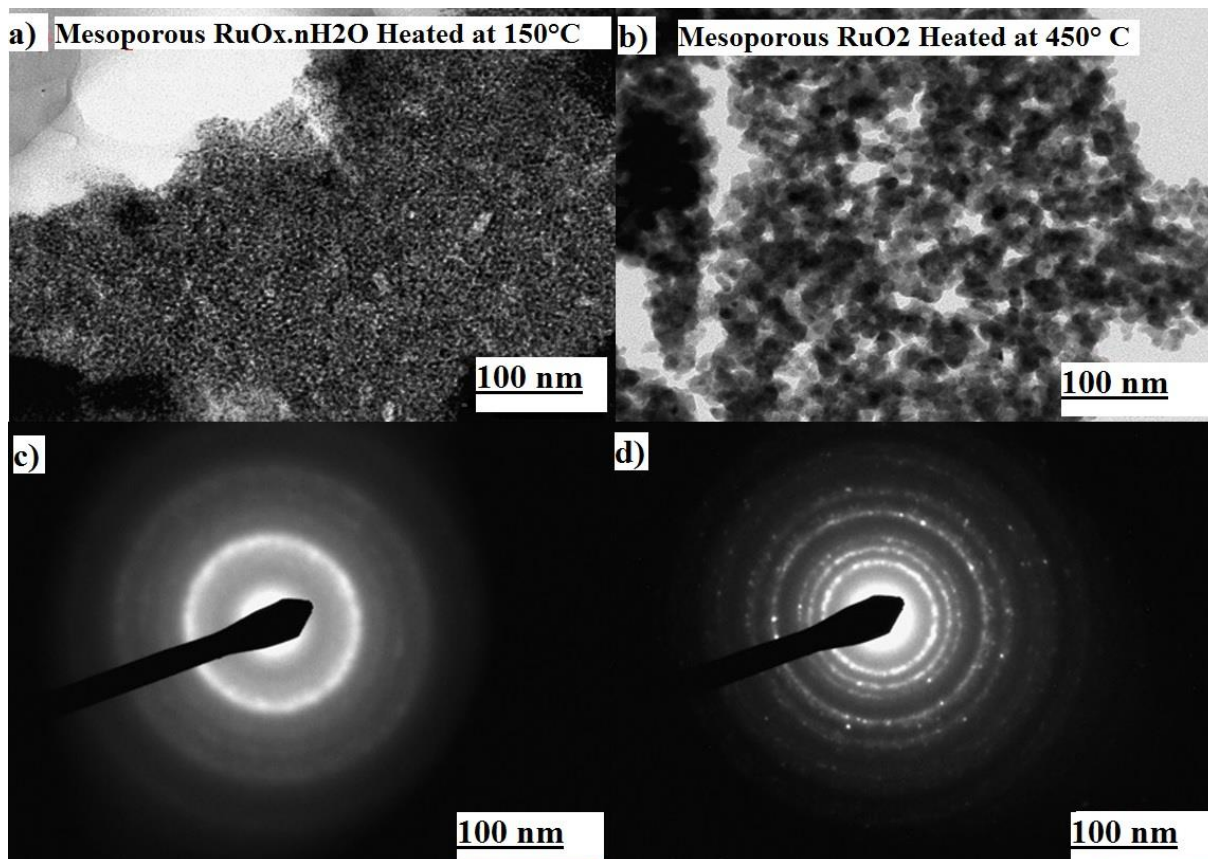


Fig. V-6. TEM images with corresponding SAEDs for as-prepared mesoporous $\text{RuO}_x \cdot n\text{H}_2\text{O}$ heated at 150°C (a, c) and (b, d) mesoporous RuO_2 calcinated at 450°C .

Fig. V-6a reveals nanoparticles of $\sim 2\text{-}3\text{ nm}$ but the porosity is not evident and difficult to measure for the 150°C sample. Furtherly when the film is thermally treated up to 450°C the most distinguishable change is the appearance of grown aligned grains of around $6\text{-}7\text{ nm}$ and also the clear existence of intergrain porosity (fig. V-6b). The observations are accompanied by the corresponding electron diffractions where diffuse rings at 150°C (because of small size of crystallites) turn to very well pronounced distances for the calcined analogues at 450°C . In this case, nanoscale domains create a network of highly porous structure as already mentioned [18,19]. We note also the change of the crystallographic structure of the film (Ru (hcp) to RuO_2 (tetragonal) like the compact film.

(iii) The Effect of Structuration on Hydrous Ruthenium Oxide Films:

Finally, a comparison between both compact and mesoporous $\text{RuO}_x \cdot n\text{H}_2\text{O}$ is shown in figure V-7 in which both morphological and crystallographic information are shown. There is no trace of small nanosize domains with intergrain porosity in compact film, the SAED pattern on the other hand reveals more clear rings with measurable distances in compact film suggesting that the compact $\text{RuO}_x \cdot n\text{H}_2\text{O}$ is more crystalline.

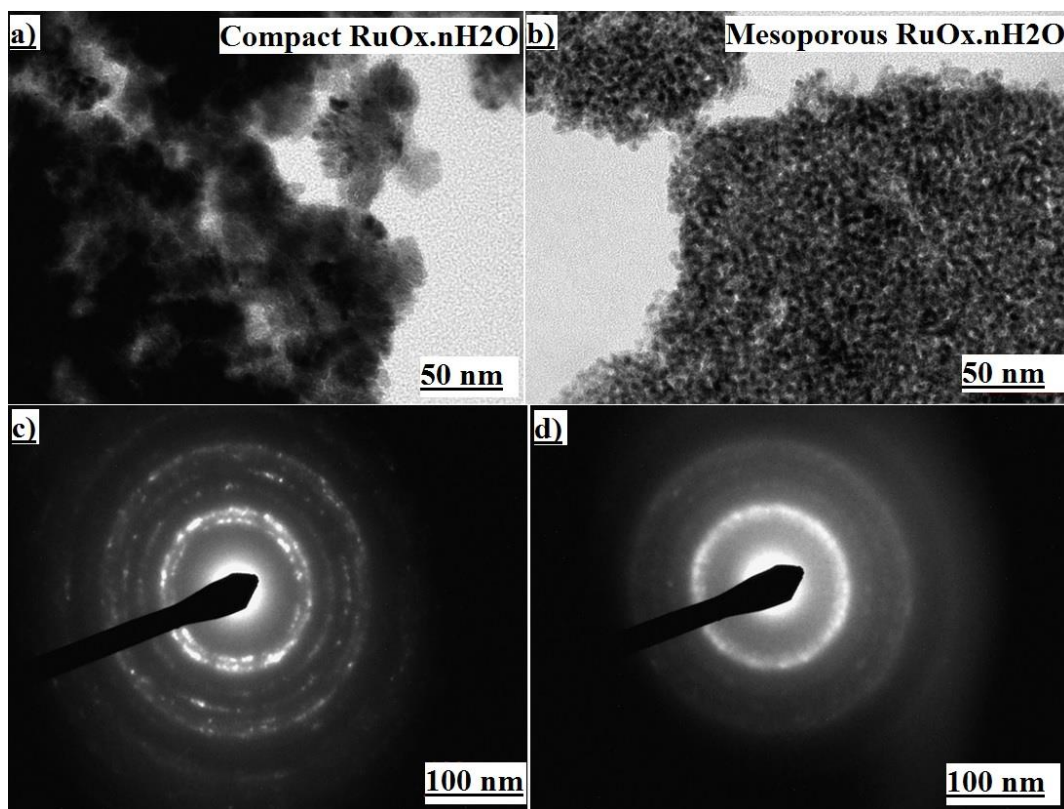


Fig. V-7. TEM images with corresponding SAEDs for as-prepared compact (a, c) and mesoporous $\text{RuO}_x \cdot n\text{H}_2\text{O}$.

II-4. HR-TEM Results

(i) Mesoporous Ruthenium oxide:

In order to observe more precisely the pore characteristics, HR-TEM images of both non-porous and mesoporous $\text{RuO}_x \cdot n\text{H}_2\text{O}$ (Fig. V-8a, V-8b) along with an image of annealed RuO_2 at 450°C are presented here (Fig. V-8c). The term non-porous and/or compact $\text{RuO}_x \cdot n\text{H}_2\text{O}$ is used to differentiate the films prepared by classical electrodeposition from mesoporous films prepared by surfactant-assisted electrodeposition using CTAB.

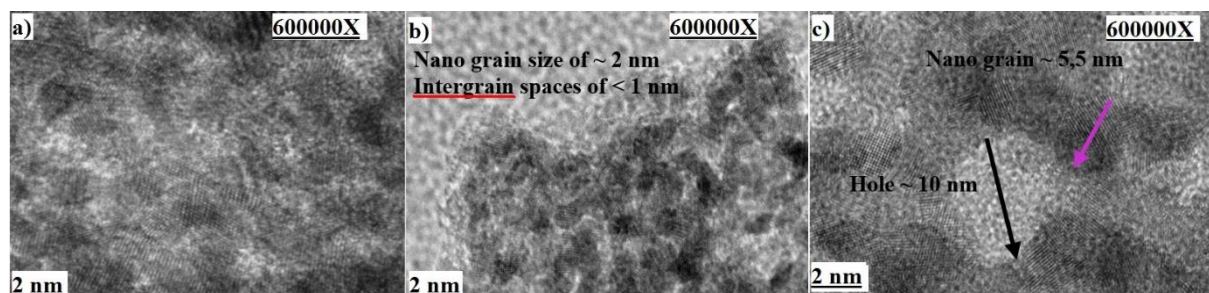


Fig. V-8. HR-TEM images for (a) as-prepared compact (b) as-prepared mesoporous and (c) 450°C annealed $\text{RuO}_x \cdot n\text{H}_2\text{O}$.

Pores are not detected in fig. V-8a, however the attached spherical nanoparticles of hydrated ruthenium oxide are observed. Fig. V-8b corresponds to mesoporous sample when the CTAB molecules are removed by rinsing: small nano-grains of around 2 nm appear. In fact, the particle size is the same as compact film and the main difference is the presence of intergrain spaces less than 1nm which highlights the apparition of porosity. Then, when the sample is heated up to 450°C, the obvious changes in both nanoparticles size and intergrain porosity are observed: the nanoparticles are now grown to around 5 nm, the porosity is developed and easily visualized. The diameter of a trapped pore is shown and measured in figure V-8c. It indicates that after the heat treatment, the different structures aggregate to form bigger particles or pores.

(ii) SWCNTs / RuO_x.nH₂O:

HR-TEM was also conducted to provide supplementary information about the structure of our as-synthesized composite film. Figure V-9 shows hydrous ruthenium oxide nanoparticles which are dispersed and well sheltered among filaments of CNTs. The inset shows the dimension of a single nanotube.

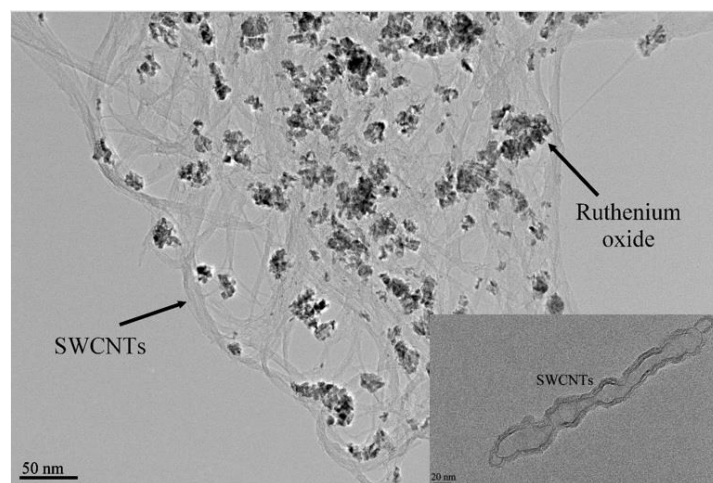


Fig. V-9. HR-TEM images of SWCNT/RuO_x.nH₂O; the inset shows a sole SWCNT.

II-5. XPS Characterization, The impact of Heat Treatment

As previously discussed in the experimental section the mechanism of RuO_x.nH₂O electrodeposition is not fully understood [12–14,20,21]. Hydrated ruthenium chloride, the salt used in the solution of electrogeneration, is a heterogeneous ionic material with an average ruthenium oxidation state between 3 and 4, close to 4. The oxidation degree of annealed RuO₂ in rutile structure is 4. The mechanism of formation of pure RuO₂ from RuCl₃·nH₂O precursor is rather complex. Nevertheless, when it comes to the potential application of this metal oxide

as supercapacitor there are several reports accentuating on the preferable functionality of hydrated ruthenium oxide, $\text{RuO}_x \cdot n\text{H}_2\text{O}$ [22–24]. Therefore, it is curious to follow the evolution of oxidation states when both compact and mesoporous films lose their hydration content by progressive thermal treatment and to compare their binding energy values with what is reported in the literature. To follow this investigation, first $\text{RuCl}_3 \cdot x\text{H}_2\text{O}$ as the main precursor is analyzed. This provides a reference for both O1s and Ru3d binding energies as shown in fig. V-10.

(i) XPS results of $\text{RuCl}_3 \cdot x\text{H}_2\text{O}$ Precursor:

The acquisition reveals a Ru ($3d_{5/2}$) signal at 282.5 eV (Fig. V-10b) with the corresponding $3p_{3/2}$ peak at 464.1 eV (not presented here). These values are in good agreement with those obtained by D. J. Morgan [15]. The peak at 530,5 eV in the O(1s) signal (Fig. V-10a) is attributed to the OH as opposed to the formation of Cl–O bonds, an assignment supported by the absence of any signal above 202 eV attributable to Cl–O bond formation (Cl ($2p$) level not presented here).

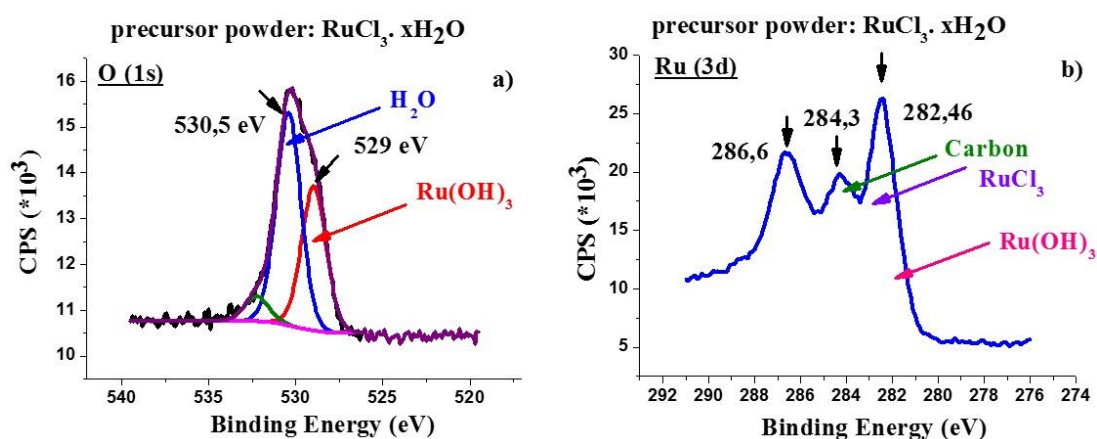


Fig. V-10. XPS results of $\text{RuCl}_3 \cdot x\text{H}_2\text{O}$ used as the precursor for the electrodeposition: O 1s (a), Ru 3d (b) core level spectra.

Here, the ratio of Ru (282.5 eV)/Cl (199 eV) signals is in excellent agreement with that expected for stoichiometric RuCl_3 supporting the assignment of the signal at 199 eV to Ru(III)–Cl bond and consistent with a range of transition metal trichlorides. It has been shown that RuCl_3 is inherently a hygroscopic compound and commercially sourced ruthenium chloride is not a homogeneous compound. The Ru peak at 282.5 eV can be explained by consideration of the O (1s) region (Fig. V-10a). With a BE (binding energy) in the range already identified for Ru (III) compounds in our analysis and also in ref [15], it is expected that this would be attributable to trivalent ruthenium. The O (1 s) signal at 530.5 eV is assigned to OH groups, and the ratio of

the fitted photoelectron peaks gives a Ru/O ratio of ~0.3 and is attributed to Ru(OH)₃, an assignment in line with hydrolysis products. The small deviation in the ratio probably due to C–O containing species presents as evident from the C(1 s)/Ru(3d) region. The Ru–Cl bond were identified and assigned to the signal at 199 eV. The changes at the surface of RuCl₃, XPS reveals two co-existing Ru(III) species, RuCl₃ and Ru(OH)₃, where Ru (3d_{5/2}) signal at 282.5 eV and Cl (2p_{3/2}) at 199eV are due to RuCl₃.

Based on previously discussed conventional XRD and SAED results of samples, RuO₂ annealed at 450°C has the rutile structure, this was very well supported by our XPS results. Also the presence of structural water in the as-prepared and 150°C heated RuO_x.nH₂O samples is the reason of their differences with RuO₂ in rutile structure. However, their XPS spectra remain quite similar, proving the co-existence of Ru metallic and hydrous RuO_x.nH₂O in the as-prepared and 150°C annealed sample, the pure rutile RuO₂ for the 450°C heated sample.

Compound	Peak	Binding Energy (eV)	Std. Dev.
Ru (0)	Ru 3d_{5/2} Ru 3d_{3/2}	279.8 284.0	0.1
RuO₂	Ru 3d_{5/2} Ru 3d_{3/2} Ru 3d_{5/2sat.} Ru 3d_{3/2sat.}	280.8 284.8 282.5 286.7	0.6
RuO₂. nH₂O	Ru 3d_{5/2} Ru 3d_{3/2} Ru 3d_{5/2sat.} Ru 3d_{3/2sat.}	280.8 285.0 282.7 286.9	0.6
RuCl₃ and Ru(OH)₃	Ru 3d_{5/2} (chloride) Ru 3d_{3/2} (chloride) Ru 3d_{5/2} (hydroxide) Ru 3d_{3/2}(hydroxide)	282.8 287 282.3 286.4	

Table V-1. Reference binding energies of Ru 3d core level for different Ru compositions [15].

(i) $\text{RuO}_x \cdot n\text{H}_2\text{O}$ and RuO_2

Figures V-11 to V-13 show the Ru (3d) and O (1s) regions for hydrated RuO_2 (fig V-11 and V-12) and anhydrous RuO_2 . Hydrated RuO_2 exhibit a broad peak envelope whilst rutile RuO_2 is composed of sharp, asymmetric narrow features reminiscent of metallic ruthenium. There is no apparent difference for the Ru (3p) level, with identical peak shapes and BEs observed (not presented here). The broader 3d peak structure of the hydrate initially suggests the presence of multiple oxidation states, and many have assigned higher BE features to the presence of RuO_3 . However, RuO_3 is known not to exist in a stable bulk phase and previous reports have relied on its isolation in the physisorbed state [25]. Kim et al. [26] studied carbon-free, stoichiometric RuO_2 and determined the broad structure of the Ru (3d) to be due to satellite structure from core-hole screening rather than mixed oxidation states.

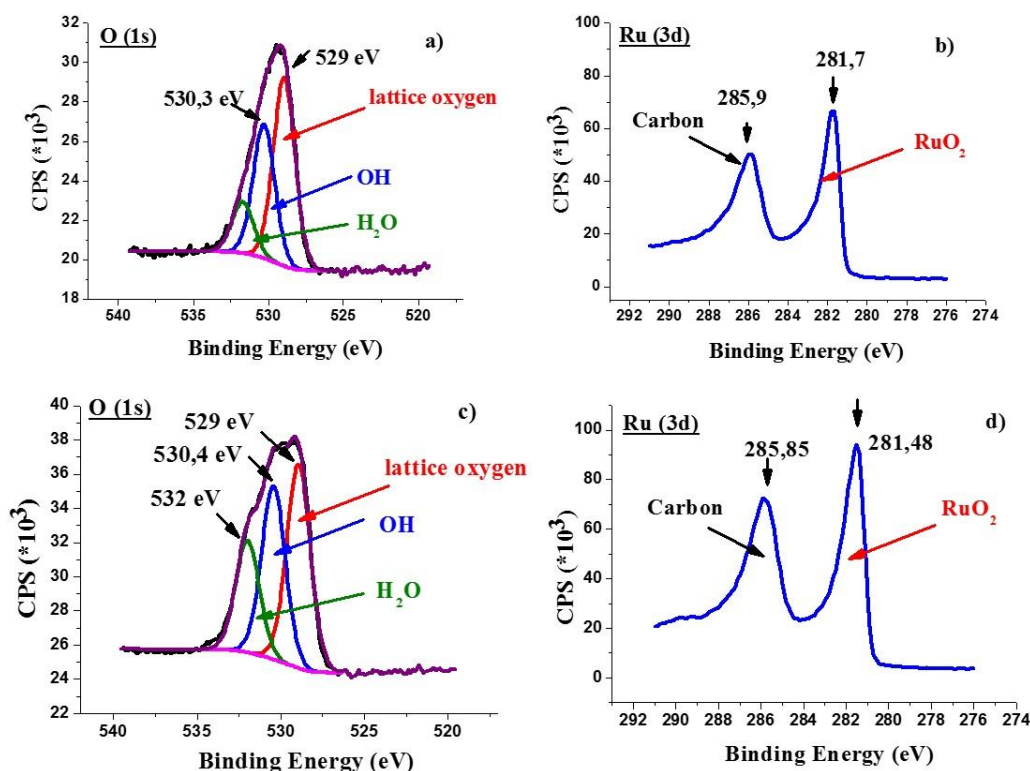


Fig. V-11. XPS results for as-prepared compact (a, b) and mesoporous (c, d) $\text{RuO}_x \cdot n\text{H}_2\text{O}$: O 1s (a, c), Ru 3d (b, d) core level spectra.

Foelske et al. [27] determined that a peak centered at 282.6 eV and developed at temperatures above 150 °C was indicative of an amorphous crystalline transition. The development of this peak with increasing temperature (compare Fig V-12 and V-13) suggests that this feature is an indication of ruthenium oxide hydration level and crystallinity, its onset in accordance with kinetic and thermal data indicating the loss of structural water. Assignment of this peak to RuO_3 is discounted because of the Ru/O stoichiometry already discussed in respect to the 3d orbitals.

This process is also applied to the O (1s) region, with a Shirley background, lattice oxygen and satellite component line shapes equivalent to those used for the Ru (3d) level. This methodology has been previously applied to conducting oxide systems including RuO₂ [15].

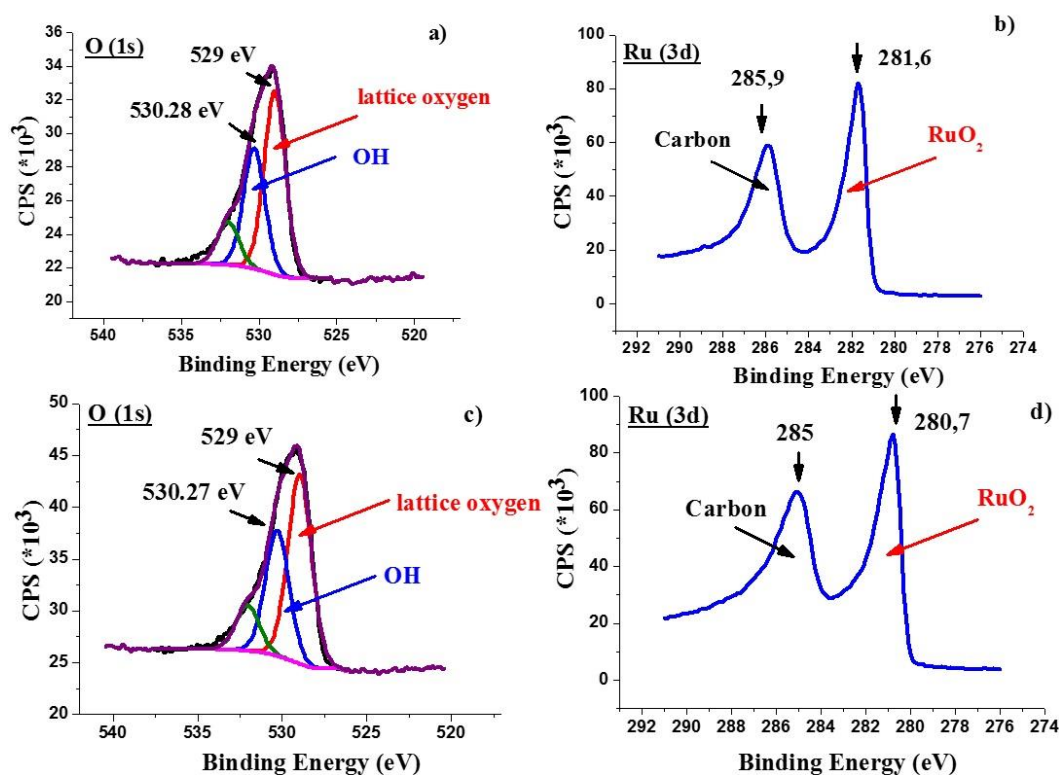


Fig. V-12. XPS results for as-prepared compact (a, b) and mesoporous (c, d) RuO_x.nH₂O annealed at 150°C for 2h: O 1s (a, b), Ru 3d (b, d) core level spectra.

For O (1s) peak assignment, we first consider the anhydrous oxide and assign lattice oxygen to the signal at 529-529.1 eV. Since the sample is annealed at high temperature, it is equally difficult to assign this signal to water. The fitting of the Ru(3d)/C(1s) level indicates the presence of oxygen containing carbon bonds and so assigns this O (1s) energy to organic C–O bonds. This is confirmed by the absence of significant concentration of such species in the hydrated ruthenium oxide Ru (3d)/C (1s) spectrum. The remaining peak at 530.8 eV is at first readily assigned to surface hydroxide and supported by the extra intensity in the hydrated RuO₂ sample (Fig. V-11); however, it is clear from the thermal studies that the overall density of any OH groups for the anhydrous sample is low. Therefore, it is proposed that the majority of the intensity of this feature for the anhydrous oxide is primarily due to many-body screening effect of the conduction electrons as observed.

In respect of the hydrated oxide (figures V-11 and V-12), the reverse is true, and the major intensity of this peak is due to hydroxyl groups; however, a small percentage of this overall intensity, as for the anhydrous rutile oxide, is attributed to the screened structure. Clearly, the

model applied herein for both anhydrous and hydrated ruthenium oxide is in excellent agreement with the expected Ru/O stoichiometry supporting the peak shapes and assignments recently published in ref [15] (see Table V-1).

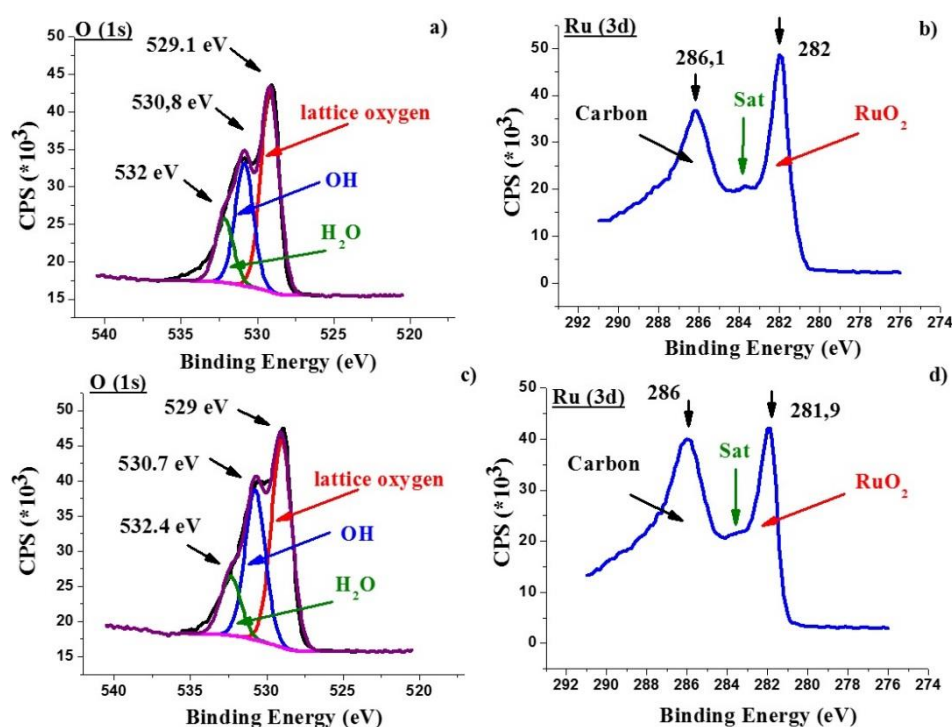


Fig. V-13. XPS results for compact and mesoporous RuO₂ annealed at 450°C for 2h: O 1s (a, b), Ru 3d (b, d) core level spectra.

Therefore, in the confirmation of previously discussed results of conventional XRD and SAED on heated samples, herein our XPS spectra also confirmed the presence of hydrated ruthenium oxide in the surface of both as-prepared and 150°C heated samples. The annealed samples at 450°C confirm the existence of anhydrous RuO₂ with rutile structure.

III. Electrochemical Characterization: Cyclic Voltammetry and Classical EQCM Study

III-1. Cyclic electrogravimetry

As previously introduced in the experimental chapter, EQCM is a simultaneous measurement of the resonant frequency variation of a quartz resonator determined by QCM and of the current during CV measurements. A typical EQCM curve gives the potential vs current profile, simultaneous to the microbalance frequency variation vs applied potential as shown in fig. V-14. The quartz resonant frequency variations are converted into mass changes through the

Sauerbrey relation (chapter II eq. 1). By this way, the mass changes of the electrodes during ions transfer can be monitored.

It is to be noted that most effective electrochemical behaviour for $\text{RuO}_x \cdot n\text{H}_2\text{O}$ especially in terms of specific capacitance is reported in H_2SO_4 . Even though, the same high value of current is not observed in other sulfate mediums including Li_2SO_4 , Na_2SO_4 or K_2SO_4 , here, the electrochemical behaviour is also studied in Na_2SO_4 in order to study the cation size effect.

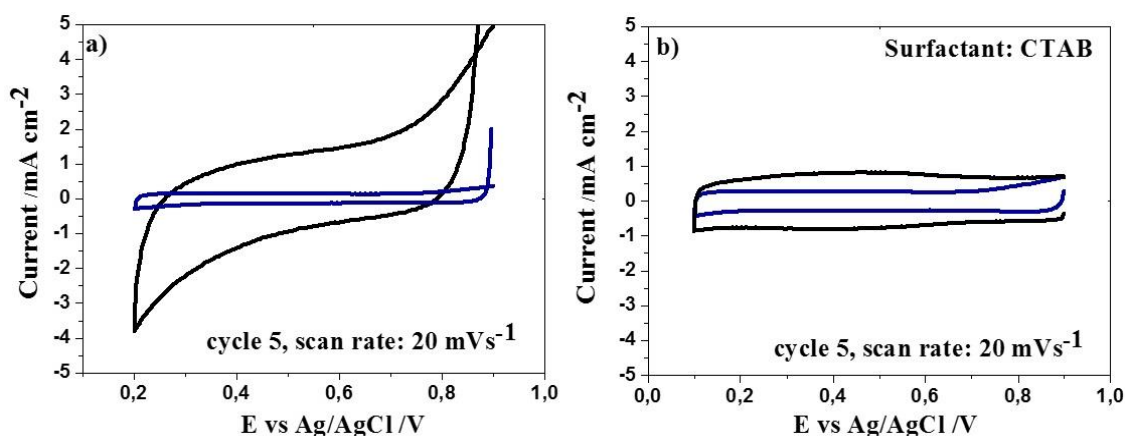


Fig. V-14. CVs for both compact (a) and mesoporous (b) $\text{RuO}_x \cdot n\text{H}_2\text{O}$ in H_2SO_4 0.5 M (black) and Na_2SO_4 0.5 M (blue).

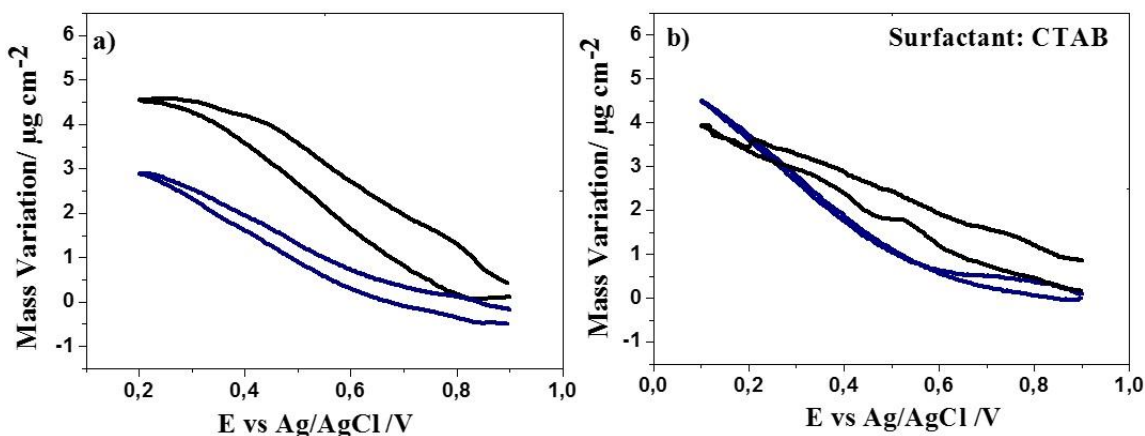


Fig. V-15. Mass changes for both compact (a) and mesoporous (b) $\text{RuO}_x \cdot n\text{H}_2\text{O}$ in H_2SO_4 0.5 M (black) and Na_2SO_4 0.5 M (blue).

The EQCM results of compact and mesoporous $\text{RuO}_x \cdot n\text{H}_2\text{O}$ film tested at room temperature in aqueous 0.5M H_2SO_4 and 0.5M Na_2SO_4 electrolytes are presented in Fig. V-14 (I vs. V) and Fig. V-15 (mass vs. V). The CV curves show a typical rectangular type capacitive response in the potential range of 0.2 V to 0.9 V vs Ag/AgCl. In agreement with the literature data under similar dynamic conditions, a symmetric capacitive voltammogram is obtained suggesting the same rate of ions exchange at this scan rate (Fig. V-14).

The mass responses shown (Fig. V-15) in the reduction branches correspond to the resonant frequency drops of the modified quartz microbalance due to the mass increases of the films during reduction bias. In a reverse process, during oxidation bias, the inner species are expelled out from the film, resulting in a decrease of the electrode mass. By looking through these results following observations can be extracted. On the one hand, in compact $\text{RuO}_x \cdot n\text{H}_2\text{O}$, the mass variations in H_2SO_4 are 1.5 times more important than in Na_2SO_4 : it could be assumed that the amount of small ionic radius H^+ ions transferred at the interface is more important than larger Na^+ ions. Maybe it is mainly due to confined intergrain species in compact $\text{RuO}_x \cdot n\text{H}_2\text{O}$ compared to mesoporous film. This assumption could be also supported by previously shown HR-TEM images. On the other hand, mesoporous $\text{RuO}_x \cdot n\text{H}_2\text{O}$, with a larger specific surface area developed by nanometric pore volumes accommodate equally even larger species including Na^+ whether hydrated or accompanied by free solvent molecules. As a consequence, the same quantity of mass variation is observed for both H_2SO_4 and Na_2SO_4 medium.

Among similar works there are only few reports on the use of classical EQCM as an electrochemical tool to study Ru/RuO₂ behaviour. J. Juodkazyte et al. [20] studied and compared the voltammetric and microgravimetric behavior of active Ru, electrochemically passivated ruthenium (Ru/RuO₂) and thermally formed RuO₂ electrodes in a H₂SO₄ electrolyte. In their study, cycling the potential of thermally formed RuO₂ electrode led to continuous decrease in electrode mass, this has been attributed to irreversible dehydration of RuO₂ layer. M. Vukovic et al. [28] used cyclic voltammetry and EQCM measurements for the characterization of electrodeposited ruthenium under the conditions of repetitive potential cycling in 0,5 M sulfuric acid solution. Several types of non-stoichiometric surface reactions, which include the formation of various ruthenium oxyhydroxide species, were proposed. The stability of the electrodeposited ruthenium layer (prepared galvanostatically) was investigated. Their electrodeposited Ru on gold plated quartz crystal exhibited a capacity of 870 F g⁻¹ which is comparable with the capacitances reported for hydrous ruthenium oxide [22–24].

III-2. Specific Capacitance Calculation

Also, as previously mentioned in the bibliography section and reported by several publications, it is in its hydrous form ($\text{RuO}_x \cdot n\text{H}_2\text{O}$) that this oxide exhibits the highest capacitance values that have been described. Recently, Zhang et al. [24] attributed the increase of the specific capacitance to a contribution of the RuO₂ bulk: the bulk of $\text{RuO}_x \cdot n\text{H}_2\text{O}$ can be permeable to the

electrolyte ions due to some highly hydrated channels. The specific capacitance of $\text{RuO}_x \cdot n\text{H}_2\text{O}$ films could be calculated from previously shown CVs by the following equation [25]:

$$C_s = \frac{I\Delta t}{m\Delta V}$$

where C_s is the specific capacitance calculated from I , applied current (A) divided by scan rate (V s^{-1}) and normalized by the quantity of mass (g) electrodeposited. It is to be mentioned that mesoporous films are produced by surfactant assisted electrodeposition and that the mass of mesoporous film is calculated after rinsing and thermal treatment of the film for CTAB removal. Since this step is not controlled electrochemically the quantity of mass deposited might not be the exact value as the mass obtained by classical electrodeposition. The estimated instantaneous specific capacitance for two types of films are presented in Fig. V-16. A specific capacitance of $\sim 300 \text{ F g}^{-1}$ for non-porous $\text{RuO}_x \cdot n\text{H}_2\text{O}$ is obtained in acid medium which is over 6 times higher than the value $\sim 40 \text{ F g}^{-1}$ obtained in Na_2SO_4 . For mesoporous $\text{RuO}_x \cdot n\text{H}_2\text{O}$ the estimated specific capacitance is 818 F g^{-1} . This value is much more important than $\sim 280 \text{ F g}^{-1}$ which are calculated in Na_2SO_4 for the same film and over 2 times higher than the value estimated for compact $\text{RuO}_x \cdot n\text{H}_2\text{O}$ in H_2SO_4 . Also, the obtained value for mesoporous film stands higher and/or in some cases as high as other estimations reported for hydrated RuO_2 in the literature (see Chapter I) [23,24,29–31]. What could be concluded from these estimations is the advantageous aspect of mesoporosity. Having larger surface area due to pore volumes obviously provides easiness of transfer and transport for the involved species and facilitates their transfer/transport.

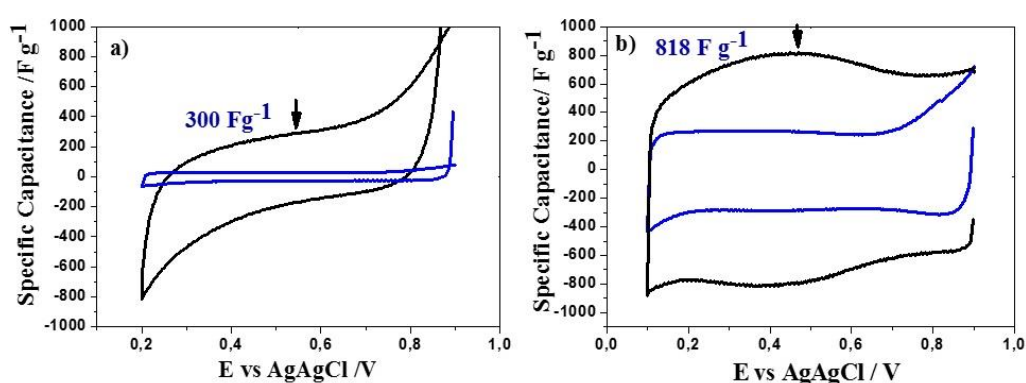


Fig. V-16. Specific Capacitance for both compact (a) and mesoporous (b) $\text{RuO}_x \cdot n\text{H}_2\text{O}$ in H_2SO_4 0.5 M (black) and Na_2SO_4 0.5 M (blue).

III-3. Relative Molecular Mass Estimation,

Fig. V-17 depicts the variation of $F \times \frac{\Delta m}{\Delta q}$ values as a function of the applied potential for compact (fig. V-17a and V-17b) and mesoporous film (fig. V-17c and V-17d). According to this calculation, an absolute molecular mass value of $\sim 1 \text{ g mol}^{-1}$ was only obtained for mesoporous films measured in 0.5 M H_2SO_4 with a scan rate of 20 mV s^{-1} , which is close to the molecular weight of H^+ (Fig. V-17c). In the other cases, a clear identification is not possible as shown in the other three figures (V-17a, V-17b and V-17d).

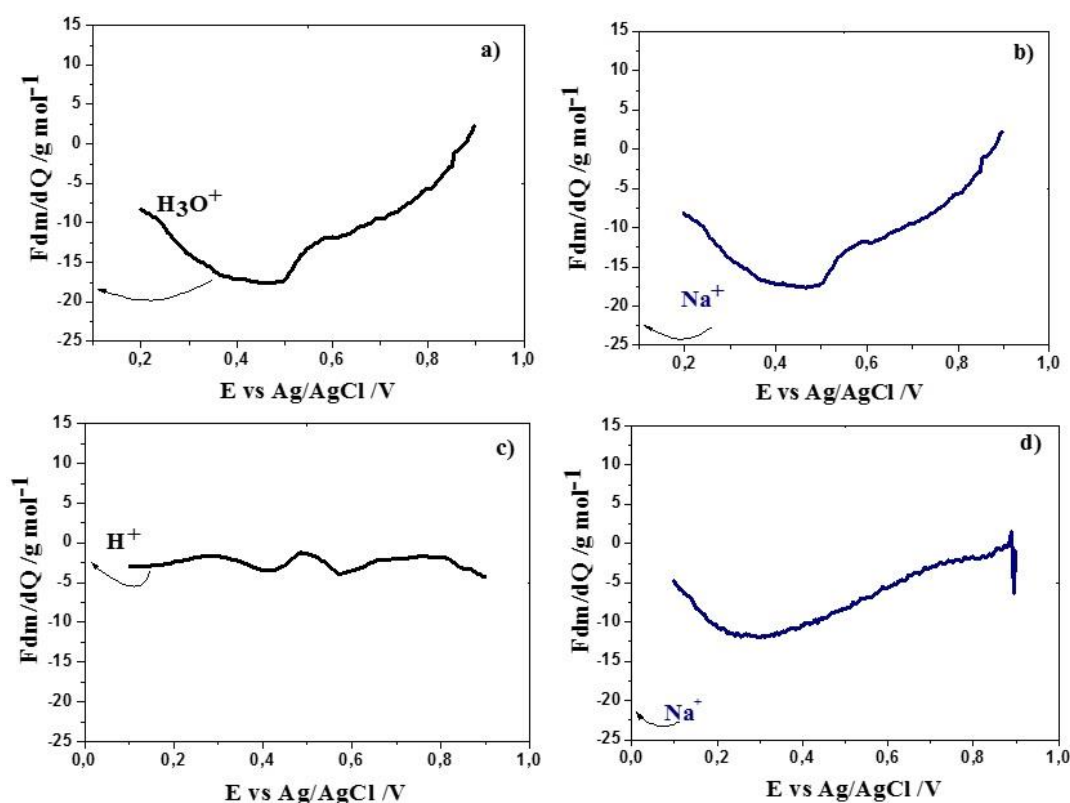


Fig. V-17. $F \times \frac{\Delta m}{\Delta q}$ values corresponding to the average molecular weight of the species involved in the charge compensation process as a function of the potential for a compact $\text{RuO}_x \cdot n\text{H}_2\text{O}$ film in (a) H_2SO_4 (b) Na_2SO_4 and for a mesoporous $\text{RuO}_x \cdot n\text{H}_2\text{O}$ in (c) H_2SO_4 (d) Na_2SO_4 (obtained from the reduction branch of the EQCM results at a scan rate of 20 mV s^{-1}).

Moreover, for a complex electrochemical process, these values correspond to an average molecular weight related to the various species, and it is actually an average in terms of mass and kinetics [32]. Therefore, at this point, one can arguably discuss that at this scan rate (20 mV s^{-1}), H^+ ions are exclusively involved in the charge compensation process (Fig. V-17c). However, it cannot guarantee the absence of any other species which may have different time

constants and cannot be detected at this scan rate (such as heavier ions including SO_4^{2-} , hydrated forms of proton or sodium ions, or free water molecules).

In a similar report, M. C. Santos et al. [21] used EQCM for the study of RuO_2 thin films, prepared by a sol-gel precursor method. According to their study, the CV corresponded to different redox transitions including: Ru^{2+}/Ru^{3+} , Ru^{3+}/Ru^{4+} and Ru^{4+}/Ru^{6+} with formal redox potentials of 0.56, 0.85 and 1.2 V vs NHE. From their EQCM measurements performed in acidic medium (H_2SO_4) at 25°C, the relative molecular mass of the transferred species was calculated from the slope of Δm vs ΔQ , (the mass variation as a function of charge transferred in RuO_2 thin film electrodes). Their results showed that the proton identification occurs only in the intermediate potentials (in their case 0.8-1.1 V vs NHE) associated with the Ru^{3+}/Ru^{4+} transition. They also suggested that hydroxide ions can also participate even with this same negative slope. This result is in fact debatable since this approach cannot discriminate clearly the ion contribution. Also, for more cathodic potentials a molecular mass of 32 g mol⁻¹ was obtained which is attributed to water molecules detection, but this is not a precise identification.

Indeed, these results show the limitations of the classical EQCM technique. The EQCM gives a global response, and does not provide unambiguous information on which of the possible scenarios actually takes place. To investigate the subtleties that cannot be reachable by EQCM method, *ac*-electrogravimetric studies were performed on mesoporous $RuO_x \cdot nH_2O$ films and compared with their compact analogues.

IV. ac-electrogravimetric results for compact and mesoporous $RuO_x \cdot nH_2O$

To further investigate and identify the nature of species involved in the charge compensation process at the interface of compact and mesoporous $RuO_x \cdot nH_2O$, *ac*-electrogravimetric results are presented in this section.

IV-1. ac-electrogravimetric results for compact and mesoporous $RuO_x \cdot nH_2O$ in H_2SO_4 0.5 M aqueous solutions:

For a chosen potential, for example 500 mV, the charge/potential transfer functions (TFs), $\frac{\Delta q}{\Delta E}(\omega)$, are given in Fig. V-18a and b. These TFs allow the ionic contribution without any possibility to identify the ionic species involved to be done. Here, the contribution of a parasitic reaction, occurring at very low frequencies, was removed for keeping only the ionic transfer

response. A large and slightly suppressed loop was obtained for both compact and mesoporous $\text{RuO}_x \cdot n\text{H}_2\text{O}$ thin films without a fair separation of different ionic transfers. From the theoretical functions (continuous line in fig. V-18) it seems that there are more than one charged species involved in both cases. However, the time constants corresponding to each ionic transfer appear to be very close to each other. At this level, it is not possible to distinguish whether the contribution of the involved species correspond to anions or cations. Meanwhile, the K_i and G_i constants were determined for two ions (for compact) and three ions (for mesoporous). The values of these parameters are shown in Table V-2 and were used in the following fittings. This set of parameters were kept for all the TF fitting for a certain film.

The K_i and the G_i constants are determined by fitting the experimental data using previously defined theoretical functions for $\frac{\Delta q}{\Delta E}(\omega)$, $\frac{\Delta E}{\Delta I}(\omega)$ and $\frac{\Delta m}{\Delta E}(\omega)$ with the criteria of achieving a good agreement between the experimental and theoretical data (strictly for all of the TFs, including partial mass/potential TFs). The equivalent weight of the charged and uncharged species is determined by the electrogravimetric TF, $\frac{\Delta m}{\Delta E}(\omega)$ which provides the identification of the species (Table V-2).

In the mass/potential TF ($\frac{\Delta m}{\Delta E}(\omega)$, Fig. V-18c and V-18d), one big loop appears in the third quadrant. This loop can be attributed to either two species or three species where their time constants are not sufficiently different from each other. The loops in the third quadrant are characteristic for cation contributions or free solvent molecules in the same flux direction. Another contribution also appears in Fig. V-18d (for the mesoporous $\text{RuO}_x \cdot n\text{H}_2\text{O}$ thin film) at very low frequencies in the fourth quadrant (either anions or water molecules with opposite flux direction compared to cations) highlighting the challenge in obtaining an exact identification of these loops. Therefore, several configurations were tested using theoretical functions to determine the exact contribution of each species. The mass/potential TF response of a compact $\text{RuO}_x \cdot n\text{H}_2\text{O}$ thin film was fitted by considering three species cation 1 ($c_1 = \text{H}^+$), free solvent molecules ($s = \text{H}_2\text{O}$) and cation 2 ($c_2 = \text{H}_3\text{O}^+$) (Fig. V-18c). In the case of a mesoporous $\text{RuO}_x \cdot n\text{H}_2\text{O}$ film, a similar response is obtained, but with an additional contribution from another charged species, the anion ($a = \text{SO}_4^{2-}$), which appears at very low frequencies (Fig. V-18d).

500 mV vs Ag/AgCl	f_i (Hz)	Cap_i (mF cm ⁻²)	K_i (s cm ⁻¹)	G_i (mol s ⁻¹ cm ⁻² V ⁻¹)	$Rt_i = \frac{1}{FG_i}$ (Ω cm ²)	$\frac{\Delta C_i}{\Delta E}(\omega) = -\frac{G_i}{K_i}$ (mol cm ⁻³ V ⁻¹)
Compact RuO_x.nH₂O						
c_2 (cation 2): H_3O^+ 19 g mol^{-1}	$f=0.15 \text{ Hz}$	2.9	0.47×10^{-4}	0.028×10^{-6}	366	-6×10^{-4}
s (solvent): H_2O 18 g mol^{-1}	$f=5.5 \text{ Hz}$		17.3×10^{-4}	0.86×10^{-6}	12	-5×10^{-4}
c_1 (cation 1): H^+ 1 g mol^{-1}	$f=6 \text{ Hz}$	17	18.9×10^{-4}	6.6×10^{-6}	1.57	-35×10^{-4}
Mesoporous RuO_x.nH₂O						
c_2 (cation 2): H_3O^+ 19 g mol^{-1}	$f=3 \text{ Hz}$	1.93	$1,885 \times 10^{-4}$	0.377×10^{-6}	27.5	-20×10^{-4}
s (solvent): H_2O 18 g mol^{-1}	$f=11 \text{ Hz}$		6.9×10^{-4}	0.345×10^{-6}	30	-5×10^{-4}
c_1 (cation 1): H^+ 1 g mol^{-1}	$f=40 \text{ Hz}$	15	25×10^{-4}	39×10^{-6}	0.26	-155×10^{-4}
a (anion): SO_4^{2-} 98 g mol^{-1}	$f=0.04 \text{ Hz}$	0.08	0.025×10^{-4}	-0.00024×10^{-6}	-48510	0.85×10^{-4}

Table V-2. Estimated values for K_i (kinetics of transfer), G_i (the inverse of the transfer resistance), R_{ti} (transfer resistance) and $-G_i/K_i$ (the quantity transferred per potential unit) parameters extracted from the fitting results of *ac*-electrogravimetric measurements in aqueous 0.5M H₂SO₄ at 500 mV vs. Ag/AgCl for dense and mesoporous RuO_x.nH₂O films.

Then, to identify and clarify the contribution of the charged and also the uncharged species (*i.e.* free solvent molecules), the mass/potential transfer functions, $\frac{\Delta m}{\Delta E}(\omega)$ are examined carefully.

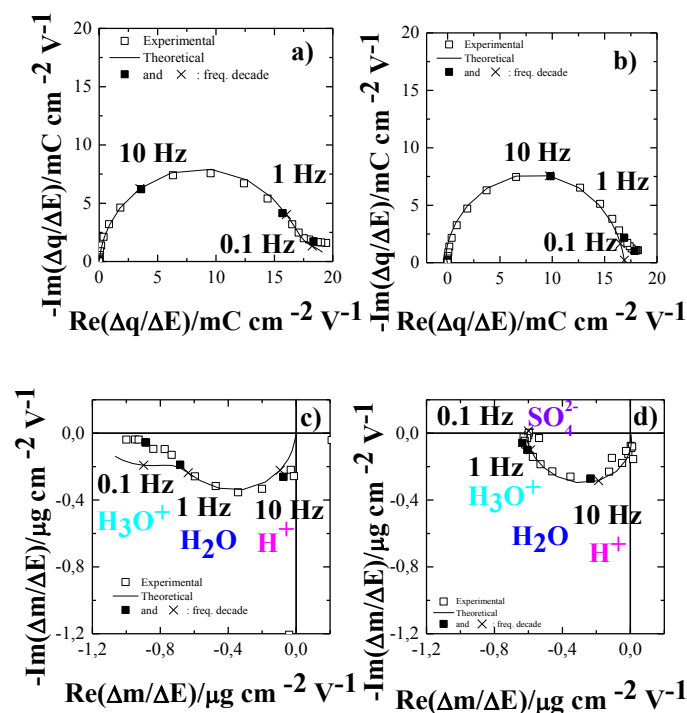


Fig. V-18. *ac*-electrogravimetric results for both compact (left side images) and mesoporous (right side) $\text{RuO}_x \cdot n\text{H}_2\text{O}$ at 500 mV in H_2SO_4 0,5M. (a,b) Charge/Potential Transfer Function: $\frac{\Delta q}{\Delta E}(\omega)$, (c,d)

Mass/Potential Transfer Function: $\frac{\Delta m}{\Delta E}(\omega)$.

The partial mass/potential TFs were analyzed to validate our previous hypothesis involving three and four different species for dense and mesoporous films, respectively. Partial mass/potential TFs are estimated for dense films (not shown), for example by removing the c_2

contribution, calculating $\left. \frac{\Delta m}{\Delta E} \right|_{th}^{c1s}$ or by removing the c_1 contribution, calculating $\left. \frac{\Delta m}{\Delta E} \right|_{th}^{c2s}$ as only

three species are involved in the case of a dense film (Fig V-19a and V-19c). The partial TFs

for mesoporous films were also analyzed, specifically, $\left. \frac{\Delta m}{\Delta E} \right|_{th}^{c1as}$, and $\left. \frac{\Delta m}{\Delta E} \right|_{th}^{c2as}$ (Fig. V-19b and

V-19d) and all exhibited a good agreement between the theoretical and experimental data.

These partial mass/potential TFs provide a crosscheck for validating the hypothesis involving multiple species and for obtaining a better separation of the various contributions. When the H_3O^+ contributions are removed (Fig. V-19a and V-19b), a pseudo anion response is determined. Indeed, the apparent mass of H^+ is negative due to the method of calculation of the partial TFs; a negative value given by $1-19 = -18 \text{ g mol}^{-1}$ must be used in this case for representing the H^+ gravimetric response which leads to an apparent anion response located in the fourth quadrant.

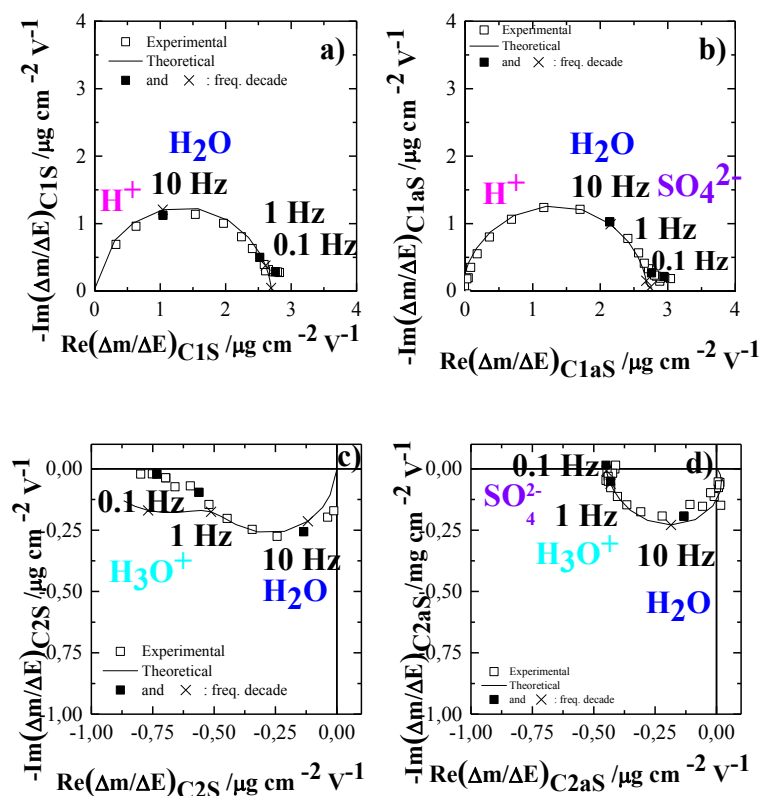


Fig. V-19. Partial Mass/Potential transfer function for both compact (a and c) and mesoporous (b and d) $\text{RuO}_x \cdot n\text{H}_2\text{O}$ at 500 mV in H_2SO_4 0,5M: partial $\frac{\Delta m}{\Delta E}(\omega)$ when c2 contribution is eliminated (a and b) $\frac{\Delta m}{\Delta E}(\omega)$ when c1 contribution is eliminated (c and d).

The characteristic frequencies, f_i , obtained from *ac*-electrogravimetry at 500 mV vs Ag/AgCl reveal the transfer rates of species at the electrode/electrolyte interface. For both dense and mesoporous $\text{RuO}_x \cdot n\text{H}_2\text{O}$ thin films: (i) H^+ species contribute at high frequencies (the fastest species), (ii) free water molecules appear at the intermediate frequencies, and (iii) H_3O^+ appears at low frequencies (the slowest species). In the case of mesoporous $\text{RuO}_x \cdot n\text{H}_2\text{O}$ thin films, an additional contribution is observed at the lowest frequency range corresponding to the anions transfer (SO_4^{2-}) and their transfer kinetics is slower than cationic species and free water molecules (see values in Table V-2). When the two types of films are compared some difference in the level of its rapidity are observed between these two structures: H^+ is over ten times faster in mesoporous film while both H^+ and H_2O are observed very close in the middle frequencies (around 12 Hz) in dense counterparts. The second main difference is the absence of anion in compact $\text{RuO}_x \cdot n\text{H}_2\text{O}$ films while even very slight presence of anion at very low frequencies is identified in mesoporous film. Also, the H_3O^+ ions which appear at low frequencies below $\sim 1\text{Hz}$ in the compact film are fastened almost ten times in mesoporous analogues. About the

instantaneous capacitances, Cap_i , presented in Table V-2, values are quite identical for the two films. The major contribution is due to the H^+ species with the highest values 6 and 10 times higher compared to capacitance of H_3O^+ for the compact and mesoporous films respectively. The faster species transferred are the smaller one, H^+ , this could indicate that it is related to electroadsorption process. On the contrary, the slowest transferred species, i.e. H_3O^+ , can be associated to a redox process. To confirm this hypothesis, the transfer resistance, R_t , of H_3O^+ for the compact film reaches the biggest value ($366 \Omega \text{ cm}^{+2}$) as a very small value is obtained in the case of H^+ for mesoporous films ($0.26 \Omega \text{ cm}^{+2}$).

To explore more deeply the global electrochemical process in the whole potential range, the electrogravimetric evolution for each applied potential was examined. According to $\frac{\Delta m}{\Delta E}(\omega)$ TFs, for compact $\text{RuO}_x \cdot n\text{H}_2\text{O}$ at 300 mV, there is no trace of solvent and two cations are identified: H^+ , at a few Hz which is the main contribution and H^+ again around 0.1 Hz. The partial mass/potential transfer functions give nothing since here the two cations involved are identical. It could be suggested at this stage that one of these H^+ corresponds to the redox sites and another one to the capacitive sites. The instantaneous capacitance, Cap , related to the faster H^+ is 18 mF cm^{+2} and for another 4.5 mF cm^{+2} . Similarly to the experiments shown previously at 500 mV, the main contribution is related to the fastest species. At 400 mV, the same conclusion as at 300 mV persists with the exception of a small solvent contribution. At 500 mV, same conclusions as for the previous potential: at HF, H^+ is detected around 6 Hz with an associated capacitance of 17 mF cm^{+2} , however, the other H^+ cation, around 0.15 Hz, is now hydrated. Free solvent is also detected with the same magnitude as at 400 mV. At 600 mV: the same conclusion persists compared to 500 mV. At 700 mV, anion contribution is detected at HF and is followed by an H^+ response. It should be noted that the anion contribution is around 0.1 mF cm^{+2} and therefore very small compared to H^+ contribution, 13 mF cm^{+2} . At 800 mV, the observation is similar compared to 700 mV.

For mesoporous $\text{RuO}_x \cdot n\text{H}_2\text{O}$, $\frac{\Delta m}{\Delta E}(\omega)$, TFs were also studied for the same potential window.

At 300 mV, the participation of 4 species are detected with the following order: H^+ is observed around 40 Hz with an instantaneous capacitance of 13 mF cm^{-2} , then, at middle frequencies around 13 Hz free solvent appears. At LF, H_3O^+ is identified with an instantaneous capacitance of 2.4 mF cm^{-2} , and finally at very LF there is a slight participation of anion with only a

capacitance value of 0.07 mF cm^{-2} . This sequence in terms of rate of transfer is illustrated in figure V-20. For all the other potentials, the same configuration of 4 species persists.

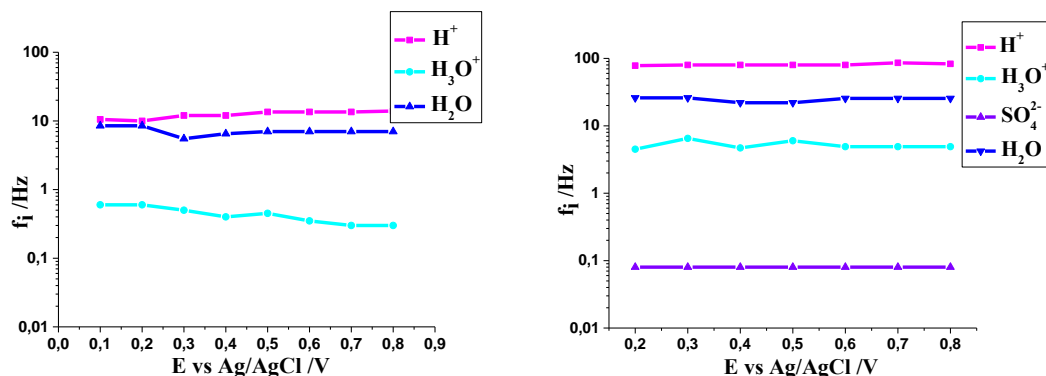


Fig. V-20. Evolution of characteristic frequencies of each species, f_i , as a function of applied potential for compact (left) and mesoporous (right) $\text{RuO}_x \cdot n\text{H}_2\text{O}$ in H_2SO_4 0,5M.

Coherent to what was already explained in the previous paragraph, from the evolution of characteristic frequencies, f_i , of species (fig. V-20) in both cases, the rate of transfer is higher in the case of mesoporous films, and this allows a possible fast charge or discharge to be performed.

Another useful information that could be obtained is the instantaneous capacitance of each species over the applied potential as shown in Fig. V-21. This parameter could indeed be defined as the capacity of the film to accommodate each of previously mentioned involved species as a consequence of a potential perturbation.

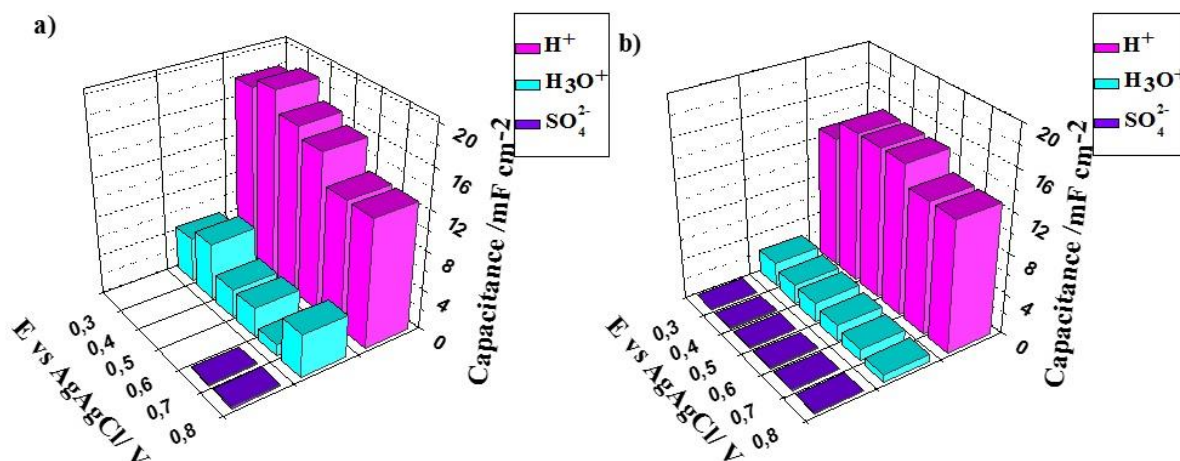


Fig. V-21. Evolution of Instantaneous Capacitance for each species, Cap_i , as a function of applied potential for compact (left) and mesoporous (right) $\text{RuO}_x \cdot n\text{H}_2\text{O}$ in H_2SO_4 0,5M.

By comparing these values in the case of compact $\text{RuO}_x \cdot n\text{H}_2\text{O}$ film, it could be seen that the most important capacitance belongs to H^+ ions meaning that compact film having still

nanometric intergrain spaces could more easily accommodate small protons but since the hydrated ions have larger ionic diameter the capacitance values remain somehow small for H_3O^+ . The anions appear only for the last two anodic potentials and the instantaneous capacitance attributed to them remains very small. The similar sequence is observed for mesoporous $RuO_x \cdot nH_2O$ with instantaneous capacitances in the same order of magnitude.

The G_i parameters permit to calculate the transfer resistance, Rt_i , of each species (Fig. V-22). The G_i values determined from the *ac*-electrogravimetric study are related to the transfer resistance, ($Rt_i = \frac{1}{FG_i}$) which can explain the ease or the difficulty of the ionic/non-ionic

transfer at the electrode/electrolyte interface. The transfer resistance, Rt_i , values follow the order which is the inverse of that observed for the kinetics parameters (K_i) (Table V-2). Specifically, for compact films, it pursues the order: $Rt_i (H_3O^+) > Rt_i (H_2O) > Rt_i (H^+)$, and for mesoporous films the similar order persists: $Rt_i (SO_4^{2-}) > Rt_i (H_3O^+) > Rt_i (H_2O) > Rt_i (H^+)$, except the presence of additional SO_4^{2-} anions exhibiting the highest transfer resistance. There are two cationic species (H^+ and H_3O^+) detected in both dense and mesoporous thin films. The kinetic parameters of transfer, f_i and the transfer resistance, Rt_i , values for their interfacial transfer can be compared in Fig V-20 and V-22. One of the most remarkable differences is the Rt_i values associated to H_3O^+ for compact films which are higher than that of mesoporous film. This strongly suggests that the transfer of hydrated proton species at the interface is much easier in mesoporous $RuO_x \cdot nH_2O$ thin films than in compact counterparts. Thus, the transfer of larger hydrated proton species H_3O^+ is favored when $RuO_x \cdot nH_2O$ films are mesoporous. Based on f_i values, the H^+ species are transferred rapidly in the case of mesoporous films but their transfer resistance is in the same order of magnitude compared to compact films. These results indicate that mesoporous films facilitate both H^+ and H_3O^+ transfer compared to compact $RuO_x \cdot nH_2O$ films. The $Rt_i (H_2O)$ is higher in mesoporous film suggesting that mesoporous film selectively favors ionic species participation but not free solvent molecules. The SO_4^{2-} anions contribution was detected in mesoporous films for all the potentials, but their transfer is slow and more difficult compared to other species.

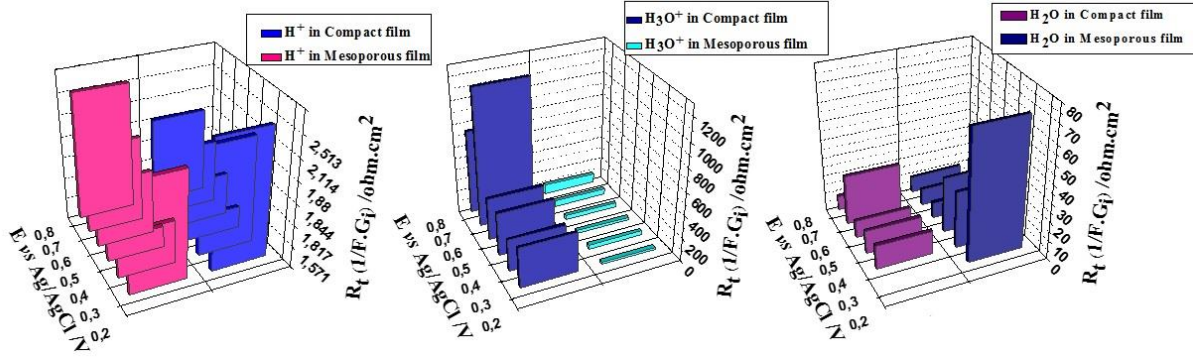


Fig. V-22. Evolution of transfer resistance, R_{t_i} , for each Species as a function of applied potentials; comparison between each involved species in both compact and mesoporous $\text{RuO}_x \cdot n\text{H}_2\text{O}$ in H_2SO_4 0,5M.

To quantify the role of each species, $\left. \frac{\Delta C_i}{\Delta E} \right|_{\omega \rightarrow 0} = -\frac{G_i}{K_i}$ has been estimated as a function of the

applied potential. The integration of the $\left. \frac{\Delta C_i}{\Delta E} \right|_{\omega \rightarrow 0}$ against potential gives the insertion

isotherm. Fig. V-23 presents the concentration change, $(C_i - C_0)$ for H^+ , H_3O^+ , H_2O and SO_4^{2-} species for compact (Fig. V-23a) and mesoporous $\text{RuO}_x \cdot n\text{H}_2\text{O}$ (Fig. V-23b) thin films. A significant difference is observed in the relative concentration change of the species when $\text{RuO}_x \cdot n\text{H}_2\text{O}$ thin films are mesoporous. Both the $(C_i - C_0)$ values for H^+ and H_3O^+ cations are magnified for mesoporous films. Specially, the number of exchanged H^+ ions are increased for ~ 3 times in mesoporous films. It is important to note that the characteristic frequency values, f_i , for H^+ species were higher (faster kinetics) in mesoporous films compared to compact films, and their ease of transfer was in the same order of magnitude (Fig. V-20 and Fig. V-22). This point underlines a good agreement between kinetics and thermodynamics related to the transferred H^+ species. However, despite the relative rapidity of H_3O^+ and H_2O in mesoporous film compared to compact film, in terms of thermodynamics the major contribution remains to be attributed to H^+ ions indicating that large number of these small species are transferred. The $(C_i - C_0)$ values for H_3O^+ are only slightly higher in mesoporous films than that in the compact films. The $(C_i - C_0)$ value for SO_4^{2-} anions is low compared with the cationic species, thus only a small quantity is transferred.

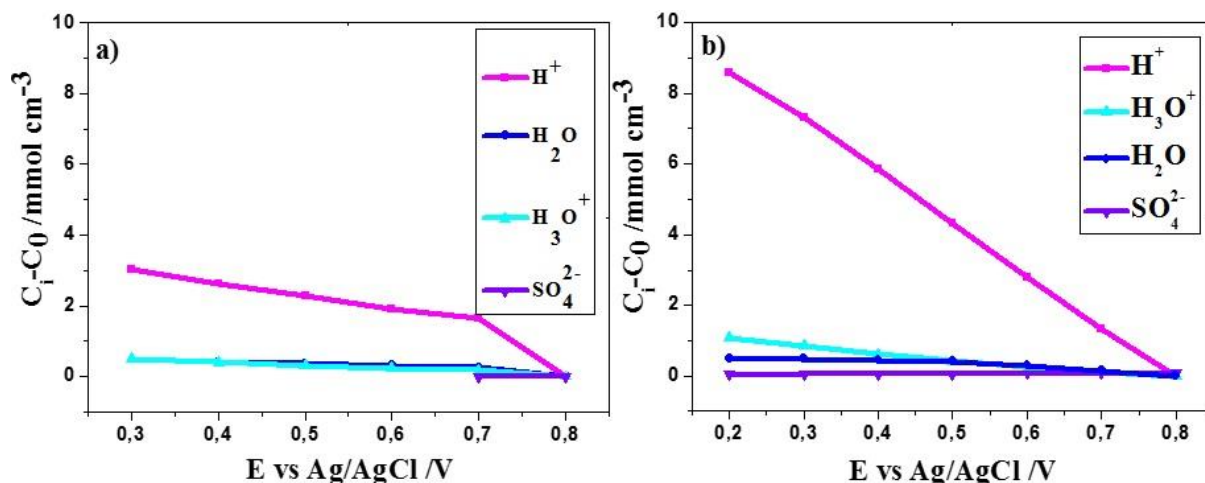


Fig. V-23. Evolution of the concentration changes, $C_i - C_0$, of each species over the potential applied for compact (a) and mesoporous (b) $\text{RuO}_x.n\text{H}_2\text{O}$ in H_2SO_4 0,5M.

Overall, the contribution of the charged species is magnified in mesoporous $\text{RuO}_x.n\text{H}_2\text{O}$ films compared to the compact films. This qualitative and quantitative study of ionic and non-ionic species contribution in the charge compensation process, together with dynamic information of their interfacial transfer further proves the advantageous nature of structuration of $\text{RuO}_x.n\text{H}_2\text{O}$ films for energy applications. The beneficial aspect of mesoporous $\text{RuO}_x.n\text{H}_2\text{O}$ films is more likely related to the better accommodation of both H^+ and H_3O^+ cations. Particularly, H^+ ions are transferred rapidly and easily at the mesoporous electrode/electrolyte interfaces, and their concentration variations in the electrode is significantly higher with respect to that in their compact analogues. The resulted deconvolution of species from our *ac*-electrogravimetric results led to distinguish and attribute the two cationic species with different time constants to two possible reactions at the interface of (pseudo)capacitive $\text{RuO}_x.n\text{H}_2\text{O}$. Indeed, the interaction of these two species occurs undoubtedly at two different sites in the film, since H^+ ions are the fastest species they could be attributed to fast capacitive reactions and the slower H_3O^+ ions to the faradaic reaction.

IV-2. ac-electrogravimetric results for compact and mesoporous $\text{RuO}_x.n\text{H}_2\text{O}$ in Na_2SO_4 0.5 M aqueous solution:

It is to be pointed out that in the majority of reports covering pseudocapacitive behavior of hydrated ruthenium oxide as a subject, the most important specific capacitance values are reported in H_2SO_4 electrolyte [6,20,21]. In previously discussed section, it was concluded that small protons are kinetically favorable, they are more easily and rapidly transferred at the mesoporous electrode/electrolyte interface. In this part, in order to see the effect of cation size the same electrodes were studied in Na_2SO_4 electrolyte and the results of this investigation are

presented and discussed. The K_i and G_i constants were determined for three/four species (for compact) and only two charged species (for mesoporous). The values of these parameters are shown in Table V-3 and were used in the following fittings. The charge/potential transfer functions (TFs), $\frac{\Delta q}{\Delta E}(\omega)$, at 500 mV are given in Fig. V-24. Similarly, to the observation for H_2SO_4 , a large suppressed loop was obtained for both compact and mesoporous $\text{RuO}_x \cdot n\text{H}_2\text{O}$ thin films. For compact film, the demi-circle is separated by the appearance of a very small loop at LF. The theoretical functions (continuous line in fig. V-24) could suggest that there are more than one charged species involved in both cases.

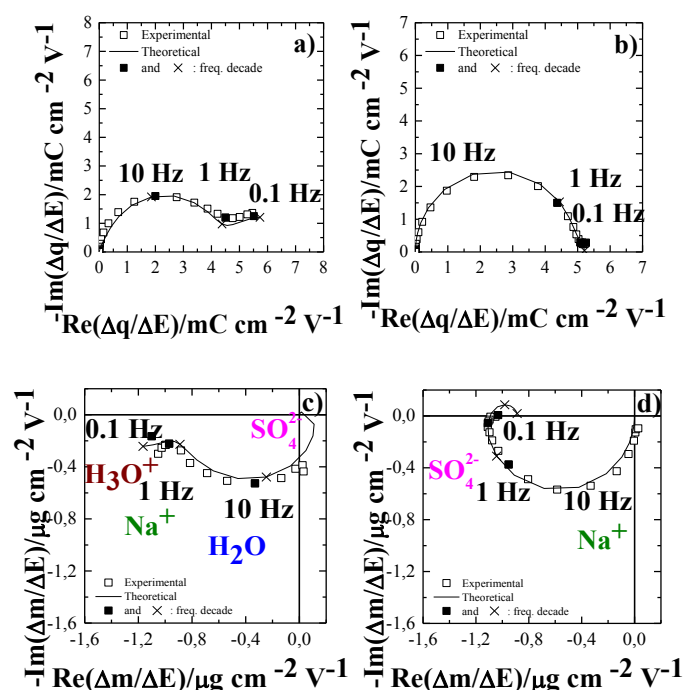


Fig. 24. *ac*-electrogravimetric results for both compact (a,c) and mesoporous (b,d) $\text{RuO}_x \cdot n\text{H}_2\text{O}$ at 500 mV in Na_2SO_4 0,5M. (a,b) Charge/Potential Transfer Function: $\frac{\Delta q}{\Delta E}(\omega)$, (c,d) Mass/Potential Transfer

Function: $\frac{\Delta m}{\Delta E}(\omega)$.

For the mass/potential TF, $\frac{\Delta m}{\Delta E}(\omega)$, in the case of compact film (fig. V-24c), a small and not well defined loop appears at HF in the second quadrant which corresponds to an anion contribution followed by a big loop in the third quadrant characteristic for cation or free solvent contributions. For the mesoporous $\text{RuO}_x \cdot n\text{H}_2\text{O}$ thin films (Fig. V-24d), the HF anion response disappears but another contribution appears at low frequencies in the fourth quadrant: either anions or water molecules with opposite flux direction compared to cations can be involved.

Ac-electrogravimetric results of a compact $\text{RuO}_x \cdot n\text{H}_2\text{O}$ film were fitted by considering four species listed in term of rapidity: sulfate anions ($a = \text{SO}_4^{2-}$), free solvent molecules ($s = \text{H}_2\text{O}$) sodium cations partially dehydrated ($c_1 = \text{Na}^+$) and hydronium cations ($c_2 = \text{H}_3\text{O}^+$). However, in the case of mesoporous $\text{RuO}_x \cdot n\text{H}_2\text{O}$ film, a completely different response was obtained. Only two charged species appear: cations ($c_1 = \text{Na}^+$) and anions ($a = \text{SO}_4^{2-}$) appear at lower frequencies in the fourth quadrant (Fig. V-24d).

The different responses over the total applied potential window could be summarized as following. For compact $\text{RuO}_x \cdot n\text{H}_2\text{O}$, at 300 mV, there is no trace of solvent and the anion appears at HF around 40 Hz. Two cations are identified: Na^+ at ~15 Hz with the main contribution and also a small one related to H^+ at 0.1 Hz. The instantaneous capacitance related to Na^+ is 4.3 mF cm^{-2} while for both H^+ and SO_4^{2-} this capacitance is very small, 0.6 and 0.2 mF cm^{-2} respectively. At 400 mV, the same conclusion as at 300 mV persists. At 500 mV, an anion appears at HF with a very small instantaneous capacitance of only 0.24 mF cm^{-2} . Na^+ is detected at ~13 Hz with an associated capacitance of 4 mF cm^{-2} and now the other H^+ cation is now hydrated with an associated capacitance of 3.9 mF cm^{-2} . At 600 mV: the same conclusion persists compared to 500 mV. At 700 mV anion contribution at HF is followed by Na^+ around 21 Hz and finally, H_3O^+ response at LF (0.4 Hz). At 800 mV, the observation is similar to 700 mV.

For mesoporous $\text{RuO}_x \cdot n\text{H}_2\text{O}$ the participation of only two charged species are detected for all the studied potentials. This includes Na^+ observed around 15 Hz with an instantaneous capacitance of ~5 mF cm^{-2} followed at LF by sulfate anion participation with a small instantaneous capacitance of ~0.3 mF cm^{-2} . The main difference between the two types of films (example at 500 mV presented at fig. V-24c and V-24d) is the apparition of anions at HF for compact films while in mesoporous counterpart the anion is only detected at very LF. Also in the contrary to what was expected from previously discussed results for mesoporous in H_2SO_4 , here, only two charge species contribute. Therefore, at this stage it could be speculated that mesoporous film could provide accommodation for only two charged species, a cation and an anion.

500 mV vs Ag/AgCl	f_i (Hz)	Cap_i (mF cm ⁻²)	K_i (s cm ⁻¹)	G_i (mol s ⁻¹ cm ⁻² V ⁻¹)	$Rt_i = \frac{1}{FG_i}$ (Ω cm ²)	$\frac{\Delta C_i(\omega)}{\Delta E} = -\frac{G_i}{K_i}$ (mol cm ⁻³ V ⁻¹)
Compact RuO_x.nH₂O						
c_1 (cation 1): Na ⁺ 23 g mol ⁻¹	$f=13$ Hz	3.95	4×10^{-4}	1.67×10^{-6}	6.19	-0.004
c_2 (cation 2): H ₃ O ⁺ 19 g mol ⁻¹	$f=0.17$ Hz	3.86	5.34×10^{-6}	2.1×10^{-8}	485	-0.004
s (solvent): H ₂ O 18 g mol ⁻¹	$f=12$ Hz		3.7×10^{-4}	3.4×10^{-7}	30.5	-9×10^{-4}
a (anion): SO ₄ ²⁻ 98 g mol ⁻¹	$f=25$ Hz	0.24	0.00236	-5.89×10^{-7}	-17.6	2.5×10^{-4}
Mesoporous RuO_x.nH₂O						
c_1 (cation 1): Na ⁺ 23 g mol ⁻¹	$f=15$ Hz	4.95	4.7×10^{-4}	2.4×10^{-6}	27.5	-0.0051
a (anion): SO ₄ ²⁻ 98 g mol ⁻¹	$f=0.7$ Hz	0.29	2.2×10^{-5}	-6.6×10^{-9}	30	3×10^{-4}

Table V-3. Estimated values for K_i (kinetics of transfer), G_i (inverse of the transfer resistance), Rt_i (transfer resistance) and $-G_i/K_i$ (the quantity transferred per potential unit) parameters extracted from the fitting results of *ac*-electrogravimetric measurements in aqueous 0.5M Na₂SO₄ at 500mV vs. Ag/AgCl for dense and mesoporous RuO_x.nH₂O films.

The characteristic frequencies, f_i , obtained from *ac*-electrogravimetry at 500mV (presented in fig. V-25) reveal the rate of transfer over the applied potential. For compact RuO_x.nH₂O films: (i) SO₄²⁻ species contribute at high frequencies (the fastest species), (ii) Na⁺ ions appear at the intermediate frequencies, and (iii) H₃O⁺ appears at low frequencies (the slowest species). In the case of mesoporous RuO_x.nH₂O thin films Na⁺ is the rapidest species and the contribution observed at the lowest frequency range corresponds to the anions transfer (SO₄²⁻) with their transfer kinetics slower than cationic species (see values in Table V-3). It is difficult to compare

the two types of films, with the exception of Na^+ which appear at MF in both cases. The anion apparition is quite different in these two films as in compact $RuO_x.nH_2O$, sulfate ions appear at HF but at LF in mesoporous films.

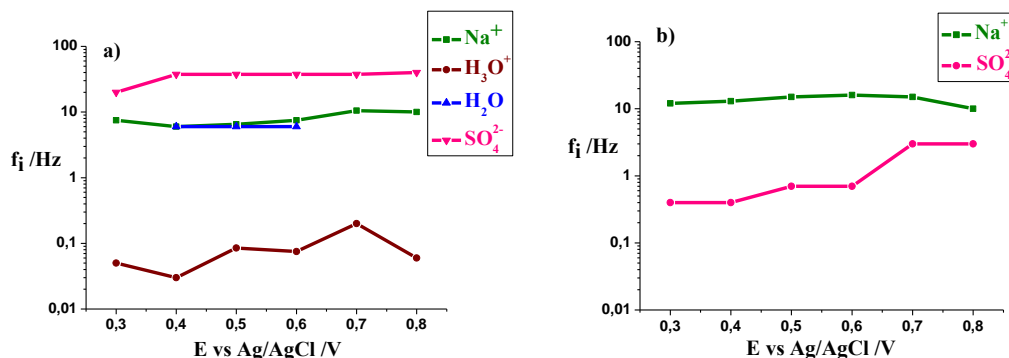


Fig. V-25. Characteristic frequencies, f_i , evolution as a function of applied potential for compact (left) and mesoporous (right) $RuO_x.nH_2O$ in Na_2SO_4 0,5M.

The instantaneous capacitances, Cap_i , are presented in fig. V-26. Both in compact and mesoporous $RuO_x.nH_2O$, except the irregularities observed at 500 mV and 800 mV for H_3O^+ , the most important values are attributed to Na^+ . Also, in mesoporous $RuO_x.nH_2O$, the instantaneous capacitance grows gradually and reaches a maximum of 5.2 mF cm^{-2} for the most cathodic potential at 300 mV. For the anions, this capacitance remains very small in both types of film suggesting that the film's capacity to accommodate SO_4^{2-} species is not noticeable.

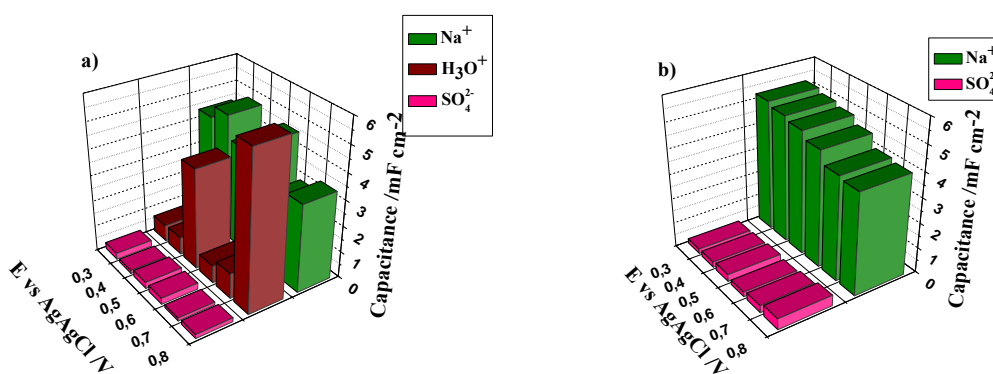


Fig. V-26. Evolution of the Instantaneous Capacitance, Cap_i , as a function of applied potential for compact (left) and mesoporous (right) $RuO_x.nH_2O$ in Na_2SO_4 0,5M.

The G_i parameters were used to calculate the transfer resistance, Rt_i , for each species, (not shown here.). For compact films, it pursues the order: $Rt_i (H_3O^+) > Rt_i (SO_4^{2-}) \approx Rt_i (H_2O) > Rt_i (Na^+)$, and for mesoporous films: $Rt_i (SO_4^{2-}) > Rt_i (Na^+)$, except the presence of additional SO_4^{2-}

anions exhibiting the highest transfer resistance. These results indicate that for both films Na^+ transfer is facilitated.

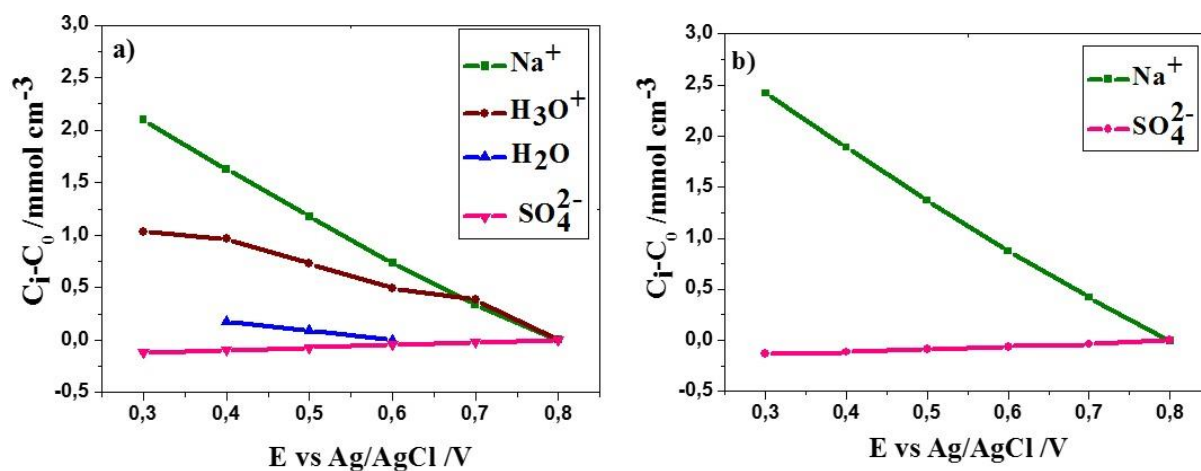


Fig. V-27. Evolution of the concentration, $C_i - C_0$, of each species over the potential applied for compact (a) and mesoporous (b) $\text{RuO}_x.n\text{H}_2\text{O}$ in Na_2SO_4 0,5M.

The integration of the $\left. \frac{\Delta C_i}{\Delta E} \right|_{\omega \rightarrow 0} = -\frac{G_i}{K_i}$ against potential gives the insertion isotherm. The

concentration change, $(C_i - C_0)$ for Na^+ , H_3O^+ , H_2O and SO_4^{2-} species for compact $\text{RuO}_x.n\text{H}_2\text{O}$ is shown in Fig. V-28a. The Na^+ ions are the majority of species exchanged at the interface. The pH of Na_2SO_4 solution is ~ 5.7 , at this pH, the number of present H_3O^+ ions are minor. This explains why the number of H_3O^+ species exchanged at the interface is smaller compared to Na^+ ions. This is also supported kinetically by already noticed high R_{ti} of H_3O^+ . The free solvent molecules appear for only three potentials with minor contributions. For SO_4^{2-} anions, the concentration changes appear for all the potentials but with small changes. At the interface of mesoporous $\text{RuO}_x.n\text{H}_2\text{O}$ electrode/electrolyte the major exchanged species are Na^+ and SO_4^{2-} exchange remains very small.

At this stage, when both kinetic and thermodynamic information are compared it could be suggested that the contribution of Na^+ may correspond to the redox sites while SO_4^{2-} ions are related to the capacitive sites, and their identification is only due to their adsorption at the surface, therefore, the major role is owing to Na^+ ions.

To conclude this section, the major contribution in both compact and mesoporous $\text{RuO}_x.n\text{H}_2\text{O}$ films is related to Na^+ cations. The qualitative and quantitative study of ionic and non-ionic species contribution in the electrochemical process in Na_2SO_4 solution doesn't clearly show the advantageous nature of $\text{RuO}_x.n\text{H}_2\text{O}$ films structuration. First, this could be related to the neutral

pH of this electrolyte: in H_2SO_4 solution H^+ ions could most efficiently interact with hydrated $\text{RuO}_x \cdot n\text{H}_2\text{O}$ electrodes as the concentration of these species is high. The second hypothesis could be related to the cation size effect and the fact that bigger Na^+ ions might not be preferable compared to H^+ ions. This later hypothesis, however is debatable since both ionic radius of H^+ and Na^+ are small enough to be able to find their way through the nanometric pore volumes in mesoporous films. Another speculation could come from the inaccessibility of the pores or the fact that the transfer of ions in a confined pore volume impose Na^+ ions to lose their hydration shell and this indirectly influences on their rapidity and also the number of these ions willing to be transferred at the interface.

V. Nanocomposite films of CNTs / $\text{RuO}_2 \cdot x\text{H}_2\text{O}$ Investigated by ac-Electrogravimetric Methods

V-1. EQCM study of SWCNTs/ $\text{RuO}_2 \cdot x\text{H}_2\text{O}$ film in aqueous solution

The EQCM results of SWCNTs and SWCNTs/ $\text{RuO}_x \cdot n\text{H}_2\text{O}$ films tested at room temperature in aqueous 0.5M H_2SO_4 and 0.5M Na_2SO_4 electrolytes are presented in Fig. V-28 (i vs. E), (mass changes vs. E) and (specific capacitance vs. E). The CV curves show a rectangular type capacitive response in the potential range of 0.2 V to 0.9 V vs Ag/AgCl.

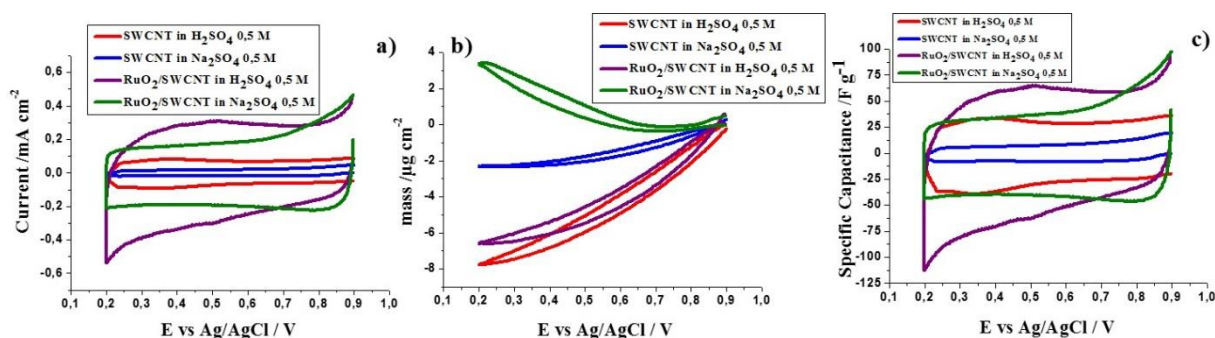


Fig. V-28. CVs, Mass variations and Specific Capacitance estimation for SWCNTs and SWCNTs/ $\text{RuO}_x \cdot n\text{H}_2\text{O}$ in H_2SO_4 0.5M (red and purple curves) and in Na_2SO_4 0.5M (blue and green curves).

By comparing the current values of pure SWCNTs with SWCNTs/ $\text{RuO}_x \cdot n\text{H}_2\text{O}$ films, in both aqueous 0.5M H_2SO_4 and 0.5M Na_2SO_4 electrolytes, it could be noticed that higher currents correspond to SWCNTs/ $\text{RuO}_x \cdot n\text{H}_2\text{O}$ composites. Therefore, this reflects directly on the estimated specific capacitance values (Fig. V-28c). The specific capacitances of SWCNTs/ $\text{RuO}_x \cdot n\text{H}_2\text{O}$ films are over 2 times higher than what is estimated for pure SWCNTs in aqueous 0.5M H_2SO_4 and ~ 4 times higher when pure SWCNTs and SWCNTs/ $\text{RuO}_x \cdot n\text{H}_2\text{O}$ composite films are tested in aqueous 0.5M Na_2SO_4 .

Although these values might not stand among the highest values reported in the literature for SWCNTs/RuO_x.nH₂O [8–10,33] composite which could be due to the simplicity of our preparation method and the small RuO_x.nH₂O quantities used here. But here the main goal was not to reach high performances rather to understand deeply the electrogravimetric behaviour of these films. So, what is promising here is the fact that electrodeposition of even a very thin layer of RuO_x.nH₂O on pure SWCNTs electrodes enhances the current values as well as the capacitances. It is also believed that this improvement in the electrochemical behaviour of the RuO_x.nH₂O/CNT film electrode is attributed to the large interfacial area between the ruthenium oxide and the solution due to the high surface area of the initial CNT film substrate.

In a recent report by I-H Kim et al. [33] an electrochemical route was employed to procure a 3D structure for RuO₂. The author mentioned that a very thin, nanometric, ruthenium oxide layer on the CNTs substrate contributed to largely increase the specific capacitance. The author have also indicated that a large portion of RuO₂ under the film surface layer is unreacted and left behind a dead volume, which eventually causes reduction of the specific capacitance. Therefore, the RuO₂/CNT films exhibit enhanced properties because of using the CNT film substrate which provides three-dimensionally interconnected nanoporous structure. When mass changes were recorded in aqueous 0.5M H₂SO₄ (fig. V-28b) it could be seen that SWCNTs/RuO_x.nH₂O behaves similar to SWCNTs, meaning that when the potential is cycled from anodic to cathodic values, the frequency increases meaning that the mass of the film drops due to expulsion/desorption of charged species and/or free solvent molecules. Surprisingly, in 0.5M Na₂SO₄, the composite behaves differently corresponding to what was previously observed for RuO_x.nH₂O. In this case (the green curve in fig. 28b) when the potential is scanned to cathodic direction, the frequency drops so that the mass of the film increases, One could conclude that the SWCNTs/RuO_x.nH₂O composite behaves similar to pure SWCNTs electrodes in aqueous 0.5M H₂SO₄. In the contrary, its behaviour in 0.5M Na₂SO₄ looks like the typical responses for MO_x electrodes.

V-2. ac-electrogravimetric study of SWCNTs/RuO_x.nH₂O film in H₂SO₄ aqueous solution

Three different films (SWCNTs, RuO_x.nH₂O and SWCNTs/RuO_x.nH₂O) were tested here in order to provide a larger window for discussion and to follow the differences and/or similarities that comes with this new composite electrode.

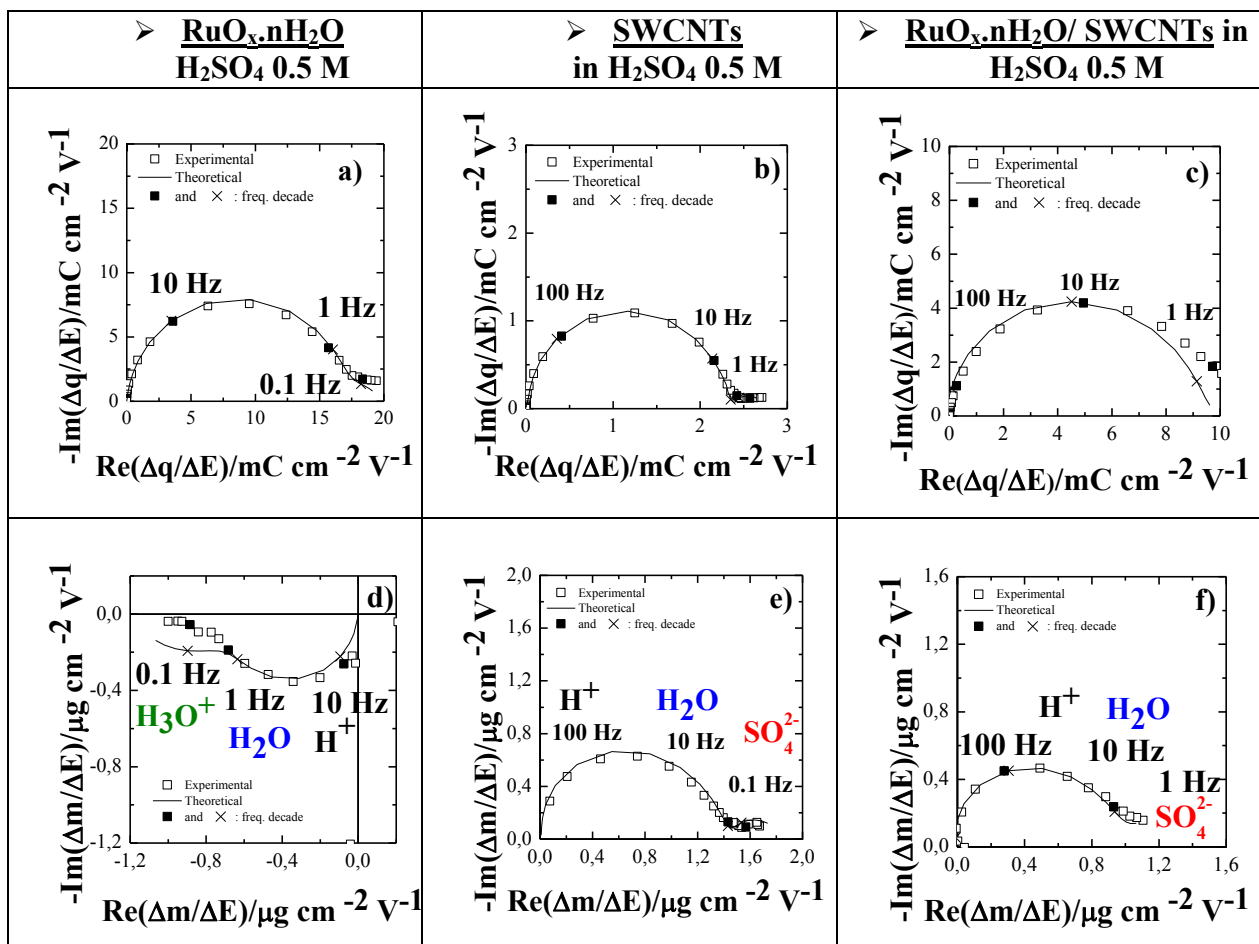


Fig. V-29. *ac*-electrogravimetric results: Charge/Potential Transfer Function, $\frac{\Delta q}{\Delta E}(\omega)$, and Mass/Potential Transfer Function, $\frac{\Delta m}{\Delta E}(\omega)$, for RuO_x.nH₂O (a and d), SWCNTs (b and e) and SWCNTs/RuO_x.nH₂O (c and f) at 500 mV in H₂SO₄ 0,5M.

The charge/potential transfer functions (TFs), $\frac{\Delta q}{\Delta E}(\omega)$, at 500 mV are shown in Fig. V-29.

Similarly, to the observation for RuO_x.nH₂O, a large suppressed loop is obtained for both SWCNTs and SWCNTs/RuO_x.nH₂O films. The semi-circle is continued through the appearance of a separated very small loop at LF. The theoretical functions (continuous line in fig. V-29) could suggest that there is more than one charged species involved in both cases. At this stage, it is not possible to identify whether the contribution of the species correspond to the anions or cations, the only distinguishable difference between SWCNTs and SWCNTs/RuO_x.nH₂O films is the fact that the contribution of charged species in composite films is over 3 times larger than the corresponding $\frac{\Delta q}{\Delta E}(\omega)$ for pure SWCNTs. For further investigation, the K_i and G_i constants were determined for three species in both SWCNTs and SWCNTs/RuO_x.nH₂O films. These parameters in aqueous 0.5M H₂SO₄ electrolyte are shown

in Table V-4 and were used in the following fittings. Then, to identify and clarify the contribution of the charged and also the uncharged species (*i.e.* free electrolyte molecules), the mass/potential transfer functions, $\frac{\Delta m}{\Delta E}(\omega)$, are carefully examined.

500 mV vs Ag/AgCl in H ₂ SO ₄ 0.5 M	f_i (Hz)	Cap_i (mF cm ⁻²)	K_i (s cm ⁻¹)	G_i (mol s ⁻¹ cm ⁻² V ⁻¹)	$Rt_i = \frac{1}{FG_i}$ (Ω cm ²)	$\frac{\Delta C_i}{\Delta E}(\omega) = -\frac{G_i}{K_i}$ (mol cm ⁻³ V ⁻¹)
<u>SWCNTs</u>						
c_1 (cation 1): H ⁺ 1 g mol ⁻¹	$f=80$ Hz	2.36	25×10^{-4}	6.16×10^{-6}	1,68	-24.5×10^{-4}
s (solvent): H ₂ O 18 g mol ⁻¹	$f=30$ Hz		$9,42 \times 10^{-4}$	$-7,73 \times 10^{-6}$	1,34	82×10^{-4}
a (anion): SO ₄ ²⁻ 96 g mol ⁻¹	$f=0.1$ Hz	0.38	0.031×10^{-4}	-0.0012×10^{-6}	8240	4×10^{-4}
<u>SWCNTs/RuO_x.nH₂O</u>						
c_1 (cation 1): H ⁺ 1 g mol ⁻¹	$f=15$ Hz	9.65	4.7×10^{-4}	4.7×10^{-6}	2.2	-100×10^{-4}
s (solvent): H ₂ O 18 g mol ⁻¹	$f=10$ Hz		3.14×10^{-4}	-1.92×10^{-6}	6597	61×10^{-4}
a (anion): SO ₄ ²⁻ 96 g mol ⁻¹	$f=0.1$ Hz	0.48	0.031×10^{-4}	-0.0016×10^{-6}	5.4	5×10^{-4}

Table V-4. Estimated values for K_i (kinetics of transfer), G_i (the inverse of the transfer resistance), Rt_i (transfer resistance) and $-G_i/K_i$ (the quantity transferred per potential unit) parameters extracted from the fitting results of *ac*-electrogravimetric measurements in H₂SO₄ 0.5M at 500 mV vs. Ag/AgCl for SWCNTs and SWCNTs/RuO_x.nH₂O films.

In the mass/potential TF, $\frac{\Delta m}{\Delta E}(\omega)$, (Fig. V-29), one big loop appears in the fourth quadrant in case of $\text{RuO}_x \cdot n\text{H}_2\text{O}$ (Fig. V-29d) and in the first quadrant when SWCNTs and the composite films are studied (Fig. V-29e and V-29f). This loop can be attributed to either two species or three species. The loop in the first quadrant appears when anions contribution and/or free solvent molecules are in the same flux direction. Several configurations were tested using theoretical functions to determine the exact contribution of each species. The mass response of both SWCNTs and SWCNTs/ $\text{RuO}_x \cdot n\text{H}_2\text{O}$ thin films was fitted by considering three species: protons ($c_1 = H^+$), sulfate anions ($a = \text{SO}_4^{2-}$) and free solvent molecules ($s = \text{H}_2\text{O}$) (Fig. V-29e and V-29f). Indeed, the H^+ contribution is located in the fourth quadrant but is not really visible due to the small H^+ mass. In a global point of view, the evolution for species over the total applied potential window could be summarized as following.

For SWCNTs, over the whole potential window, a constant appearance of species is observed: The H^+ cation appears at HF (~ 90 Hz), free solvent molecules are then detected at MF ~ 30 Hz and finally at very LF ~ 0.1 Hz anions appear. From 100 mV to 400 mV the instantaneous capacitance of H^+ cation rises from 2 mF cm^{-2} and reaches a maximum value of 2.7 mF cm^{-2} at 400 mV and then, gradually drops to 2 mF cm^{-2} at 800 mV. For anions the instantaneous capacitance increases slowly from 0.1 mF cm^{-2} at 100 mV to 0.46 mF cm^{-2} at 800 mV. For SWCNTs/ $\text{RuO}_x \cdot n\text{H}_2\text{O}$ composite films, H^+ cations do not appear as fast as in SWCNTs, these species appear at MF with a slight rise from ~ 8 Hz at 100 mV to ~ 18 Hz at 800 mV. This is followed by the free solvent contribution very close to cations ~ 10 -12 Hz and anions appear again at LF ~ 0.1 -0.2 Hz. The instantaneous capacitance for H^+ ions remains constantly high ~ 8 -10 mF cm^{-2} while similar to SWCNT films the anion capacitances remains very small.

The characteristic frequencies, f_i , obtained from *ac*-electrogravimetric results give the transfer rates of each species at the electrode/electrolyte interface. Fig V-30 (a, b and c) presents this evolution as a function of potential for $\text{RuO}_x \cdot n\text{H}_2\text{O}$, SWCNTs and SWCNTs/ $\text{RuO}_x \cdot n\text{H}_2\text{O}$. In $\text{RuO}_x \cdot n\text{H}_2\text{O}$ films: (i) SO_4^{2-} anions appear only at two anodic potentials at HF ~ 20 Hz (the fastest species), (ii) both H^+ ions and H_2O appear at intermediate frequencies, and (iii) the second cation H_3O^+ appears at low frequencies (the slowest species). In SWCNTs film: (i) there is no trace of H_3O^+ cations in contrary to $\text{RuO}_x \cdot n\text{H}_2\text{O}$ and (ii) H^+ cations are the fastest species appearing at HF. Then, (iii) free solvent molecules appear constantly at MF and lastly, (iv) the SO_4^{2-} anions are identified to be the slowest species present only at very LF. Finally, in SWCNTs/ $\text{RuO}_x \cdot n\text{H}_2\text{O}$ similar to $\text{RuO}_x \cdot n\text{H}_2\text{O}$ (i) both H^+ ions and H_2O appear at the MF, but in

contrary to $\text{RuO}_x \cdot n\text{H}_2\text{O}$ and similar to SWCNTs the anions are the slowest species detected at LF.

The evolution of instantaneous capacitance, Cap_i , is shown in Fig V-30 (d, e and f) for $\text{RuO}_x \cdot n\text{H}_2\text{O}$, SWCNTs and SWCNTs/ $\text{RuO}_x \cdot n\text{H}_2\text{O}$, respectively. Compared to SWCNTs which does not exhibit high capacitance values for H^+ (average value around 2 mF cm^{-2}), the capacitances measured for SWCNTs/ $\text{RuO}_x \cdot n\text{H}_2\text{O}$ are over 4 times magnified and this film specifically favors H^+ ions which is comparable to what was observed for pure $\text{RuO}_x \cdot n\text{H}_2\text{O}$. One could arguably discuss that this is the outer $\text{RuO}_x \cdot n\text{H}_2\text{O}$ layer of composite which gives a similar response as pure $\text{RuO}_x \cdot n\text{H}_2\text{O}$. But there are visible differences between these two films. First, there is no trace of a second cation H_3O^+ among the participating species in composite film and secondly, the anions which are detected only for two potentials in $\text{RuO}_x \cdot n\text{H}_2\text{O}$ are continuously present in composite films. So, the SWCNTs/ $\text{RuO}_x \cdot n\text{H}_2\text{O}$ film has an intermediate behavior compared to pure SWCNTs and $\text{RuO}_x \cdot n\text{H}_2\text{O}$. A common observation among all these three films is the low capacitance of the film against SO_4^{2-} anions.

The evolution of the transfer resistance is shown in (Fig. V-30g, h and i) for the three films. In SWCNTs film, the following order persists: $Rt_i (SO_4^{2-}) > Rt_i (H^+) \approx Rt_i (H_2O)$, the similar order is pursued in SWCNTs/ $\text{RuO}_x \cdot n\text{H}_2\text{O}$ composite film: $Rt_i (SO_4^{2-}) > Rt_i (H_2O) > Rt_i (H^+)$ and in the case of pure $\text{RuO}_x \cdot n\text{H}_2\text{O}$, differences are observed: $Rt_i (H_3O^+) > Rt_i (SO_4^{2-}) > Rt_i (H_2O) > Rt_i (H^+)$. These results indicate that H^+ ions are the easiest species to be transferred in all these types of films contrary to the transfer of SO_4^{2-} anions which remains to be the most difficult ions to transfer. The resistance of anions in case of SWCNTs and SWCNTs/ $\text{RuO}_x \cdot n\text{H}_2\text{O}$ composite films is much more important than what was observed for $\text{RuO}_x \cdot n\text{H}_2\text{O}$.

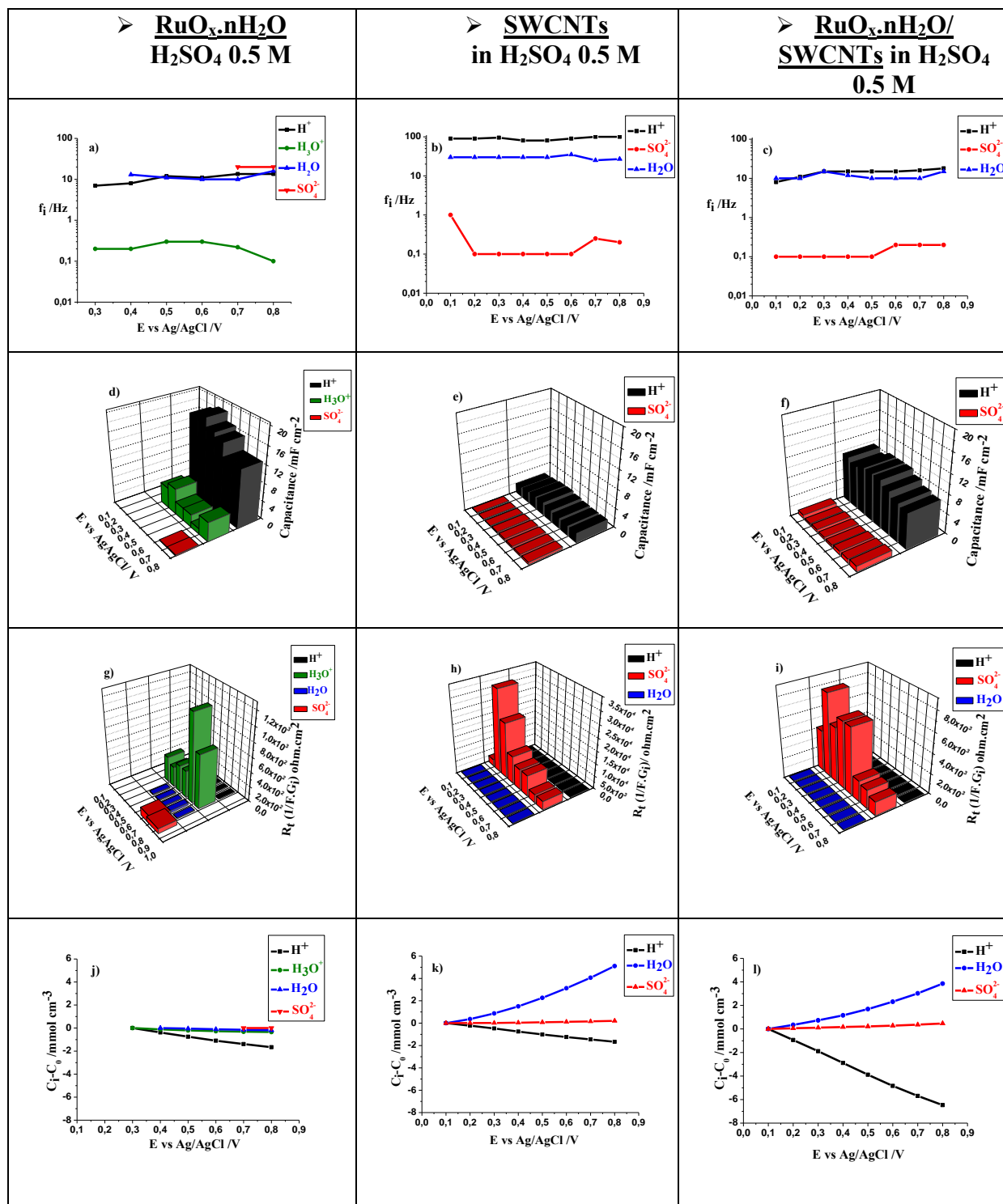


Fig. V-30. Evolution of Characteristic frequency (f_i), Instantaneous Capacitance of Species (Cap_i), transfer Resistances of each Species (R_t) and the relative concentration of species ($C_i - C_0$) as a function of potential for $\text{RuO}_x \cdot n\text{H}_2\text{O}$, SWCNTs and SWCNTs/ $\text{RuO}_x \cdot n\text{H}_2\text{O}$ at 500 mV in H_2SO_4 0,5M.

The concentration changes of the species, ($C_i - C_0$) as a function of potential is depicted for $\text{RuO}_x \cdot n\text{H}_2\text{O}$, SWCNTs and SWCNTs/ $\text{RuO}_x \cdot n\text{H}_2\text{O}$, respectively (fig. V-30j, k and l). These graphs show clearly the advantageous aspects of composite's 3D structure. Starting first with

RuO_x.nH₂O film, the concentration profile shows that small H⁺ cations are the most populated number of ions that are transferred into the hydrated ruthenium oxide films. The SWCNTs film accommodates the same magnitude of H⁺ cations. And interestingly, the most important number of inserted H⁺ ions belong to SWCNTs/RuO_x.nH₂O composite films with an increase of over 3 times. Also, clearly the majority of the charged species participation belongs to cations since finally, a very minor number of anions seems to participate, and the values remain close to zero.

It is also noticeable to observe that finally for the composite films both kinetical (fig. V-30) and thermodynamic information go well in the same direction. From the evolution of characteristic frequency, f_i , it was observed that H⁺ cations are the fastest species compared to the anions which remain to be very slow over the whole potential window. Then from instantaneous capacitance, Cap_i , estimation and the evolution of the transfer resistance, R_{t_i} , it was furtherly concluded that the most important capacitance belongs to H⁺ cations and these species are the easiest transferred species against bigger SO₄²⁻ anions having high transfer resistances and negligible capacitances. Similar to these kinetical parameters, from a thermodynamic point of view, the concentration change profiles reveal that the H⁺ cations are the majority of species exchanged with the film while the participation of SO₄²⁻ anions remains minor.

VI. Conclusion

In the first part of this chapter an attempt was made to show the usefulness of fast electrogravimetric methods to provide a comprehensive comparison between compact and mesoporous hydrated ruthenium oxide. Mesoporous RuO_x.xH₂O thin films were synthesized by surfactant assisted electrodeposition method. The idea of using an ionic surfactant (CTAB) during the electrochemical preparation of RuO_x.nH₂O films led to the creation of ~7-10 nm mesopores which are templated by the corresponding micelles. The compact analogues were also electrochemically synthesized under similar conditions but in the absence of CTAB templates. The pseudocapacitive behavior of the hydrated ruthenium oxide films as their permeability related to the ions intercalation/electroadsorption for mesoporous and compact RuO₂.xH₂O thin films were investigated by coupled time resolved characterization methods (*ac*-electrogravimetric method). The chemical nature and the role of each species (ions, solvated ions, and free solvent molecules), directly or indirectly involved in the electrochemical processes were estimated for the very first time.

In 0.5 M aqueous H_2SO_4 solution, it is possible to identify the role of several charged species (H^+ , H_3O^+) in the charge compensation process; H_2O molecules indirectly contribute to the process in both compact and mesoporous $RuO_{2.x}H_2O$ films following the same flux direction as the cations which indicates an electrodragging process. Even a slight contribution of SO_4^{2-} ions was detected in the case of mesoporous films. The contribution of the charged species is magnified in mesoporous $RuO_x.nH_2O$ films compared to the compact counterparts. This qualitative and quantitative study of ionic species contribution in the charge compensation process, together with dynamic information of their interfacial transfer further proves the advantageous nature of $RuO_x.nH_2O$ structured films for energy applications. The mesoporous $RuO_x.nH_2O$ film better accommodates both cationic species, H^+ and H_3O^+ . The H^+ ions in particular, are transferred quite fast at the mesoporous electrode/electrolyte interfaces, and their concentration profile is significantly higher with respect to the values obtained in their compact analogues. The results of the transfer resistances of the cations are much lower when the $RuO_x.nH_2O$ films are mesoporous.

In 0.5 M aqueous Na_2SO_4 solution, the major contribution of the charged species in both compact and mesoporous $RuO_x.nH_2O$ films corresponds to Na^+ . However, neither from kinetic parameters (f_i vs E , R_{st} vs E , Cap_i vs E) nor thermodynamic parameters (C_i-C_0 vs E), mesoporous films do not show any advantage. This could be related to the neutral pH of this electrolyte, the most appreciable results of $RuO_x.nH_2O$ are reported in H_2SO_4 solution since H^+ ions could most efficiently interact with available bonds of hydrated $RuO_x.nH_2O$ electrode. The second hypothesis could be related to a cation size effect and the fact that bigger Na^+ ions might not be preferable compared to smaller H^+ ions. Another reason might be related to the inaccessibility of the pores or the fact that the transfer of ions in a confined pore volume impose Na^+ ions to lose their solvation shell and this indirectly influences on their rapidity.

The second part of this chapter was attributed to an enlarged comparative study between three main different structures. First, three-dimensional composite film of SWCNTs/ $RuO_x.nH_2O$ was elaborated via a simple two-step procedure route and then, bare SWCNTs, bare $RuO_x.nH_2O$ films were compared. The results of our studies in 0.5 M aqueous H_2SO_4 electrolyte showed a promoted behaviour for SWCNTs/ $RuO_x.nH_2O$ composite films. This advanced behavior includes: (i) an ameliorated instantaneous capacitance, Cap_i (ii) Low transfer resistance, Rt_i and (iii) an amplified number of cations willing to be transferred into the film. This composite

structure benefits both from a high conductivity and a large surface area of CNTs but also from the pseudo capacitive character of thin layer $\text{RuO}_x \cdot n\text{H}_2\text{O}$.

VII. References:

- [1] M.-G. Jeong, K. Zhuo, S. Cherevko, W.-J. Kim, C.-H. Chung, Facile preparation of three-dimensional porous hydrous ruthenium oxide electrode for supercapacitors, *J. Power Sources*. 244 (2013) 806–811.
- [2] T.P. Gujar, V.R. Shinde, C.D. Lokhande, W.-Y. Kim, K.-D. Jung, O.-S. Joo, Spray deposited amorphous RuO_2 for an effective use in electrochemical supercapacitor, *Electrochem. Commun.* 9 (2007) 504–510.
- [3] Y. Xie, D. Fu, Supercapacitance of ruthenium oxide deposited on titania and titanium substrates, *Mater. Chem. Phys.* 122 (2010) 23–29.
- [4] V. Augustyn, P. Simon, B. Dunn, Pseudocapacitive oxide materials for high-rate electrochemical energy storage, *Energy Environ. Sci.* 7 (2014) 1597–1614.
- [5] A. Ferris, S. Garbarino, D. Guay, D. Pech, 3D RuO_2 Microsupercapacitors with Remarkable Areal Energy, *Adv. Mater.* 27 (2015) 6625–6629.
- [6] C.-C. Hu, K.-H. Chang, M.-C. Lin, Y.-T. Wu, Design and tailoring of the nanotubular arrayed architecture of hydrous RuO_2 for next generation supercapacitors, *Nano Lett.* 6 (2006) 2690–2695.
- [7] R.B. Rakhi, W. Chen, M.N. Hedhili, D. Cha, H.N. Alshareef, Enhanced rate performance of mesoporous Co_3O_4 nanosheet supercapacitor electrodes by hydrous RuO_2 nanoparticle decoration, *ACS Appl. Mater. Interfaces.* 6 (2014) 4196–4206.
- [8] F. Pico, E. Morales, J.A. Fernandez, T.A. Centeno, J. Ibáñez, R.M. Rojas, J.M. Amarilla, J.M. Rojo, Ruthenium oxide/carbon composites with microporous or mesoporous carbon as support and prepared by two procedures. A comparative study as supercapacitor electrodes, *Electrochimica Acta.* 54 (2009) 2239–2245.
- [9] H. Li, R. Wang, R. Cao, Physical and electrochemical characterization of hydrous ruthenium oxide/ordered mesoporous carbon composites as supercapacitor, *Microporous Mesoporous Mater.* 111 (2008) 32–38.
- [10] R.-R. Bi, X.-L. Wu, F.-F. Cao, L.-Y. Jiang, Y.-G. Guo, L.-J. Wan, Highly dispersed RuO_2 nanoparticles on carbon nanotubes: facile synthesis and enhanced supercapacitance performance, *J. Phys. Chem. C.* 114 (2010) 2448–2451.
- [11] Y. Meng, L. Wang, H. Xiao, Y. Ma, L. Chao, Q. Xie, Facile electrochemical preparation of a composite film of ruthenium dioxide and carboxylated graphene for a high performance supercapacitor, *RSC Adv.* 6 (2016) 33666–33675.

- [12] I. Zhitomirsky, L. Gal-Or, Ruthenium oxide deposits prepared by cathodic electrosynthesis, *Mater. Lett.* 31 (1997) 155–159.
- [13] C.-C. Hu, Y.-H. Huang, Effects of preparation variables on the deposition rate and physicochemical properties of hydrous ruthenium oxide for electrochemical capacitors, *Electrochimica Acta.* 46 (2001) 3431–3444.
- [14] C.-C. Hu, K.-H. Chang, Cyclic voltammetric deposition of hydrous ruthenium oxide for electrochemical supercapacitors: effects of the chloride precursor transformation, *J. Power Sources.* 112 (2002) 401–409.
- [15] D.J. Morgan, Resolving ruthenium: XPS studies of common ruthenium materials, *Surf. Interface Anal.* 47 (2015) 1072–1079.
- [16] Y. Guillemin, J. Ghanbaja, E. Aubert, M. Etienne, A. Walcarius, Electro-assisted self-assembly of cetyltrimethylammonium-templated silica films in aqueous media: critical effect of counteranions on the morphology and mesostructure type, *Chem. Mater.* 26 (2014) 1848–1858.
- [17] A. Walcarius, E. Sibottier, M. Etienne, J. Ghanbaja, Electrochemically assisted self-assembly of mesoporous silica thin films, *Nat. Mater.* 6 (2007) 602–608.
- [18] D. Muñoz-Rojas, M. Casas-Cabanas, E. Baudrin, Effect of particle size and cell parameter mismatch on the lithium insertion/deinsertion processes into RuO₂, *Solid State Ion.* 181 (2010) 536–544.
- [19] D. Muñoz-Rojas, M. Casas-Cabanas, E. Baudrin, Evolution of the electrochemical processes vs. Li in RuO₂ as a function of crystallite size, *Solid State Ion.* 180 (2009) 308–313.
- [20] J. Juodkazytė, R. Vilkauskaitė, G. Stalnionis, B. Šebeka, K. Juodkazis, EQCM study of Ru and RuO₂ surface electrochemistry, *Electroanalysis.* 19 (2007) 1093–1099.
- [21] M.C. Santos, A.J. Terezo, V.C. Fernandes, E.C. Pereira, L.O.S. Bulhoes, An EQCM investigation of charging RuO₂ thin films prepared by the polymeric precursor method, *J. Solid State Electrochem.* 9 (2005) 91–95.
- [22] H.-S. Nam, K.-S. Jang, J.M. Ko, Y.-M. Kong, J.-D. Kim, Electrochemical capacitance of nanoporous hydrous RuO₂ templated by anionic surfactant, *Electrochimica Acta.* 56 (2011) 6459–6463.
- [23] V.D. Patake, C.D. Lokhande, O.S. Joo, Electrodeposited ruthenium oxide thin films for supercapacitor: Effect of surface treatments, *Appl. Surf. Sci.* 255 (2009) 4192–4196.
- [24] Y.-Y. Liang, H.L. Li, X.-G. Zhang, Solid state synthesis of hydrous ruthenium oxide for supercapacitors, *J. Power Sources.* 173 (2007) 599–605.
- [25] K.S. Kim, N. Winograd, X-ray photoelectron spectroscopic studies of ruthenium-oxygen surfaces, *J. Catal.* 35 (1974) 66–72.

- [26] Y.J. Kim, Y. Gao, S.A. Chambers, Core-level X-ray photoelectron spectra and X-ray photoelectron diffraction of RuO₂ (110) grown by molecular beam epitaxy on TiO₂ (110), *Appl. Surf. Sci.* 120 (1997) 250–260.
- [27] A. Foelske, O. Barbieri, M. Hahn, R. Kötz, An X-ray photoelectron spectroscopy study of hydrous ruthenium oxide powders with various water contents for supercapacitors, *Electrochem. Solid-State Lett.* 9 (2006) A268–A272.
- [28] M. Vuković, D. Čukman, Electrochemical quartz crystal microbalance study of electrodeposited ruthenium, *J. Electroanal. Chem.* 474 (1999) 167–173.
- [29] A.V. Rosario, L.O. Bulhoes, E.C. Pereira, Investigation of pseudocapacitive properties of RuO₂ film electrodes prepared by polymeric precursor method, *J. Power Sources.* 158 (2006) 795–800.
- [30] K.-H. Kim, K.S. Kim, G.-P. Kim, S.-H. Baeck, Electrodeposition of mesoporous ruthenium oxide using an aqueous mixture of CTAB and SDS as a templating agent, *Curr. Appl. Phys.* 12 (2012) 36–39.
- [31] U.M. Patil, S.B. Kulkarni, V.S. Jamadade, C.D. Lokhande, Chemically synthesized hydrous RuO₂ thin films for supercapacitor application, *J. Alloys Compd.* 509 (2011) 1677–1682.
- [32] F. Razzaghi, C. Debiemme-Chouvy, F. Pillier, H. Perrot, O. Sel, Ion intercalation dynamics of electrosynthesized mesoporous WO₃ thin films studied by multi-scale coupled electrogravimetric methods, *Phys. Chem. Chem. Phys.* 17 (2015) 14773–14787.
- [33] I.-H. Kim, J.-H. Kim, K.-B. Kim, Electrochemical characterization of electrochemically prepared ruthenium oxide/carbon nanotube electrode for supercapacitor application, *Electrochem. Solid-State Lett.* 8 (2005) A369–A372.

General Conclusion & Perspectives

During this thesis project different types of MO_x thin films were studied by means of multi-scale time-resolved electrogravimetric methods for the very first time. An attempt was made to improve their electrochemical performance by using a nanostructuring approach in order to procure new morphologies of materials with favorable functionalities.

First, the results of our classical EQCM studies for various morphologies of TiO_2 prepared by reactive magnetron RF sputtering showed the advantageous role of the porous structure when compared with less porous and compact analogues. A fine study was then conducted by *ac*-electrogravimetry which proved a better performance of highly porous structures from both kinetic and thermodynamic points of view. While the exact identification of ions and their separation from free solvent molecules could not be achieved by our classical EQCM results, the involvement of different charged and non-charged species participating in the charge compensation process was detected and fairly separated from *ac*-electrogravimetric results. Moreover, in a comparison to understand the impact of accompanying solvent (either organic or aqueous) on the targeted parameters, the favorable nature of the aqueous electrolyte was revealed.

The advantageous impact of nanostructuring was also achieved by synthesizing mesoporous WO_3 thin films with surfactant assisted electrodeposition method using SDS molecules as porogen. *ac*-electrogravimetry was used to compare the mesoporous electrode with the compact counterparts. Due to an increased surface area provided by the presence of pores with a diameter of $\sim 2\text{-}5$ nm, it was underlined:

- ✓ The participation of anion even slightly as absent in results of dense WO_3
- ✓ A facilitated transfer of species especially larger charged cationic species,
- ✓ A larger quantity of charged species which can be stored in the film but also free solvent molecules transferred through the electrode/electrolyte interface.

The same electrochemical route was chosen to produce mesoporous hydrous $\text{RuO}_x \cdot n\text{H}_2\text{O}$ by using CTAB molecules as an ionic surfactant ($\sim 7\text{-}10$ nm of pore diameter). Again, our *ac*-electrogravimetric results demonstrated the attractive aspect of the mesoporous structure in particular when studied in acidic medium due to the better interaction of small H^+ ions with the hydrous $\text{RuO}_x \cdot n\text{H}_2\text{O}$ structure.

- ✓ This porous structure showed a high specific capacitance which stands well enough among other values reported in the literature.
- ✓ An ameliorated instantaneous capacitance was observed for the involved species.
- ✓ Lower transfer resistance of species was observed at the interface of mesoporous electrode/electrolyte.
- ✓ An amplified number of cations were willing to be transferred at the interface of this porous film.

In a final step of this project, it was aimed to pursue a similar concept for improving the performance of $\text{RuO}_x \cdot n\text{H}_2\text{O}$ electrodes by preparing a three-dimensional composite film based on SWCNTs/ RuO_x structure. A promoted behavior for this new structure was observed from our *ac*-electrogravimetric results. We observed that this structure benefited both from the high conductivity and large surface area of CNTs but also from the pseudocapacitive character of the thin $\text{RuO}_x \cdot n\text{H}_2\text{O}$ layers composed of nanometric grains. More precisely,

- ✓ An ameliorated instantaneous capacitance also lower R_{ti} compared to pure SWCNTs.
- ✓ An amplified number of cations willing to be transferred into the film compared to both bare SWCNTs and $\text{RuO}_x \cdot n\text{H}_2\text{O}$.

Indeed, the major originality of this work was brought by *ac*-electrogravimetry as a combined single body technique which allows the study of ions intercalation/electroadsorption phenomena to be performed in situ. This unique methodology permits the exact nature of the transferred ionic species, their dynamics of transfer at the interface as well as effects of ions solvation to be clearly investigated. The use of this combined technique for the characterization of our elaborated metal oxides and particularly its eligibility to underscore the real impact of their nanostructuration was reported for the first time. Therefore,

- ✓ The establishment of the *ac*-electrogravimetry characterization in the energy materials domain is significant for designing structurally optimized materials by any other up-to-date routes for the next-generation of high energy density supercapacitors. The latter subject of study discussed regarding composite materials could indeed be vastly developed in order to study and to compare the combination of pseudocapacitive metal oxides with CNTs.
- ✓ Another interesting category of insertion materials, namely “Layered Double Hydroxides (LDHs)” were developed in a first step by our EQCM studies on the thin films of $\text{Ni}_2\text{Al-NO}_3$ and $\text{Co}_2\text{Al-NO}_3$ showed very promising results, the combination

of LDHs with CNTs or even their sole study by *ac*-electrogravimetry remains as another original perspective to achieve. The comparison brought to discussion in the third chapter regarding the impact accompanying solvent (whether it is aqueous or organic) could be effectively expanded to a larger window for study by including ionic liquids to this comparison.